STUDY OF EVOLUTION OF MAGNETIC INHOMOGENEITIES ON THE SUN USING NARROW BAND IMAGING

A Thesis
Submitted for the Degree of
Doctor of Philosophy (Technology)

Submitted by

SAJAL KUMAR DHARA

Department of Applied Optics & Photonics
University College of Technology
University of Calcutta

August 2015

To my Family,

Friends & Teachers ...

Acknowledgements

First and foremost, I offer my sincerest gratitude to Dr. B. Ravindra and Dr. Ravinder Kumar Banyal, who supported me through out my thesis with their patience, knowledge and encouragement. I have enjoyed working with them and always found them open to discussions. Without their advice, guidance and experience, it would have been impossible to write this Thesis. I am also grateful to them for allowing me to travel and to attend to a number of scientific conferences and meetings. All in all, I will be indebted to them my entire life for all that they have given me within a short span of just five years and I am sure they will stand by my side in my future endeavors.

Many Many thanks to the Director, Dean and BGS of our institute for providing me with all the necessary facilities for my research work. I thank to Mr. K. Shankaranarayanan, Mr. Monnappa and Ms. Meena for helping me with various BGS related administrative procedures. Special thanks to the Librarian, Mr. B. S. Mohan, Mr. Prabhakar and the other staff of library for assisting me in accessing books and journals. I thank Dr. Baba Varghese, Mr. Fayaz, Mr. Ashok and Mr. Anish for their help in computer related issues. I also thank to Mr. Periyanayagam and Mr. Thimmaih N. for their help in making the mechanical items for our instruments. I thank to Kodaikanal Solar Observatory staff members Mr. Hariharan, Mr. Devendran and others for helping me carry out the observations at Tunnel Telescope and I also thank to Mr. Basha and other support staff for their hospitality during my stay at Kodaikanal.

I offer my heartiest thanks to Prof. P. Venkatakrishnan and Dr. Shibu K Mathew of Udaipur Solar Observatory for providing me Hα *filter for our Narrow Band Imager and also helping me in developing the temperature controller for the filter.*

Many Thanks to our Administrative Officer, Personnel Officer, Accounts Officer and all other administrative staff for their timely help in completing *the administrative related work.*

I would like to thank Prof. A. Ghosh, Prof. L. N. Hazra, Prof. K. Bhattacharya, Prof. R. Chakraborty, Prof. A. Basuray, Prof. M. Ray, Prof. A. K. Datta, Prof. A. K. Chakraborty and Prof. S. K. Sarkar for teaching me basic Optics, Electronics and Instrumentation during our course work in Calcutta University. I would also like to offer my sincerest gratitude to Prof. A. Ghosh who helped me a lot for joining this course. I thank to Chandan da, Biswajt Da, Saibal da and other staff members of Applied Optics and Photonics Department for helping me with various administrative procedures.

I am thankful to Prof. S. K. Saha who taught me basic speckle imaging techniques and helped me throughout our course. I thank to Prof. K. E. Rangarajan and Prof. K. Sankarasubramaniam for teaching me polarization and spectropolarimetry. I thank to Prof. D. Banerjee for teaching me solar physics during our course work. I am also thankful to other IIA faculties who has taught us during our course work.

I would like to offer my special thank to Arun surya, Anantha Chanumolu and Vineeth Valsan for all their help. They have been very entertaining (:)), joyful (:D), sad (:(), angry (X-(), co-operative and I learnt a lot from them. I thank to Sasikumar Raja for all his help during our course. I would like to thank IPhD batch mates Manpreet Singh and Avijeet Prasad for all their help and wonderful time I spent with them.

It is my pleasure to thank Samyaday, Krishna Prasad, Chandrasekhar, Jayashree Di, Amit Sukhla, Girijesh Gupta, Tanmoy, Arya, Prashanth, Indu, Ramya P. and all those who made my stay at IIA memorable. I indeed feel lucky to have so wonderful colleagues and Juniors and would like to express my thanks to Prasanta, Avrajit, Samrat, Anirban, Chayan, Subhamoy, Deepanwita, Megha, Rubinur, Bhumika, Snehalata, Tridib, Varun, Sireesha, Sreekanth, Ambily, Annu, Avinash, Sreejit, Hemanth, Joby, Joice, Sowmya, Supriya, Sangeetha, Prasanna S., Rakesh, Mayuresh, Mugundhan, Nancy, Nirmal, Prasanna Deshmukh, Drisya, Susmitha, Honey, Priyanka, Ramya, *Rathna, Dinesh, Sudha, Hema, Sindhuja, Shubham, Panini, Hariharan, D.V.S Phanindra, Anshu, Sudip, Jyotirmoy, Tarun, Narsi, Soumi, Amita, Kishore, Mageshwaran, Vaibhav, Manjunath Hegde, Amit, Anand MN, Anand Maitrey, Smitha S., Ananth Da, Madhulita Di, Tapan Mishra, Blesson Mathew, Sreeja S, Vigeesh G, Veeresh Singh, Ramya S, Bharat, Maitrayee, Deepthi, Estrella, Maya, John, Sriram, Darshan and Sripathy. I thank to Vemareddy for helping me out for the corrections of my thesis. I thank to Muthu Priyal, Priya and Kamesh for overwhelming time I spent with them. Specially, I would like to thank Kamesh for taking me out in his bike for site seeing in Kodaikanal.*

I would like to offer thank to Serampore College teachers, Ramakrishna Mission Residential College teachers for teaching me science subjects and Maharajas (Satya Da, Monomay Da and others) at Ramakrishna Mission Residential College for helping me through out M.Sc. career. I would also like to thank my B.Sc. and M. Sc. classmates Bholanath, Arnab, Suman, Soumen, Sayok, Mahatsab, Mintu and others. I cannot forget to mention all my wonderful friends Subhankar Da, Arup Da, Sanjit Da, Manas Da, Sourav Da, Swarup Da, Sailen Da, Dilu Da, Milan, Nirup, Suman, Santu, Amit for amazing time I spent with them in Krishnarampur. I am grateful to Sujay Da and other "Mahamondal" staff members for helping me all the time. My sincere gratitude to Becharam Dhara, Ramakrishna Dhara and my other uncles for supporting me all the time.

At last but not the least, I would like to thank my parents, uncle Asit Dhara, grandfather Manikchandra Parui and all the family members for their encouragement, blessings and everlasting heartily support, which is beyond the words. I am also grateful to my sister Kajal, brother Ujjwal, sister-in-law Mantu and cousins for their love and affection, which cannot be expressed here.

Sajal Kumar Dhara

List of Publications

I. Papers in Refereed Journals:

1. *Filament eruption in association with rotational motion near the filament footpoints*, **Dhara, Sajal Kumar**, Ravindra, B., Banyal, Ravinder Kumar, 2014, *New Astronomy,* **26**, 86 – 97 [1].

2. *Observations of Photospheric Vortical Motions During the Early Stage of Filament Eruption*, **Dhara, Sajal Kumar**, Ravindra, B., Banyal, Ravinder Kumar, 2014, *Solar Physics,* **289**, 4481 – 4500 [2].

3. *Fabry-Pérot based Narrow Band Imager for Solar Filament Observations*, **Dhara, Sajal Kumar**, Ravindra, B., Banyal, Ravinder Kumar, 2015, *Research in Astronomy and Astrophysics* (*Accepted for publication*) [3].

II. Papers in Proceedings:

1. *Performance Evaluation of a Visible wavelength range Fabry-Pérot Interferometer*, **Dhara, Sajal Kumar**, B. Ravindra, Banyal, Ravinder Kumar, *Frontiers in Optics and Photonics 2011, XXXVI OSI Symposium,* INS, 260–263 [4].

2. *Eruption of filament associated with active region NOAA 11444 as observed by AIA and HMI*, **Dhara, Sajal Kumar**, B. Ravindra, Banyal, Ravinder Kumar, *31st ASI Meeting, ASI Conference Series, 2013,* Vol. 9, pp 107 [5].

---

[5] Presented in Chapter 2

[1] Presented in Chapter 3

[2] Presented in Chapter 4

[3] Presented in Chapter 5

[4] Presented in Chapter 5

Presentations:

1. Poster presentation on '*On the role of photospheric velocity and magnetic field in the filament eruption as observed by HMI AIA/SDO*' at the meeting of the *Coupling and Dynamics of Solar Atmosphere, IUCAA Pune, November 10 - 14, 2014*, Pune, India.

2. Poster presentation on '*Development of Fabry-Perot based Narrow Band Imager for Solar Studies*' at the meeting of the *Astronomical Society of India, IISER Mohali, March 20 - 22, 2014*, Mohali, India.

3. Poster presentation on '*Eruption of filament associated with active region NOAA 11444 as observed by AIA and HMI* ' at the meeting of the *Astronomical Society of India, IISER-TVM, IIST and IRC Kochi, February 20 – 22, 2013*, Trivandrum, India.

4. Poster presentation on '*Filament Eruption associated with the C-class flare as observed by Solar Dynamic Observatory*' at the 39th *COSPAR Scientific Assembly, 14–22 July, 2012*, Mysore, India.

5. Oral presentation on '*Development of a Narrow Band Imager using Visible Wavelength range Fabry-Perot Interferometer for Solar Studies*' at *Inhouse meeting, February, 2012*, IIA, India.

6. Poster presentation on '*Performance Evaluation of a Visible Wavelength range Fabry-Perot Interferometer*' at *XXXVI OSI SYMPOSIUM (FOP11), IIT Delhi, December 3-5, 2011*, New Delhi, India.

7. Poster presentation on '*Characterization of Variable Gap Fabry-Perot Interferometer*' at *IONS-1, IIT Delhi, December 1-2, 2011*, New Delhi, India.

8. Oral presentation on '*Performance Evaluation of a Visible Wavelength range Fabry-Perot Interferometer*' at *GC-I meeting, February, 2011*, IIA, India.

Abstract

The solar atmosphere is structured by the evolving magnetic fields. These structures occur on different spatial scales. On small scale - bright points with thin boundaries have been observed. On large spatial scale - plages, sunspots and filaments/prominences have been observed. In the large scale structures, the magnetic field dominates and convection is inhibited. In each of these structures the magnetic field varies spatially and temporally. The spatial variation depends on the structures and the temporal variation depends on the flux emergence, cancellation and shear motions of its foot points. One such magnetic structure is solar filament which contain dense and cool ($\sim 10^4$ K) plasma embedded in the tenuous and hot corona. They normally form in active regions, though not very uncommon in quiet regions. Filaments appear above a boundary between the opposite polarity of magnetic fields on the Sun, normally called as polarity inversion line. When viewed in Hα, filaments appear to be aligned along the PIL and the field lines are mostly non-potential in nature. Their presence is visible in the chromosphere and lower part of the corona. The quiet filament structures are highly stable and most of them will survive for weeks to months. On the other hand, the active region filaments evolve rapidly and they can survive over a period varying from few hours to days. Most often, the filament ends up with eruption associated with solar flares and CMEs. In this thesis, I have studied a few active region filament eruption using high resolution coronal data from AIA/SDO and ground based Hα data from BBSO and GONG.

Filaments/prominences exhibit a variety of dynamical processes during their formation, evolution and prior to eruption. The observation made in multiple wavelengths around a chromospheric spectral line are used to infer dynamical processes such as converging motions and rotational motions in the ends of the filaments during the eruption. In this thesis, another work is to develop a narrow band imager using Fabry-Perot interferometer, which can provide images at the chromospheric height in the solar atmosphere and also it is capable of producing dopplergrams to study the line-of-sight motions during the filament eruptions. This thesis is organized as follows:

The first chapter highlights the different trigger and instability mechanisms behind filament eruptions studied in the past. I have discussed different dynamical processes often seen during filament eruptions. This chapter also discussed the motivation to build a narrow band imager to study the rotational motion at the legs of the filaments/prominence during eruption. Finally, a brief content of each chapters are presented.

In the second chapter, I have discussed about different data set used for the observational study of the filament eruption events. A two-stage filament eruptions associated with the active region NOAA 11444 have been studied to understand sequence of events occurred during eruptions. A detailed study about converging motion and flux cancellation in connection with pre-eruption brightening and bright flow at the coronal images during activation of first phase of eruption are presented here. During the second phase of eruption, the flux cancellations, expansion of loops, brightened cusp shaped loops and the contraction of overlying coronal loops near the filament have been observed. The importance of the magnetic flux cancellations, expansion of loops, reconnection and contraction of overlying coronal loops towards the second phase of filament eruption are also discussed in this chapter.

In the third chapter, the study of an another active region filament eruption event is presented in EUV and visible wavelength regime. The filament eruption occurred in the southern hemisphere of the Sun on 08 July 2011. The study suggests that the emerging flux, converging motion and injection of opposite magnetic helicity could be responsible for destabilization of the western footpoint of the filament leading to eruption. As an interesting phenomena, an anti-clockwise rotational motion in both the footpoints just after the onset of filament eruption is observed during the eruption. In this chapter, a plausible reason for the eruption in the context of observed rotational motion has been discussed.

Primary objective of the fourth chapter is to understand the relation between the occurrence of the rotational/vortical motion observed near the ends of the filament and eruption of the filaments. Several active region filament eruptions are presented in details. For all the reported events, the rotational/vortical motion in the photosphere near the ends of all active region filaments during their initial phase of eruption or at the onset phase of the fast rise of the filament are observed. The importance of this rotational/vortical motions at the endpoints of the filaments during their activations towards eruptions are discussed in this chapter.

Fifth chapter describes the development of the narrow band imager (NBI) using Fabry-Perot (FP) interferometer and an order sorting filter. The FP and filter have been tested in a series of experiments carried out in the laboratory. The NBI is capable to imaging the solar atmosphere at 6563 Å chromospheric Hα line. The observed data are used to produce dopplergrams at the chromospheric height to study the rotational motion near the legs of the filaments during its activation. At the end, I have presented several observed filaments using NBI and made few dopplergrams of the filament region at chromospheric height.

The last chapter provides the summary and conclusions of this thesis work. The thesis ends with a brief descriptions of the planned future work in which research can be carried out further.

Contents

1 Introduction 1

List of Figures

List of Tables

Chapter 1

Introduction

1.1 The Sun

The Sun is our nearest star. The Sun is a common main sequence star of spectral class G2V. There are more than 100 million G2 class stars in our galaxy, so the Sun is not peculiar from the astronomical point of view. However, the Sun is the only star we can observe with highest spatial, temporal and spectral resolution. Study of the Sun aided us to understand the physical properties of other stars. In a way Sun is the key to understand the rest of the universe.

The Sun is in plasma state throughout with hydrogen as the major content. The structure of the Sun can be considered as a series of concentric spherical layers, each of them characterized by a unique combination of physical processes. The center of the Sun is the nuclear burning core. Traveling outward, one encounters first radiative zone, then convective zone and then solar atmosphere. The solar atmosphere is divided into the photosphere, the chromosphere, the transition region and the corona. The cartoon in Figure 1.1 shows the different layers of the Sun.

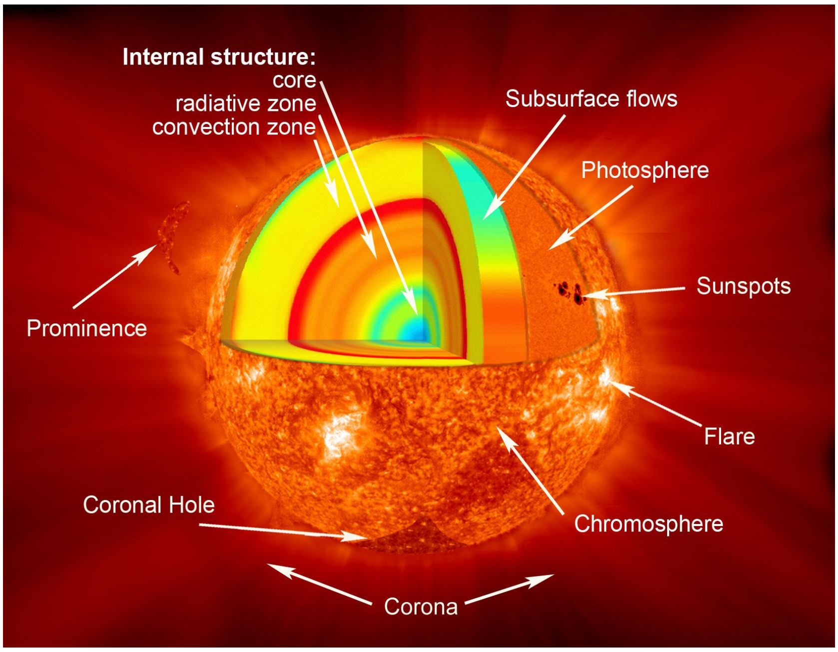

Figure 1.1: The cartoon shows the different layers of the Sun from interior to solar atmosphere. The solar interior is divided as the core, the radiative zone and the convection zone. The solar atmosphere is divided as the photosphere, the chromosphere, a transition region and the corona (Image Credit: NASA).

1.2 Solar Atmosphere

1.2.1 Photosphere

The visible surface of the Sun is called *photosphere* from where energy generated at the Sun's core begins to escape into space as radiation. Photosphere has the thickness of about 300 - 500 km. It is a region where optical depth τ, is unity for radiation of wavelength 5000 Å. The temperature at this surface is about 6400 K. On the photosphere one can see sometimes small or big dark regions called sunspots. Apart from these, there are convective patterns - the granulation and near the limb one can also see bright patches called faculae. Sunspots and faculae both have strong magnetic fields. They are the two main photospheric activities that vary in magnitude and location with time. Appearance of sunspots is the direct indication of solar activities. All these features survive from a few minutes to several months. For example, faculae may survive for a few weeks and the sunspots last for a few hours to several months, the normal lifetime of a granule pattern is about 3 to 12 minutes.

1.2.2 Chromosphere

The *chromosphere* situated just above the visible surface of the sun extends to about 10,000 km height. Chromosphere (chromos meaning "*color*") was named by 19th century solar astronomers because of the distinct reddish (because of strong Balmer Hα emission) arcs seen in this layer during a total solar eclipse. This layer consists of a tenuous gas having a density much less than photosphere. The density decreases as a function of radial distance or height from the surface. Assuming local thermodynamic equilibrium (LTE), according to hydrostatic standard models the temperature of the solar atmosphere reaches first a minimum of around 4300 K at a height of around 500 km above the photosphere and then increases gradually to 10,000 K in the upper chromosphere, but at the same time the hydrogen density drops by about a factor of 10^6 over the same chromospheric height range. One can also see some interesting features with appropriate narrow band optical filters in this layer. These features are best seen in the strong Fraunhofer lines of ionized Calcium, Magnesium and neutral Hydrogen. The chromospheric features are spicules, filaments/prominences, Ca-II and Hα network etc.

1.2.3 Transition region and Corona

The region where temperature reaches $\approx 10^6$ K and densities are very low compared to the chromosphere is known as the solar *corona*. There is a sharp increase of temperature from about 10^4 K at the top of the chromosphere to 10^6 K in the corona. This change occurs in a very narrow region of few hundred kilometers of the solar atmosphere, which is called the *transition region*. This transition region is best observed in the strong EUV resonance lines such as Fe IX, Fe XII, Fe XV, He II and Mg IX etc. The solar corona is optically thin at visible wavelengths and the optical radiation are not absorbed while traversing the corona over the solar disk like the chromosphere and photosphere, hence the coronal features are not seen in the visible light on the solar disk. The solar corona is highly structured and it consists of fine filamentary coronal loops and plumes, helmets-shape features, streamers etc., which are outwardly directed and extended far out from the solar disk. These coronal features are visible in X-rays and EUV radiation.

1.3 The Sun and the Earth

The Sun is essential for us since it is a source of light and energy, which supports life on the Earth. Apart from providing energy and steady light, the Sun affects the near Earth space and terrestrial atmosphere in a variety of ways. High energy radiation and particle emission are the two processes by which it can affect the Earth's atmosphere. Sun is the source of *solar wind* which is a flow of gases that streams off in all directions at speeds exceeding 500 km s^{-1}. This solar wind, which is flowing against Earth's magnetic field, shapes the near-Earth space environment. Disturbances in the solar wind shake Earth's magnetic field and pump energy into the radiation belts. Regions on the surface of the Sun often flare and emit ultraviolet rays and X-rays that heat up the Earth's upper atmosphere and also create ionosphere. The coronal mass ejections (CMEs) are the large eruption of magnetized plasma from the corona in the form of charged particles that propagates outward into interplanetary space. These charged particles can physically damage satellites, communication systems, power grids and pose a threat to astronauts. These charged particles also cause the aurora in the polar region. Solar magnetic fields play a major role in production of particle emission and high energy radiation. Hence, the evolution of magnetic fields in the solar atmosphere influences some aspects of the space weather, near Earth space environment and Earth climate. It is very important to study the evolution of magnetic field to predict the space weather and long-term variations in the Earth's climate.

1.4 Solar Magnetic Field

The solar magnetic fields control all the dynamics observed in the solar atmosphere. Solar activity rises and falls with an 11-year cycle, called solar cycle. The total radiation from the Sun is also known to be varied with the solar cycle. Increased solar activity includes enhancement in extreme ultraviolet and X-ray emissions. The polarities of the global magnetic field of the Sun is reversed in every 11-year. Figure 1.2 shows a synoptic mapping of surface magnetic field of the Sun. It shows that the polarities of the poloidal magnetic field component undergoes cyclic variations and changes polarities at the times of sunspot maximum. The East-West magnetic field orientations in the active regions is found to be opposite in northern and southern hemispheres and it also shows reversal in every 11-year cycle. The total magnetic flux reaches maximum during the peak of the solar cycle and drops to almost zero during the minimum of the solar cycle.

1.5 Solar Magnetic Field Evolution

Evidently, the solar atmosphere is structured by the evolving magnetic fields. These structures occur on different spatial scales. On small scale - bright points with thin boundaries have been observed. On large spatial scale - plages, sunspots and filaments/prominences have been observed. Convection is one of the energy transport mechanisms which results in convective patterns on the Sun such as granulation, mesogranulation, supergranulation and giant cells. Only granules and supergranules have been observed and well studied. These convective cells are embedded within small scale magnetic fields (Leighton, Noyes, and Simon, 1962; Simon and Leighton, 1964). In

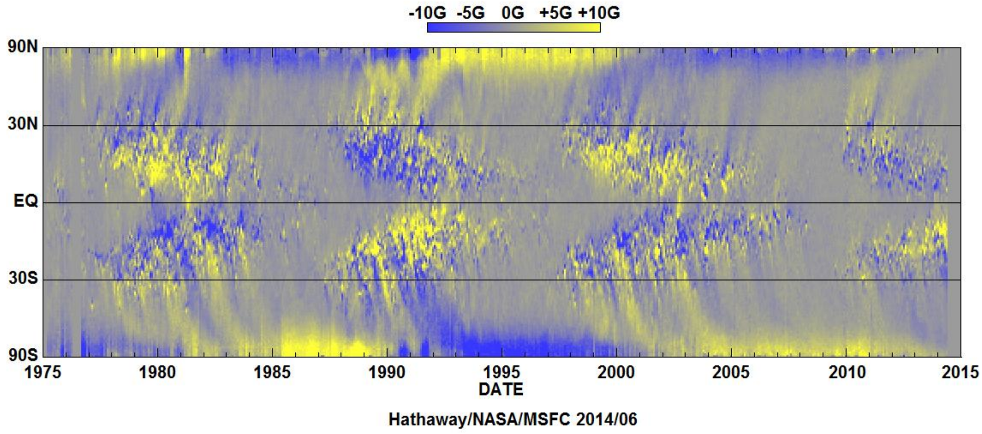

Figure 1.2: Synoptic magnetogram of the radial component of the solar surface magnetic field obtained from instruments on Kitt Peak and SOHO. This figure illustrates polar field reversals. (courtesy of D. Hathaway, NASA/MSFC; http://solarscience.msfc.nasa.gov /images/magbfly.jpg).

association with the magnetic field, supergranulation forms a pattern called network cells (Hart, 1956; Simon and Leighton, 1964; Simon *et al.*, 1988). The magnetic network is not regularly distributed on the boundaries of supergranulation cells but rather concentrates into localised structures. The edges of the network coincide with boundaries of the photospheric velocity cells. The horizontal plasma motions inside the supergranulation push the frozen-in field line towards the cells boundaries.

In the large scale structures (active regions and plages), the magnetic field dominates and convection is inhibited. In each of these structures the magnetic field varies spatially and temporally. The spatial variation depends on the structures and the temporal variation depends on the flux emergence, cancellation and shear motions of its footpoints. Most of the small scale structures contribute to the solar irradiance (*e.g.,* Schnerr and Spruit 2011). However, the large scale structures not only contribute to the solar irradiance (*e.g.,* Mordvinov and Willson 2003), they also affects the space weather in the form of mass ejections from the solar corona (*e.g.,* Fainshtein and Ivanov 2010).

Large scale magnetic fields are the sites of sudden release of magnetic energy. Solar flares and coronal mass ejections (CMEs) are powered by the release of magnetic energy stored in coronal magnetic fields (*e.g.,* Gold and Hoyle 1960; Sturrock 1980). Solar flares are explosive phenomena observed in the solar atmosphere and the energy releases during a flare are about 10^{30}–10^{32} ergs. Flares are observed in a wide range of electromagnetic wavelength such as radio, visible light, X-rays, and gamma rays. Emissions in these wavelengths come from the chromosphere to the corona of the solar atmosphere. In Hα chromospheric image, one can see a flare often shows two ribbons of bright patches, and the distance between these ribbons increases with time (Svestka, 1976; Zirin, 1988). The frequency of occurrence of these events is related to the 11-year solar cycles, but unlike global magnetic fields, these events have duration of few minutes to hours. During solar maxima, several large as well as small solar flares can be observed on most of the days. These solar flares are always located near the sunspots and plage regions. They occur very often when sunspot number is large. This does not mean that sunspots are the direct cause of flares but rather indicate that solar flares are associated with the magnetism of the sunspots. These spectacular and energetic events affects the space weather and near earth environment. They may have direct bearing on human life on Earth.

Coronal mass ejections (CME) are spectacular eruptions in the solar atmosphere. They have loop like structure, expands in the forward direction and carries material to the interplanetary space. One example of CME is shown in Figure 1.3, which occurred on 02 December, 2002. While propagating from the low corona to the interplanetary space, they frequently interact with the Earth (and other planets), producing a series of impacts on the terrestrial environment and influence the performance and reliability of human spaceborne and ground-based technological systems (*e.g.,* Pulkkinen 2007; Schwenn 2006). CMEs tend to occur, when the upward forces dominate over the downward forces in a balanced coronal loop. At coronal heights the plasma $\beta \ll$

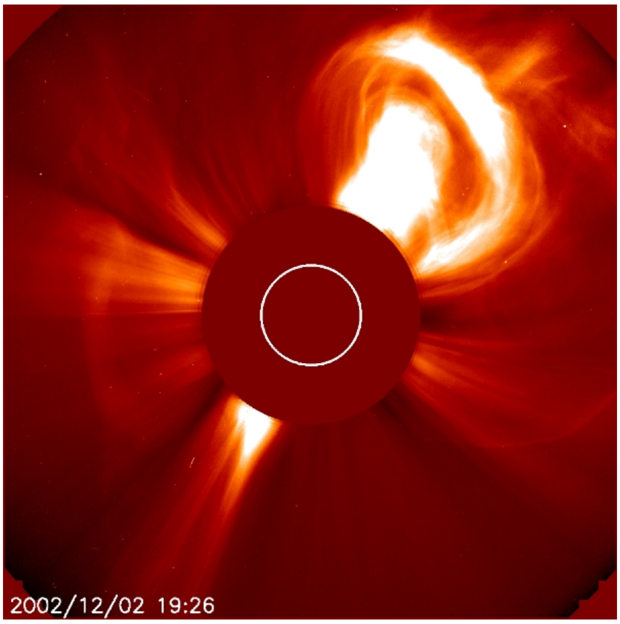

Figure 1.3: Image shows a large coronal mass ejections on 02 December, 2002 (from SOHO/LASCO database), where the white circle marks the solar photosphere.

1 that implies the magnetic pressure dominates the plasma pressure, especially in the active regions. Hence, magnetic energy is the one that can push the materials to the distant heliosphere. The photospheric motions e.g., the differential rotation, supergranular, and granular convections etc. drag the footpoints of all the magnetic field lines to move in both organized and random ways which builds up a highly stressed coronal magnetic field (Forbes, 2000). As a result, Poynting flux is continuously injected into the corona and the magnetic energy is thus accumulated gradually. Though most of the CMEs are followed by the flares, on many occasions the filament/prominence eruptions are the major source of CMEs (*e.g.,* Gilbert *et al.* 2000) and they are also strongly related (*e.g.,* Gopalswamy *et al.* 2003a; Jing *et al.* 2004), as shown in Figure 1.4. The part of the erupting filament becomes the bright core of the CME, with the remaining part falling back to the solar surface. In order to understand the severity of the space weather, it is important to understand the dynamics of solar flares and the associated filament/prominence eruptions.

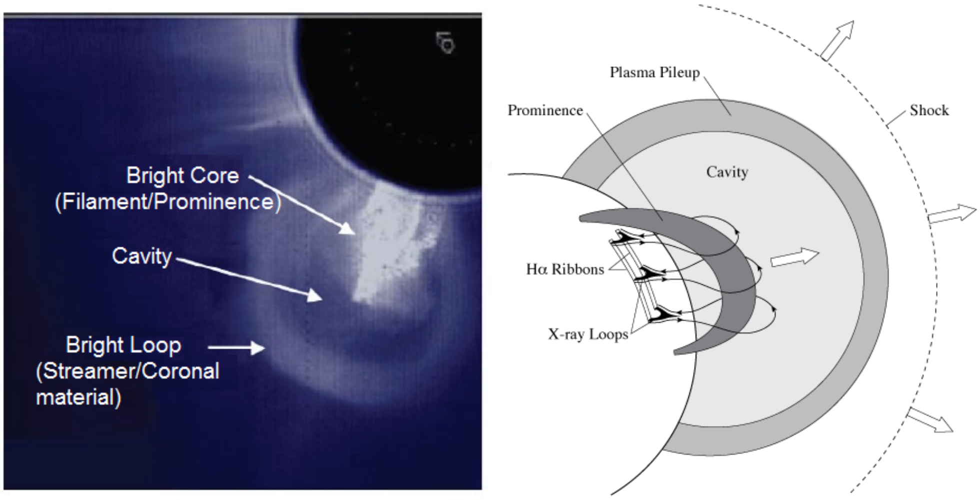

Figure 1.4: Left: A Solar Maximum Mission archive image showing the principal features of a CME Image (Courtesy of van Driel-Gesztelyi and Culhane 2009, copyright by Springer). Right: A schematic view of the CME features (Courtesy of Forbes 2000).

1.6 Solar Filaments/Prominences

Solar filaments are large magnetic structures which contain dense and cool ($\sim 10^4$ K) plasma embedded in the tenuous and hot corona. They are observed on the solar disk and appear as dark, thin threads for example in Hα 6562.8 Å and in He-II 304 Å wavelengths (which is among the brightest lines produced by the chromosphere). Filaments absorb all of the light in the Hα line and re-emit it. In the direction of the observer the amount of light the filament re-emits is very less compared to light coming from the rest of the solar disk in the same wavelength band. As a result, the filament appears dark on the solar disk. When the filaments are observed on or above the solar limb, they appear as bright arcade-like structures (or thin and long clouds). In this case they were historically called *prominences*. The light emitted by prominences towards the observer is more than that scattered by the tenuous corona and as a result they appear bright. Thus, filaments and prominences are two different perspectives of looking at the same solar feature. Figure 1.5 shows a full disk image of the Sun in Hα from Kodaikanal

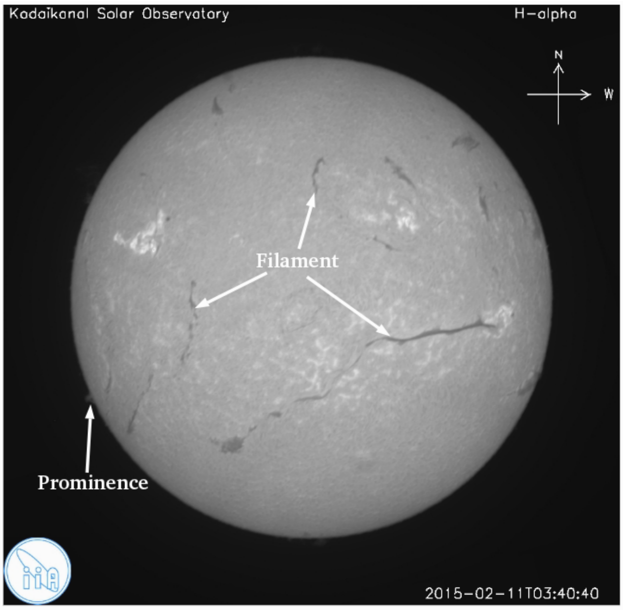

Figure 1.5: A full disk image of the Sun in Hα wavelength obtained on 11 February 2015 using 20 cm Hα telescope installed at Kodaikanal Solar Observatory. The image has the resolution of 1.2$''$/pixel. On the disk, the filaments appear darker than the surrounding quiet Sun. The off-limb prominence appears as bright structure.

Solar Observatory, taken on 11 February 2015. Few long filaments in each hemisphere on the solar disk, can be seen in the image, in addition to several smaller ones and a prominence structure is also visible above the solar limb. Filaments/prominences are observed in the layer of solar atmosphere, such as the chromosphere, or the lower corona.

Apart from the Hα (6562.8 Å), other lines in the solar spectrum are also used to observe filaments. Filaments are not seen in the photospheric images such as continuum and G-band images. However, their presence is visible in the chromosphere and lower part of the corona. From 1995, the Extreme-Ultraviolet Imaging Telescope (EIT; Domingo, Fleck, and Poland 1995) on board Solar and Heliospheric Observatory (SOHO; Delaboudinière *et al.* 1995) has been extensively used to observe filaments as well as prominences in He II 304 Å wavelength. These are also visible as dark structure in the coronal images taken in 171 Å(Fe IX), 195 Å (Fe XII) and 284 Å (Fe XV) etc.

Filaments normally form in active regions, though not very uncommon

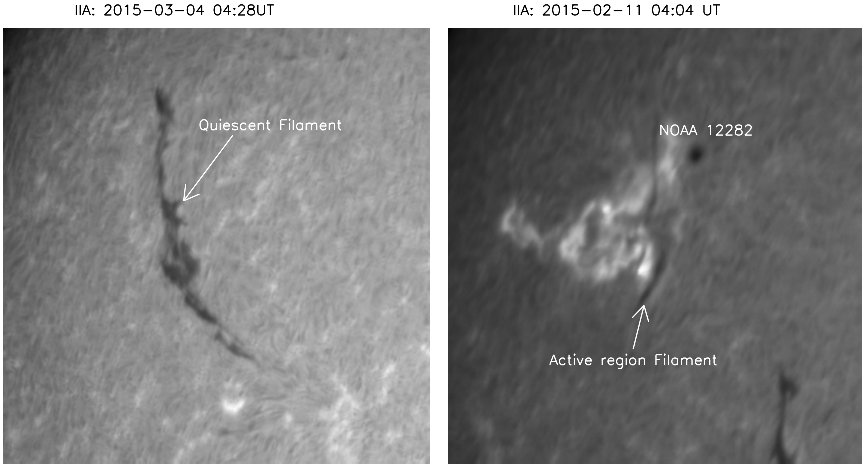

Figure 1.6: Left: A quiescent filament observed on 04 March 2015 from 20 cm Hα telescope installed at Kodaikanal Solar Observatory. Right: A filament associated with active region NOAA 12282, observed from the same telescope on 11 February 2015. The images have the resolution of $1.2''$/pixel.

in quiet regions. They are classified as active region and quiescent filament based on their formation region. Figure 1.6 shows the active region and quiescent filament observed from Kodaikanal Solar Observatory. The active region filaments are found in and around the active regions, i.e., areas with high magnetic fields. On the other hand, the quiescent filaments are found in the quiet Sun region or areas with low magnetic fields. The long axis of the filament, often seen as a well-defined sharp edge is known as the *spine*. The spine lies above a boundary between the opposite polarity of magnetic fields on the Sun, normally called as polarity inversion line (PIL; Babcock and Babcock 1955). When viewed in Hα, filaments appear to be aligned along the PIL and the field lines are mostly non-potential in nature. Filaments on the disk show that they are supported by a series of legs, which extend outwards on either side of the spine. These legs are known as *barbs*, which are anchored in the low chromosphere and photosphere (Engvold, 1998). The quiescent filaments are highly stable and most of them survive for weeks to months (Martin, 1998a). On the other hand, the active region filaments evolve rapidly and they can survive over a period varying from few hours to days.

Most often, the filament ends up with eruption associated with solar flares and as core of CMEs (Gopalswamy *et al.*, 2003b; Schmieder *et al.*, 2002).

1.7 Filaments/Prominences Eruption

This thesis attempts to study the active region solar filament eruption for few events. The active region filament structure can sustain for a few hours to days in the corona. The equilibrium of this structure in the solar atmosphere is maintained by the balance between several forces. Some of these forces acting upwards (buoyancy force and magnetic pressure) and others acting downward (magnetic tension and gravitation). The equilibrium structure of a system of magnetic field and plasma on the Sun can be described by the magnetohydrodynamics equation as,

$$-\nabla p + \frac{1}{\mu}(\nabla \times \mathbf{B}) \times \mathbf{B} - \rho \nabla \Phi = 0 \tag{1.1}$$

Where, p is the plasma pressure, $\mathbf{B}$ is the magnetic field, ρ is the density, and Φ is the gravitational potential on the Sun's atmosphere. Using the vector identity

$$(\nabla \times \mathbf{B}) \times \mathbf{B} = (\mathbf{B} \bullet \nabla)\mathbf{B} - \nabla(\frac{B^2}{2}) \tag{1.2}$$

eq. 1.1 can be written as

$$-\nabla p + \frac{(\mathbf{B} \bullet \nabla)\mathbf{B}}{\mu} - \nabla(\frac{B^2}{2\mu}) - \rho \nabla \Phi = 0 \tag{1.3}$$

It is clear from the eq. 1.3 that the magnetic field introduces a pressure $B^2/2\mu$ and other term $(\mathbf{B} \bullet \nabla)\mathbf{B}/\mu$ is of nature of a tension force along the magnetic field lines. The equilibrium of the filament is ensured by the downward acting gravitational force and a component of the tension force, upwardly directed magnetic and gas pressure.

The ratio of plasma and magnetic pressures is given by

$$\beta = \frac{p}{B^2/2\mu} \tag{1.4}$$

In the chromosphere and coronal regions, the magnetic field generally dominates the plasma pressure and gravity forces. In the corona, $\rho = 10^9 cm^{-3}$, $B = 10\ G$ and $T = 10^6\ K$, the plasma $\beta << 1$. Where, ρ is the plasma density at the thermal temperature T with ambient magnetic field of magnitude B. Hence, the equilibrium can be written as, approximately

$$(\nabla \times \mathbf{B}) \times \mathbf{B} = 0 \tag{1.5}$$

This eq. 1.5 defines the force-free magnetic field, in which Lorentz force balances by itself. From Ampere's law, $\nabla \times \mathbf{B} = \mu \mathbf{J}$, where $\mathbf{J}$ is current density, so, one can also write force-free equation in terms of currents as, $\mathbf{J} \times \mathbf{B} = 0$.

The destabilization of the filaments can happen internally or it may be caused by some external factor. Pre-eruption phase and activity near the filament are important to understand the trigger mechanism for the eruption and rapid energy release. As an external trigger, several models are proposed to explain the solar eruptions and to examine the role of the initial magnetic reconnection which set up the conditions that are favorable for the magnetic core fields to erupt. In the past decades, several triggering mechanisms have been proposed either conceptually or through MHD analysis and/or simulations. An overview of the few possible triggering mechanisms that favorable for filament eruption are described below.

1.7.1 Tether-cutting reconnection mechanism

Tether cutting mechanism is an implosive/explosive reconnection process which occurs within the twisted and deep sheared core field of a bipole above the polarity inversion line of the arcade (Moore and Labonte, 1980; Moore *et al.*, 2001). Moore and Labonte (1980) analyzed a filament eruption event which occurred on 29 July 1973, associated with a large expanding two-ribbon solar flare. They found that the magnetic field is strongly sheared near the magnetic neutral line and the eruption was proceed by small Hα brightenings and mass motion along the magnetic neutral line. This Hα brightening and the initial brightening of the flare are both located in the vicinity of the steepest magnetic field gradient. Following the observation, the tether-cutting mechanism is depicted in Figure 1.7. A filament is supported somehow on dips, by magnetic field, which is nearly aligned with the PIL. The magnetic field is strongly sheared (the field lines AB and CD), which could correspond to the associated SXR sigmoid (for details see review paper by Chen (2011)). Before the filament eruption, the downward magnetic tension force is balanced by an outward magnetic pressure force. When the magnetic shear increases, the field line AB become close to be anti-parallel to the other field line CD, which forms a strong current sheet in between (see Figure 1.7 left panel). The line-tied field lines AB and CD are now like tethers constraining the filament. After magnetic reconnection commences, the line-tied field lines AB and CD are cut from being tied to the photosphere, which finally forms a long field line AD and a short loop CB (see Figure 1.7 middle panel). This kind of reconnection could produce Hα brightenings and mass motions along PIL. After the reconnection, the loop AD is concave-upward near the reconnection site, which finally pulls up the filament to rise by imposing an upward magnetic tension force. The short loop CB is concave-downward, which may even submerges downward. Sterling, Moore, and Freeland (2011) analyzed an active region filament eruption occurred on 12 May 2010, which was due to the onset of a magnetic instability and/or runaway tether cutting. Recent results show a direct observational evidences for 'Tether-Cutting' mechanism in at least two events (Chen *et al.*, 2014).

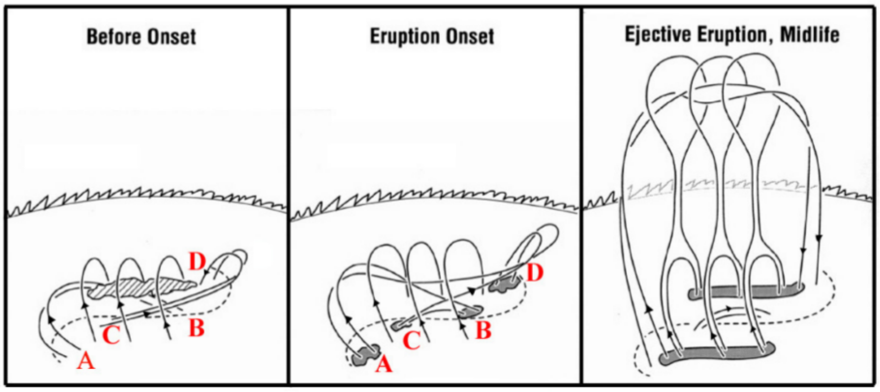

Figure 1.7: The cartoon depicts the idea of tether-cutting triggering mechanism sequentially in three panels (figure courtesy of Chen 2011; Moore *et al.* 2001). The dashed curve represents the photospheric polarity inversion line, dividing line between the two opposite-polarity domains of the bipoler magnetic roots. Left: The strongly sheared core field lines AB and CD are restrained by the overlying less-sheared envelope field. Middle: The reconnection is happening between field lines AB and CD, which triggers the core field to move upward. Right: Following the reconnection outflow, the long loop AD expands upward and the small loop CB shrinks downward.

1.7.2 Flux cancellation mechanism

Simulation by van Ballegooijen and Martens (1989) suggest that the magnetic flux cancellation near the magnetic neutral line of a sheared magnetic arcade could produce helical magnetic flux rope, that can support a filament. If the flux cancellation continue further, which could result in the eruption of the previously-formed filament (Amari *et al.*, 2003). The flux cancellation model is the same as the tether-cutting model in nature. The flux cancellation model might emphasize a more gradual evolution of magnetic reconnection in the photosphere, while tether-cutting is a relatively more impulsive process occurring in the low corona. The flux cancellation allows the flux rope to move upward. Chen, Jiang, and Ma (2009) studied a Hα filament eruption associated the active region NOAA 10044 on 29 July 2002. Their study shows that as an internal trigger, opposite polarity magnetic flux cancellation at the footpoints of the filament and along the main magnetic neutral line, lead to the destabilization and eruption of the filament.

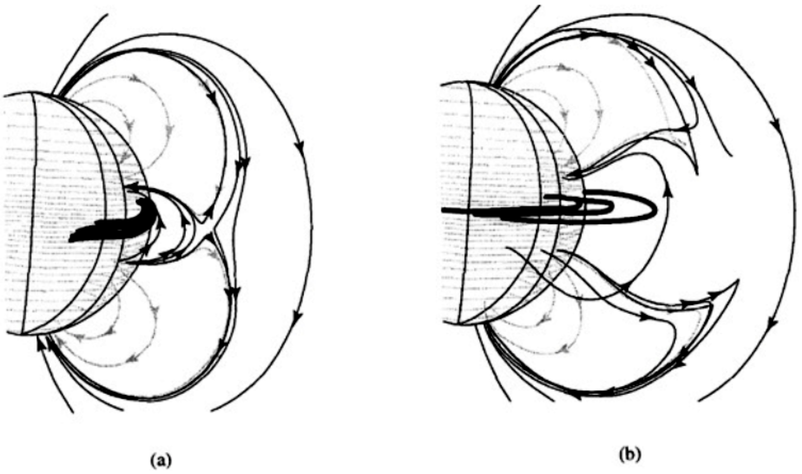

Figure 1.8: Depiction of the evolution of the magnetic field in the breakout model. The reconnection above the central flux system removes the constraint over the core field (thick lines) and which finally ends up with drastic eruption (figure courtesy of Antiochos, DeVore, and Klimchuk 1999).

1.7.3 Breakout model

There is another reconnection process named as ‘breakout’, as shown in Figure 1.8. In this case the topology of the erupting system is multi-polar and it is a tension release mechanism that occurs between a sheared arcade and neighboring flux system which triggers the eruption (Antiochos, 1998; Antiochos, DeVore, and Klimchuk, 1999). The null point is located above the central flux system. When the central flux system experiences shear motions, it expands upward, pressing the X-type null point to form a current layer. If one now consider the gas pressure and resistivity, the current sheet would undergo magnetic reconnection owing to anomalous resistivity or other non-ideal effects. This reconnection process removes the constraint of the higher magnetic loops, which leads to drastic formation and eruption of the core field (thick lines in the Figure 1.8). This magnetic breakout model can be regarded physically same as the tether-cutting mechanism, and it can be considered as the external tether cutting. Lynch *et al.* (2004) has compared the MHD simulation results of such an eruption process with the CME features in observations. Aulanier *et al.* (2000) presented the first evidence supporting the breakout model for the active region 8270, associated with a M3-class flare on 14 July 1998. They found a null point above the source region in the extrapolated coronal magnetic field. Ugarte-Urra, Warren, and Winebarger (2007) attempted to test current initiation models of CMEs, with an emphasis on the magnetic breakout model and they found the initiation of 7 out of 26 CME events in their study can be interpreted in terms of the breakout model.

1.7.4 Instability

As we know filament eruptions happen in a very short time scale as compared to the time scale of the coronal magnetic energy accumulation, hence there should be some kind of instability related to the trigger of the eruption. Following this, various instability mechanisms have been modeled (see review by Forbes 2000). Sakurai (1976b) numerically analyzed the development of the kink instability of a twisted flux tube. He selected three types of prominences (arch type, loop type, and gigantic arch type, identified on the basis of their shapes) to clarify the relationship between the motion and the magnetic field in eruptions of chromospheric prominences. His study suggests that the kink instability can explain the observed height-time profile of an erupting prominence. By taking into account the line-tying effect of the photosphere on the kink instability of the twisted flux tubes, Hood and Priest (1979) mentioned that there is a critical twist, above which the flux tube is unstable. This value depends on the aspect ratio of the loop, the ratio of the plasma to magnetic pressure and the detailed transverse magnetic structure. In their analysis, the critical twist ranges from 2π to 6π. However, we can not rule out the effect of the external magnetic field overlying the twisted flux tube. If the overlying magnetic arcade decreases slowly with height, the kink instability would be suppressed, which may lead to failed eruption, and if the overlying magnetic field decreases very rapidly, the kink instability would lead to an eruption

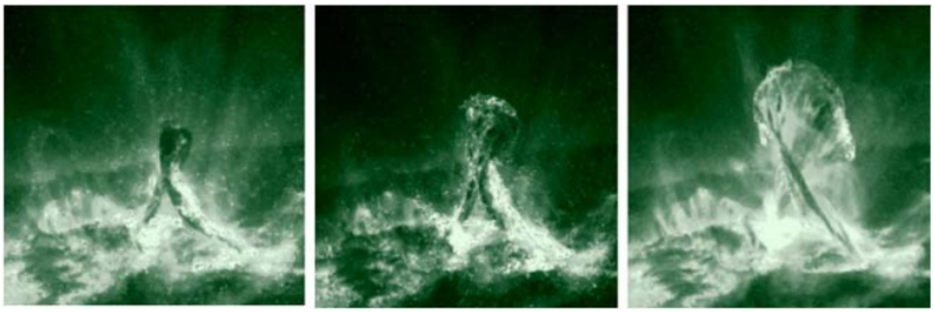

Figure 1.9: Filament eruption event on 27 May 2002 shows a significant kinking, as observed by TRACE 195 Å (figure courtesy of Gilbert, Alexander, and Liu 2007).

(Török and Kliem, 2005). There are several observational evidences where the kink instability is the trigger mechanism for the solar filament eruption. One of the recent example of a filament eruption is analyzed by Yan *et al.* (2014) for the active region NOAA 11485. Their study showed that the leg of the filament rotated up to 2.83π around the axis of the filament with a maximum rotation speed 100 degrees/minute. Figure 1.9 shows an example of a significant kinking during eruption. This failed filament eruption occurred on 27 May 2002 as observed by TRACE 195 Å. The kinking motion is clearly seen when observed in projection, it exhibit a clear " inverted gamma" shape formed by the crossing of the filament legs.

The filament/flux rope can face an another type of instability called "torus instability"(see, Kliem and Török 2006; Zuccarello *et al.* 2014). Using MHD numerical simulations in a three-dimensional spherical geometry, Fan and Gibson (2007) studied the emergence of a flux rope from the subsurface into the magnetized corona. Their study suggests that when the background magnetic field decreases slowly with height, a strongly-twisted flux tube emerging out of the solar surface, which may rupture through the arcade field via kink instability. But when the background magnetic field decreases rapidly with height, then the flux rope can become unstable to the lateral expansion and then it erupts. This kind of loss of equilibrium could be interpreted as "torus instability" (Chen, 2011). In this model, a current ring of major radius R

is embedded in an external magnetic field (B_{ex}). The current rings are subjected to a radially outward-directed hoop force. When the ring expands, the hoop force decreases. If the inward-directed Lorentz force due to the external field (B_{ex}) decreases faster with radius R than the hoop force, the system is unstable to perturbations. The decay index for a current ring of major radius R and embedded in an external field B_{ex}, is defined as follows (Zuccarello *et al.*, 2014):

$$n = -R\frac{d}{dR}(lnB_{ex}) \tag{1.6}$$

Assuming external magnetic field $B_{ex} \propto R^{-n}$, Bateman (1978) numerically showed such an instability will occur when $n > n_{critical} = 1.5$. Recently Zuccarello *et al.* (2014) present an analysis of the observation of a filament eruption which occurred on 4 August 2011 and the eruption mechanism agrees with the torus instability model. They also mentioned that some pre-eruptive processes such as magnetic flux cancellation at the neutral line and magnetic reconnection during the observed flares, triggered the eruption and helps to bring the filament to a region where the magnetic field was more vulnerable to the torus instability.

The filament eruptions can be triggered in a variety of ways. It could be either by instability or reconnection or both. Hence, it is very important to study which of these above mentioned mechanisms dominate under what circumstances for a successful eruption. One of the aims of this thesis is to examine and understand the detailed mechanism behind the filament eruption in a few selected events.

1.8 Motivation to Build Narrow Band Imager

During the formation, evolution and prior to eruption, filaments exhibit a variety of dynamical processes. Bidirectional flows of plasma were observed within quiet region filament (Zirker, Engvold, and Martin, 1998) as well as in active region filament (Alexander *et al.*, 2013). Oscillations were observed in

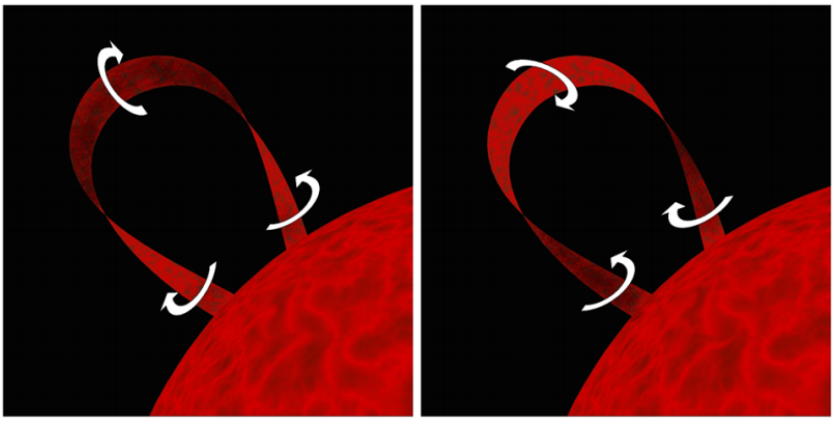

Figure 1.10: Schematic of the two forms of the roll effect in erupting prominence, which initiates at the top of a prominence and propagates downward into the legs (Courtesy of Panasenco *et al.* 2013).

erupting filaments (Bocchialini *et al.*, 2012). Panesar *et al.* (2013) observed tornado-like rotations along the side of the erupting prominence. Liggett and Zirin (1984) studied rotational motion in 5 non-eruptive prominences. In some events they reported only a part of the prominence rotating while in other the entire body was in rotation. They interpreted the rotation in terms of a twisting of magnetic structure resulting from the reconnection. When a filament erupts non-radially, as frequently happens, the top of its main axis bends first to one side and propagates into sideways rolling motion, known as the *roll effect*. The rolling motion propagates down the legs of erupting prominences/filaments, which results in a large scale twists in both legs of erupting filaments (*e.g.,* Bangert, Martin, and Berger 2003; Filippov, Gopalswamy, and Lozhechkin 2001; Panasenco and Martin 2008; Panasenco *et al.* 2011, 2013). Figure 1.10 depicts the rolling of the spine of prominences initiates structural twist with opposite chirality in the two legs. When filament rises slowly upwards, it is observed that the rotational motions with the opposite signs of twist in the two legs flow downward.

Another reason for the *roll effect* could be due to the vortical motions in the legs of prominences/filaments in the chromosphere, which might readily propagate upward in prominences/filaments and lead to a similar topological pattern (Bangert, Martin, and Berger, 2003; Martin, 2003a). The sign of rotation/twist in filaments could be resolved by observation during eruption when they clearly reveal their twisted structure. Time series of data on the Doppler shifts in the legs of erupting prominence/filament can help to differentiate between initiation of the rolling motion near the top of the prominence or at the base of its legs. If the Doppler shifts of rotation are sufficiently large, the sense of twist and rotation can be understood definitely. Hence, either spectra or narrow band filtergrams can be used for observing filament eruption when the filaments are close to the limb (>60°). The observation made in multiple wavelengths around a chromospheric spectral line could provide valuable data to infer the sense of rotation/twist. In this thesis, another work is to develop a narrow band imager using Fabry-Perot interferometer, which can provide images at the chromospheric height in the solar atmosphere and also with some technique it is capable of producing dopplergrams to study the rotational motions during the onset of filament eruptions.

1.9 Outline of the Thesis

As has been mentioned already, every filament invariably ends up with eruption, usually as the core of a CMEs. Most often, the filament ends up with eruption associated with solar flares and CMEs, which affects the Earth's atmosphere and space weather by high energy radiations and particle emission. Hence it is important to study the filament eruptions mechanism to understand the CMEs initiations and broadly, to predict the space weather and Earth's atmosphere. Many have studied the filament eruptions in different context and several events to understand the possible trigger and instability mechanisms for the filament eruptions. But the sequence of events occurred during the filament activation and the relation between the initiation of the eruption and sequence of events occurred in the active region are needed to understand from the recent high resolution observations for different active region filament eruption events. In this thesis, we have studied a few active region filament eruptions to understand the sequence of events occurred during the eruptions and the possible trigger and instability mechanisms towards eruptions using high resolution imaging and magnetograms data. The next three chapters are devoted to study the active regions filament eruptions and the rotational motions during the filament eruptions. In the end, we discussed about the development of the narrow band imager and some initial observations made using this instrument.

The thesis is organized as follows:

- In the second chapter, we discuss about different data set used for the observational study of the filament eruption events. We have studied a two-phase filament eruptions associated with the active region NOAA 11444 using space-based data. Our aim is to study the sequence of events occurred before the filament eruption and find out the connection between the initiation of the filament eruption and sequence of events. A converging motion between opposite-polarity sunspots resulted in a cancellation of magnetic field for few hours around the magnetic neutral line, close to the main axis of the filament, are observed before and during first phase of filament activation. This filament's buildup toward eruption shows pre-eruption brightenings of the strands near the filament in coronal images. The importance of the magnetic flux cancellations, brightenings towards first phase of filament eruption is discussed in this chapter. During the second phase of eruption, we have observed the flux cancellations, expansion of loops, brightened cusp shaped loops and contraction of loops near the filament. The importance of the magnetic flux cancellations, expansion of loops, reconnection and contraction of overlying coronal loops towards the 2nd phase of filament eruption are also discussed in this chapter.

- In the third chapter, we have studied another filament eruption occurred in the southern hemisphere of the Sun on 08 July 2011. The filament was located close to the active region NOAA 11247. We posed the question if there is any single mechanism responsible for this filament eruption or several mechanisms which occurred one after another in sequence? We found that the emerging flux, converging motion and injection of opposite magnetic helicity could be responsible for destabilization of the Western footpoint of the filament leading to eruption. As an interesting phenomena, we observed an anti-clockwise rotational motion in both the footpoints just after the onset of filament eruption which lasted for 6 min during the eruption process. We conjuncture that the torque imbalance between the expanded portion of the flux tube and the photosphere is believed to have caused the rotation in the footpoint region. However, various possible different mechanisms for the rotational motion are discussed in the next chapter of the thesis.

- Now the question is whether the observed rotational motion near the footpoints of the filament is just a coincidence of a normal feature of the photosphere which occurs randomly or is it really related to the filament eruption? To answer this question, we needed statistically significant samples. Therefore, we extended this study in the fourth chapter to several erupting active region filaments and searched for such rotational motions in and around the end points of these filaments. We have observed the rotational/vortical motion in the photosphere near the ends of all active region filaments during their initial phase of eruption, at the onset of the fast rise phase. In many events, in the vicinity of the conjugate ends of the filament the direction of rotation was opposite. In this chapter of my thesis, we have discussed about the importance of this vortical motions at the endpoints of the filaments during their activations towards eruptions.

- Panasenco *et al.* (2011, 2013) observed rotational motion in legs of erupting prominences in the chromospheric images. Such rotational motion was explained as 'roll effect'. We can study such events with narrow band imager, which is capable of producing dopplergrams at chromospheric height. In the fifth chapter of the thesis, we describe the development of the narrow band imager at the Indian Institute of Astrophysics using Fabry-Perot interferometer and an order sorting filter. The entire instrument comprises: i) a parallel plate scanning Fabry-Perot unit ii) an electronic controller for maintaining the plate parallelism and accurate cavity tuning iii) the CCD camera for taking the images and iv) a temperature stabilized order sorting filter to select the desired wavelength band and eliminate the multiple orders. We have tested the Fabry-Perot interferometer in the laboratory in series of experiments. This instrument is capable to image the solar atmosphere at 6563 Å chromospheric Hα line. The observed data are used to produce dopplergrams at the chromospheric height.

In summary, we studied a few selected active region solar filaments eruption in this thesis work. Attempts have been made to understand and explain the eruption mechanism using multi-wavelength observations. We found that mostly filament eruption is associated with the converging motion and subsequent flux cancellation/emergence near the footpoints of the filament or in PIL for these selected events. But from the progress of the individual events towards eruption, our study suggests that in each event the onset of instability could be different. To study the dynamics of filament at different heights in the solar atmosphere and also to study dynamics in the erupting limb filaments, we have developed a narrow band imger using Fabry-Perot Interferometer. We are able to scan the chromospheric Hα spectral line using this instrument. The data are obtained from the scan at a few positions on line profile for filament regions. Finally, I end the thesis by summarizing the results obtained in each chapters and the planned future work for further improvement of the instrument and observations.

Chapter 2

A study of two - phase filament eruption observed in AR NOAA 11444 in association with flux cancellations and coronal loop dynamics

2.1 Introduction

Filaments/prominences are chromospheric and coronal features, relatively cool, dense plasma material suspended along the polarity inversion line (PIL) between the regions of opposite magnetic polarities. When these features erupt, the plasma and magnetic fields both expel together. The flares and CMEs are often associated with such eruptions (Gopalswamy *et al.*, 2003b; Schmieder *et al.*, 2002), which eventually affect the space weather. The fundamental processes responsible for these eruptions are of magnetic in origin (Priest and Forbes, 2002).

The filament mass and the associated magnetic structure are coupled to each other. Observationally it is possible to distinguish between them while eruption. The filament mass sometimes remains confined in the lower corona throughout the eruption along the channel, but the supporting magnetic structure can erupt and disturbs the corona (e.g., Liu, Alexander, and Gilbert 2007). To understand the relation between the filament mass and corresponding supporting magnetic structure, Gilbert, Alexander, and Liu (2007) defined the filament eruptions observationally as “full”, “partial” and “failed” eruptions. In case of “full eruption”, the most of the filament mass ($\geq$ 90%) escapes along with the entire magnetic structure without falling back to the solar surface. But for the “failed eruption”, none of them escapes the Sun. The “partial eruption” is the most complex one to define observationally. The partial eruption can be of two categories. In first category, the entire magnetic structure erupts with the eruption containing either some or none of its supported pre-eruptive filament mass. In the second category, the magnetic structure partially erupts with some or none of the pre-eruptive filament mass.

Several observations show that the activity occurring near the filament location is important during its pre-eruption phase. Small scale magnetic reconnection occurring during the pre-eruptive phase triggers the large scale flares which involve large scale reorganization of the magnetic connections. Therefore, it is very important to know the location and height of the small scale reconnection sites. Several models are proposed to examine the role of the initial magnetic reconnection which set up the conditions that are favorable for the magnetic core fields to erupt. One of the mechanisms is ‘tether cutting’ in which implosive/explosive reconnection occurs within the twisted and deep sheared core field of a bipole above the polarity inversion line (PIL) of the arcade (Moore and Labonte, 1980; Moore *et al.*, 2001). They explained that these slowly driven internal tether cutting mechanism lead to the instability of the overlying field (see Section 1.7.1 for more details). There is another reconnection process named as ‘breakout’. In this model the topology of the erupting system is multi-polar and a tension release mechanism that occurs between the sheared arcade and neighboring flux systems triggers the eruption (Antiochos, 1998; Antiochos, DeVore, and Klimchuk, 1999) (see Section 1.7.3 for more details). In the context of these models, the role of magnetic reconnection for the eruption can be understood by examining their observational signatures during the pre-eruption phase.

The magnetic reconnection can also happen at low level in the solar atmosphere (e.g., Wang and Shi 1993; Nelson *et al.* 2013). In the photosphere it is seen as a cancellation of magnetic features (Priest, Parnell, and Martin, 1994). Flux cancellation (Martin, Livi, and Wang, 1985) is the process where the magnetic flux disappear at the PIL; as formulated by van Ballegooijen and Martens (1989). This cancellation occurring a few hours prior to eruption is a commonly observed phenomenon. The gradual flux cancellation continuing over an extended period triggers the filament eruption (Sterling *et al.*, 2010). Green, Kliem, and Wallace (2011) observed that flux cancellation at the PIL leads to the formation of X-ray sigmoid which eventually triggers the CME. Newly emerging magnetic flux adjacent to the filament over a longer period can lead to the slow rise of the filament due to magnetic reconnection and eventually triggers the filament eruption (Sterling, Harra, and Moore, 2007).

Initially filaments often undergo relatively slow rising motions before the onset of eruptions (Kahler *et al.*, 1988; Liewer *et al.*, 2009; Nagashima *et al.*, 2007; Sterling, Harra, and Moore, 2007; Sterling, Moore, and Freeland, 2011; Xu, Jing, and Wang, 2010). These early slow rise motion was considered as one of the reason to trigger the eruption (Moore and Sterling, 2006; Sterling, Harra, and Moore, 2007; Sterling *et al.*, 2010). On several occasions a transient brightening at or near the polarity inversion line (PIL), coincident with emerging and/or canceling magnetic flux has been observed. This kind of brightenings are considered as precursors to the flare and filament eruption (Chifor *et al.*, 2007; Kim *et al.*, 2007; Liu *et al.*, 2009; Martin, 1980; Sterling, Moore, and Freeland, 2011).

The filament eruption and flares are sometimes associated with the contraction of coronal loops. Liu and Wang (2009) observed the contraction of the EUV corona in the wake of filament eruption. When the filament rose explosively, the loops started to contract due to the reduced magnetic pressure underneath with the filament escaping. The loop was overlying on the flaring region during the early phase of a C-class flare. It was started to contract at the speed of about 100 km s^{-1} and was sustained for about 12 minutes. Liu and Wang (2010) have reported for September 8, 2005 event that a coronal loop overlying the active region NOAA 10808 started to contract at the peak of X-class flare. This loop contraction was initiated during the flare preheating phase with a speed about 6 km s^{-1} and then after few minutes it began a fast contraction at about 120 km s^{-1}. Yan *et al.* (2013) observed the rotational motion of the sigmoid filament and the contraction of overlying coronal loop during its eruption on 22 May 2012. They suggested that due to the rising filament the magnetic pressure is reduced suddenly underneath the filament that could have caused the contraction of the coronal loop.

In this chapter, we present the study of a filament eruptions that occurred in the vicinity of the active region NOAA 11444, observed in different wavelengths regime. We choose this event because:

- the filament erupted in two phases consecutively within a short time period of ∼1 hr 27 min associated with the same active region,
- the filament eruption was associated with the small C-class flares, there by the energy involved in the event is less,
- the data was available in all possible AIA's [Atomospheric Image Assembly (Lemen *et al.*, 2012)] wavelength and hence we could cover the event from photosphere to the corona,
- even the magnetic fields configuration is simple and largely it shows only the bipolar configuration.

The first part of the filament has started activation at ∼01:56 UT on 27 March 2012. The other part of the filament eruption initiated at ∼04:20 UT on the same day. The eruption was initiated between the positive and negative polarity region of the sunspot that had been converging for an extended period before the eruption. We observed pre-eruption brightening beneath the main axis of the top filament near the polarity inversion line about 30 min prior to first phase of the eruption. Gradual magnetic flux cancellations were also observed at the same location over which the filament was located. We observed the post flare loops which are contracting over the filament. There is also a rise of coronal loops on the east side of the filament, reconnected with the overlying loops. The 2nd part of the filament erupted after the reconnection. Here we present the important morphological changes in and around the filament prior to the eruption and the possible triggering mechanism of the first and second part of the filament associated with AR NOAA 11444.

This chapter is organized as follows. In the next section, we describe about the different instruments which are used in this study as well as in other chapters. A brief description about the filament and the sequences of the events in the corona, chromosphere as well as in the photosphere are presented in Section 2.4. Finally, a brief summary of the results and discussions is presented in Section 2.5.

2.2 Instruments

Data collected from different ground and space based instruments were used for the filament eruption study in this thesis. A few important details about the instruments, purpose and spatial, temporal resolutions are presented in the next subsections.

2.2.1 Instruments on board the Solar Dynamics Observatory

The *Solar Dynamics Observatory* (SDO; Pesnell, Thompson, and Chamberlin 2012) is one of the largest solar observing space- craft ever placed in the orbit. It is the first mission launched for NASA's Living With a Star (LWS) Program. Instruments is designed to understand the causes of solar variability and its impacts on Earth. It was launched from Kennedy Space Centre in Florida on 11 February 2010. SDO's inclined geosynchronous orbit was chosen to allow continuous observations of the Sun and enable its exceptionally high data rate through the use of a single dedicated ground station. SDO spacecraft with different instruments on board is shown in Figure 2.1. The main goal of SDO is to understand the Sun's influence on Earth and Near-Earth space by monitoring the solar interior and different layers of its atmosphere with high spatial and temporal coverage and in many wavelengths simultaneously. There are three main instruments on board SDO.

- Atmospheric Imaging Assembly (AIA) built in partnership with the Lockheed Martin Solar & Astrophysics Laboratory (LMSAL),
- Helioseismic and Magnetic Imager (HMI) built in partnership with Stanford University, and
- Extreme ultraviolet Variability Explorer (EVE) built in partnership with the University of Colorado at Boulder's Laboratory for Atmospheric and Space Physics (LASP).

The individual instruments (AIA and HMI) are discussed in the following sections. Only EVE is not described here, since the data from this instrument was not used in this thesis work.

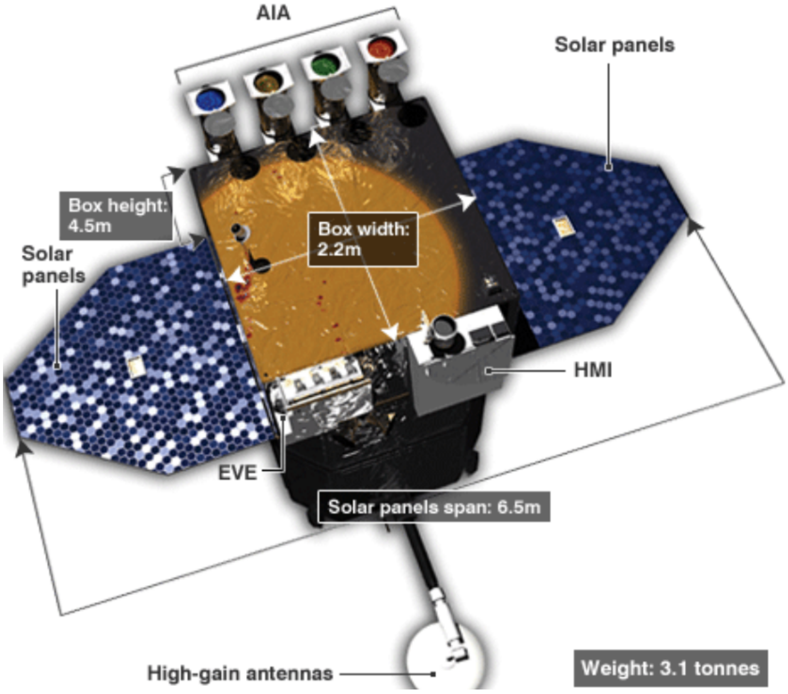

Figure 2.1: Figure shows the SDO spacecraft with all the three instruments on board (Image credit: NASA).

2.2.1.1 Atmospheric Imaging Assembly

The *Atmospheric Imaging Assembly* (Lemen *et al.*, 2012) on board SDO provides multiple simultaneous high-resolution full-disk images of the corona and transition region up to 0.5 solar radii of the solar limb with 1.5$''$ spatial resolution and 12 second temporal resolution. It was launched as a part of NASA's SDO mission on 11 February 2010. The AIA instrument consists of four generalized Cassegrain telescopes. Each telescope has a 20-cm primary mirror and an active secondary mirror. Each telescope field of view is approximately 41 arc-min circular diameter and captures the full-disk over a 4k × 4k CCD at a spatial resolution of 0.6$''$ per pixel. A dedicated guide telescope is mounted on the side of the telescope tube and consists of an achromatic refractor with a band-pass entrance filter centered at 570 nm and a Barlow-lens assembly. The active secondary is pointed in response to the signals from guiding telescope. The telescope mirrors are fabricated on Zerodur substrates, which provide a low coefficient of thermal expansion. The AIA consists of four telescopes that employ normal-incidence, multilayer-coated optics to provide narrow band imaging of seven extreme ultraviolet (EUV) bandpasses centered on specific lines: Fe XVIII (94 Å), Fe IX (171 Å), Fe VIII, XXI (131 Å), Fe XII, XXIV (193 Å), Fe XIV (211 Å), He II (304 Å), and Fe XVI (335 Å). One telescope observes C IV (1600 Å) and the nearby continuum (1700 Å) and has a filter that observes in the visible (around 4500 Å) to enable co-alignment with images from other telescopes. Entrance filters at the telescope aperture suppress unwanted UV, visible and IR radiation for the EUV channels. Two filter materials, aluminum and zirconium are used for the filters. Filters are located in a wheel in front of the focal plane, which are used to select the wavelength channel of interest in three of the telescopes. A selector mechanism is used to choose the desired wavelength for the fourth telescope. To regulate the exposure time, a mechanical shutter has been used. The instrument calibration, wavelength responses and other related information can be found in Boerner *et al.* (2012). The temperature diagnostics of the EUV emissions cover the range from $6{\times}10^4$ to $2{\times}10^7$ K. The response functions for the six EUV bandpasses that are dominated by iron emission lines are shown in Figure 2.2. The primary ions for each wavelength band and their characteristic emission temperatures, along with regions of solar atmosphere observed are given in Table 2.1.

2.2.1.2 Helioseismic and Magnetic Imager

The *Helioseismic and Magnetic Imager* (HMI; Scherrer *et al.* 2012; Schou *et al.* 2012a) is part of the NASA Solar Dynamics Observatory (SDO) mission. The instrument designed to study oscillations and the magnetic field at the solar surface, or photosphere using the 6173 Å Fe I absorption line. The HMI instrument consists of three main parts: 1) an optics package, 2) an electronics box, and 3) a harness to connect the two. HMI optics package contains a front-window filter, a telescope, a set of waveplates for polarimetry,

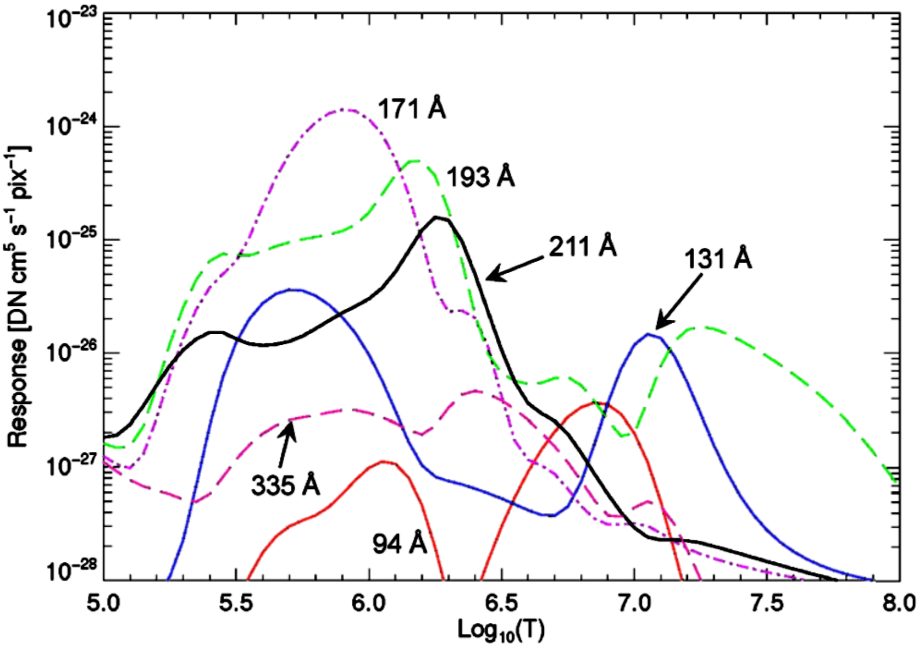

Figure 2.2: Temperature response functions for the six EUV channels. These channels are dominated by iron emission lines calculated from the effective area functions and assuming the CHIANTI model for the solar emissivity (courtesy of Lemen *et al.* 2012).

a blocking filter, an image-stabilization system, a five-stage Lyot filter with one tunable element, two wide-field tunable Michelson interferometers, a pair of 4k×4k cameras with independent shutters. The front-window filter of bandpass 50 Å is used to limit the heat input to the instrument. The telescope is a two-element refracting telescope with a 140 mm clear aperture, giving an image with a nominal diffraction limit of 0.91 arcsec. The primary lens is convex spherical on the back surface and convex aspherical on the front surface. The secondary lens is bi-concave. Both the lenses are connected with a low coefficient-of-thermal-expansion metering tube, which is made of a carbon fiber composite to maintain focus. The details of the telescope and key parameters of the optical system can be found in Schou *et al.* (2012a). The polarization selectors consist of three quartz waveplates, which are used to convert the desired incoming polarization into the fixed linear polarization selected by the polarizing beamsplitter. The nominal retardances of these waveplates are 10.5, 10.25, and 10.5 waves in a sequence. The details of the

Table 2.1: The list of seven EUV and three UV-visible channels used in AIA. The primary ions observed by AIA. Many are species of iron covering more than a decade in coronal temperatures (Courtesy of Lemen *et al.* 2012).

Channel	Primary ion(s)	Region of atmosphere	Char. log(T)
4500 Å	continuum	photosphere	3.7
1700 Å	continuum	temperature minimum, photosphere	3.7
304 Å	He II	chromosphere, transition region	4.7
1600 Å	C IV+cont.	transition region, upper photosphere	5.0
171 Å	Fe IX	quiet corona, upper transition region	5.8
193 Å	Fe XII, XXIV	corona and hot flare plasma	6.2, 7.3
211 Å	Fe XIV	active-region corona	6.3
335 Å	Fe XVI	active-region corona	6.4
94 Å	Fe XVIII	flaring corona	6.8
131 Å	Fe VIII, XXI	transition region, flaring corona	5.6, 7.0

polarimetric design of the instrument can be found in Schou *et al.* (2012b). The blocking filter is an dielectric interference filter with a FWHM bandpass of 8 Å. It rejects the unwanted orders of the Lyot and Michelson filters and limits the heat input into the oven. The Lyot filter uses the same basic design as *Michelson Doppler Imager* (MDI; Scherrer *et al.* 1995) where some of the elements were doubled in order to reduce unwanted side lobes in the untuned part. The narrowest filter element of the Lyot filter is tuned by a rotating half-wave plate. The bandpass of the untunned part of it is 612 mÅ. Two solid tunable Michelson interferometers with clear apertures of 32 mm are used and they have nominal free spectral ranges of 345 mÅ and 172 mÅ. Tuning of the two Michelson interferometers is accomplished by rotating a combination of a half-wave plate, a polarizer and a half-wave plate. Figure 2.3 shows the six tuning positions with respect to the Fe I solar line at disk center and at rest.

HMI uses the Zeeman effect of Fe I absorption line at 6173 Å, to measure the Stokes parameters required to make both longitudinal and vector magnetograms (maps of the photospheric magnetic field) of the entire visible disk of the Sun. The magnetogram has pixel resolution $0.5''$. HMI also measures full-disk scalar quantities - dopplergram (map of solar surface velocity), continuum intensity, line depth, and line width - using a repeating sequence of

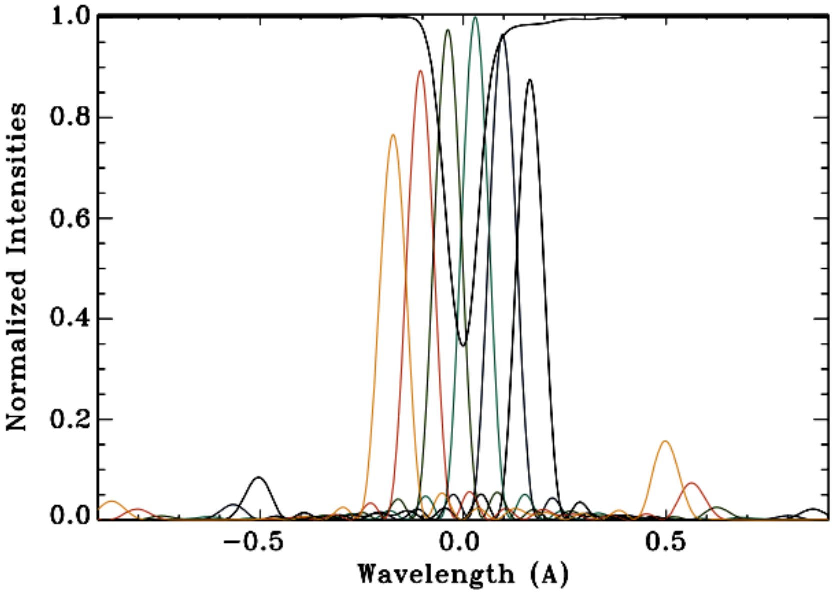

Figure 2.3: The plot shows an example of HMI tuning-position profiles obtained from the wavelength-dependence calibration procedure (courtesy Schou *et al.* 2012a).

narrow-band images recorded every 45 seconds at resolution of 0.5″ per pixel with a 4k×4k camera called the "Doppler" camera (Hoeksema *et al.*, 2014). The HMI telescope feeds a solar image through a series of bandpass filters onto two CCD cameras. Each camera records a full-disk image of the Sun in a 76 mÅ wavelength band selected by tuning the final stage of a Lyot filter and two Michelson interferometers across the line profile in every 3.75 seconds. Six wavelengths are measured in different polarizations in a sequence. The right and left circular polarization at each wavelength is measured by one camera, completing a 12-filtergram set every 45s from which the Doppler velocity, line-of-sight (LOS) magnetic field, and intensities are determined. The second camera measures six polarization states (I±V, I±Q, and I±U) at every 90 - 135s and ordinarily averaged into a 12-minute product, where I, Q, U, and V are the Stokes polarization parameters. Very Fast Inversion of the Stokes Vector (VFISV; Borrero *et al.* 2011), an inversion code for the polarized radiative transfer equation routinely analyze pipeline data from HMI and provides full-disk maps of the magnetic field vector on the solar photosphere every ten minutes.

2.2.2 Global Oscillation Network Group

The *Global Oscillation Network Group* (GONG; Harvey *et al.* 1996) is a community-based program to conduct a detailed study of solar internal structure and dynamics using helioseismology. It operate a six-site helioseismic observing network to do the basic data reduction, provide data and software tools to the community, and to coordinate analysis of the rich data set. The GONG network began full operation in October 1995. Since mid-2010 the GONG has collected Hα images at six-station network of extremely sensitive, and stable velocity imagers located around the Earth to obtain nearly continuous observations of the Sun. The H-alpha system is an additional system to the normal GONG helioseismology instrument and it does not interfere with regular observations. The six sites comprising the GONG Network are Big Bear Solar Observatory in California, USA, High Altitude Observatory at Mauna Loa in Hawaii, USA, Learmonth Solar Observatory in Western Australia, Udaipur Solar Observatory in India, Observatorio del Teide in the Canary Islands, and Cerro Tololo Interamerican Observatory in Chile. The dark, flat, smear corrected and compressed Hα images are available with almost 1-minute cadence. These Hα images are obtained with 2k×2k pixel CCD camera whose pixel resolution is about $1''$(Harvey *et al.*, 2011).

2.2.3 Geostationary Operational Environmental Satellites

The Geostationary Operational Environmental Satellites (GOES) program consists of a series of geostationary satellites, which are orbiting the Earth at a height of 35,790 km (Donnelly, Grubb, and Cowley, 1977; Grubb, 1975). The satellites overlap in time so that there are always one to three spacecraft present and hence, guarantee an essentially uninterrupted time series of solar soft X-ray fluxes, besides continuous meteorological observations of the Earth. The GOES cover over 40 years during the period of 1974 – 2015.

The GOES first satellite (GOES-1) was launched on 1974 October 16 and GOES-2 and GOES-3 followed in 1977 and 1978. Then a series continued up to GOES-15, was launched on 4th March 2010. The future satellites GOES-R and GOES-S (with soft X-ray imaging capabilities) are in the queue for a launch in March, 2015 and 2017, respectively (Ref: *http://www.goes-r.gov/mission/history.html*). More details about operational and technical details of GOES satellites can be found in Donnelly, Grubb, and Cowley (1977); Garcia (1994); Grubb (1975); Lemen *et al.* (2004); Neupert (2011); Pizzo *et al.* (2005); Stern *et al.* (2004), or the National Oceanographic and Atmospheric Administration (NOAA) Web site *http://www.oso.noaa.gov/goes/*, or the NASA *Web site http://goespoes.gsfc.nasa.gov/project/index.html.* The National Oceanic and Atmospheric Administration's (NOAA) GOES spacecraft includes an X-ray telescope that monitors the Sun for predicting solar energetic events and for providing information about the large-scale solar magnetic field (Lemen *et al.*, 2004). GOES N includes Solar X-ray Imager, which made use of a super-polished grazing incidence mirror, a highly efficient back-thinned CCD, and thin metalized filters to observe the million-degree corona with 10-arcsec resolution. The Solar X-ray Imager data are used to forecast space weather. For our study, we are concerned with the soft X-ray light curves that are integrated sunlight measured at 1 AU. These are recorded in two energy channels: 1) the softer energy range of 1–8 Å and 2) the harder energy range of 0.5–4 Å. The light curves for both energy ranges are available with a cadence of 3 sec and 2 sec, respectively, after 2009 December 1. According to the X-rays peak flux ($Watts/m^2$) of 1–8 Å near Earth as measured by XRS instrument on-board GOES-15 satellite, the solar flares are classified as A, B, C, M and X. The Table 2.2 shows the classification of solar flares. Each X-ray class category is divided into a logarithmic scale from 1 to 9, such as C1 to C9, B1 to B9, etc.

Table 2.2: The classification of solar flares based on GOES soft X-ray data.

Class	$Watts\ m^{-2}$ (between 1 – 8 Å)
A	$< 10^{-7}$
B	$\geq 10^{-7} < 10^{-6}$
C	$\geq 10^{-6} < 10^{-5}$
M	$\geq 10^{-5} < 10^{-4}$
X	$\geq 10^{-4}$

2.3 Data Analysis

The filaments appear with high contrast in the chromospheric Hα and EVU images. We have used the EUV images obtained from AIA on board the SDO to study the filament eruption in detail. In particular we have used the data obtained in the wavelength of 171, 193, 335 and 304 Å which correspond to the imaging of the corona and chromosphere of the Sun. We have obtained the data at Level-1.0 which have been converted from Level-0, with corrections including bad-pixel removal, despiking due to high energy particles and flat-fielding. Then we used *aia_prep.pro* routine available in SSW packages to co-align the images from all of the AIA channels (171, 193, 335 and 304 Å) to a specified pointing, rescale the images to a common plate scale and derotate the images. We also normalized the images to 1-sec exposure time for all the wavelengths (171, 193, 335 and 304 Å). From these data set the filament regions are extracted and tracked over time. We acquired the data starting from 22:00 UT on 26 March 2012 till 07:00 UT on 27 March 2012 which covers activation of the filament eruption and subsequent runaway motion for the entire event.

In order to examine the changes in the photospheric magnetic field near the filament footpoints, we obtained the full-disk line-of-sight magnetograms at level-1.0 for about little more than a day starting from 26 March 2012 from HMI with a cadence of 45 sec. Both the EUV images and magnetograms have slightly different spatial resolutions. Hence, we used *aia_prep.pro* routine available in SSW packages to upgrade HMI magnetogram to level-1.5 from level-1.0 so that it is interpolated to the AIA pixel-resolution. We have tracked the region-of-interest (ROI) by utilizing the heliographic co-ordinate information and finally corrected for the line-of-sight effect by multiplying $1/\cos\theta$, where θ is the heliocentric angle. We then averaged 4 magnetograms to reduce the noise level to about 10 G. These magnetograms have been used to study the evolution of magnetic fields in and around the filament at the photospheric level.

The morphology of the filament at the chromospheric heights can be studied with Hα images. We obtained full-disk Hα images from GONG, starting from 23:00 UT on 26 March 2012 till 06:00 UT on 27 March 2012. The data set covers first and second eruption of the filament and subsequent flares for the entire event. The ROI was extracted in the image using the heliographic co-ordinate information.

2.4 Observations and Results

2.4.1 AIA observations of the filament eruption

The filament was formed in the active region NOAA 11444 when it was at a location 19° North and 26° East of the central meridian point and survived for almost 3 days. On 27 March 2012, before the eruption, the filament was observed in the same active region at heliographic position of N21 W17. The filament appeared as inverse J shaped in Hα (top-left), He II 304 (top-right), 193 Å (bottom-left) and 171 Å (bottom-right) images in Figure 2.4, respectively. The arrows in Figure 2.4 show the filament and the arrow followed by letter ‘A’ in Hα image indicates the location of the protrusion which appears as barb. The inverse J shape of the filament indicates the filament has the right handed twist and it is consistent with hemispheric rule. The appearance of the filament in the coronal images (193 and 171 Å) are also shown in

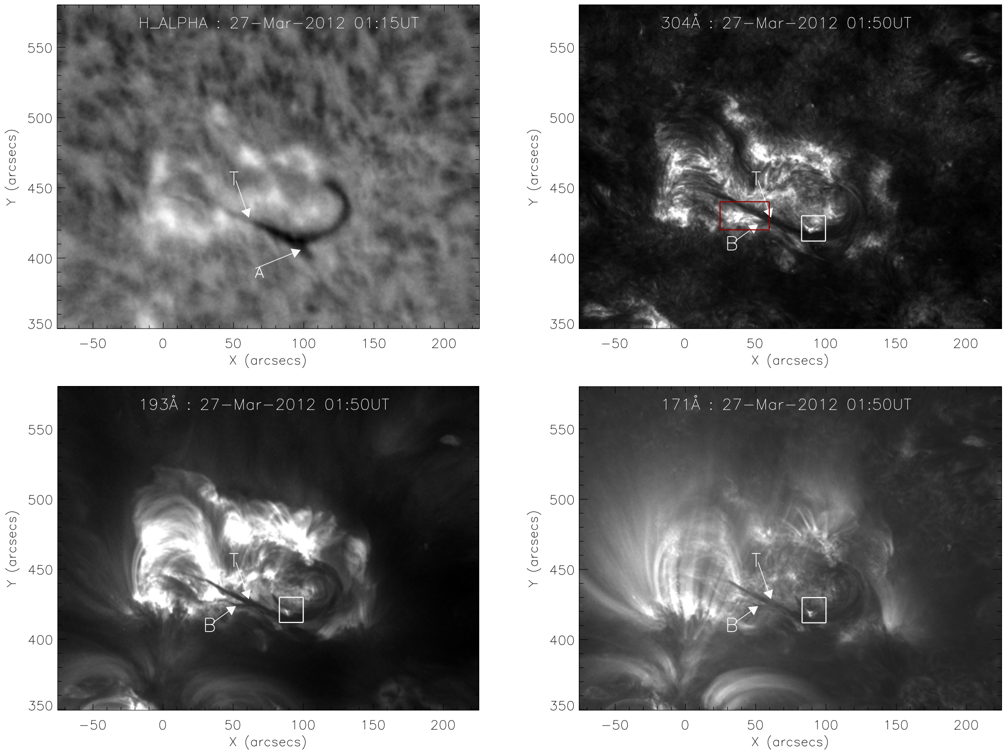

Figure 2.4: Filament observed in Hα image (top-left), 304 Å (top-right), 193 Å (bottom-left) and 171 Å (bottom-right) channel of AIA. The top and bottom filament locations are shown by white arrow with 'T' and 'B' symbol respectively. The arrow with 'A' symbol in Hα image shows the location of the protrusion which appears as barb of the filament. The white boxed region in 304, 193 and 171 Å images shows the surge location close to the filament. The red boxed region in the top-right panel shows the location of the preflare brightening in 304 Å image.

Figure 2.4 (bottom-left and right, respectively).

The filament appears to have two elements. One is broad inverse J shaped which is visible in Hα–6563, 171, 193 and 304 Å wavelengths. This filament region is shown by an arrow with letter 'T' symbol, indicating the top most filament. One more thin filament sitting below the top filament or it could be just a bifurcation of the main filament. It appears to start at a location of $\sim35''$ in the horizontal direction and at $\sim425''$ in the vertical direction in EUV images. It bends down at $\sim45''$ and later continues with the main 'T' filament, also taking inverse J shape. The bottom side or bifurcated filament is shown by the letter 'B' in Figures 2.4 and 2.5.

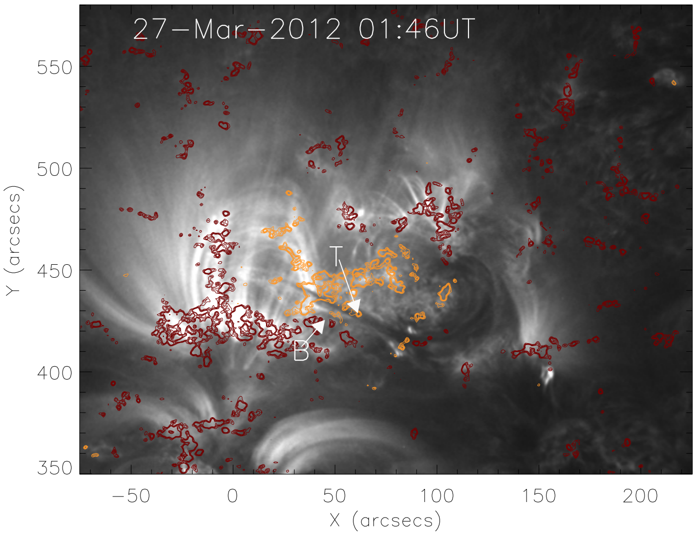

Figure 2.5: Filament observed in 171 Å channel of AIA. The top and bottom filament locations are shown by white arrow with 'T' and 'B' symbol respectively. The contours of the magnetic fields are overlaid on the images. The orange and red contours represent the positive and negative polarities with magnetic field strength values of ± 100, 150, 200 and 250 G, respectively.

In order to study the filament eruption in detail, we have made a movie of the erupting filament in 304, 171, 193 and 335 Å channel of AIA. The movie clearly shows that the filament erupted in two stages. In the first stage, the southern portion of the filament erupted. This eruption is followed by C5.3 class flare identified by GOES detector at ∼02:52 UT. The second eruption initiated at around 3:50 UT, during that time the northern part of the filament got activated and accelerated at 4:20 UT followed by C1.7 class flare observed in the active region at ∼04:25 UT. The movies are made in 171, 193, 304 and 335 Å wavelengths and available in the web linked with this site *http://skdhara2.webnode.com/videos/solar-event-videos/*[1]. The zoomed-in versions of the erupting filament is also shown in the same movies.

The contours of photospheric magnetic fields overlaid upon the 171 Å images, shown in Figure 2.5 indicate that the filament is passing through the neutral line and the southern portion of the filament ending in the bipolar

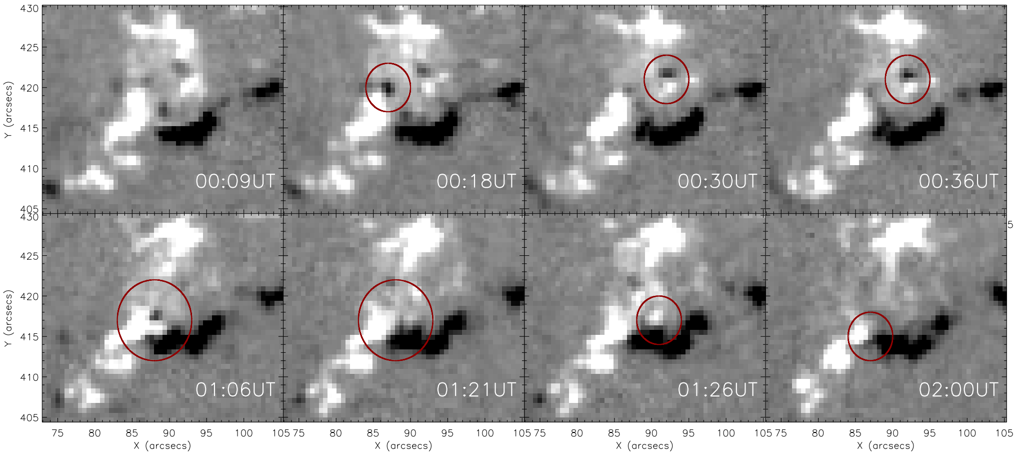

Figure 2.6: A sequence of line-of-sight magnetograms showing the location of the bright ejecta, seen in the white boxed region in Figure 2.4. The white and black region represent the positive and negative polarities of the magnetic field respectively. The locations of flux cancellations and emergence are shown by circles.

regions where the magnetic fields are canceling. The surge in the cusp shaped regions observed close to the filament is shown by white boxed region in the 304, 193 and 171 Å wavelengths in Figure 2.4. This reconnecting region is repeatedly becoming bright and expels some dark ejecta. Over the period of 2.5 hrs starting from 00:00 UT to 02:30 UT (on 27 March 2012), it became bright 5 times periodically and ejected the mass. In the same location, the photospheric magnetograms showed repeated emergence and cancellations of magnetic flux. Figure 2.6 shows the sequence of line-of-sight magnetograms for the same location at different times during the surge event. The emergence and cancellation of magnetic flux regions are marked by circles in the time sequence of magnetograms.

---

[1] Movies generated from SDO/AIA 171, 193, 304 and 335 Å images of the filament eruption associated with active region NOAA 11444 discussed in this chapter are available on our website (http://skdhara2.webnode.com/videos/solar-event-videos/). The movies are named according to the wavelengths of observations of the event.

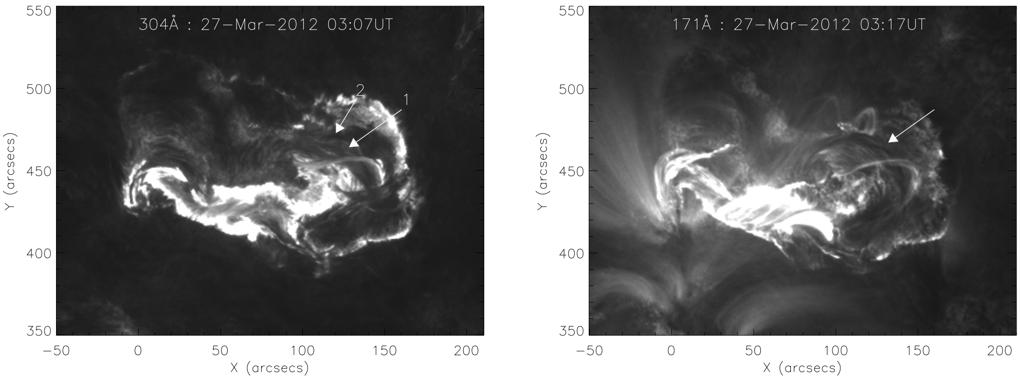

Figure 2.7: Left: The filament channel is shown by arrow 1 and 2 in the 304 Å image. Right: The filament portion after the first eruption, appeared in 171 Å image is shown by white arrow.

2.4.2 Pre-flare brightening and initiation of filament eruption

Near the east end of the bottom-side filament, a brightening was observed starting at 01:56 UT. The brightening location is shown in 304 Å channel by a red box in Figure 2.4 (top-right). This brightening occurred at a location of ∼38″ on the x-axis in Figure 2.5. The brightening was followed by a bright flow which moved from east end of the filament to the west. During the flow, the filament appeared as a sequence of bright and dark threads. The bright flow reached the barb like protrusion at 02:03 UT. During that time the bottom or bifurcated filament moved up little and also raised the top or main filament. Later, in the top portion of the filament we observed a dark flow moving towards the east direction from west direction and in the bottom portion the bright flow direction was from east to west. At around 2:35 UT the separation between the bright and dark threads of the filament became large and in the west side, one end of the filament started moving upward. At around 2:53 UT there was a C5.3 class flare and during that time a large amount of bright mass was ejected along with the filament eruption.

Soon after the first part of the filament erupted, bright and dark long threads were visible in the location of northern portion of the filament in coronal as well as upper chromospheric images. These bright and dark threads appeared to be a filament channel whose positions are shown by arrows 1 and 2 in 304 Å image in Figure 2.7 (left). A dark filament portion appeared over this bright and dark thread at 3:14 UT. This portion is shown by an arrow in 171 Å image in Figure 2.7 (right). At, around 4:20 UT this filament showed acceleration followed by C1.7 class flare that occurred in the same location. The filament disappeared from the field-of-view at around 4:30 UT in 171 Å images.

2.4.3 Space-time diagram of filament eruption

The entire filament was erupted in two phases. In the first phase the southern portion of the filament erupted and in the second phase the northern portion of the filament erupted. The space-time (ST) maps are helpful in understanding the evolution of filament over a fixed region. We have constructed space-time maps from a series of 304 Å and 171 Å images. The ST map for the first filament eruption is extracted from slit-I and the second eruption is extracted from slit-II (shown in Figure 2.8 (top)). The ST maps are shown in Figure 2.8 for 304 and 171 Å images. The ST maps have been constructed from a series of 304 and 171 Å images starting from 27 Mar 2012 at 01:00 UT. The position of the filament in ST map generated from 304 Å images (middle-left image), is shown by an arrow ‘A’. It is located at about 50th pixel in the Y-direction. At or around ∼01:56 UT there was a pre-flare brightening close to the filament. The location of the brightening in ST map is shown by an arrow ‘Br’. A similar brightening is also visible in other ST map, generated from 171 Å images (bottom-left). Then onward the filament showed an indication of slow-rise. At around 2:30 UT there was another brightening which could be related to the C5.3 class flare. The filament started to rise little faster during this time and showed a different slope. This location is indicated by a vertical line close to the filament in ST map. The peak time of the flare occurred at around 3:08 UT. After that the filament accelerated and erupted with a projected speed of 130.1±2.9 km/sec.

We have constructed space-time maps from a series of 304 Å and 171 Å images for the second eruption too and these were extracted from slit-II (shown in Figure 2.8 (top)). The initial position of the filament before activation is shown by an arrow in the ST map (middle and bottom-right image), which is located at about 90th pixel in the y-direction. This filament erupted in a different manner compared to the previous eruption. After its activation it took an anti-clockwise turn and then moved away towards south. The projected distance traveled by the filament is visible in both 304 and 171 Å ST maps. This filament accelerated and erupted with a projected speed of 37±2.1 km/sec. This event was followed by C1.7 class flare occurred in the same location.

2.4.4 Temporal evolution of light curves during slow and erupting phase of filament

Figure 2.9 shows the intensity variations in 171, 304, 335 and 193 Å wavelength images close to the end point of the bottom filament where the pre-flare brightening was observed. The light-curve is obtained by integrating the intensity in a small box shown in Figure 2.9 (top-left). The box is also shown in the magnetogram and the magnetic flux is computed from the boxed region (shown in Figure 2.9 (top-right)). The light-curves in 171, 193, 335 and 304 Å wavelengths showed a brightening at around 01:56 UT in the boxed region. The ST maps indicated that the filament activation started at the same time. Later, at around 2:50 UT there was a jump in the GOES X-ray curve in the 1.0–8.0 Å band. At the same time we observed a jump in intensity of all the 304, 335, 171 and 193 Å wavelength bands. The peak in

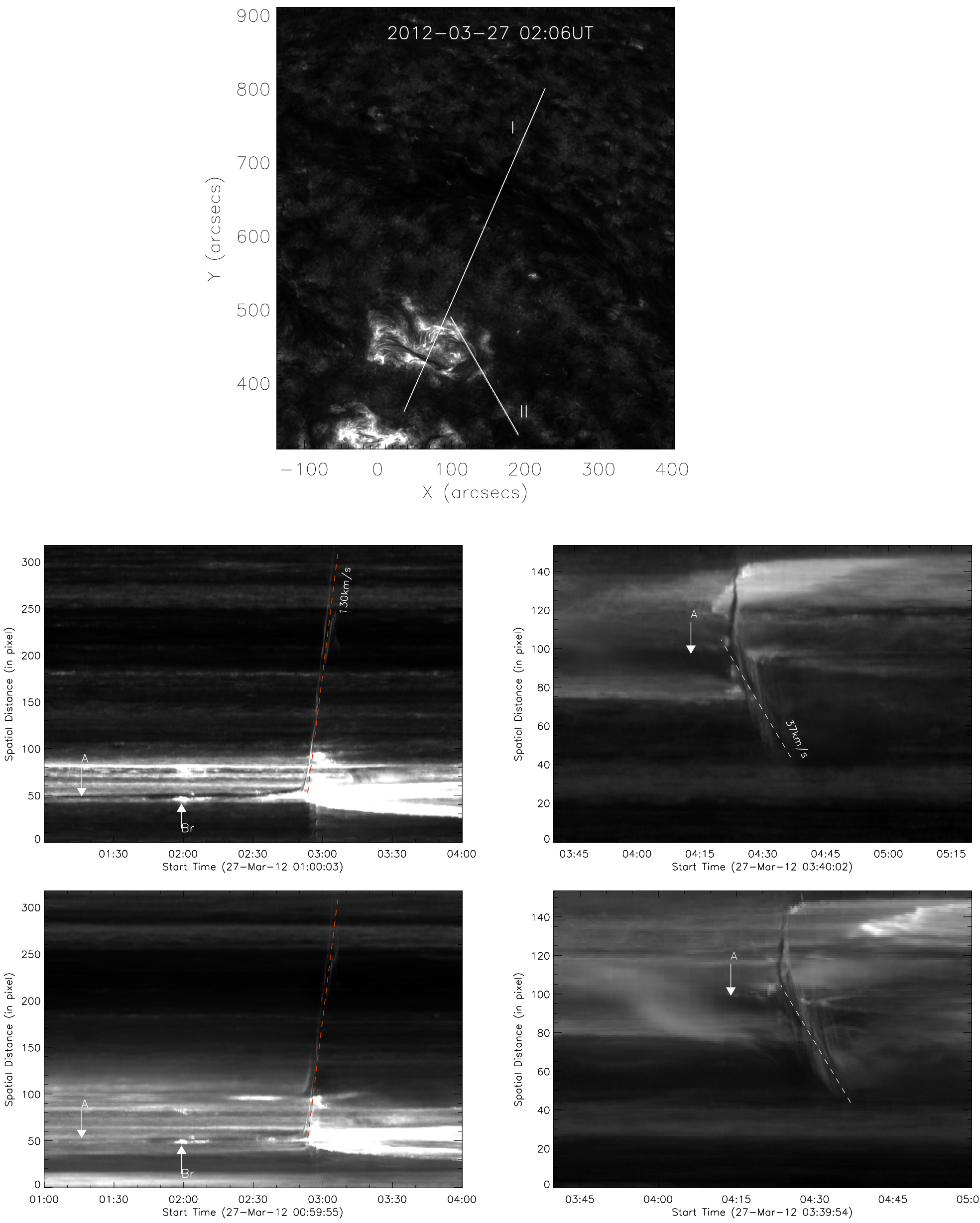

Figure 2.8: Top: The filament is shown in 304 Å image. Two white slits overlaid on the image represent the position from which the space–time maps have been generated. The slit-I crosses 1st eruption of the filament. The slit-II crosses 2nd eruption of the filament. Middle: The space–time map of filament eruption for slit-I (left) and for slit-II (right) respectively extracted from 304 Å images. Bottom: The space–time map of filament eruption for slit-I (left) and for slit-II (right) respectively extracted from 171 Å images. A dark bent portion of the filament represents the path of the filament while erupting. The white arrow followed by letter 'A' (left images) shows initial position of the filament before eruption. Other white arrow followed by letter 'Br' shows the brightening position during eruption.

the 171 and 195 Å wavelength bands coincided with the peak in GOES X-ray curve indicating that the soft X-ray and EUV channel observe a similar temperature layer in the solar atmosphere. The brightening in the GOES and in other EUV wavelengths reaches the background level over a period of about 40 minutes after the flare.

During the initiation of the C5.3 class flare the filament showed an acceleration and eventual eruption. The magnetic flux computed inside the boxed region. The negative flux in the boxed region decreased till the onset of the flare with some undulations indicating that the flux cancellations in the same locations. The positive flux also decreased starting from 01:00 UT till the beginning of flare. Over the period of 2-hrs almost a similar amount of flux ($\sim$0.15$\times$10^{20} Mx) canceled in both the polarities. The change in flux could be due to several reasons. The decrease in the flux is due to the flux cancellations and the increase in flux is due to the emergence as well as the magnetic flux entering into the boxed region from the surrounding region.

2.4.5 Contraction of the coronal loop in the first phase

Just a few minutes before the first phase of filament eruption there was one coronal loop contracted on the eastern part of the filament. In that location the top filament (T) was ending. The loop contraction was visible starting from 2:32 UT till 2:35 UT. Figure 2.10 (top – 1st panel) shows the contraction of the coronal loop in a sequence of 171 Å images in different time epoch. Magnified portion of the contracting loop regions (blue boxed region) are shown in Figure 2.10 (top – 2nd panel) for the corresponding time of the top – 1st panel images. The time sequence of high-pass filtered 171 Å images for the contraction loop are shown in Figure 2.10 (bottom – 1st panel) for better contrast. Magnified portion of the contracting loop regions (blue boxed region) are shown in Figure 2.10 (bottom – 2nd panel) for the corresponding time of the bottom – 1st panel filtered images. These high-pass filtered images

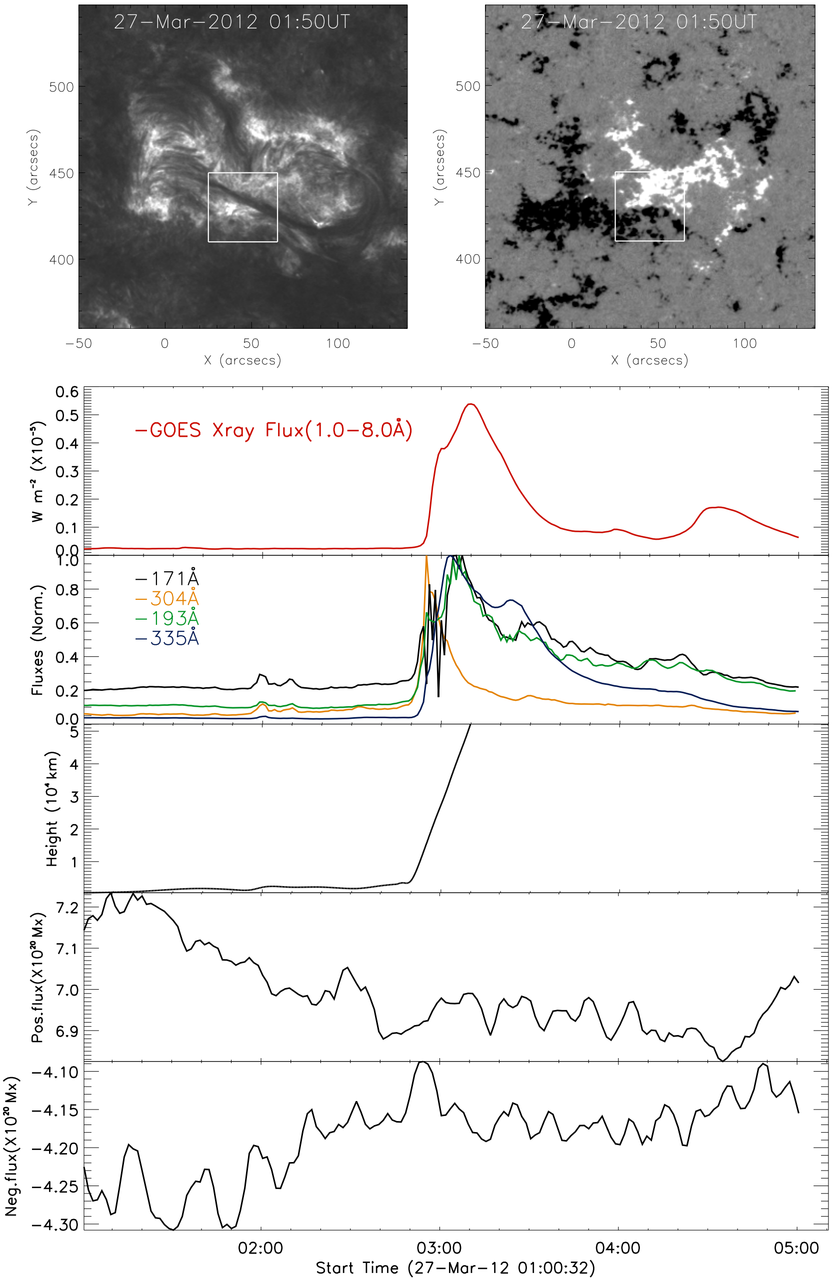

Figure 2.9: Top-left: The boxed region shows the brightening region in 304 Å image. Top-Right: Line of sight magnetogram for the same region and the boxed region is also shown here. Bottom: top plot: GOES 1-8 Å flux profile. The normalized fluxes are plotted for the boxed region at wavelengths 171 Å, 193 Å and 304 Å (2nd plot from top). The projected height–time plot for the 1st eruption is shown in 3rd plot. The calculated positive and negative fluxes for the boxed region (from top-right magnetogram) are also shown in the subsequent plots.

are obtained by using the wavelet transform (Young, 2007). The contracted loop is shown by arrow in every images in both the panels. During collapsing period it covered about 15″ in height. Later, though its signature is not visible due to the weakening of its brightness, we do see some drop of material on to the filament at 2:37 UT indicating the collapsing loop reaching the filament location at that time. Soon after the collapse of the loop the filament started to erupt.

2.4.6 Contraction of the postflare loop

After the first eruption of the filament, the north-west portion of the filament got into activation. One of the post-flare loop started to shrink over the filament which is shown by an arrow (L) in Figure 2.11 (top). The loop height reduced over the time. During this period, there was a westward flow in the dark portion of the filament. Once the shrinking loop disappeared in 171 Å channel, a dark feature appeared to be moving towards western side at 3:40 UT. After this, several loops around the filament cooled down and the length of the dark feature increased in size at 4:15 UT.

To find the height of the loop and the rate at which it was shrinking we have extracted the loop using the wavelet transform based low-pass filtering as above. Later we fitted a semi-circle to the identified loop and extracted its radius over the time. We then plot a reduction in radius over the time and is shown in Figure 2.12. The loops were identified in 3 wavelengths, 171, 304 and 335 Å images. The loop first disappeared in 335 Å wavelength, later it disappeared in 171 Å wavelength and finally in 304 Å wavelength. In 304 Å wavelength it was visible for about 30 minutes.

In sequence of Hα images, the shrinking loop was not visible, but the motion of the dark feature in the filament channel was visible over the time. At 3:20 UT, a dark arc shaped filament in the northern portion of the two ribbon flare was visible and is shown in Figure 2.11 (bottom).

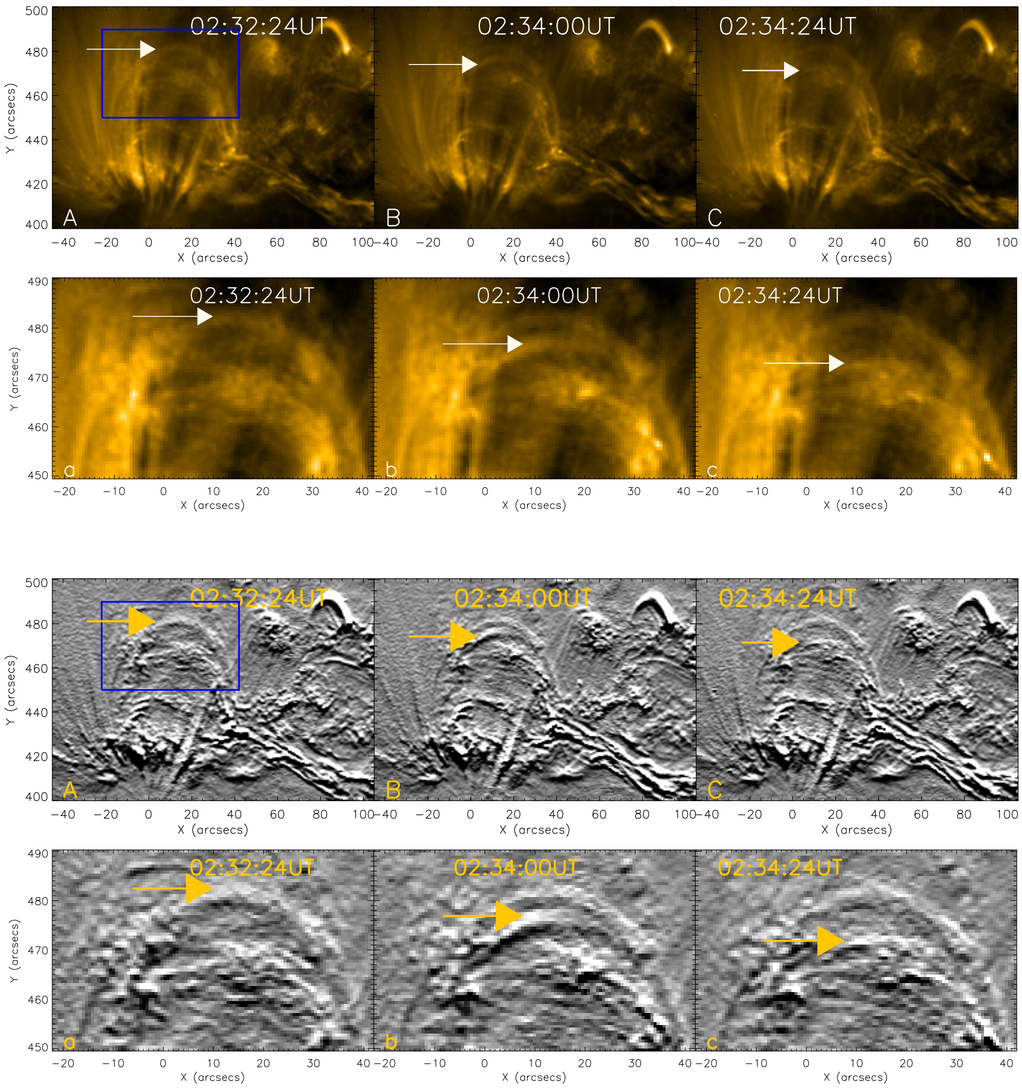

Figure 2.10: Top – 1st panel: Sequence of 171 Å images (A, B, C) for the east portion of the filament just before the first eruption showing the contraction of the loop over time. The white arrow shows the bright loop which was contracting. Top – 2nd panel: Sequence of 171 Å images (a, b, c) (zoomed portion of the blue boxed region of 1st panel image) showing the contraction of the loop. Bottom – 1st panel: Sequence of 171 Å high-pass filtered images (A, B, C) for showing the contraction of the loop. Bottom – 2nd panel: Sequence of 171 Å high-pass filtered images (a, b, c) (zoomed portion of the blue boxed region of 1st panel image) showing the contraction of the loop.

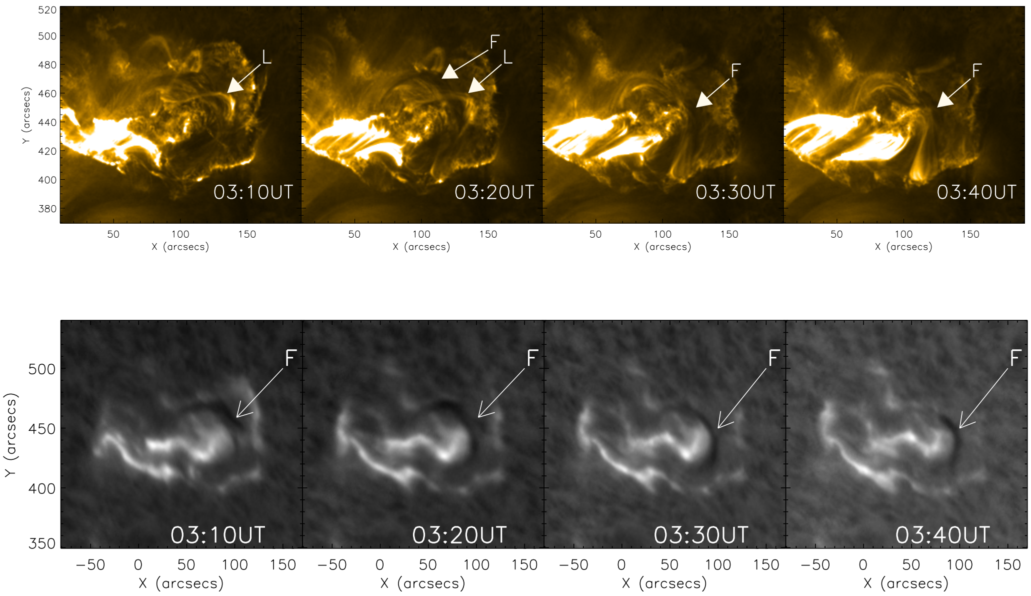

Figure 2.11: Top: Sequence of 171 Å images for the north-west portion of the filament after the first eruption showing the contraction of one of the post-flare loop. The white arrow followed by 'L' shows the bright loop which was contracting before the second activation. The white arrow followed by 'F' indicate the filament location. Bottom: Sequence of H_α images showing the filament position by white arrows (F) with time.

2.4.7 Expansion, reconnection and collapse of coronal loops near the filament ends

Near the east side of the filament, several post flare loops were visible. At around 03:45 UT, there was an expansion of loops towards higher heights in those regions, as shown in a sequence of 171 Å images in Figure 2.13 (panel A–F). The arrow followed by '1' shows the expanding loops. A small brightening was observed at around 03:40 UT in EUV channel in the eastern footpoint location of the expanding loop. This brightening location is shown by a blue rectangular box in Figure 2.13 (panel A & B) in 171 Å channel. In the same location, a small scale magnetic flux cancellation was observed during the brightening (shown in boxed region in Figure 2.14 (panel A)). The magnified view of the boxed region in magnetograms are also shown in the same Figure 2.14 (panel B – I) with time. In the magnified magnetograms, the circled region show the canceling features wherein the positive polarity

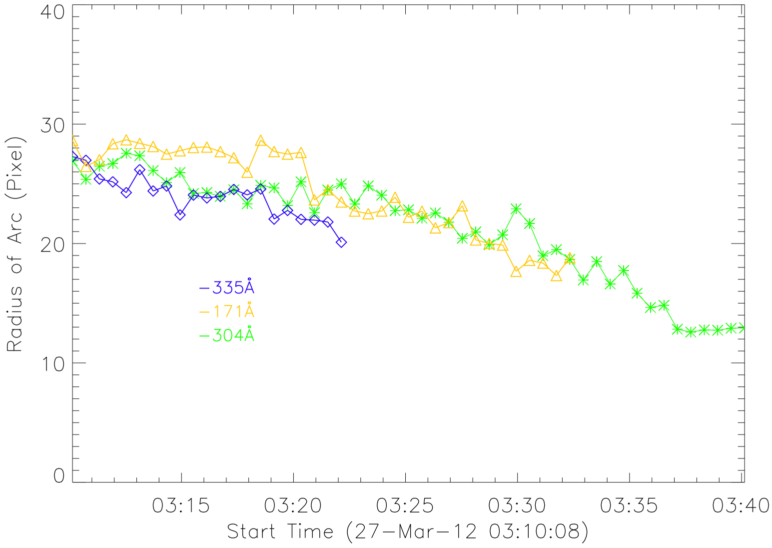

Figure 2.12: The radius of the loop (shown in Figure 2.11) is plotted over time observed in 335 (blue plot), 304 (green plot) and 171 (orange plot) Å images.

region moved towards the negative region and eventually canceled. During the time period 03:45 UT to 04:21 UT expanding loops reached about $60''$ in height from initial position with a projected speed of 20±2.3 km/sec, while the collapsing coronal loops came down by $35''$ with a projected speed of 11.9±2.0 km/sec. While the loop is raising, the brightening was seen in the adjacent loop top. This brightened loop was cusp shaped, as shown by white arrow '3' in the sequence of 171 Å images in Figure 2.13 (panels F – J). The magnified view of the green boxed region (shown in Figure 2.13 (panel J)) are shown in 171, 304 and 193 Å wavelengths in the panels (a – f) of Figure 2.13. One can observe that the brightened cusp shaped loop is visible in 171 and 193 Å channels, but not in 304 Å channel. This brightened loop is shown by arrow '3' in 171 and 193 Å channels and the erupting filament is shown by arrow 'F' in 304 Å channel. The contour of the erupting filament extracted from 304 Å channel (panel b) is overlaid on the 171 and 193 Å channels, shows the position of the filament. This brightened loop was visible from ∼04:16 UT till ∼04:27 UT. The brightening could be due to the reconnection between the rising and overlying loops. At the same time the filament got activated and started to raise in height. The top coronal loop on the western side of the filament started to collapse at the time ∼03:59 UT. The arrow followed by ‘2’ in Figure 2.13 (panel C & D) shows the collapsing of the coronal loops. Later, the filament rose to higher heights and the overlying loop in the western footpoint collapsed. While erupting, the filament appeared as twisted into the helical form and eventually disappeared from the FOV. On the east side of the filament the loops moved in upward direction and expanded. On the west side of the filament the loops moved in downward direction and shrunk.

2.4.8 Photospheric flow in and around filament region

The filament was formed at the polarity inversion line of the plage region. In order to find the direction of flows in and around the filament at the photospheric level we applied a Differential Affine Velocity Estimator (DAVE; Schuck 2006, 2008) to the time sequence of magnetograms. The DAVE incorporates the advantages of differential local correlation tracking (LCT; November and Simon 1988, see Section 3.3.4 for more details about LCT.), including a quantitative measure of the goodness of the affine flow model (Schuck, 2005). In this technique, a local affine velocity model is assumed allowing linear spatial deformations of the velocity within the apodizing window. The measured velocity satisfies induction equation in a least-square sense within the apodizing window. In brief, this technique is compatible with the induction equation, has ability to detect flow patterns inside the apodizing window and allow high time cadence images. Hence, DAVE can estimate photospheric velocities from magnetograms. This tracking method depends on two parameters, 1) the apodizing window size and 2) the time interval between the images. For a given time, the window size should be large enough so that tracked features remain confined within the window and also, it should be small enough to be consistent with an affine velocity profile.

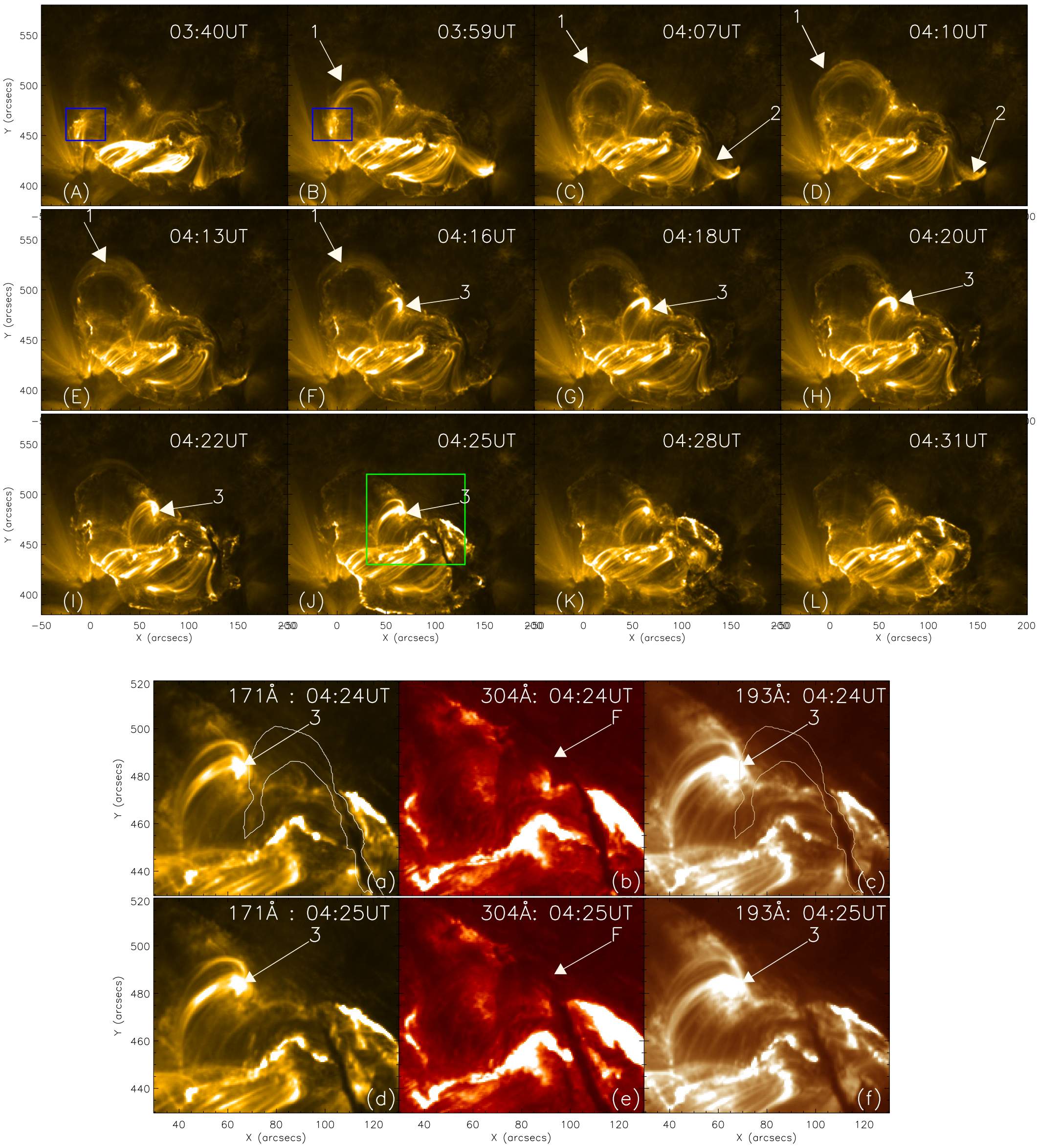

Figure 2.13: Panel (A)–(L): sequence of 171 Å images for the north-west portion of the filament before the second eruption showing the expansion and collapse of coronal loops. The white arrow 1 and 2 show the expansion and collapse of coronal loops, respectively over time. The white arrow 3 in the panels F–J shows the brightened loop close to eastern footpoint of the filament during filament activation. The blue boxed region (panel A & B) shows the brightening close to eastern footpoint of the expanding loops. Panel (a)–(f): magnified version of the green colored boxed region of panel J image, are shown here in three different wavelengths 171, 304 and 193 Å, respectively. The brightened loops are shown by arrow '3' in 171 and 193 Å images and the erupting filament is shown by arrow 'F' in 304 Å image (panel b & e). The erupting filament contour overlaid on 171 and 193 Å images is extracted from 304 Å image.

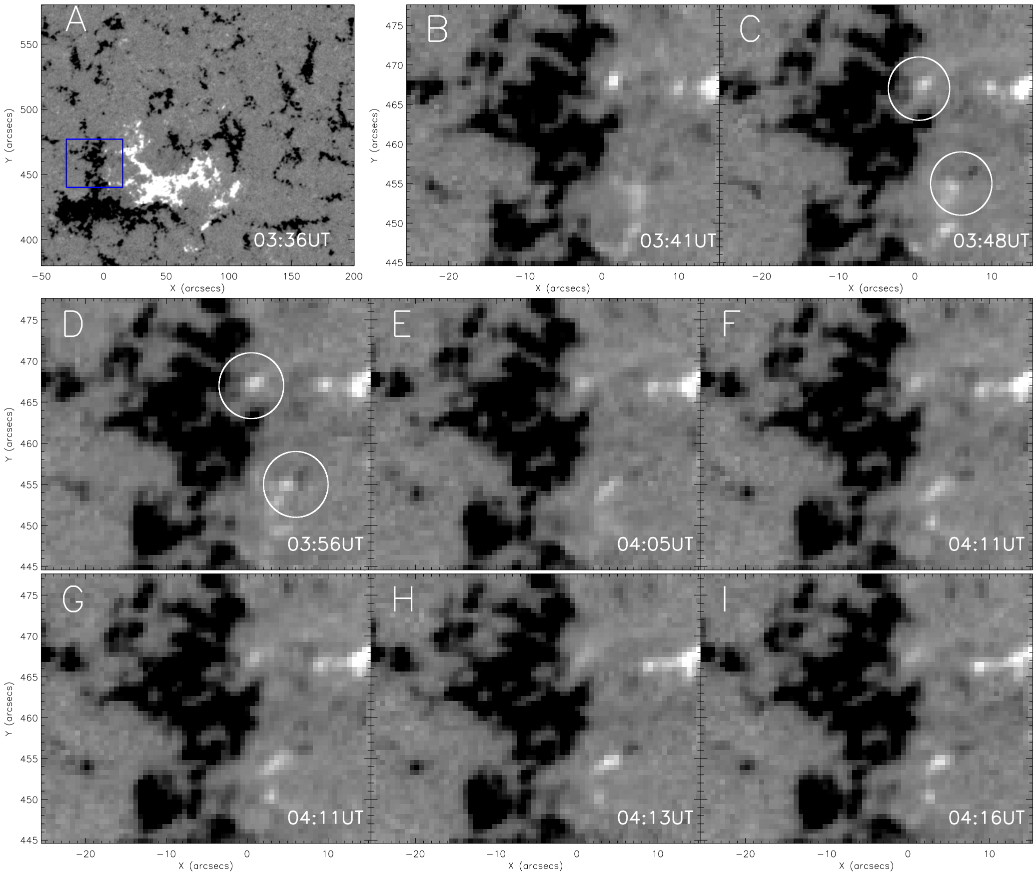

Figure 2.14: Panel A shows the line-of-sight magnetogram for the similar field of view of the top 171 Å images of Figure 2.13. The boxed region is the same region as shown in Figure 2.13. The zoomed version of the boxed region of this magnetograms are displayed in a time sequence in which circled regions indicate the flux canceling region over time (Panel B - I).

It has been observed that rectangular size apodizing window seems to work better than the square window (Welsch *et al.*, 2007). After several trials we have chosen a window size of $12'' \times 10.8''$ and time difference of 4.5 minutes to compute the velocities. The obtained velocity v_x and v_y are averaged over 5 hr to find the steady flow directions. Figure 2.15 (top) shows the long lived flow field in and around active regions, obtained after averaging over 5 hr starting from 22:50 UT (on March 26) to 03:50UT (on March 27). Clearly in the figure, it is easy to see the supergranular flows in and near the plage regions. These are shown by the blue polygon which are drawn at the edges of the flow which meets from opposite sides. The average size of these polygon

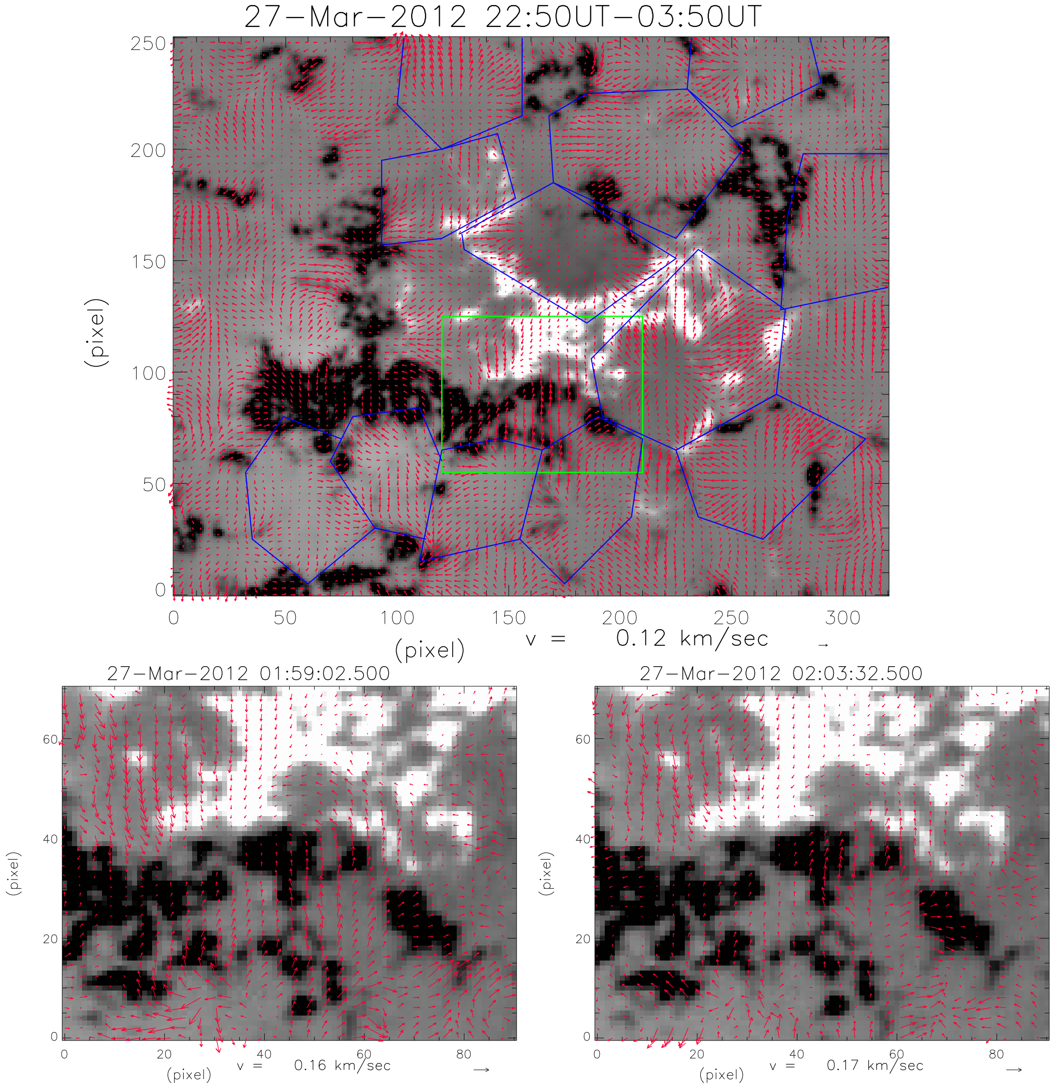

Figure 2.15: Top: The horizontal averaged velocity vectors shown in arrows are overlaid upon the 4 hr averaged magnetogram. The averaging time interval is given above the figure. The supergranular flows near the PIL and plage regions are shown by the blue polygons. Bottom: A blow up view of the velocity flow fields near the PIL (green boxed region of top figure) during the brightening time.

is about $40''$. The flows are convergent near the PIL where the positive and negative polarity fields meet. The supergranular flows are responsible for the continuous converging flows near the PIL. The PIL region is shown by the green colored rectangular box. Magnified view of the velocity flow for this boxed region are shown in Figure 2.15 (bottom) without averaging during the pre-flare brightening time. It also shows a continuous motion of opposite polarity features moving towards each other. A solar rotational motion removed (2 km/sec), 5 hr averaged dopplergram also shows the supergranular flows with upflows in the center of the supergranulation and downflows near the periphery of the boundary of the supergranular flows. Clearly, the supergranular flows is responsible for the observed converging motion of features near the PIL.

2.4.9 Photospheric magnetic field

The magnetogram shows that the filament location is near the PIL of the two opposite polarity plage regions (Figure 2.9 (top)). A time sequence of magnetograms before and during the first phase of filament activation is shown in Figure 2.16 (top). It is observed that the opposite polarity magnetic regions are interacting with each other at the PIL. The cancellation of magnetic flux was observed in this region. This region also showed a pre-flare brightening at around 01:56 UT on 27 March 2012. Some of the canceling features during the observation of pre-flare brightening are marked by the red circles in the magnetograms at the PIL. The flux cancellations near the PIL could be the cause for the preflare brightening near the filament.

Figure 2.16 (bottom-left) shows the magnetogram few minutes before preflare brightening. Magnetic flux in the active region was computed within the contoured region shown in Figure 2.16 (bottom-left). This contour encloses the bipolar region of interest. Figure 2.16 (bottom-right) shows the calculated negative and positive fluxes for this contoured region. It is observed that

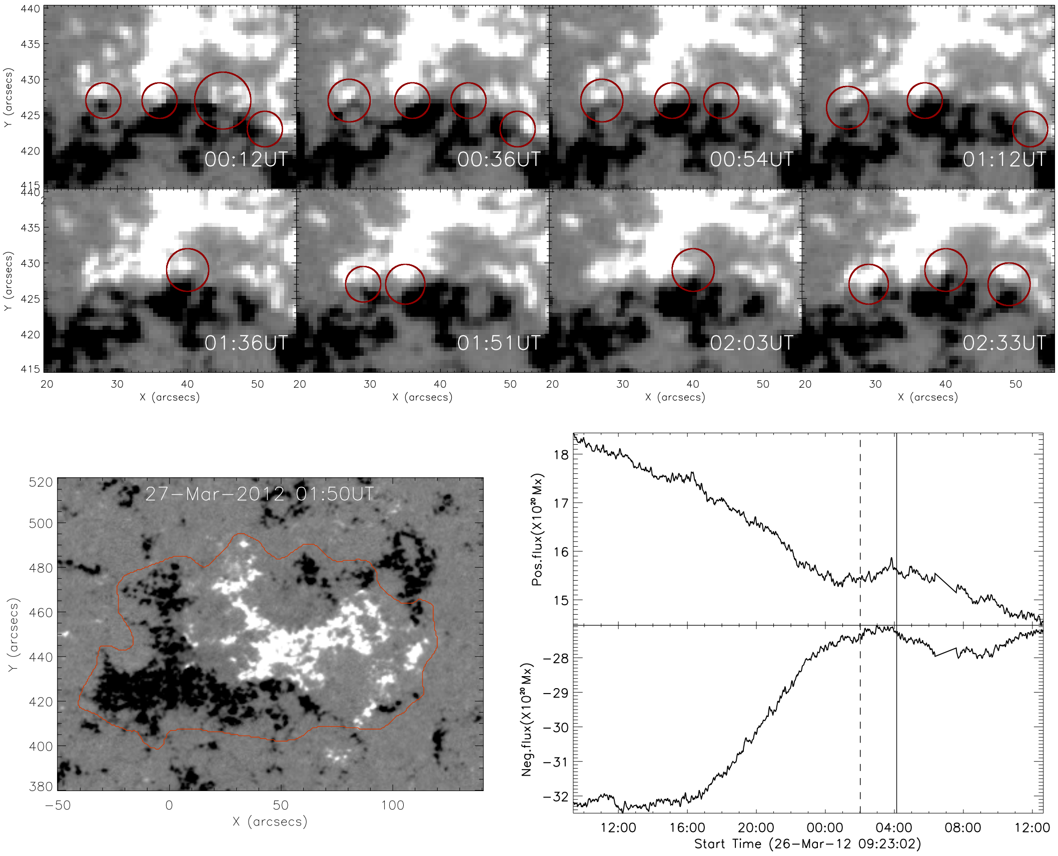

Figure 2.16: Top: A sequence of line-of-sight magnetogram show the flux cancellation at the PIL during pre-flare brightening. The flux cancellation regions are marked by the circles. Bottom–Right: The plot shows the calculated positive and negative fluxes for the irregular contour (Bottom–left line-of-sight magnetogram). The dashed and solid vertical lines represent the onset time of first activation and second activation of the filament eruptions, respectively.

the flux is not balanced in this region. The magnetic flux in the negative polarity is larger than in the positive polarity. The flux start to decrease in both the polarities from the beginning of observations. However, in the negative polarity region the flux started to decrease clearly after 16:00 UT. The flux decreased at a rate of 2.52×10^{19} Mx/hr in the positive and $5.89\ \times10^{19}$ Mx/hr in the negative polarity regions over 9 hours time period starting from 16:00UT on 26th Mar 2012. When the flux decrease is stopped we observed the first event of the filament eruption followed by C5.3 class flare (shown by dashed line in the plot). The second event occurred when there was a slight increase of negative flux and decrease in positive flux (shown by solid line in the plot). The temporal evolution of the flux suggests us that there was a continuous cancellations of the flux in this region.

2.5 Summary and Discussions

We observed an eruption of filament associated with an active region NOAA 11444 that located in the northern hemisphere at a latitude of 21°. The filament was inverse 'J' shaped and located along the polarity inversion line. It has erupted in two different phases. In the first phase of the eruption the southern portion of the filament erupted, while in the second phase the northern portion erupted. The sequential progress of the events are given in the Table 4.1. These two phases of eruptions were accompanied with a GOES C5.3 and C1.7 class flares respectively.

The transient brightening in EUV started at ∼01:56 UT at the location of one end of the filament. Photospheric magnetograms showed continuous cancellation of the flux near the PIL and the DAVE derived velocity showed converging motion in the same location. After the transient brightening, the filament rose slowly at a velocity of 1.5±0.3 km s^{-1}. Later, it accelerated during the flare. That is the time the rate of flux cancellation has decreased near the PIL. The slow rise of the filament in the first phase of the eruption could be caused by the reconnection occurred in the low level as explained by Moore and Roumeliotis (1992). The reconnection occurring in the low level can reduce the tension of the overlying twisted fields, there by the over powered magnetic pressure could have pulled the filament to higher heights.

The flux cancellation in the photosphere emphasize gradual progress of magnetic reconnection in the upper layers, while tether-cutting is relatively more impulsive process occurring in the lower corona. Sterling, Moore, and Freeland (2011) analyzed an active region filament eruption which occurred on 12 May 2010. In their case, they observed a gradual magnetic flux can-

Table 2.3: Progress of events during eruption.

Time (UT)	Observation
∼01:56	A brightening was observed (red boxed region in Figure 2.4 (top-right)) in 171, 193, 335 and 304 Å.
∼01:57 – ∼02:35	A bright flow was observed, which moved from east side of the filament to the west side.
∼02:30	One more brightening was observed near the east end of the filament which is related to preflare brightening of C5.3 class flare (see Figure 2.8) and filament showed an acceleration.
∼02:32 –∼02:35	Contraction of coronal loop on the eastern part of the filament (see Figure 2.10).
∼02:53	C5.3 class flare and a large amount of bright mass ejected along with the filament eruption.
∼03:08	Peak time of the C5.3 class flare.
∼03:14	A dark filament portion appeared over the bright and dark filament channel (see Figure 2.7).
∼03:14 –∼03:40	The north-west portion of the filament started activation. Shrinking of one of the post-flare loop is visible (see Figure 2.11).
∼03:45	There was an expansion of loops towards higher heights in the east side of filament. At the same time a contraction of loops in the west side are also visible and these loops were sitting over the filament (see Figure 2.13).
∼04:15	Several loops around the filament cooled down and length of the dark feature increased in size.
∼04:16 – ∼04:26	A brightened cusp shaped loop was observed near the east end of the filament, as shown by arrow '3' in the Figure 2.13 (panel a – f).
∼04:20	This filament eruption started followed by C1.7 class flare.

cellation under the filament, which built the filament flux rope over the time, causing it to rise gradually. The filament eventually erupted due to the onset of a magnetic instability and/or runaway tether cutting. During the onset and early development of the explosion for six bipolar events, Moore *et al.* (2001) observed that in each of the events the magnetic explosion was unleashed by runaway tether-cutting via reconnection in the middle of the sigmoid. Their study suggest that this internal reconnection is essential for the starting of sigmoid eruption and grows in step of the magnetic explosion in eruptive flares. Recent results show a direct observational evidences for 'Tether-Cutting' mechanism in at least two events (Chen *et al.*, 2014). We believe that the observed brightening near the low lying filament end followed by a bright flow along the filament could be the reconnection occurred in the lower layers and a signature of 'Tether-Cutting' mechanism which could have initiated the slow rise of the filament.

Flux cancellation across the neutral line could be one of the reason by which the overlying field could destabilize. The underlying field after the flux cancellation gets submerged, the imbalance in the magnetic tension and pressure of the overlying layer could cause the expansion of the field lines. Numerical simulations indicated that the flux cancellations along the PIL can form the twisted helical flux rope which support the filament (Chae, 2003; van Ballegooijen and Martens, 1989) and the same processes can also destabilize the filament (Amari *et al.*, 2003; Martin and Livi, 1992). The flux cancellation at the polarity inversion line can lead to the coronal structure evolving towards highly sheared fields which eventually can erupt in the later stage (Green, Kliem, and Wallace, 2011). Sterling *et al.* (2010); Zuccarello *et al.* (2007) observed that the filament ejection being triggered by flux cancellation between the positive flux elements and the surrounding negative field. The work reported here supports the flux cancellation at the PIL could have destabilized the filament which eventually erupted during C5.3 class flare.

In summary for the first phase of eruption, our observations show that there was a continuous converging flows and magnetic flux cancellation near the PIL followed by transient brightening related to the tether-cutting mechanism. This could eventually destabilized the bottom filament in the first phase of eruption and pushed the top filament to little higher heights. The top filament showed a slow rise, followed by the bright flows and it eventually started to erupt during the coronal loop collapsing phase which could be due to the decreasing of the tension force under the coronal loop after the small reconnection beneath the bottom of the loop.

Further, in the same active region NOAA 11444, we observed a second phase filament eruption, after ∼1 hr 27 min of the first filament eruption. It was suggested that in the flaring region a decrease of the magnetic pressure after the stored energy released could cause a contraction of the overlying loops (Liu and Wang, 2009). Further, we observed there was an expansion of the coronal loops near the east end of the filament. The collapsing/shrinking loops and simultaneous outward moving loops during the decay phase of solar flare could reconnect (Khan, Fletcher, and Nitta, 2006). The expansion of these coronal loops may lead to the reconnection (with the overlying/collapsing loops), which could remove a sufficient amount of overlying flux, making an opening for a flux rope, as numerically explained by Török *et al.* (2011). A brightened cusp shaped loop was observed near the east end of the filament, which tells us that there was a reconnection between the expanding loop and the collapsing/overlying loops. In summary for the 2nd phase of eruption, converging motion, cancellation of magnetic flux, raising loops, reconnection with the overlying loops all suggest that the flux cancellation is responsible for the activation and eventual eruption of the filament in the second phase too. The brightened loop closer to the eastern end of the filament indicate the reconnection occurred at coronal level, which could have made an opening for a flux rope by removing a sufficient amount of overlying flux, leading to the eruption of the filament. The reason for the collapsing loop observed near the western end of the filament is not clear. However, Liu and Wang (2010); Yan *et al.* (2013) explained that the collapsing of the loops could be due to the reduced magnetic pressure underneath the filament.

The increasing spatial resolution in the EUV wavelength and high temporal cadence observations provided a good data to study the very complicated events like the one studied here. In the next chapter, we have reported one more active region filament eruption event to understand the sequences of events occurring before the filament eruption in EUV wavelength regime from a large pool of data observed by the AIA telescope and Hα images from Big Bear Solar Observatory (BBSO; Denker *et al.* 1999).

Chapter 3

A study of an active region filament eruption associated with rotational motions near the footpoints

---

3.1 Introduction

Twisted magnetic fields support the filaments in the corona. The equilibrium loss initiated by kink-mode instability in twisted magnetic fields is one of the leading mechanisms for filament destabilization and eruption (Sakurai, 1976a). The kink-instability occurs when the twist of the emerged flux ropes exceeds a critical value, causing *writhing* of flux rope around its axis (Fan, 2005). As a result, the flux rope can loose its equilibrium and erupt (Liu, Alexander, and Gilbert, 2007). By observing an active region filament, Romano, Contarino, and Zuccarello (2003) found that a total twist in one of the prominence threads changed from 5-turns to 1-turn as it raised during filament activation. They concluded that prominence was destabilized by kink-mode instability and magnetic field later relaxed to a new equilibrium position. Romano, Contarino, and Zuccarello (2005) suggested that in one of the filament eruption events, the injected magnetic helicity via the photospheric shearing motion exceeded the kink instability threshold.

The filament eruption could be triggered by the magnetic reconnection at low level in the solar atmosphere (Contarino, Romano, and Zuccarello, 2006; Contarino *et al.*, 2003). In the photosphere it is seen as a cancellation of magnetic features (Priest, Parnell, and Martin, 1994). Many times it has been observed that magnetic flux cancellation occurs at the photosphere near the PIL (Martin, 1998a). If the flux cancellation at the photosphere continues after the flux rope has been formed, it may result in instability leading to eruption; as formulated by Amari *et al.* (2003, 2011); van Ballegooijen and Martens (1989). It has also been observed that flux cancellation at the PIL lead to the formation of X-ray sigmoid which eventually triggers the CME (Green, Kliem, and Wallace, 2011). A successive reconnection in the coronal arcade can change the configuration such that filament below the arcade can no longer be sustained. This destabilization can cause the eruption of the filament (Zuccarello *et al.*, 2007). "Tether-cutting" mechanism is another example of magnetic reconnection where strapping of magnetic tension force is released by internal reconnection above the PIL (e.g., Moore *et al.*, 2001) to destabilize the filament. But, Aulanier *et al.* (2010) found that magnetic flux cancellations at the photosphere and the tether-cutting reconnection at the coronal heights do not initiate the CMEs in bipolar magnetic field configurations. However, they are essential to buildup flux ropes in the pre-eruptive stage. Subsequently, the flux rope rises to a height at which the torus instability can set in to cause the eruption.

Sunspot rotation in the vicinity of filament can also be responsible for the formation and ejection of active region filament (Yan *et al.*, 2012). Zuccarello *et al.* (2012) have observed a B7.4 class flare associated with filament eruption which occurred in the active region. By examining the magnetic field configuration and photospheric velocity maps they concluded that a shearing motion of the magnetic field lines could increase the axial field of the filament, thus bringing the flux rope to a height where the torus instability criteria is met to favor the eruption.

In this chapter, we present the study of a filament eruption that occurred in the vicinity of the active region NOAA 11247 that was observed in different wavelength regimes. The filament eruption occurred at about 23:20 UT on 08 July 2011 and it was followed by B4.7 class flare starting at ∼ 00:45 UT. Prior to eruption, a flux emergence in the vicinity of filament footpoint and converging flow were observed in two footpoints of the filament at the photosphere. These footpoints of the filament were rooted in the West-most plage region. Just after the filament activation, a rotational motion was also observed at the footpoint locations (Dhara, Ravindra, and Banyal, 2014a). In the next Section of this chapter, we describe the data preparation and the analysis method used. The observational results starting with flux emergence, converging flow around the filament footpoint, filament eruption and subsequent rotation in the footpoint are presented in Section 3.3. Finally, in the last section, we discuss the importance of the flux emergence and converging motion associated with filament destabilization and eruption. We also give plausible explanation for the observed rotation in the footpoints.

3.2 Observation and Data Analysis

We used EUV data from AIA at 171, 193 and 304 Å wavelengths (image cadence of 12 sec) to study the filament eruption in detail. The acquired data set starting from 15:00 UT (08 July 2011) to 04:00 UT (09 July 2011) covers the entire filament eruption event. The details about the data and analysis is given in Section 2.2.1.1. The corrected data has been tracked over the region of interest. This tracked region data cube was prepared and used to study the dynamics of the filaments at the coronal level.

Complementary to the coronal data sets, we also obtained a few full-disk H_α images from the Big Bear Solar Observatory to study the morphology of the filament at the chromospheric heights. These H_α images were acquired at BBSO (Denker *et al.*, 1999) with 2k×2k pixel CCD camera having a pixel resolution of $1''$. Similar to AIA data, we also extracted the region of interest in H_α images by tracking it in heliographic co-ordinate system. However, due to their limited availability, we used them only for the morphological study of the filament in the chromosphere.

We have obtained the line-of-sight magnetograms from HMI for about 2 days starting from 08 July 2011. The data has been interpolated to the AIA pixel resolution. Later, the obtained data has been tracked over the region of interest, corrected for the line-of-sight effect by multiplying $1/\cos\theta$, where θ is the heliocentric angle. The details about the data and analysis is given in Section 2.2.1.2. We averaged 4 magnetograms to reduce the noise level to 10 G. These magnetograms were then used to study the evolution of magnetic fields in and around the filament at the photospheric level.

Apart from these data sets, we also acquired the continuum intensity images from the HMI telescope for which the cadence and pixel resolution are same as the line-of-sight magnetograms. The obtained images have been tracked over the region of interest as has been done for the other data set mentioned above. The 'rotation-corrected' images were then used to determine the velocity of small features near the filament footpoints.

3.3 Results

3.3.1 Filament observations at various heights

The filament was located just outside the active region NOAA 11247 at a latitude of 19° in the southern hemisphere. The filament was visible on the Eastern limb when the active region turned towards Earth on 05 July 2011.

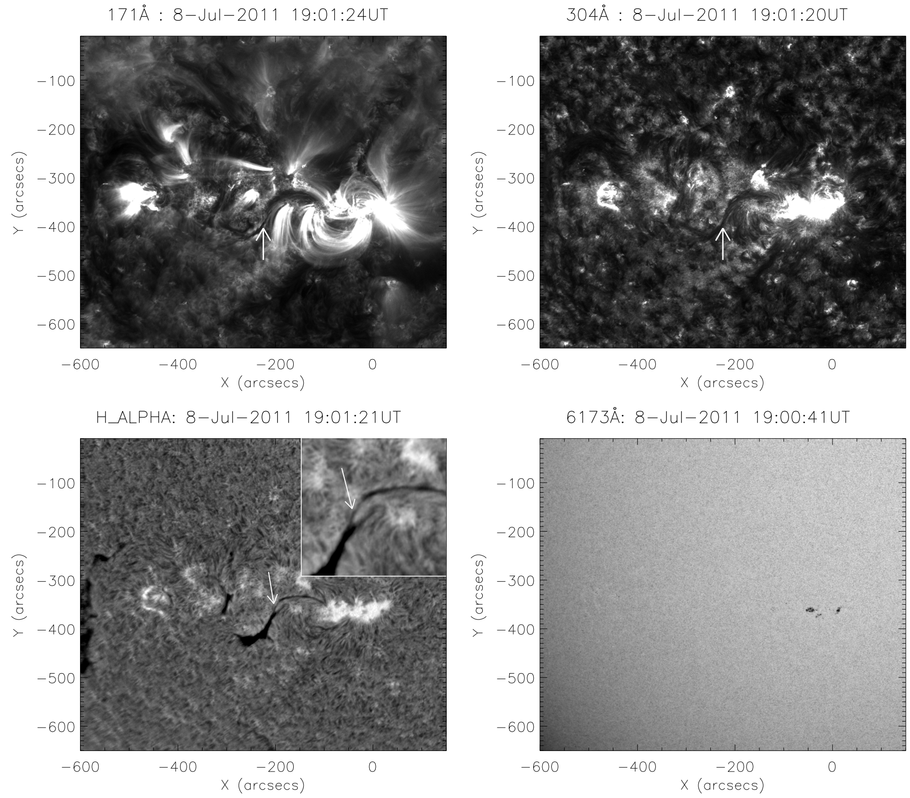

Figure 3.1: Observed filament in the 171 Å channel of the coronal image (top left), 304 Å of the transition region image (top right), Hα chromospheric image (bottom left) and photospheric continuum image (bottom right). The field-of-view is same in all the four images. In top two images, the filament location is indicated by white arrow. The inset image on the top right of H_α image shows the magnified portion of the bifurcated thin thread like structure of the filament.

During the filament eruption the active region was located at a longitude of 14° East of the central meridian. Figure 3.1 shows the active region as observed in different wavelengths from the corona to the photosphere. The 'S-shaped' filament is vividly seen in coronal 171 Å image (top-left) and in the higher chromosphere-transition region image taken in 304 Å wavelength (top-right). The filament in EUV wavelength is observed as dark feature. In the H_α image (bottom-left) the filament is visible as a thick dark structures located away from the active region and thin thread like structures extended up to bright plage region. The thin thread like structure bifurcates into two parts. The one part extends up to the plage region and the other one terminates somewhere in the quiet sun region. The bifurcation can be clearly seen in the enlarged portion displayed in the same H_α image, indicated by an arrow. Note that the thin thread like structure seen in H_α image appears as thick dark structure in the coronal image. This bifurcation of the filament in the Western footpoint is not visible in 304 Å image rather a continuous thick dark structure which ends in the Western plage region is seen. In the H_α image the filament exhibits a discontinuity at a location of -300 to -350 arcsec along the horizontal axis. The discontinuity in filament structure is also seen in coronal image (top-left) close to the East-side that is indicated by white arrow. The photospheric image (bottom-right) shows two sunspots in the AR 11247 that are located in the vicinity of the filament structure.

3.3.2 Filament eruption

Rust and Kumar (1996) suggested that the solar filaments and its neighboring structures exhibit the same sign of twist. The filament studied here appeared as 'S-shaped' structure. This suggests that the filament has left-handed chirality with positive helicity sign (Martin, 2003b). Also, the axial field of the filament is left-bearing for an observer looking at the filament from North polarity side of magnetic field (c.f. Figure 3.5) and hence the filament is sinistral (Martin, 1998b).

Figure 3.2 shows a sequence of 304 Å images while the filament is in erupting phase. In each of these images, the location of the filament is indicated by an arrow. In the middle-left panel image of Figure 3.2 we overlaid the contour of the filament extracted from an image obtained an hour before the filament eruption. It is evident that filament had started erupting at this stage. The region which is producing out of the contoured region (shown by an arrow) suggests the initiation of the filament eruption. The filament started to erupt at $\sim$ 23:20 UT on 08 July 2011 and became elongated. Later, it completely

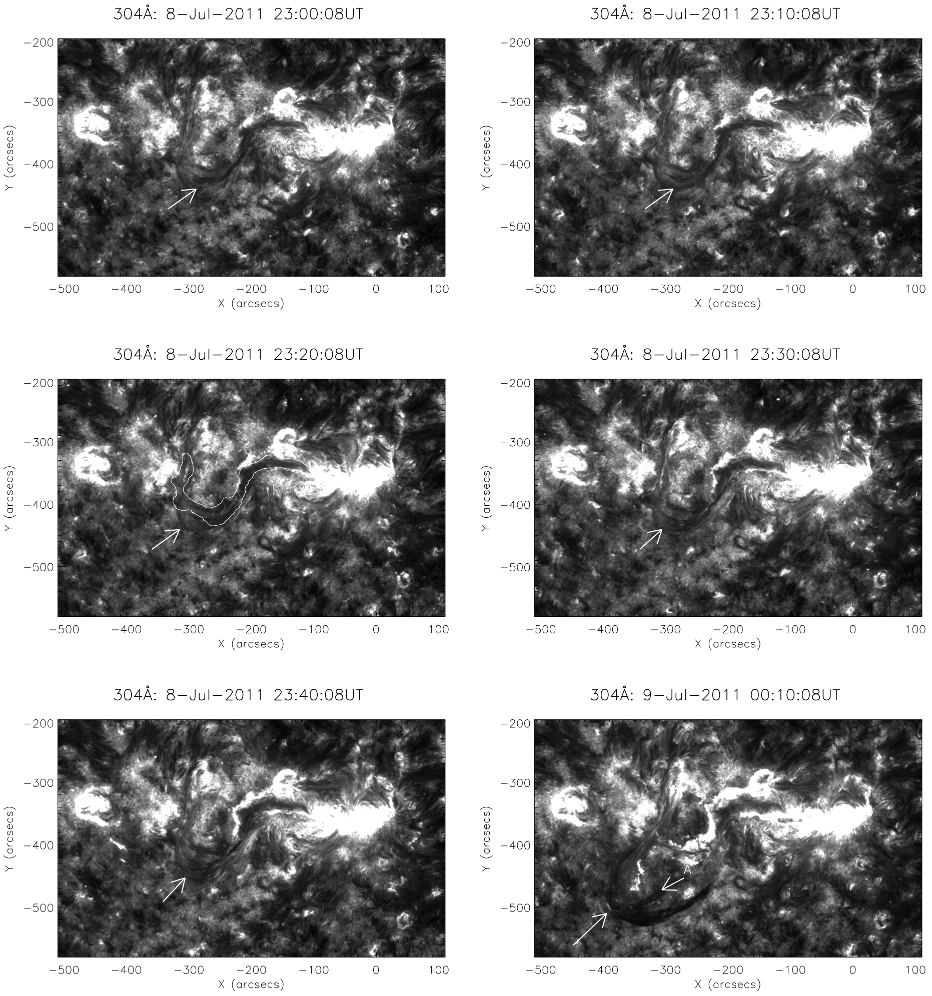

Figure 3.2: A time sequence of erupting filament is shown at different epoch in He II 304 Å images. The white arrow indicates the position of the filament and the letter 'A' (bottom-right) with an arrow shows the position of a small portion attached to the bottom side of the filament that took an anomalous path while erupting. In the middle-left image the contour of the filament channel is overlaid on the erupting filament.

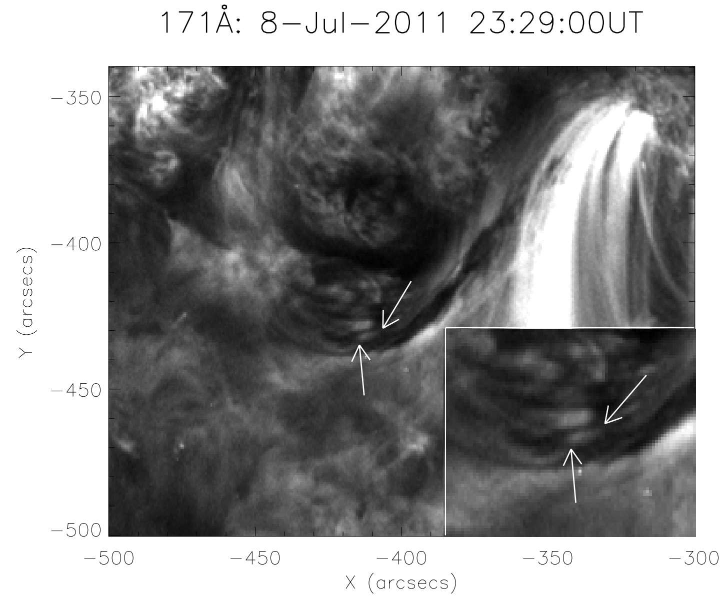

Figure 3.3: Erupting filament shown in 171 Å image taken by AIA/SDO. The arrows indicate crossing of dark threads over the bright threads. The box on the bottom right of the image shows the zoomed in version of the cross over threads.

disappeared from the field of view at around 00:29 UT on July 09. In middle portion of the filament a discontinuity was observed (see Section 3.3.1). During the eruption this portion was seen as a tail shown by a letter 'A' with an arrow in the bottom-right image of Figure 3.2. The filament eruption was followed by two-ribbon flare (B4.7 class), observed at ∼ 00:45 UT.

The erupting filament (see Figure 3.3) shows a crossing of bright and dark threads in 171 Å images. The crossing of dark features over the bright regions is easily identified in the zoomed image where a bright feature in the background is seen going from right to left while the dark feature in the foreground crosses it from left to right. This crossing corresponds to the positive mutual (type I) helicity (Chae, 2000). Overall, the filament exhibits positive sign of helicity when it is quiet and also shows the same sign while it is erupting.

The space-time map has been made using 304 Å images to study the evolution of erupting filament. The top image in Figure 3.4 shows two slit

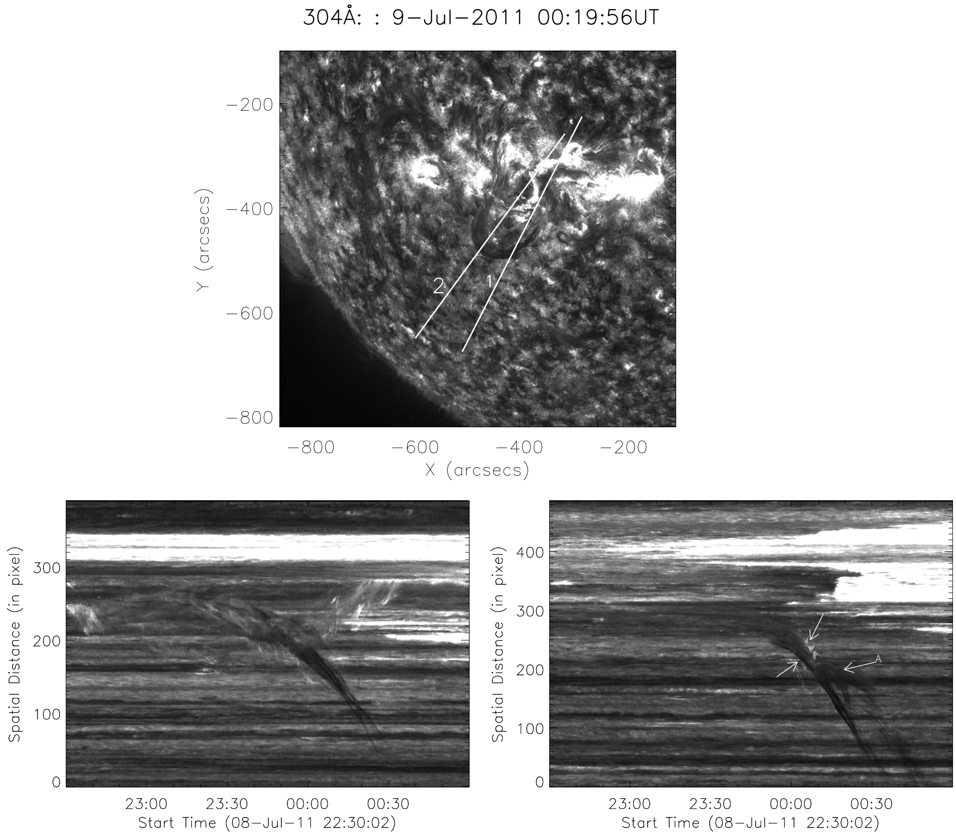

Figure 3.4: Top: The filament is shown in 304 Å image. Two white slits overlaid on the image represent the position from which the space-time maps have been generated. The slit number 1 crosses the Western footpoint of the filament. The slit number 2 crosses the filament midway between the footpoints. Bottom: The space-time map of filament eruption for slit number 1 (left) and for slit number 2 (right). A dark bended portion of the filament represents the path of the filament while erupting. The white arrow followed by letter 'A' (bottom-right image) showing portion of the filament which took a anomalous path. Other two white arrows shows the location of surge in the space-time map.

positions from which space-time maps were extracted in 304 Å wavelength. The slit position 1 provided the space-time map for the Western footpoint of the filament (bottom-left). The bottom-right image shows the space-time map for the erupting filament extracted from the slit position 2. The bottom-left space-time map shows that the filament activation started at about 23:20 UT at the Western footpoint. The space-time maps show the path of the erupting filament which is curved.

A brightening on the top and bottom part of the erupting filament from 23:55 to 00:12 UT (shown by two inward arrows) can be seen in the bottom-

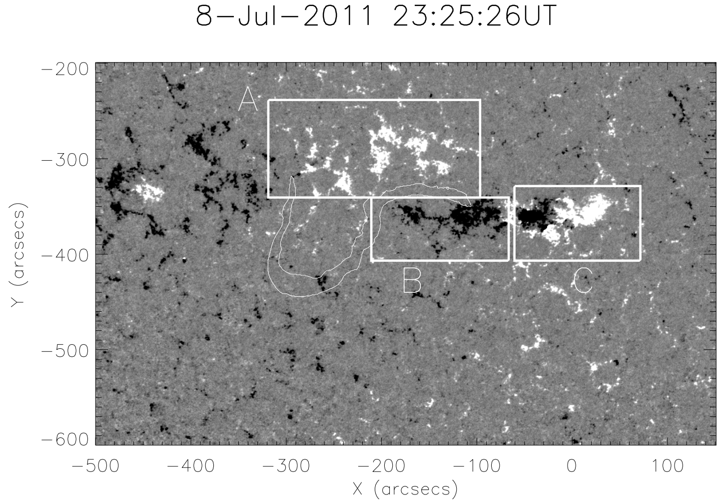

Figure 3.5: The line-of-sight magnetogram showing the location of the active region and plages. A white contours overlaid upon the magnetogram indicates the filament boundaries. The box A and B represent the plage region and box C represents the emerging flux region.

right space-time map. This type of brightening, also observed simultaneously in other wavelengths (171 Å & 193 Å), is caused by a surge which started from the footpoint of the filament and moved faster than the erupting filament.

A small portion of the filament marked as 'A' in Figure 3.2 (bottom-right) can also been seen in space-time map (shown by the letter 'A' with an arrow). Unlike normal curved path, this portion took a different trajectory and moved away from the main filament channel. This anomalous path is not visible in 171 Å images, suggesting that it may have collapsed before entering the corona. This portion arose from discontinuity in the filament region (see Section 3.3.1). The projected velocity of the erupting filament is 56 ± 1.4 km s^{-1}. This is obtained by extracting the data points on the curved portion of the path of the erupting filament in the space-time map and then fit a linear least square fit to the data points. The filament was not visible in coronal images after 00:30 UT on 09 July 2011.

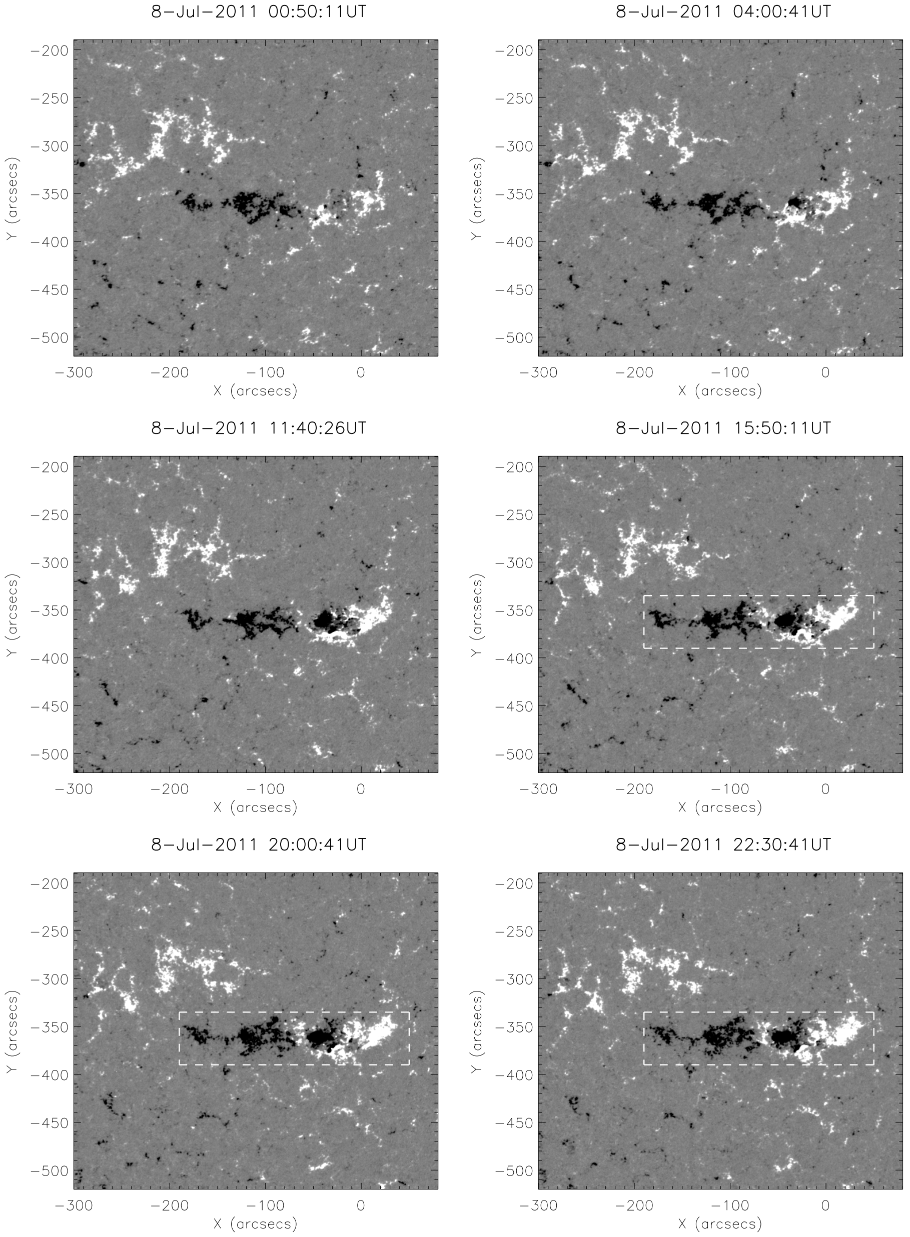

8-Jul-2011 00:50:11UT

8-Jul-2011 04:00:41UT

8-Jul-2011 11:40:26UT

8-Jul-2011 15:50:11UT

8-Jul-2011 20:00:41UT

8-Jul-2011 22:30:41UT

Figure 3.6: A time sequence of magnetograms. Black and white colors represent the negative and positive polarity of the magnetic field, respectively. The boxed region in the last three images show the quadrupolar configuration of magnetic flux distribution.

3.3.3 Emerging flux region

The location of the filament in the photosphere can be identified by overlying contour of the filament extracted from 304 Å image on the magnetogram. Figure 3.5 shows the contour map of the filament overlaid upon the magnetogram. The contour of the filament was extracted from the 304 Å image obtained at 23:20 UT on 08 July 2011 which is about 5 min before the magnetogram displayed in Figure 3.5. The East side footpoint of the filament is located in the positive polarity plage region and the West side is anchored in the negative polarity plage region. These are shown in Figure 3.5 in boxed regions A and B respectively. The box C shows the emerging flux region with positive and negative polarity flux associated with two small sunspots that were present during the eruption.

Figure 3.6 shows a sequence of magnetograms taken at different time in which the emerging flux region (region C) was visible. At about 00:50 UT on July 08, small mixed polarity regions resembling salt and pepper emerged between the positive polarity regions. At about 04:00 UT new negative magnetic flux started to emerge in the positive magnetic field region of the Western plage. In the meanwhile, at around 15:50 UT, an intrusion of positive flux is observed between the pre-existing negative flux region of plage and the newly emerged negative flux. The flux emergence and intrusion resulted in a final configuration of quadrupolar flux distribution of the Western magnetic field region. The boxed region (shown by dashed lines) in the last three panels of Figure 3.6 shows the intrusion of the positive flux into the negative flux region. The boxed region also shows the quadrupolar configuration of the magnetic field distribution.

Figure 3.7 shows the evolution of magnetic flux for locations A and B of the plage regions. The flux has been computed for those pixels whose absolute magnetic field strength is larger than 10 G in the boxed region A and B. The positive flux in the boxed region A was almost constant until

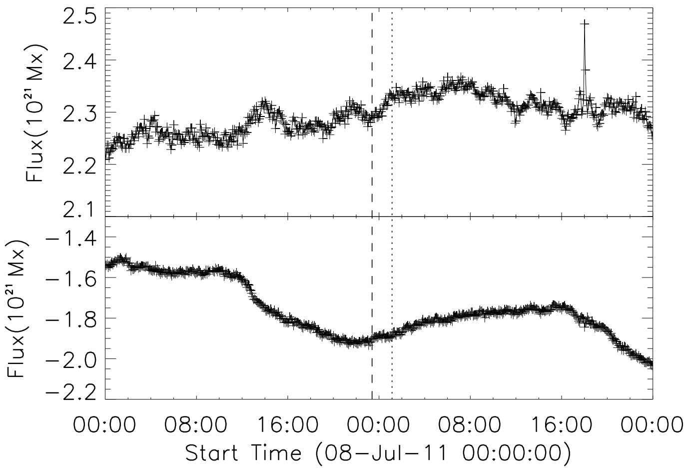

Figure 3.7: Top: The evolution of flux plotted as a function of time shown for the positive polarity plage region of Figure 3.5 (box A). Bottom: Same as top side plot but for negative polarity plage region of Figure 3.5 (box B). The first dashed vertical line represents the filament eruption time and the second dotted line represents the starting time of the flare.

about 08:00 UT on 08 July 2011. After 08:00 UT it increased slowly for few hour and became little faster after the eruption (Figure 3.7 (top)). After the B-class flare, the magnetic flux in this region became almost constant for about 5 h. The filament footpoint associated with this region were detached in the later part of eruption. The negative flux in Western footpoint of the filament (shown as box B) exhibited a different type of flux evolution. The flux started to increase from the beginning of the observations (Figure 3.7 (bottom)). This was because of a small negative flux region emerging in the vicinity of the Western plage. The increase in flux is also due to the merging of separated regions in plage, thereby increasing the strength of the plage region, though the area decreased slightly. The increase in flux was small in the beginning of 08 Jul 2011. Later, at around 12:00 UT onward the negative flux started to increase until an hour before the filament eruption. Western footpoint of the filament associated with this region had erupted at around 23:20 UT. The flux in the associated region had started to decrease about an hour before the filament eruption.

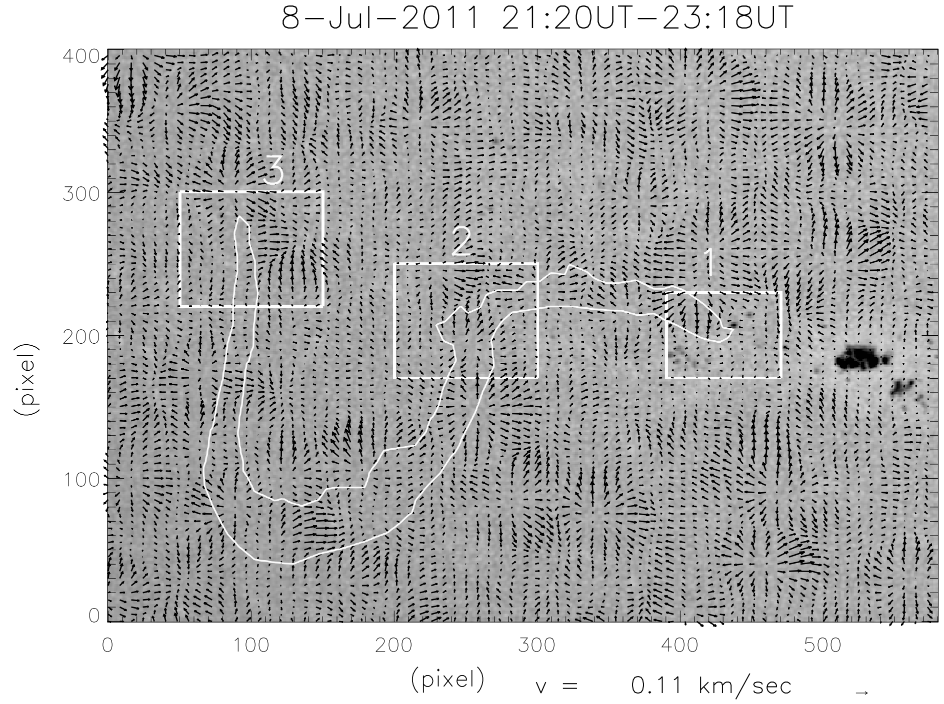

Figure 3.8: The horizontal velocity vectors shown in black arrows are overlaid upon the continuum image. The boxed region 1 and 2 show Western footpoint of the filament and the location of the bifurcation. The boxed region 3 shows the Eastern footpoint of the filament. The axes are labeled in pixel units.

3.3.4 Flows in and around the filament footpoints

Figure 3.8 shows the photospheric flow in and around the sunspot regions, plages and filament. The flow field has been obtained by using the local correlation tracking (LCT) technique applied on continuum images. The LCT is the most popular technique for inferring an optical flow from a sequence of images and it was originally developed by Leese, Novak, and Clark (1971) for tracking clouds. This technique was introduced into the solar physics by November and Simon (1988). The LCT is commonly used in motion tracking in solar physics. November and Simon (1988) used this technique to analyze white light observations made at Sacramento Peak Vacuum Tower telescope and identified the solar granular patterns from the measured vector displacements. This method is commonly applied to the intensity images to track the features and Chae (2001) first applied it to magnetograms. Before applying the LCT on the images, one needs to choose two parameters carefully, which are critical to the accuracy of LCT. These are: 1) the full width at half maximum (FWHM) of the apodizing window function and 2) the time interval between two images. The LCT method can be briefly summarized as follows. A local sub-image is first defined with a localized apodization function peaked at position x in the image taken at time t. The apodization function decreases toward the edges of the sub-image and it is mostly characterized by its FWHM, which defines the effective window. This sub-image is cross-correlated with another sub-image centered at $x + \Delta x$ in the next image (taken at $t + \Delta t$). The best correlation found, over the sub-images of the second image in the vicinity of x, defines the LCT velocity $\Delta x/\Delta t$. A velocity map is built by repeating the procedure for all x positions. After several trials we selected the optimum value of FWHM $= 4.5''$ corresponding to a time interval of 3 minute between two images to obtain the horizontal velocity of the photospheric plasma. The obtained velocity vectors were integrated over two hours period, as shown in Figure 3.8. The results mainly shows the long lived flows in and around the sunspots and plage regions. In the sunspot group an outward flow has been observed. Besides, a long lived flows in the quiet sun is a diverging motions whose size is about 30-40 arcsec. The pattern is similar to the one observed by De Rosa and Toomre (2004). These diverging flow patterns are the supergranular outflows that are seen everywhere. The box 1 shows the location of the Western footpoint and box 3 shows the Eastern footpoint of the filament. The box 2 region is a location of the another part of bifurcated footpoint in the Western side. In boxes 1 and 2 the flow direction is always converging inward.

The long term behavior of the flow field in the filament region is recorded in Figure 3.8. The space-time diagram shows that the filament activation initiated at around 23:20 UT. We have also looked at the boxed regions 1 and 2 during the filament eruption time. Figure 3.9 shows the temporal sequence of flow field in Western footpoint of the filament marked 1 in Figure 3.8. These velocity flow fields were obtained from 3-min time sequence images without

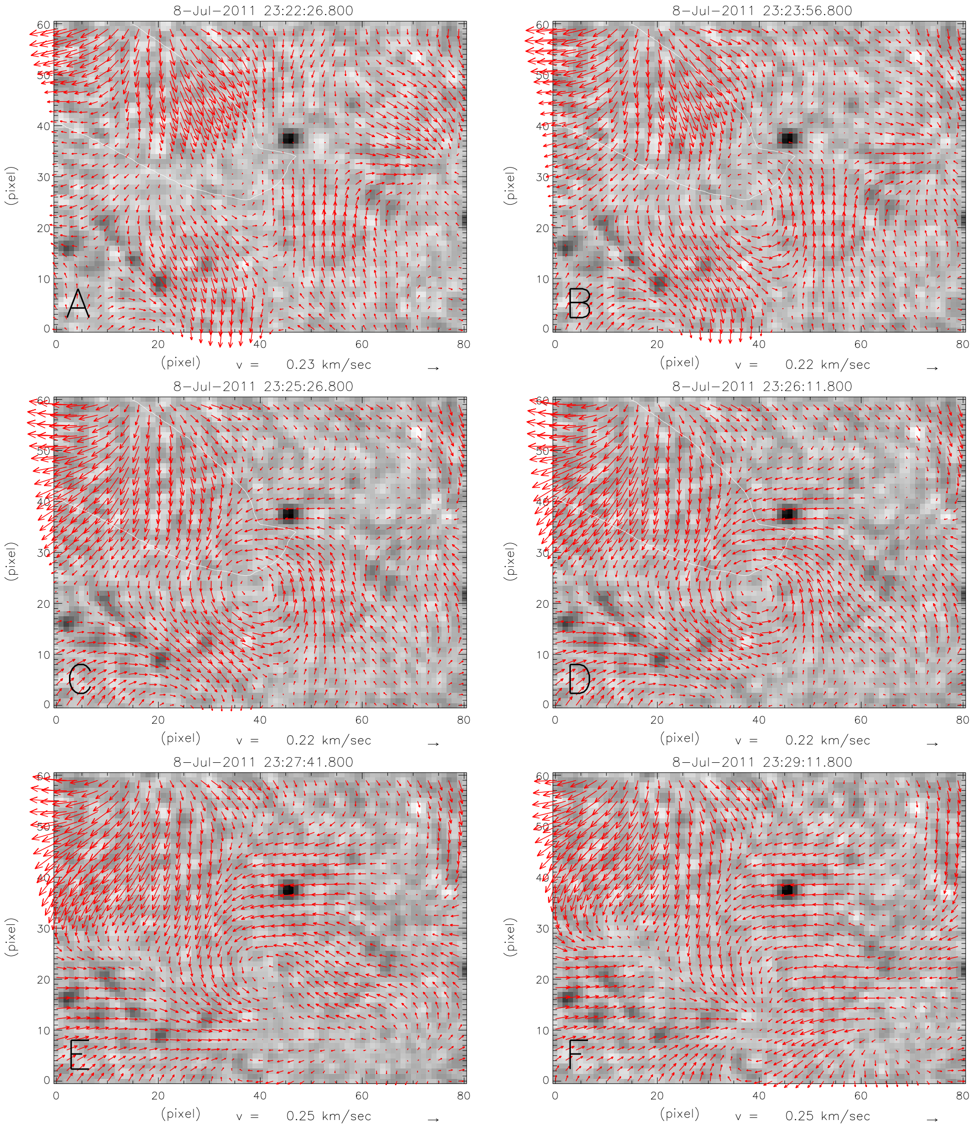

Figure 3.9: The temporal evolution of rotational velocity pattern observed in location 1 of Figure 3.8. The date and time of the computed velocity is shown on the top of each map. The size of arrow in the bottom of each map represents the magnitude of velocity. The horizontal and vertical axes are shown in terms of pixels.

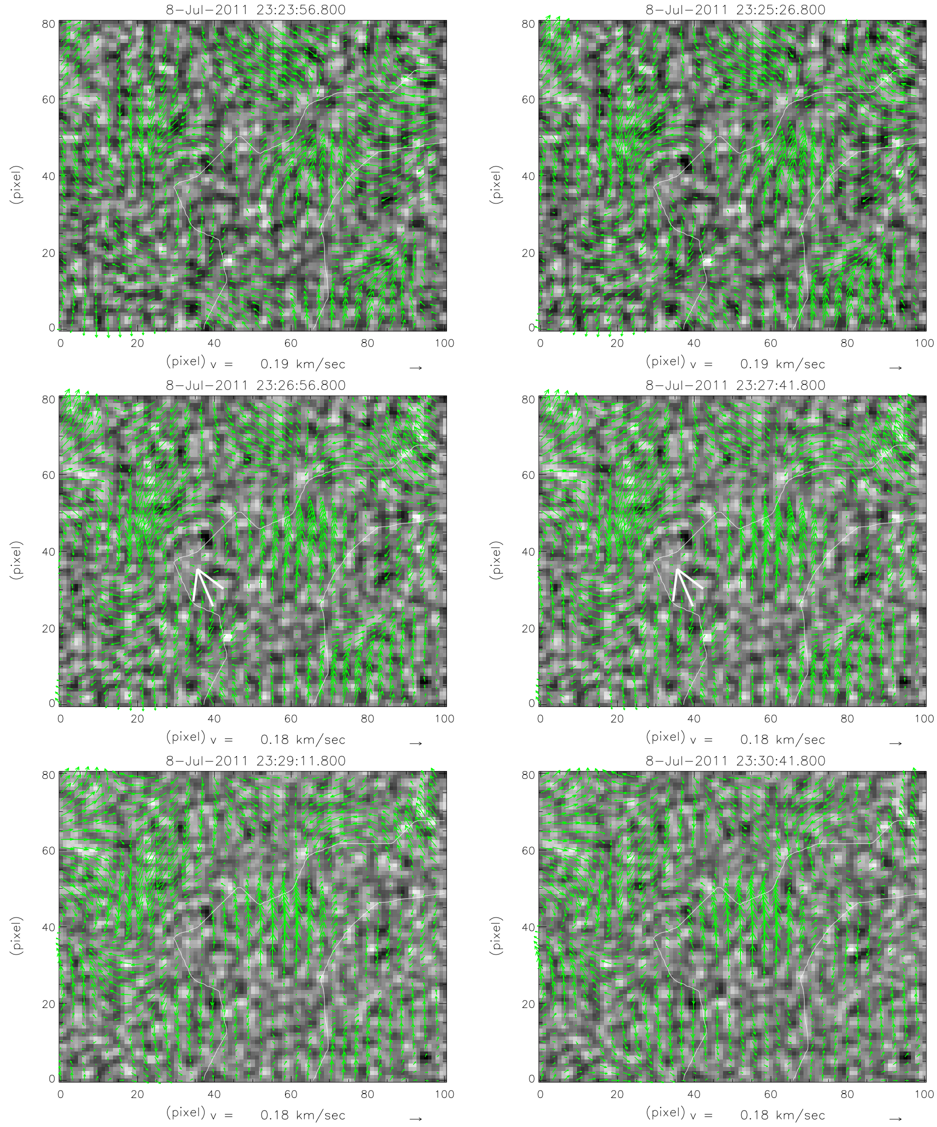

Figure 3.10: Same as Figure 3.9, but for boxed region 2 of Figure 3.8. The rotation region is shown by white arrow in the middle panels of Figure.

averaging. Until 23:22 UT on Jul 08 we see the converging flow into the small pore and filament footpoint region (Figure 3.9(top-left)). However, at 23:23 UT, the situation changed at the filament Western footpoint location and a counter clockwise rotational motion was observed. This rotational motion persisted only until 23:27 UT.

Apart from location 1, the rotational motion has also been observed in location 2 (Figure 3.10). This is the another part of bifurcated footpoint of the filament in the Western portion where the filament eruption was observed

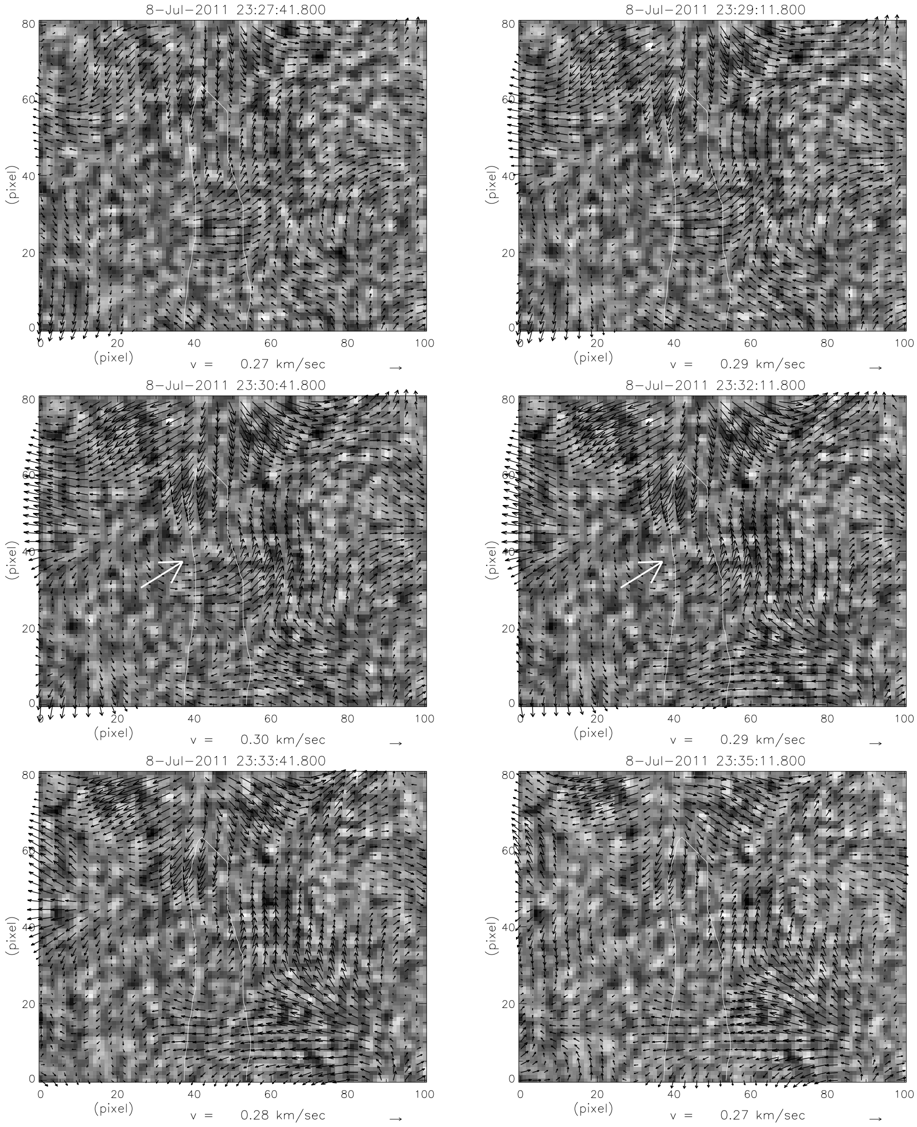

Figure 3.11: Same as Figure 3.9, but for boxed region 3 of Figure 3.8. The rotation region is shown by white arrow in the middle panels of Figure.

in coronal images. The location of the rotational motion is shown by the white arrow in the middle row of Figure 3.10. This rotational motion started at around 23:24 UT and ended at around 23:29 UT. Apart from this the rotational motion, starting from 23:27 UT to 23:31 UT, was also observed in another location in top-right corner in the middle & last row of Figure 3.10.

In Eastern footpoint of the filament (box 3 in Figure 3.8) the anti-clockwise rotational motion has been observed at around 23:34 UT (Figure 3.11). The rotational motion continued for couple of minutes before vanishing.

3.3.5 Magnetic helicity

The magnetic helicity provides information about the degree of twist in the magnetic flux ropes (Berger, 1984). It is a conserved quantity even in reconnection processes. However, it can vary because of changes occurring at the boundaries due to emergence/submergence of the magnetic fields and coronal mass ejections where the magnetic field lines opens up partially. The magnetic helicity of a divergence-free field **B** within a volume V, bounded by a surface S, is defined by (Elsasser, 1956)

$$H = \int_V \mathbf{A} \bullet \mathbf{B} dV \tag{3.1}$$

Where, the vector potential **A** satisfies the relation $\mathbf{B} = \nabla \times \mathbf{A}$. Since, the normal component B_n=$\mathbf{B} \bullet \hat{\mathbf{n}}$ vanishes on surface S, eq. 3.1 is independent of the gauge selection for **A** (i. e. independent of the transformation $\mathbf{A} \longrightarrow \mathbf{A}+ \nabla \Phi$. where, Φ is any single valued derivable scalar function of space and time). In the case, where V is part of the corona, we clearly have magnetic fluxes crossing its boundary S. Berger and Field (1984) have shown that for cases where $B_n \neq 0$ on some part of S, one can define a relative magnetic helicity, H by subtracting the helicity of the potential field B_p which has the same normal component B_n on S. A general expression for H, valid for any gauge is given by (Finn and Antonsen, 1985)

$$H = \int_V (\mathbf{A} \pm \mathbf{A_p}) \bullet (\mathbf{B} \mp \mathbf{B_p}) dV \tag{3.2}$$

The time variation of H can be expressed as Berger and Field (1984)

$$\frac{dH}{dt} = 2\int_S (\mathbf{A_p} \times \mathbf{E}) d\mathbf{S} - 2\int_V (\mathbf{E} \bullet \mathbf{B}) dV - 2\int_S \frac{\partial \psi}{\partial t} \mathbf{A_p} \bullet d\mathbf{S} \tag{3.3}$$

where, **E** is the electric field associated to **B** evolution and $B_p = \nabla\psi$ (ψ is potential field). The last term on the right is computed with the classical

Coulomb gauge $\nabla \bullet \mathbf{A_p} = 0$. If the boundary condition $\mathbf{A_p} \bullet \hat{\mathbf{n}} = 0$, the last term in eq. 3.3 vanishes. Under ideal condition, $\mathbf{E}$ = - $\mathbf{v} \times \mathbf{B}$, from the eq. 3.3, it is now possible to measure the helicity injection rate dH/dt through a surface bounding the volume as

$$\frac{dH}{dt} = 2\int_S [(\mathbf{A}_P \bullet \mathbf{B}_h) v_z] dS - 2\int_S [(\mathbf{A}_P \bullet \mathbf{v}_h) B_z] dS \tag{3.4}$$

Where, $\mathbf{A_p}$ is the vector potential of the potential magnetic field ($\mathbf{B_p}$), which is uniquely specified by the observed flux distribution on the surface (x-y plane) as

$$\nabla \times \mathbf{A_p} \bullet \hat{z} = B_z; \nabla \bullet \mathbf{A_p} = 0; \mathbf{A_p} \bullet \hat{z} = 0 \tag{3.5}$$

where, $\hat{z}$ refers to unit vector along vertical direction of Cartesian-geometry. Further details and explanation of the equ. 3.4 is given in Ravindra, Longcope, and Abbett (2008); Vemareddy *et al.* (2012). Two terms in the eq. 3.4 have a clear physical interpretations. The first term (advection term) corresponds to inflow (or outflow) of helicity through S and the second term (shear term) corresponds to helicity flux by the footpoint motions parallel to S. Several attempts have been made to estimate magnetic helicity from suitable solar observations. Chae (2001) developed a method for determining the helicity flux using the second term in equ. 3.4. It should be noted here that the current-free field $\mathbf{B}$ is fully specified by the distribution of vertical component of magnetic field B_z on the surface S. They used a time series of photospheric line-of-sight magnetograms to determine horizontal velocities by using local correlation tracking (LCT; November and Simon 1988) and obtained the vertical component of magnetic field B_z from line-of-sight magnetograms observations after correcting for geometrical effects.

Following Démoulin and Berger (2003), the eq. 3.4 can be recast in the form,

$$\frac{dH}{dt} = -2\int_S [\mathbf{U}_{lct} \bullet \mathbf{A}_P] B_z dS \tag{3.6}$$

Where, $\mathbf{U}_{lct} = \mathbf{v_h} - (v_z * \mathbf{B}_h)/B_z$ and $\mathbf{B} = \mathbf{B_h} + B_z\ \hat{z}$ is the local magnetic field vector.

Pariat, Démoulin, and Berger (2005) have shown that the helicity flux density measured using eq. 3.6 may produce some artifacts (artificial polarities of both signs in the helicity flux density maps with many flow patterns), though the net helicity flux may be correct. To overcome this problem, a modified expression for the helicity flux density whose integration provides the helicity flux as in eq. 3.6, should be used. The correct equation for the helicity flux density, therefore is,

$$\frac{dH}{dt} = -\frac{1}{2\pi}\int_S\int_{S'} \frac{d\theta(\mathbf{x}-\mathbf{x}')}{dt} B_z B_z^{'} dS dS^{'} \tag{3.7}$$

Where,

$$\frac{d\theta(\mathbf{x}-\mathbf{x}')}{dt} = \frac{[(\mathbf{x}-\mathbf{x}') \times (\mathbf{u}-\mathbf{u}')]_n}{\mid \mathbf{x}-\mathbf{x}' \mid^2} \tag{3.8}$$

where, $\frac{d\theta}{dt}$ represents relative rotation rate between the two photospheric points $\mathbf{x}$ and $\mathbf{x}^{'}$ moving on the photosphere with the flux transport velocity $\mathbf{u}$ and $\mathbf{u}^{'}$, respectively. $B_z, B_z^{'}$ are the magnetic field at two different locations. Observationally, one can measure B_z from a time series of magnetograms at the photosphere. There are several tracking methods (e. g., LCT, DAVE etc.) to estimate $\mathbf{u}$.

From eq. 3.7 the helicity flux density proxy G_θ that represents the distribution of helicity density at the photosphere is given by (Pariat, Démoulin, and Berger, 2005)

$$G_\theta(\mathbf{x}) = -\frac{B_z}{2\pi}\int_{S'} \frac{d\theta(\mathbf{x}-\mathbf{x}')}{dt} B_z{}' dS' \tag{3.9}$$

Magnetic helicity is a global quantity. The helicity flux density is only meaningful when considering a whole magnetic flux tube, which requires the

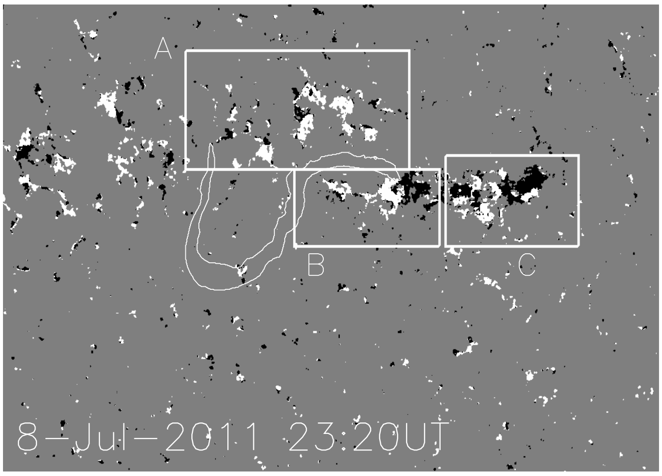

Figure 3.12: A map of helicity flux density for the active region. The boxed region is same as in Figure 3.5.

knowledge of the magnetic connectivity in the volume V (Dalmasse *et al.*, 2014; Pariat, Démoulin, and Berger, 2005). Therefore, the above eq. 3.7 for helicity flux distribution serves as a proxy only.

We have measured the helicity injection rate dH/dt at the filament footpoint using the eq. 3.7 and eq. 3.9. To compute the helicity flux density we measured the magnetic footpoint velocity using the Differential Affine Velocity Estimator (DAVE, see Section 2.4.8 for more details.) method applied to a sequence of magnetograms. In any velocity detection technique it is essential to select the proper window size and suitable time difference between the two images. While applying DAVE to the sequence of magnetograms, we have used a $9'' \times 7.2''$ pixel box size as the apodizing window and 15 min as the time difference between images in our velocity field computation which gives the best results. The computed transverse velocities along with the corresponding sequence of magnetograms have been used to calculate the helicity flux density. We used DAVE technique because this technique is consistent with the magnetic induction equation (Schuck, 2005, 2006, 2008), which governs the temporal evolution of the photospheric magnetic fields. However, we also carried out this exercise by applying LCT to derive the flow fields in magne-

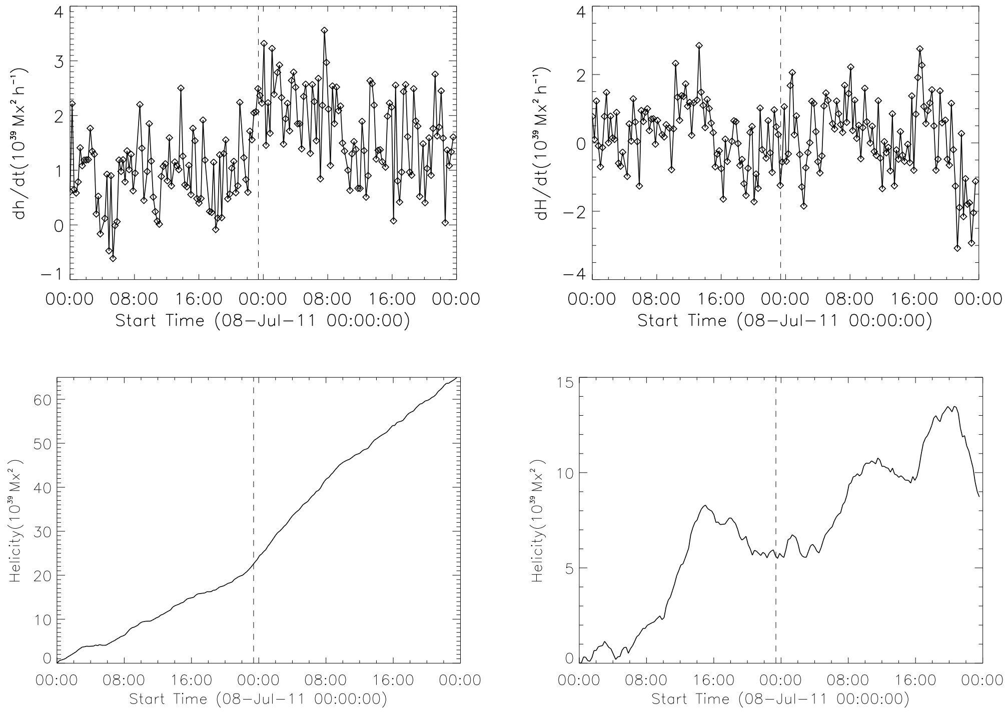

Figure 3.13: Top left: Evolution of helicity flux as a function of time shown for the boxed region A of Figure 3.12. Top right: Same as left side plot but for region B of Figure 3.12. Bottom left: The integrated helicity flux is plotted as a function of time for region A. Bottom right: Same as left side plot but for region B. The dashed vertical line represents onset time of filament eruption.

tograms. In both the cases (LCT and DAVE) we observed the similar pattern of flow fields. Since, the DAVE showed a better flow field pattern for magnetograms for a long time period (about 15 minutes), we preferred to use DAVE derived velocity to measure the helicity injection rate. The map of helicity flux density is shown in Figure 3.12. In the region A the positive helicity dominates. However, in region B, both signs of helicity flux are present.

To find how the helicity flux changed over time in each of these footpoints, we have plotted the computed helicity flux separately for both the footpoints (A & B) marked in boxes. Figure 3.13 shows the magnetic helicity flux for the box region A (top-left) and for the box region B (top-right). The injected helicity flux is almost positive in sign in box region A and it increased to double the amount just after the filament eruption and remain unchanged even 8 h after the filament eruption. But, in box region B the observed injected helicity flux is predominantly positive during the first half on 08 July 2011 and turned negative after 16:00 UT on the same day. Though some fluctuations in its sign can still be seen. This is also the time the negative flux starts to emerge in the same region. The emerged flux would have injected opposite helicity flux into the corona. The chirality of the filament located in this region is sinistral having the positive helicity sign. It should be noted here that the injected helicity flux for about 10 h duration before the filament eruption is opposite to the filament chirality. The co-existence of both sign of helicity flux in the helicity flux density map support this result (Figure 3.12). After the filament eruption the dominance of the positive helicity flux is restored in box region B.

The total accumulated helicity is positive in box region A and it was increasing with time (Figure 3.13 (bottom-left)). In box region B, though there was a net positive helicity injection, the decrease in the helicity started about 10 h before the filament eruption and increased afterward. This decrease in the net helicity is due to the injection of negative helicity flux from the emerging flux region. This can be clearly seen in the magnetic flux evolution plot in region B for the temporal coincidence. In either cases there is a net positive helicity injection in both footpoints of the filament.

3.4 Summary and Discussions

As a summary, we studied a filament eruption that was formed in the vicinity of active region NOAA 11247. While a large portion of filament was embedded in the quiet sun, the end footpoints were rooted in the plage regions. The filament was located in the southern hemisphere with ‘S-shaped’ structure. The filament is of sinistral type and has positive helicity. The filament eruption was initiated in the Western footpoint at around 23:20 UT, with a projection speed of 56 km s^{-1} at the higher chromosphere and transition region heights.

The Western end of the filament was rooted in negative polarity plage and the Eastern end was located in the positive polarity plage region. There was a flux emergence in the nearby active region. The increase in flux of the Western footpoint stopped a couple of hours before the filament eruption. During the flux emergence, the negative flux pushed the pre-existing positive flux of the active region further West. Soon after the filament activation initiated there was an anti-clockwise rotational motion for about 6 min in the Western footpoint of the filament. On the other hand the flux started to increase in the Eastern footpoint of the filament a few hours before the filament eruption was initiated. After the B4.7 class flare the increase in the flux stopped. Here also an anti-clockwise rotational motion was observed at around 23:33 UT -just after the filament activation started in the Eastern footpoint of the filament. In Eastern and Western regions of filament footpoint the computed magnetic helicity had positive sign. There was a rise in the injected helicity flux a few minutes after the filament eruption in the Eastern footpoint of the filament. But, in the Western footpoint both signs of helicity were present, though it was completely positive at 10 h before the filament activation. After the filament eruption, the dominance of positive magnetic helicity was restored.

The new magnetic flux emergence with opposite magnetic sign can destabilize the filament by decreasing the magnetic tension of the overlying field (Wang and Sheeley, 1999). Along with the flux emergence the long duration converging motions observed in the vicinity of the filament footpoints can reduce magnetic tension of the overlying field which can destabilize the filament (Amari *et al.*, 2003, 2010, 2011; Zuccarello, Meliani, and Poedts, 2012). The long lasting converging motion can also increase the axial flux of the filament by transferring the overlying field into the underlying field of the filament that eventually increase the outward magnetic pressure on the filament. The increase in the magnetic pressure can push the filament to a height where the torus instability can set in and drive the filament eruption as has been discussed in Zuccarello *et al.* (2012) and Aulanier *et al.* (2010); Démoulin and

Aulanier (2010).

On the other hand, the existence of the opposite magnetic helicity in one of the footpoints of the filament can introduce a mutual interaction of magnetic field having opposite magnetic helicity flux. In the Western footpoint of the filament there was a dominant positive helicity flux injection in the beginning. Later, there was a injection of opposite helicity flux into the existing positive helicity flux system. Finding of injection of opposite sign helicity in a local region is potentially important for eruption models (Chandra *et al.*, 2010). Kusano *et al.* (2003, 2004) concluded through numerical simulations that the coexistence of opposite helicity flux would cause a reconnection while merging of different helicity flux system takes place. The reconnection in the system can reduce the tension of the overlying field and thereby pushing the filament to higher heights in the corona and thus driving the filament eruption as discussed previously. Since we observed flux emergence, converging motion and the opposite magnetic helicity flux in the filament footpoint, we believe one or more mechanisms may be playing a major role in initiating the filament eruption. Several of these possible mechanisms are discussed in Green, Kliem, and Wallace (2011); Romano *et al.* (2011) and Schmieder *et al.* (2011).

The more interesting event is the observed rotational motion in the footpoints of the filament when the eruption had just set in. A possible explanation of the observed rotational motion is advanced as follows. Once the filament eruption starts, there is an axial expansion of the filament flux rope. If the footpoint of the flux rope is still anchored to the photosphere, the expansion of the filament flux rope usually leads to the torque imbalance between the photospheric footpoints and the coronal counter part of the expanded flux rope. The immediate consequence of the torque imbalance is the generation of the shear flows at the photospheric footpoints (Jockers, 1978; Parker, 1974). At the footpoint it is expected that unwinding motion reduced the shear at the unexpanded portion and transferred a helicity into the expanded portion. This would increase the helicity flux of the same sign in the expanded portion. The filament with sinistral chirality has positive helicity flux in the system. As the filament expands during the eruption, a change in the helicity flux from negative to positive soon after the filament eruption in the Western footpoint suggests that there was a transfer of positive helicity into the corona from the unexpanded part of the flux tube to the expanded part. Later, the Eastern footpoint also showed the rotational motion and there was a jump in the positive helicity after the initiation of the filament eruption. This can be attributed to the expansion of the filament flux rope and subsequent torque imbalance as has been suggested by Chae *et al.* (2003); Parker (1974) and observed by Smyrli *et al.* (2010); Zuccarello *et al.* (2011). This explains the observations of transient rotational motion in the photospheric footpoints and increased positive magnetic helicity flux after the filament eruption. The rotational motion was no longer observed once the footpoints were detached from the photosphere.

The filament eruption initiated just after the flux emergence stopped in one of the footpoints. This kind of flux emergence followed by converging/shearing motions will stress the overlaying fields and hence builds up energy in the corona (Feynman and Martin, 1995). In such condition, a small perturbation can trigger the filament eruption. In dynamic plasma, the presence of small triggering agents is not uncommon. Hence, it can be concluded that in each event the onset of instability could be different. What is required is to probe the magnetic shear and stress in and around the filament region at least at two heights using vector magnetic field measurements.

Now the question is whether the observed rotational motion near the footpoints of the filament is just a coincidence of a normal feature of the photosphere which occurs randomly or is it really related to the filament eruption? To understand this observation, we need statistically significant samples. Hence, it is important to look for the rotational/vortial motion at the footpoints of the filaments and associated changes in the magnetic helicity after the onset of filament eruption statistically. This can provide an important clue to the generation of torque imbalance during/after the filament eruption and help validate Jockers (1978); Parker (1974) results statistically. Therefore, we extended this study to several other erupting active region filaments in the next chapter and searched for such rotational motions in and around the end points of these erupting filaments using large data sets of *AIA*, *HMI*/SDO.

Chapter 4

Study of photospheric vortical motions during active region filament eruption

4.1 Introduction

Filaments/prominences exhibit a variety of dynamics during their formation, evolution and prior to eruption. Bidirectional flows of plasma were observed within quiet region filament (Zirker, Engvold, and Martin, 1998) and in active region filament (Alexander *et al.*, 2013). Oscillations were observed in erupting filaments (Bocchialini *et al.*, 2012). Rotational motion was observed in the erupting filaments/prominences (Panesar *et al.*, 2013).

Normally, the filament is considered as lower part of the flux rope, where the dense matter is suspending in the magnetic cavity. In the CME structure, the dark cavity, below the bright leading edge is considered as the twisted flux rope (Gibson *et al.*, 2006) and the filament is located below the dark cavity. In quiet sun regions, the large quiescent filament cavities are considered as flux-ropes. But, identification of cavities are difficult in active regions. The cavity or flux ropes are low lying, compact structures in active regions. Hence, it is not possible to identify the flux ropes in active regions prior to eruption. On many occasions the ends of filaments are considered as the ends of the lower part of flux rope that roots in the photosphere (van Ballegooijen 2004; Kliem *et al.* 2013).

During rising phase of eruptions, filaments are sometimes observed to undergo a rotation about the vertical axis (*e.g.,* Zhou *et al.* 2006; Green *et al.* 2007; Liu *et al.* 2009; Thompson 2011). This kind of filament rotation is interpreted as a conversion of twist into writhe in a kink-unstable flux rope. The flux rope axis rotation is usually clockwise (as viewed from above) if it has right-handed twist and counter-clockwise if it has left-handed twist (*e.g.,* Rust and LaBonte 2005; Green *et al.* 2007; Wang, Muglach, and Kliem 2009). Erupting prominences which are considered as magnetic flux ropes, very often develop into a helical-like structure (*e.g.,* Rust 2003; Rust and LaBonte 2005; Williams *et al.* 2005; Liu, Alexander, and Gilbert 2007), which indicates the signature of a magnetohydrodynamics (MHD) kink instability of a twisted magnetic flux rope (Rust and LaBonte, 2005). In the twisted flux rope, the upward directed kink instability leads to the upward motion of the flux rope that eventually turn into helical deformation and formation of current sheets. The helical kink instability of a pre-existing flux rope can trigger the solar eruptions (Török and Kliem, 2005). In the MHD instability, half the magnitude of the twist will be converted into writhe having the same sign as twist. The 'S' shaped stable filament reverses its shape to inverse 'S' while it is rising. During the rising phase, the shape of the erupting filament straightens out and later acquires the deformation of the axis in opposite direction suggesting the transition from 'S' to inverse 'S'. The possibility of this mechanism is confirmed in the numerical simulation of kink unstable flux rope by Török, Berger, and Kliem (2010). During the observation of such events the deformation of the shape can be seen as rotation of the axis.

The filament/flux rope can face an another type of instability due to lateral kink-instability, also called as "torus instability"(Kliem and Török 2006; Zuccarello *et al.* 2014). The toroidal current carrying flux rope experience an outward directed self Lorentz force (also called as hoop force) which counteracts with the external poloidal fields of the background magnetic fields (Chen 1989; Titov and Démoulin 1999). But, if the external poloidal field decreases faster with the radial distance in such a way that the confining force due to the external poloidal field decreases rapidly than the self Lorentz force then the flux rope can become unstable to the lateral expansion. A loss of equilibrium of the flux rope due to this effect can lead to its eruption.

Liggett and Zirin (1984) studied rotational motion in 5 non-eruptive prominences. In some events they reported only a part of the prominence rotating while in other the entire body was in rotation. They interpreted the rotation in terms of a twisting of magnetic structure that occurred due to the reconnection. Atmospheric Imaging Assembly (AIA; Lemen *et al.* 2012) observations show that the feet of solar prominences exhibit coherent rotation for over three hours in the lower corona and it was due to the material flowing along helical flux tubes (Li *et al.*, 2012).

Su *et al.* (2012) reported two solar tornadoes during the evolutionary stage of the quiet prominence. This tornado was observed for about 2 days. A systematic analysis of giant tornadoes by Wedemeyer *et al.* (2013) using AIA 171 Å images and high-resolution SST observations show that giant tornadoes are an integral part of solar prominences. The tornadoes inject mass and twist into the filament spine until it becomes unstable and erupts. Su and van Ballegooijen (2013) also reported a quiescent filament eruption in which a part of the quiescent filament exhibits a strong clockwise rolling motion.

When a filament erupts non-radially, the top of its axis bends first to one side and propagates into sideways rolling motion, known as the *roll effect* which results in a large scale twists in both legs of erupting filaments (*e.g.*, Bangert, Martin, and Berger 2003; Filippov, Gopalswamy, and Lozhechkin

2001; Panasenco *et al.* 2011; Panasenco *et al.* 2013). This rotational mass motion is observed to flow down as the structure of the filament raises to higher heights. If the observed sense of rotations were generated by the external forces at the legs of the erupting filament then sense of twist in both the legs is opposite to each other (Panasenco *et al.*, 2013). In case of asymmetric eruption with respect to the polarity inversion line, the spine of the filament bends one side which not necessarily results rotation in both legs of filament depending upon the instability (*e.g.,* Martin 2003b; Panasenco and Martin 2008).

In aforementioned cases, it is either the whole prominence is rotating around its vertical axis or individual footpoints are rotating around itself. Only in some cases a part of the prominence was rotating. Dhara, Ravindra, and Banyal (2014a) have reported a rotational motion at the ends of the filament at the photospheric level during its eruption. In that observation they have reported the rotational motion started soon after the filament eruption initiated and lasted for a few minutes.

In this chapter, we extended the work of Dhara, Ravindra, and Banyal (2014a) to twelve active region erupting filaments and searched for such rotational motions in and around the ends of each erupting filaments. The rotational motions were studied by applying local correlation tracking technique (LCT; November and Simon 1988) to the photospheric dopplergram data. We looked for the rotational motion near the ends of filaments/flux ropes during the on-set of the filament eruption. This chapter is organized as follows. In next Section, we describe the data used to detect the rotational motion near the ends of filaments during its eruption, the results of observations of rotational motion are described in Section 4.3, a brief summary and discussions are presented in Section 4.4.

4.2 Data

We obtained the chromospheric data observed in He II 304 Å wavelength from AIA/SDO for ten active regions (NOAA 11226, 11283, 11515, 11560, 11451, 11936, 12027, 12035, 12261 and 12297) associated with twelve events. The full-disk EUV images of the Sun observed in 304 Å wavelength are obtained on 07 June 2011, 07 September 2011, 02 July 2012, 02 September 2012, 07 April 2012, 31 December 2013, 01 January 2014, 04 April 2014, 15 April 2014, 12 January 2015 and 16 March 2015 that covers the twelve events of filament eruption. The obtained data is corrected for the flat fielding, the bad pixels and the spikes due to high energy particles. The details about the instruments and data are given in Section 2.2.1.1. From these data sets the filament regions are extracted and tracked over time. This process provided data cubes showing the filament eruption for each of the events.

We also acquired the dopplergram data set from HMI at a cadence of 45 sec. We obtained the dopplergram data for each event for about six hours covering the whole event of filament eruption. The obtained dopplergrams show several velocity patterns and while looking for the small scale feature motions one has to remove the long term and very short term velocity patterns in sequence. To start with, we first removed the overall solar rotation from the dopplergram data. This has been done by using the following method. We first averaged the dopplergram data set without correcting for solar rotation. The gradient part of the rotational velocity pattern was extracted and subtracted from each of the dopplergram data. This procedure removed the overall solar rotational velocity patterns in the full-disk dopplergrams. Later, we interpolated these dopplergram data set to the AIA pixel resolution to match the spatial size of each pixel in the data set. Further, the dopplergrams were differentially rotated to the central meridian passing time of the active region. The usual 5-minute oscillations in the dopplergrams were suppressed by applying a subsonic filter with a upper cutoff velocity magnitude of

4 km s^{-1}. This corrected data set is used to determine the horizontal velocity of features near the footpoints of the filament and its surrounding regions at the photospheric level. This has been done by applying the LCT technique to the processed dopplergram data set as has been done in Ravindra (2006) and De Rosa and Toomre (2004).

Along with the aforesaid data sets, we also obtained the line-of-sight magnetograms from HMI for each events at a cadence of 45 sec for about a few hours before, during and after the eruption. We corrected the data set for the solar rotation in similar way as has been done for the dopplergrams. The correction for the line-of-sight effect is made by multiplying 1/cosθ, where θ is the heliocentric angle. The details about the data analysis is given in Section 2.2.1.1. We used these magnetograms to locate the filament position in the active region (AR).

4.3 Observations and Results

4.3.1 Events description

4.3.1.1 Events 1-4

The general appearance and location of filaments are depicted in Figure 4.1 for four different events observed in He II 304 Å channel. Each of these filaments are associated with the ARs. In Figure 4.1 their location is shown by an arrow mark. The contours of the magnetic field is overlaid upon the 304 Å images to show that the filaments are associated with active regions. The location of these filaments on the Sun is listed in Table 4.1. We used the events whose apparent central meridian longitude is less than 65° to avoid large projection effects on the observations. The filament in EUV wavelengths appeared as dark features. The shape of the filament in top-right Figure appear as ‘S’ in 304 Å wavelength before the activation and the other two filaments (in the bottom panels) appeared as small arcade shaped structures. While erupting,

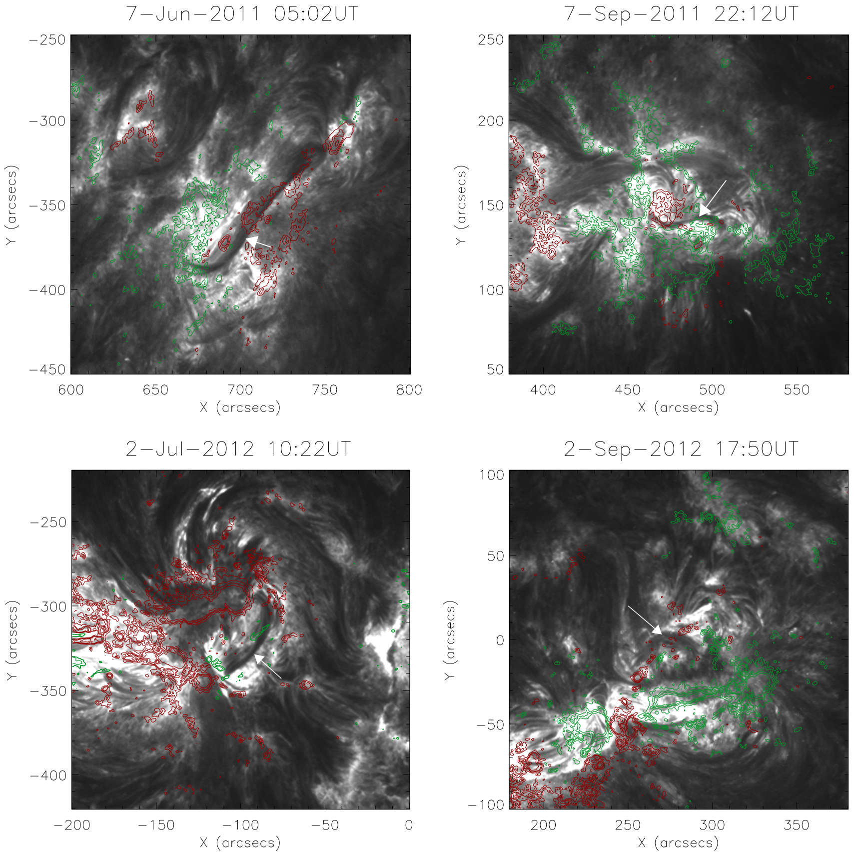

Figure 4.1: Filaments observed in the 304 Å channel of the chromosphere image in different active regions. The filament positions are shown by white arrows. The contours of the magnetic strength values are overlaid on the images. The red and green contours represent the positive and negative polarities with magnetic field strength values of ± 150, 400, 600 and 900 G, respectively.

filaments became dark over large areas and large amount of material was ejected out.

A time sequence of images showed that for events 1 and 2, both the Eastern and Western footpoints of the filament were detached near simultaneously from the solar surface after activation, reached some height and eventually fell back to the solar surface. The movies for these erupting events are available on IIA's ftp site[1]. In events 3 and 4, the eruptions took place in different manner. The Eastern footpoint of both filaments were detached first from the solar surface in association with brightening at the same location and later a bulk of filament material was seen escaping from the solar surface. As soon as the Eastern footpoint of the filament detached, the filament expanded in its structure and started to rotate. The rotational motion was observed starting from ∼10:50 UT to ∼11:45 UT for the event 3 and it was counter clockwise in direction as seen from above. A similar kind of rotational motion was observed for the event 4 which lasted for about 9 minutes starting from ∼18:11 UT to ∼18:20 UT. The direction of rotation was observed to be clockwise. These movies are available on IIA's ftp site[1]. The zoomed in versions of the erupting filaments are also shown in the same movies. This kind of rotation of the filament was not observed for events 1 and 2.

Table 4.1: Event number in accordance with the increasing date of observations is shown in the first column of the Table. The date, time, filament location on the sun and associated active region number are given in the next three columns. Filament activation time, strength of the flare and velocities of erupting filaments are listed in the next four columns.

Event No.	Date	Filament Location	AR NOAA	Activation Time	GOES Flares	Velocity (km/s)
1	07 June 2011	∼S22W64	11226	∼05:56UT	M2.5	181.7±7.1
2	07 September 2011	∼N14W30	11283	∼22:08UT	X1.8	193.9±1.9
3	02 July 2012	∼S17E03	11515	∼10:31UT	M5.6	90.9±0.8
4	02 September 2012	∼N03W18	11560	∼17:52UT	C5.5	42.9±0.4
5	07 April 2012	∼N18W30	11451	∼17:45UT	C2.4	39.4±1.6
6	31 December 2013	∼S16W32	11936	∼21:26UT	M6.4	149.0±2.7
7	01 January 2014	∼S16W46	11936	∼16:18UT	–	11.4±0.3
8	01 January 2014	∼S16W48	11936	∼18:21UT	M9.9	73.4±2.9
9	04 April 2014	∼N13E15	12027	∼13:28UT	C8.3	109.5±3.0
10	15 April 2014	∼S18E23	12035	∼17:33UT	C7.3	44.6±1.4
11	12 January 2015	∼S11E32	12261	∼14:55UT	–	49.8±5.9
12	16 March 2015	∼S18W51	12297	∼09:17UT	M1.6	27.9±1.1

By examining the time series of 304 Å images for each events we determined the filament activation time (see Table 4.1). The projected velocities of the erupting filaments also shown in Table 4.1, are computed by tracking the features on the erupting filaments within the field-of-view during their eruptions.

---

[1] Movies generated from 304 Å images of the filament eruptions associated with active region NOAA 11226, 11283, 11515 and 11560 discussed in this chapter are available on our ftp site (ftp://ftp.iiap.res.in/sajal/). The movies are named according to the date of observations of the events.

4.3.1.2 Events 5-12

The filament locations in He II 304 Å channel for the events 5-12 are displayed in Figures 4.7 to 4.14 (top-left) respectively. The date and time of the observations, filament location on the sun, associated active region number, filament activation time, strength of the flare and velocities of erupting filaments are mentioned in Table 4.1. The filament in event 5 (Figure 4.7) is long one, associated with 2 active regions. Its one end is located in AR 11451 and the other end is at 11450. Before the filament eruption, a bi-directional flow was observed in the filament. There were three filament eruptions observed in AR 11936. The event 6 (Figure 4.8) was observed on 31 December 2013. Two more events were observed on 01 January 2014. On 31 December 2013 only one filament was existing in the active region and before the eruption this filament bifurcated into two halves. The right-side half erupted and the left-side one did not erupt. Later, again the filament was formed in the same region and the bifurcation disappeared. The event 7 (Figure 4.9) also occurred in the same active region, but the filament was located at North side of the December 31 event. This filament eruption appeared as failed one. Event 8 (Figure 4.10) also occurred on the same day, couple of hours after the event 7. This filament is the same as the one which erupted on 31 December 2013. Unlike December 31st event, here the whole filament erupted without any bifurcation. But it was a failed eruption. The active region 12027 was surrounded by the filament structure in all the directions. It was not a single filament, in fact it was web of 3-4 circular filaments. On 04 April 2014 the North-East portion of the filament erupted (event 9 (Figure 4.11)). Before the eruption a large scale mass flow was observed inside the filament. The event 10 (Figure 4.12) occurred in AR NOAA 12035. The filament was hard to see before the eruption in the active region. But, during the filament activation a cusp shaped filament was observed in the active region. This filament erupted completely during the C7.3 class flare. The event 11 (Figure 4.13) was associated with the AR NOAA 12261. The filament was arcade shaped. While eruption, a brightening was observed at the eastern footpoint of the filament. The eruption was appeared as a failed eruption and it was not associated with any flare. The event 12 (Figure 4.14) occurred in AR NOAA 12297. The filament was S-shaped. While eruption, a brightening was observed beneath the spine of the filament and both the footpoints of the filament detached from the solar surface near simultaneously. This filament eruption was associated with M1.9 GOES flare and appeared as a successful eruption. The movies for the filament eruptions (events 5–12) are available on IIA's ftp site[2].

4.3.2 Flows in and around the filament footpoints

In order to identify the flow in and around sunspot regions and filaments, we applied the Fourier local correlation tracking (FLCT; Welsch *et al.* 2004) technique on dopplergrams. The two parameters such as the time difference between the two images and the size of the Gaussian apodizing window functions are crucial in finding the velocity vectors. We used the dopplergram images which are 3 minutes apart and the apodizing window width of $9''$ as a window function. The obtained velocity vectors are averaged over $\sim$1.5 hours to examine the long term flows in and around the active regions. Figure 4.2 shows the long lived flows in and around active regions for the first four events listed in Table 4.1. The contours of the filament is overlaid upon the velocity map to identify the location of the filament and its end points. These filament contours are extracted from the 304 Å images for each event. The boxed regions 1 and 2 show the Eastern and Western footpoints of the filament regions respectively. In sunspot regions a large scale outward flows are observed. In filament end points (boxed regions 1 and 2) either a converging motion or a

---

[2] Movies generated from 304 Å images of the filament eruptions associated with active region NOAA 11451, 11936, 12027, 12035, 12261 and 1229 discussed in this chapter are available on IIA's ftp site (ftp://ftp.iiap.res.in/sajal/). The movies are named according to the date of observations of the events.

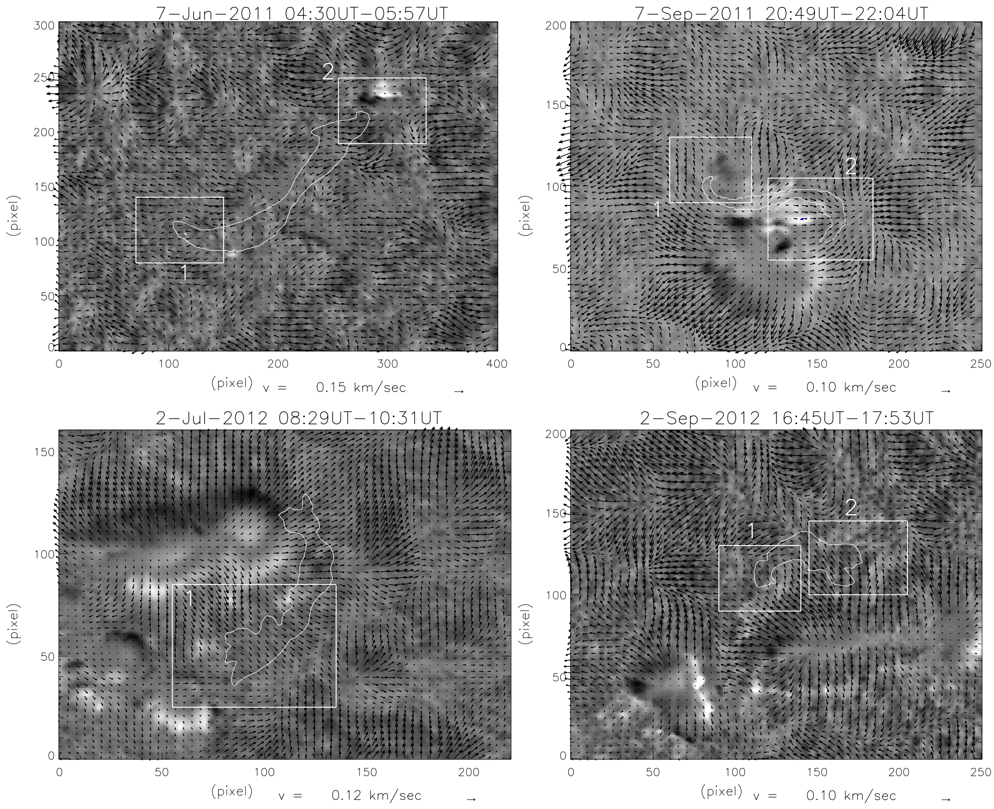

Figure 4.2: The horizontal velocity vectors shown in arrows are overlaid upon the averaged dopplergram for 1st to 4th events. The black, white and gray regions in the averaged dopplergram represent, respectively, the line-of-sight doppler velocities with upflow, downflow and close to zero velocity. The white contours of the filaments, extracted from the 304 Å images are overlaid upon the averaged dopplergram. The boxed regions 1 and 2 show the location of the Eastern and Western footpoints of the filament respectively.

large scale outflow was observed.

In the boxed regions, during the early stage of the filament eruption the situation was different. The flow fields in the boxed regions of Figure 4.2 showed a rotational motions for a few minutes. These velocity flow fields were obtained from time sequence of images without averaging the velocity maps. Figure 4.3 shows the temporal sequence of flow field in the footpoints of the filaments which erupted on 07 June 2011. We observed counter-clockwise rotation in the Eastern footpoint and clock-wise rotation in the Western footpoints. The rotational pattern persisted for 7 and 15 minutes in the Eastern and Western footpoints respectively.

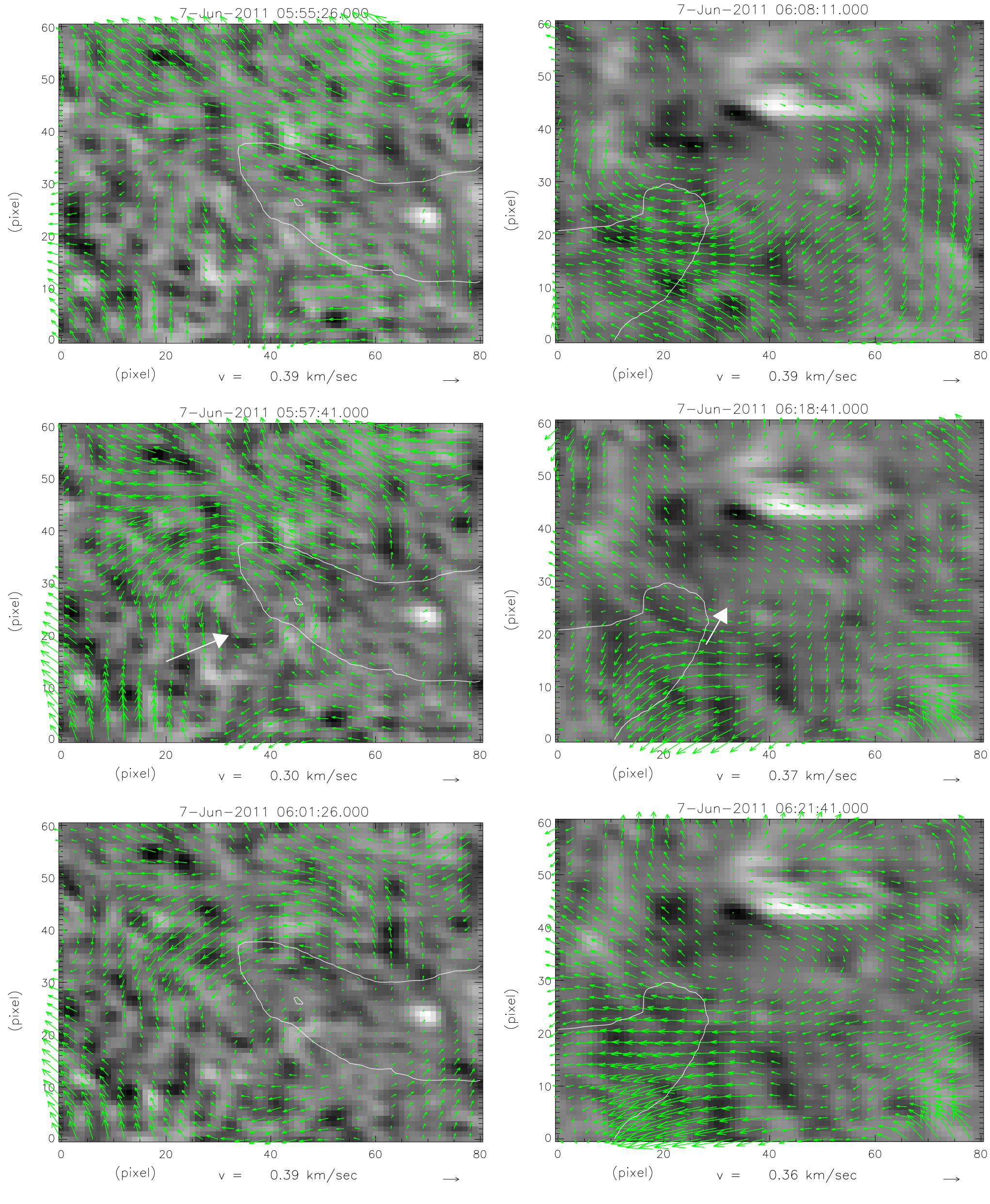

Figure 4.3: The temporal evolution of rotational velocity pattern observed for event 1. Left column corresponds to location 1 and right column for location 2 of Figure 4.2 (top-left). The filament contour extracted from the 304 Å image is overlaid upon dopplergram. The rotation region is shown by white arrow. The date and time of the computed velocity is shown on the top of each map. The size of arrow in the bottom of each map represents the magnitude of velocity.

The 07 September 2011 event showed clockwise rotation in the Eastern footpoint and anti-clockwise rotation in the Western footpoint. But, only in the Eastern footpoint of the erupting filament an anti-clockwise rotational motion was observed on 02 July 2012 event. The Western footpoint did not show any rotational motion during the filament eruption in this event. This footpoint was located close to the penumbral portion of the sunspot region. Similarly, the 02 September 2012 event showed a clockwise rotation in the Eastern footpoint and anti-clockwise rotation in the Western footpoint of the filament. In all the events the filament footpoint was located in the periphery of the rotating center. The rotation lasted for 4-29 minutes in each of these events.

The observed rotational motion is not simultaneous in both ends of the filament. There is about one to ten minute time difference between the ending of the rotational motion in one of the footpoint and starting in another footpoint of the filament. Table 4.2 provides the starting and ending time of the rotational motion seen in the ends of the filaments for all the events. The starting and ending time of the rotational motions in any one footpoint is differed by about 4-29 minutes. In each of these events, the fast rise of the filament was observed either during or after the rotational motion observed. Table 4.2 provides the direction of rotation in each of the footpoint. It should be noted here the direction of rotation is opposite in each filament ends. In two events (3 and 10), one end of the filament located in sunspot penumbral region where we did not find the rotational motion. We did not see any correlation between the speed of the filament eruption and duration of rotation. The average speed of the filament at the footpoint is about 0.2 km s^{-1}. This corresponds to the average rotational speed of about 6 deg/hr.

We have also observed rotational motions in other locations in the active region during the onset of the filament eruption. But the sizes of the rotating region is significantly smaller compared to the reported one and they survived for 2-3 minutes only. One such rotational motion can be seen in Figure 4.3

(top-right) at (70″, 50″) pixel location. The rotational region is small, 10″ in size. But, the one seen close to the filament ends are of supergranular size. The filaments are considered as the lower ends of the flux ropes which are embedded in the cavities of helical fields (Mackay *et al.* 2010; Guo *et al.* 2010). The 193 movies of four regions (events no. 1–4) provided on the ftp site[1] show that the erupting filament and the evolving bright flux rope. The details about the flux rope evolution can be obtained at Cheng *et al.* (2014).

Table 4.2: The filament activation time (AT), fast rise time (FRT) of the filament, duration and type of rotational motions observed for each events are listed here. In the fifth and seventh column of the table, the abbreviation AC corresponds to Anti-clockwise and C corresponds to clockwise direction of rotational motions.

Event No.	AT (UT)	FRT (UT)	Rotational Motion Observed in			
			Eastern footpoint		Western footpoint	
			Duration (UT)	Type	Duration (UT)	Type
1	∼05:56	∼06:14	05:55:26–06:02:11	AC	06:08:56–06:23:11	C
2	∼22:08	∼22:30	22:13:22–22:17:07	C	22:17:52–22:24:37	AC
3	∼10:31	∼10:43	10:34:25–10:46:25	AC	–	–
4	∼17:52	∼18:03	18:08:51–18:14:51	C	17:56:51–18:04:21	AC
5	∼17:45	∼17:58	17:45:34–17:52:19	AC	17:45:34–17:56:04	C
6	∼21:26	∼21:46	21:37:54–21:43:54	AC	21:16:54–21:36:24	C
7	∼16:18	∼16:23	16:09:24–16:18:24	AC	16:19:09–16:23:39	C
8	∼18:21	∼18:40	18:14:39–18:23:39	AC	18:10:09–18:25:09	C
9	∼13:28	∼13:33	13:28:17–13:39:32	C	13:46:17–13:58:17	AC
10	∼17:33	∼17:51	17:31:19–17:44:49	AC	–	–
11	∼14:55	∼15:10	14:51:24–15:03:24	C	15:10:09–15:23:39	AC
12	∼09:17	∼09:56	09:16:15–09:25:15	C	09:40:59–10:09:29	AC

The filament locations in He II 304 Å channel for the events 5-12 are displayed in Figures 4.7 to 4.12 (top-left) respectively. The positions of the filament on the dopplergram are shown by overlying their contours of the filament extracted from 304 Å images. These are shown in Figures 4.7 to 4.12 (top-right) respectively. The observed rotational motions at the ends of the filament footpoints for all the events are also shown in bottom-left and bottom-right rows in Figures 4.7 to 4.12. The starting and ending time of

---

[1] Movies generated from 193 Å images of the filament eruptions associated with active region NOAA 11226, 11283, 11515 and 11560 discussed in this chapter are available on our web site (ftp://ftp.iiap.res.in/sajal/). The movies are named according to the date of observations of the events.

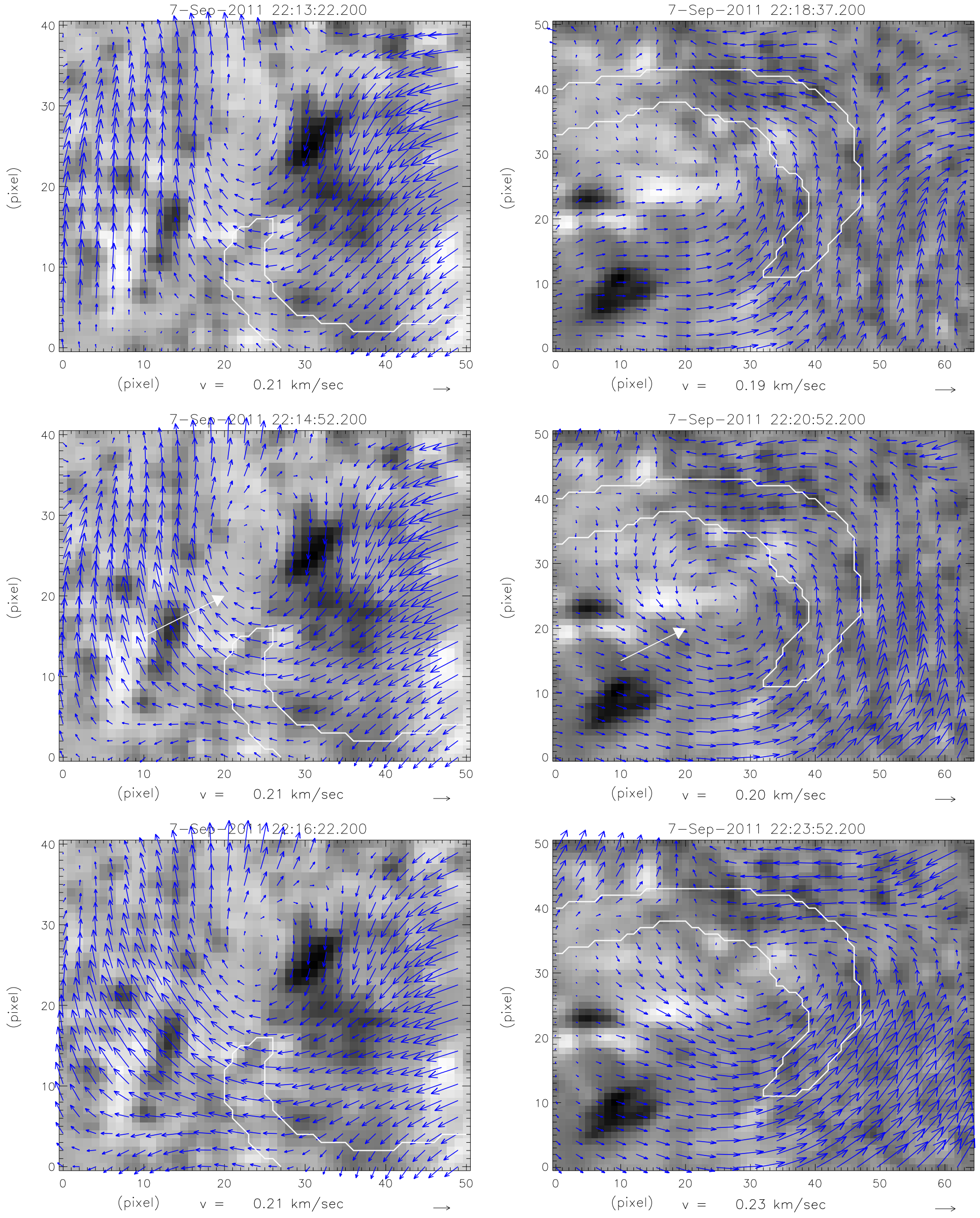

Figure 4.4: Same as Figure 4.3, but for event 2.

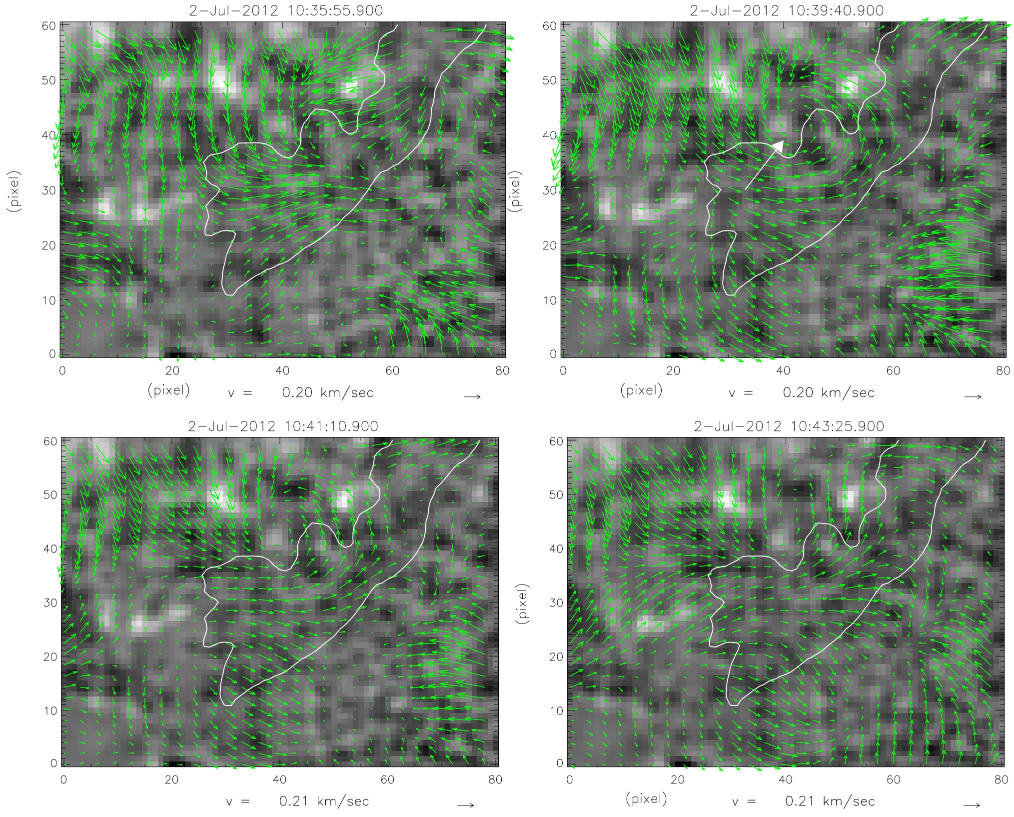

Figure 4.5: Same as Figure 4.3, but for the region 1 of the event 3.

the rotational motion seen on the ends of the filaments for all events are also shown in Table 4.2.

4.4 Summary and Discussion

We have analyzed twelve filament eruptions from ten different active regions at different times during Solar Cycle 24. Ten out of the twelve filament eruption events were followed by a flare. In one event, the filament destabilized a couple of hours before the large flare (event no. 7). During the initial stages of filament eruption, in ten events, if one type of rotational motion was observed in one end of the filament, the opposite direction of rotational motion was observed in the other end of the filament (Dhara, Ravindra, and Banyal, 2014b). In two events (3 and 10) the rotational motion was observed

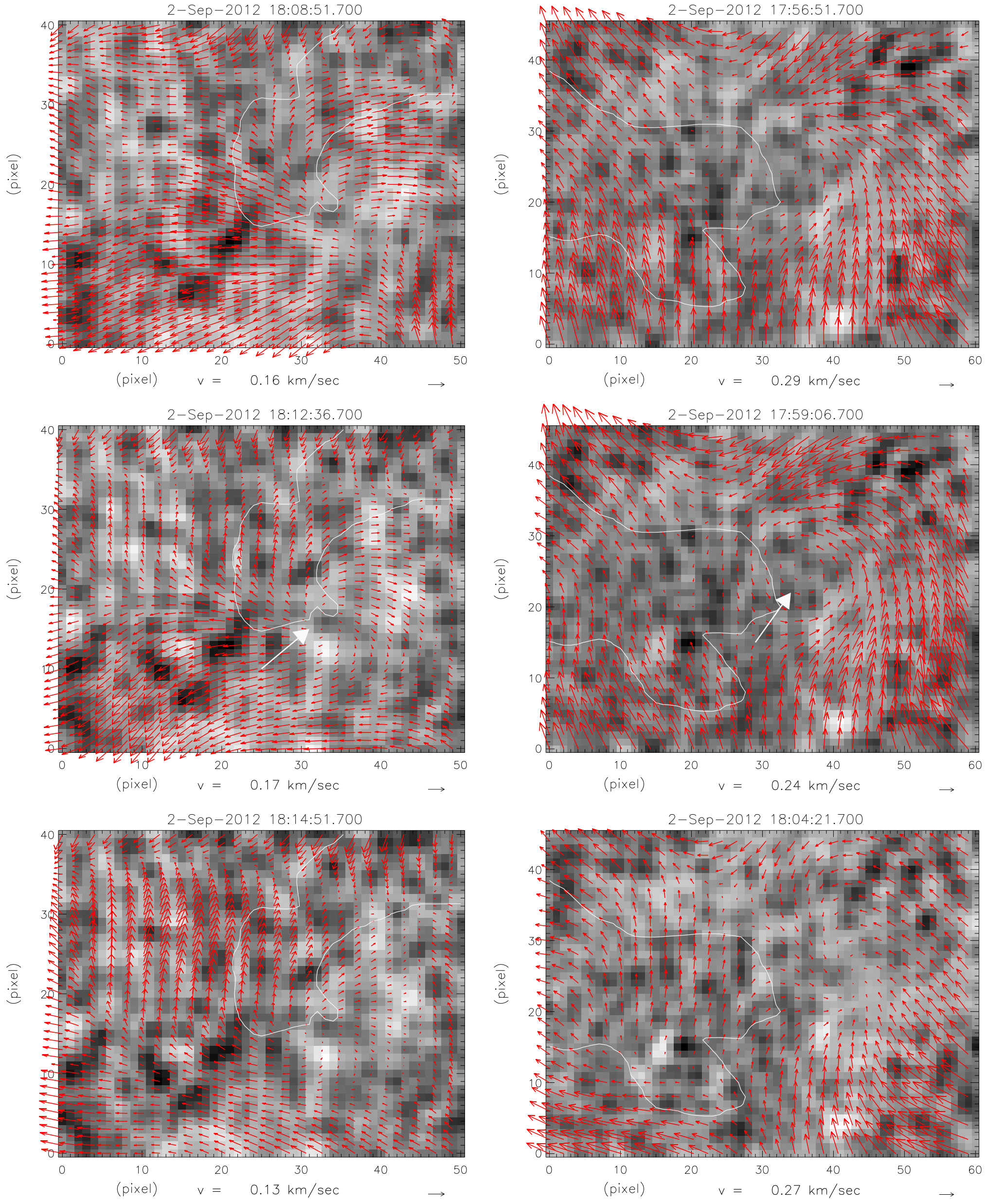

Figure 4.6: Same as Figure 4.2, but for event 4.

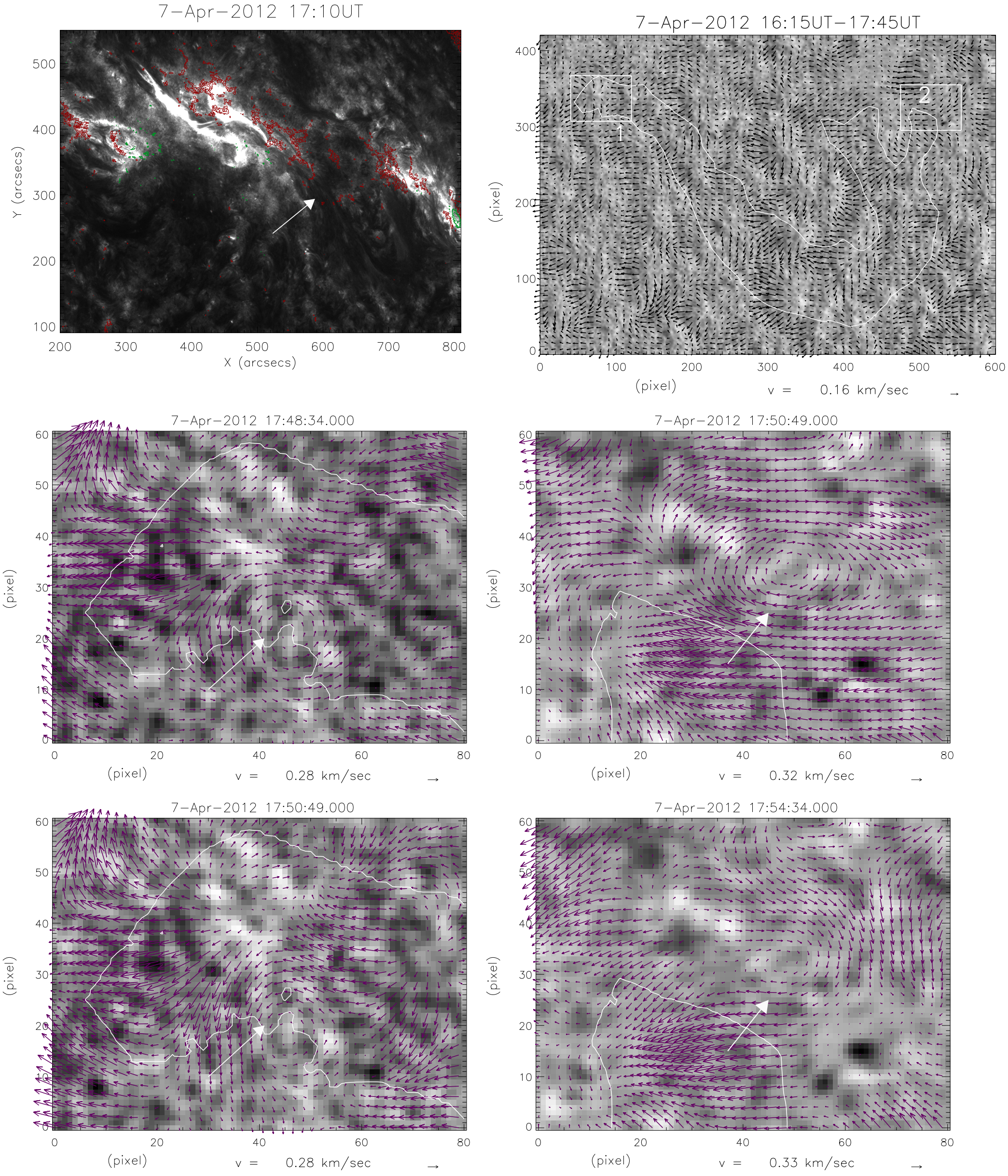

Figure 4.7: Top–Left: Filaments observed in the 304 Å channel of the chromosphere image in the active region for event 5. The filament position is shown by white arrow in Figure (top-left). The contours of the magnetic strength values are overlaid on the 304 Å image. The red and green contours represent the positive and negative polarities with magnetic field strength values of ± 150, 400, 600 and 900 G, respectively. Top–Right: The horizontal velocity vectors shown in arrows are overlaid upon the averaged dopplergram. The contour of the filament, extracted from the 304 Å image is overlaid upon the averaged dopplergram. The boxed regions 1 and 2 show the location of the Eastern and Western ends of the filament respectively. Middle & Bottom: Rotational velocity pattern observed for this event. Left side (middle and bottom) images correspond to location 1 and right side (middle and bottom) images for location 2 of top-right image.

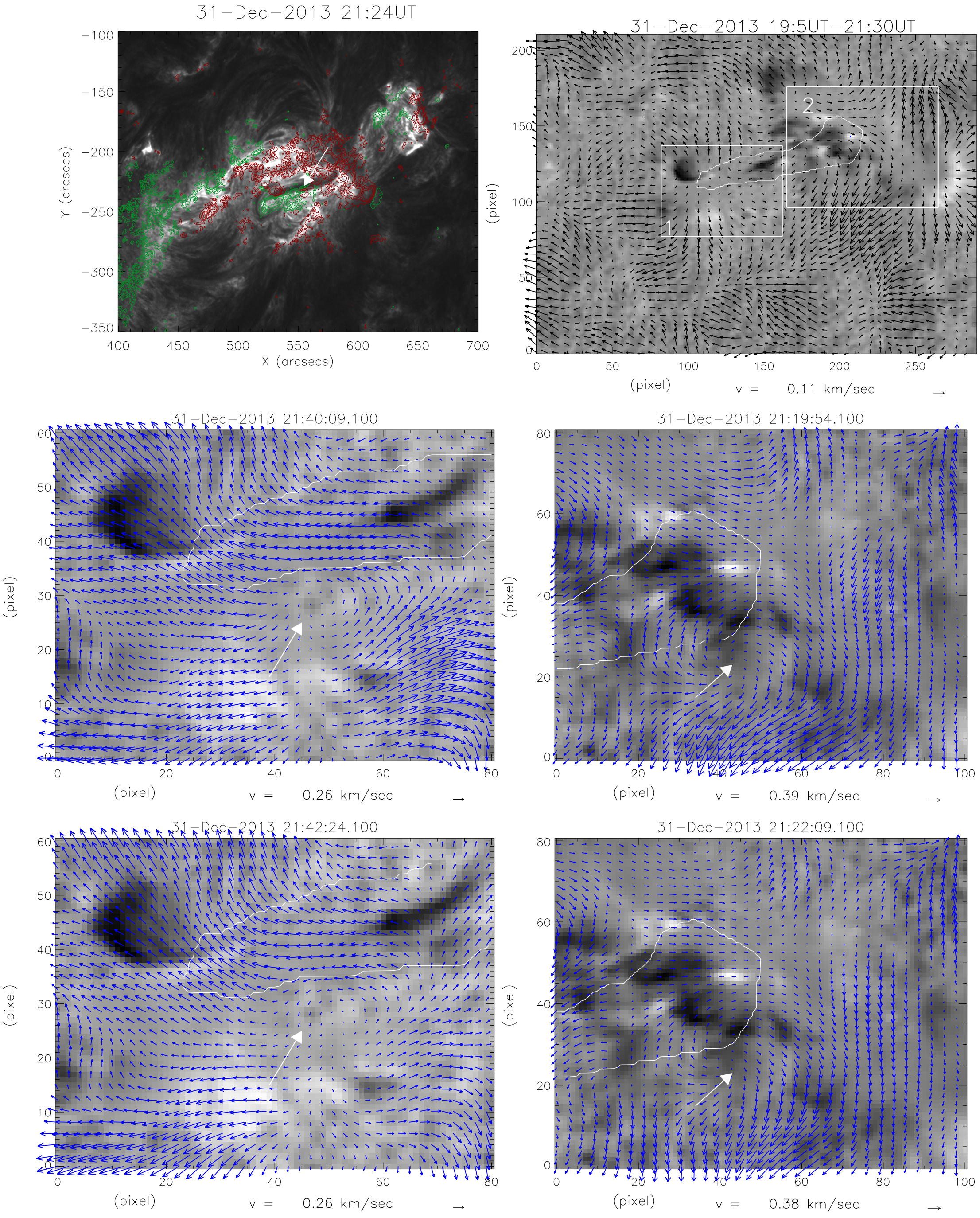

Figure 4.8: Same as Figure 4.7, but for event 6.

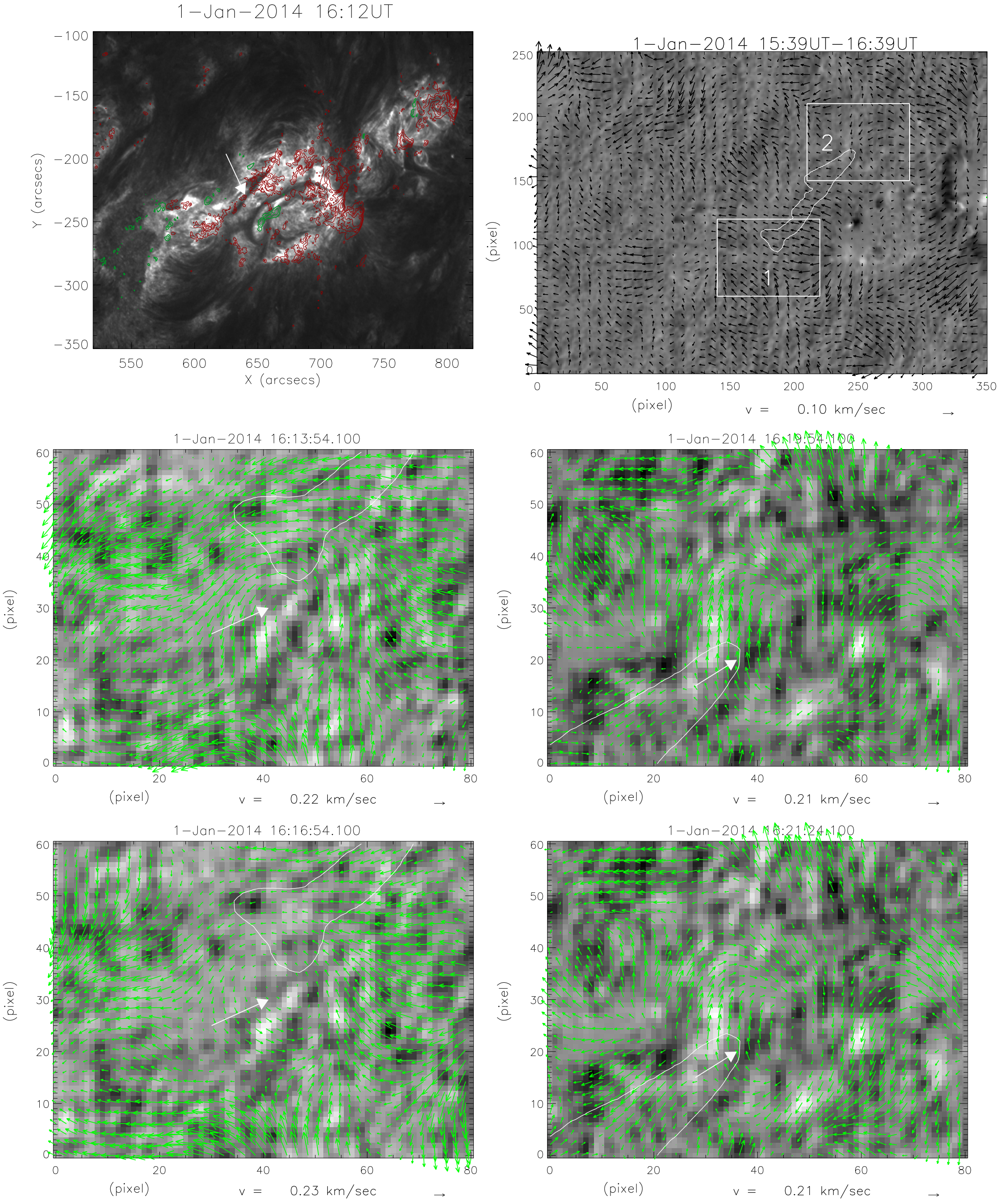

Figure 4.9: Same as Figure 4.7, but for event 7.

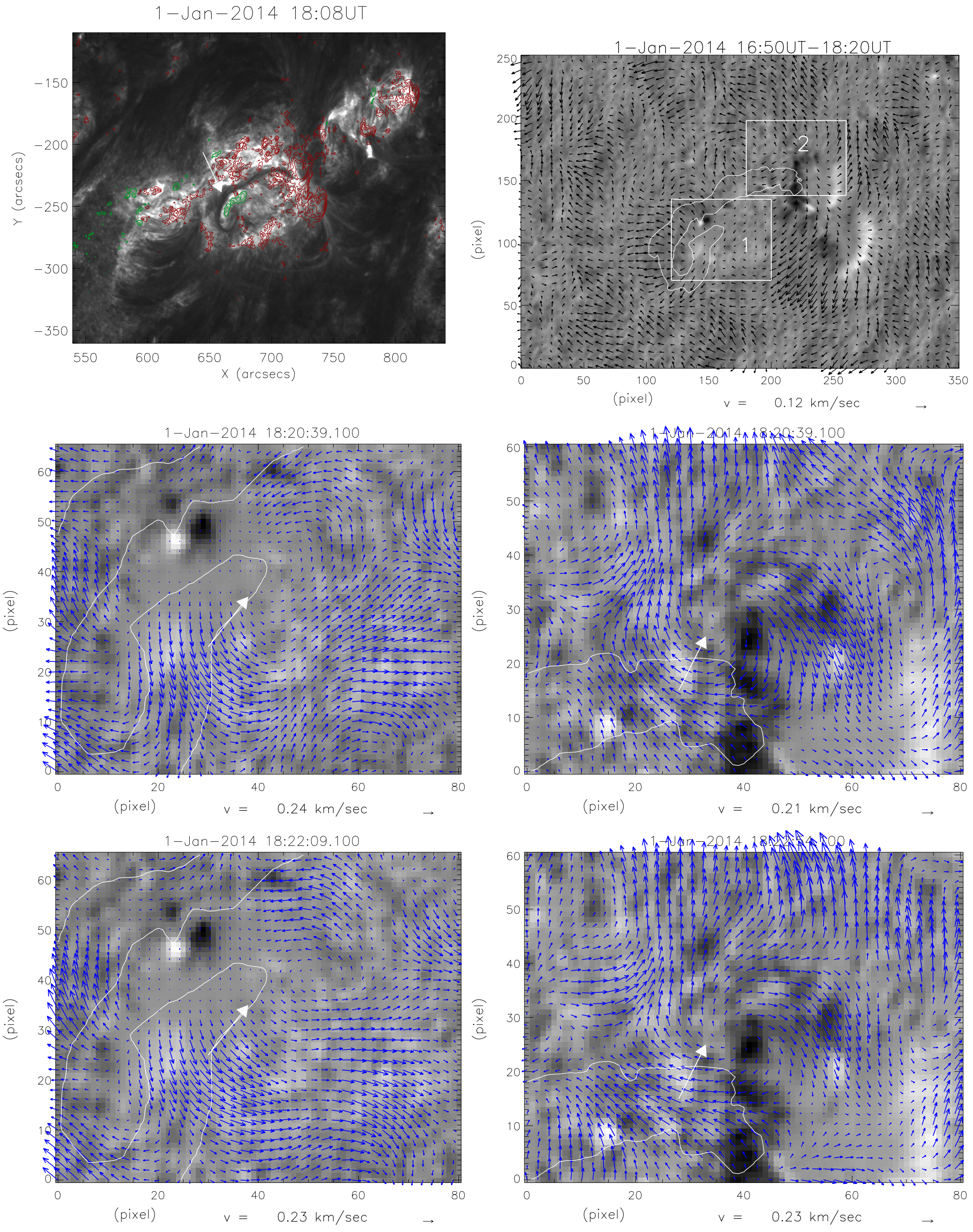

Figure 4.10: Same as Figure 4.7, but for event 8.

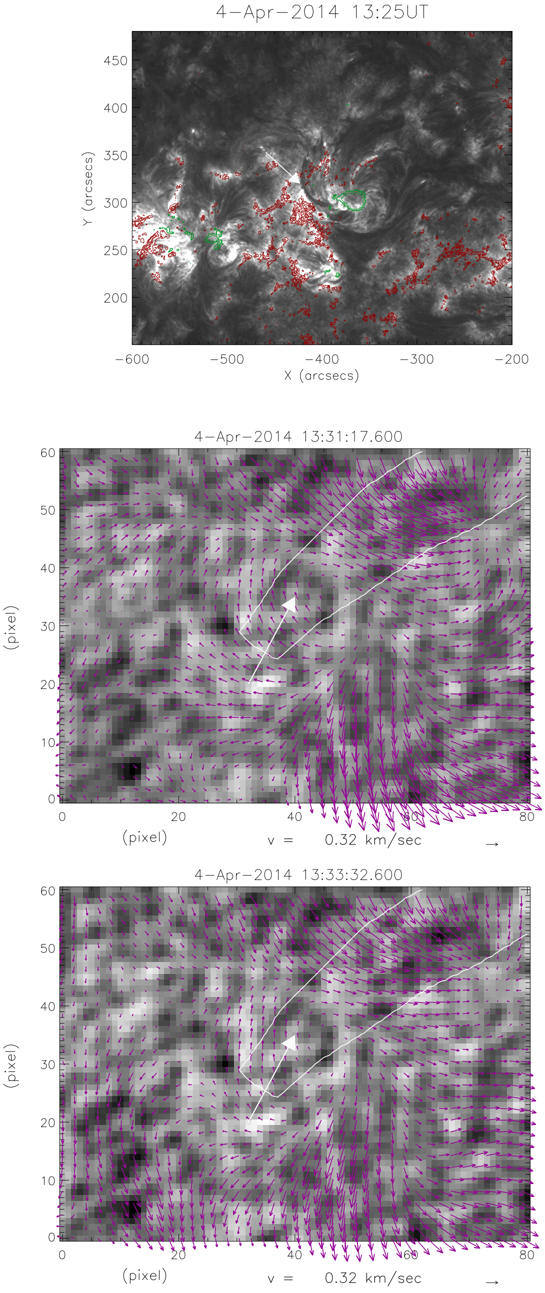

4−Apr−2014 13:25UT

4−Apr−2014 12:00UT−13:30UT

4−Apr−2014 13:31:17.600

4−Apr−2014 13:54:32.500

4−Apr−2014 13:33:32.600

4−Apr−2014 13:56:02.500

Figure 4.11: Same as Figure 4.7, but for event 9.

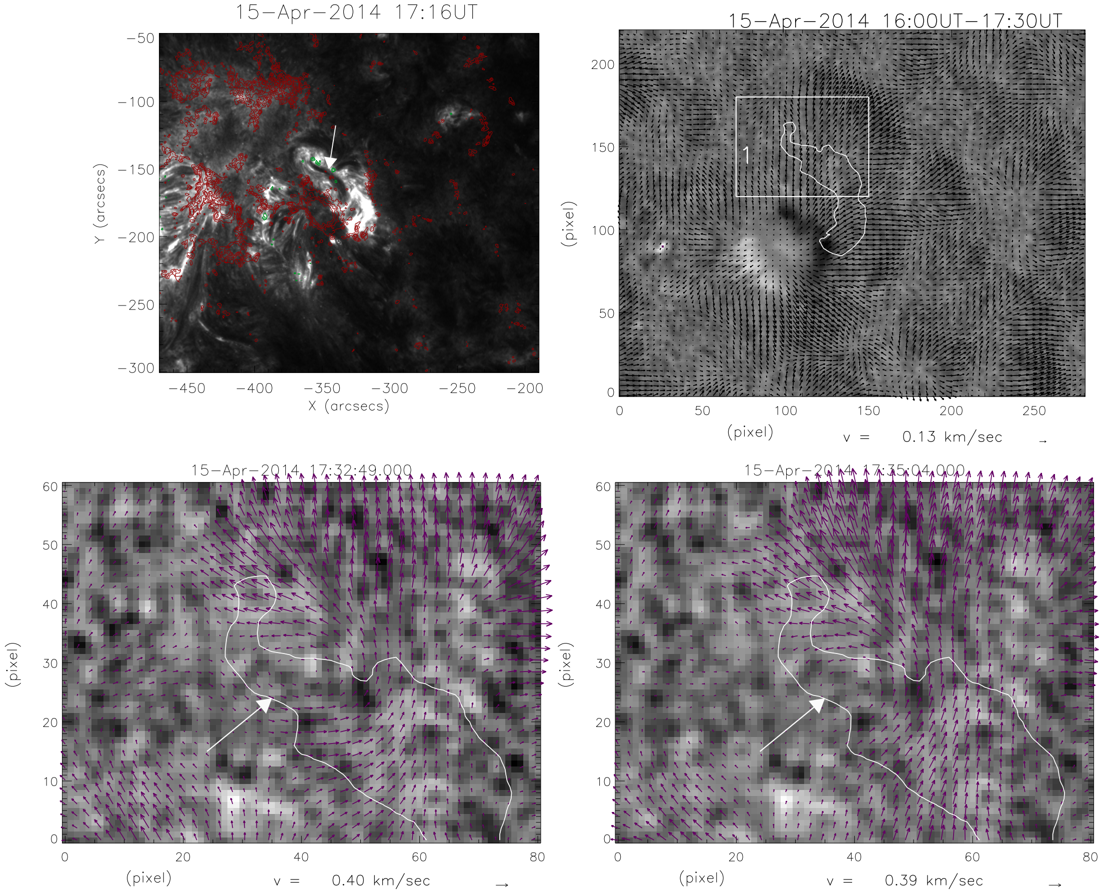

Figure 4.12: Same as Figure 4.7, but for event 10. Bottom: Rotational velocity pattern observed in the location 1 only for this event.

only in one end of the filament. The rotational motions persisted for about 4-29 minutes and the rate of rotation was about 6° hr^{-1}. The observed rotational motion in both ends of the filament is not simultaneous. There is a few minutes difference between the ending of the rotational motion at one end of the filament and starting of the rotational motion in the vicinity of another end of the filament. In all these events, the fast rising phase initiated either during the rotational motions or after it has ceased.

The filament destabilization and subsequent eruption may have been initiated due to several reasons such as kink-mode instability in twisted magnetic fields (Sakurai, 1976a), the magnetic reconnection at low level (Contarino

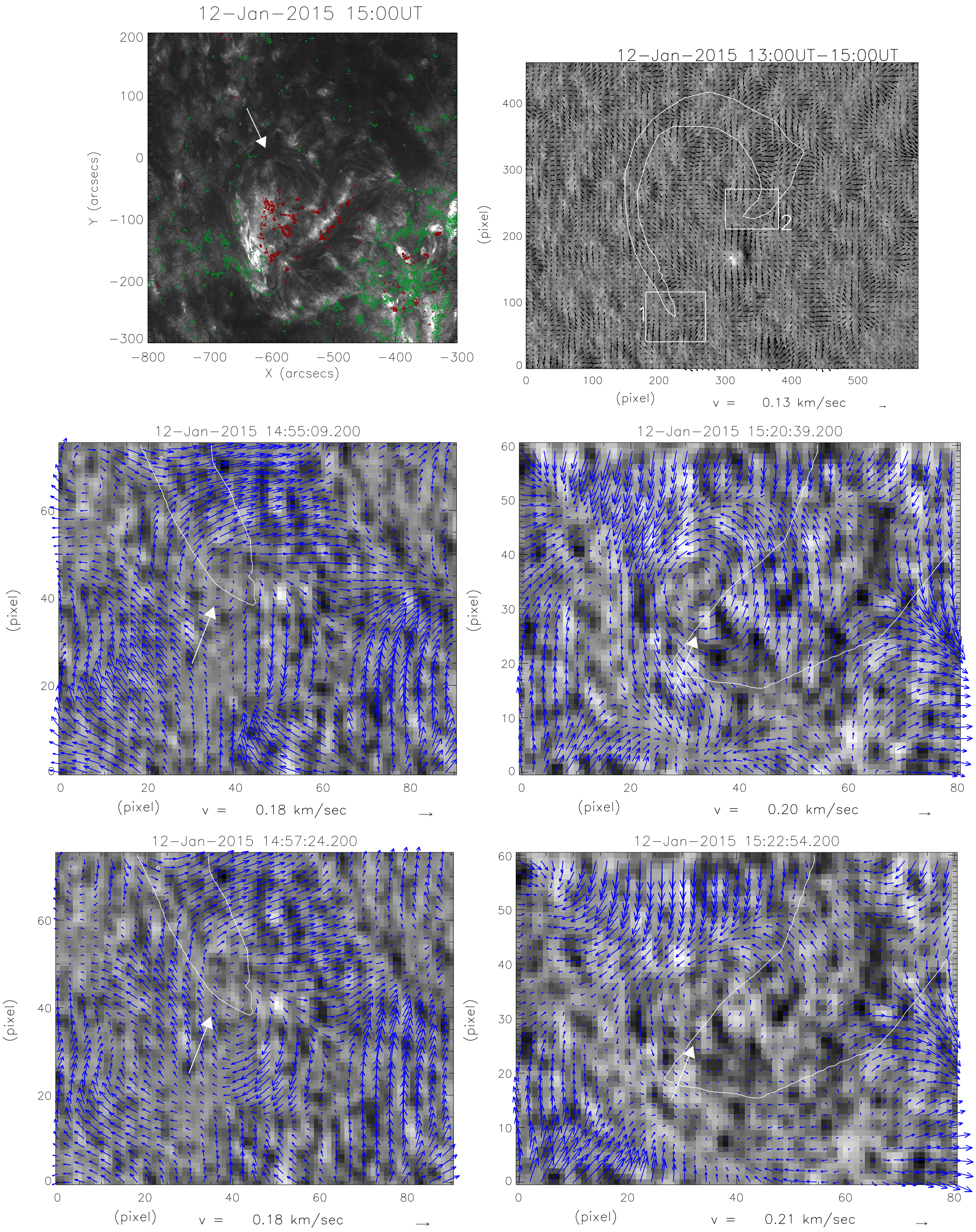

Figure 4.13: Same as Figure 4.7, but for event 11.

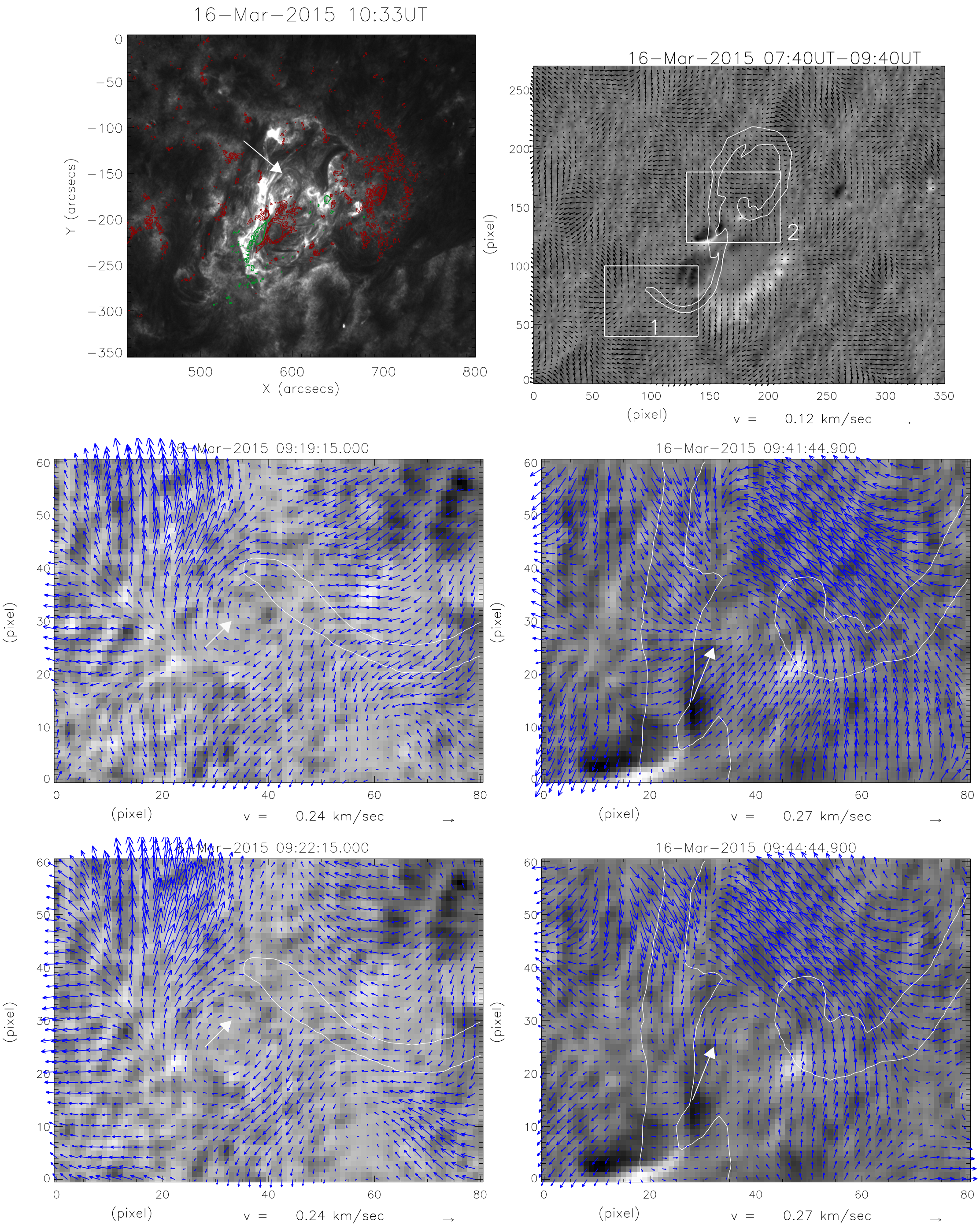

Figure 4.14: Same as Figure 4.7, but for event 12.

et al., 2003), flux cancellation at the photosphere (*e.g.,* Amari *et al.* 2003) etc.. Once the filament starts to erupt, it expands axially towards higher heights. As it rises, the local external pressure is smaller compared to the previous location of the filament. Because of the pressure difference, the top portion of the filament can expand radially thereby inducing a torque imbalance between the regions of the expanded portion and the undisturbed portion of the filament (Jockers, 1978; Parker, 1974). The consequence of the radial expansion of the filament is a rotational motion in the expanded portion of the filament. This can happen by transferring the twist from the undisturbed portion to the expanded portion. The effect of the transfer of twist from the undisturbed portion to the expanded portion can cause the rotation in the legs of the filaments which could extend from the corona to the chromosphere. In this case two footpoints of the filament should exhibit oppositely directed motions (Jockers, 1978). The plasma inside the filament will also rotate with the flux rope. However, this can not cause the observed rotational motions of the plasma in the photosphere where the plasma beta is large.

Alternatively, the bending of the top portion of the erupting filament can induce the rotation of the legs. Martin (2003b) and Panasenco and Martin (2008) have observed a bending motion of the top portion of the erupting prominence and subsequently observed an oppositely twisting motion in two legs. They name this observation as the “roll effect”. Similarly, Panasenco *et al.* (2013) mention that the non-radially erupting prominence first exhibits the bending motion of the top of the prominence and later the oppositely directed rolling motion propagates into its legs. In this mechanism the plasma inside the flux rope can rotate with the magnetic field and the rotational motion may not reach the photosphere as the torque and force required for the photospheric plasma to rotate is probably much larger than this.

The observed photospheric rotational motion near the ends of the filament could possibly be resulting from the photospheric or subphotospheric shearing flows. We observed that the fast rise of the filament was initiated during/after the vortical motion of the plasma had set in. We have also observed vortical flows offset from the ends of the filament. However, their lifetime is too short and their size is about $10''$ which is much smaller than the ones observed near the filament ends. The spatial correlation between the observed end points of the filament and the location of the rotational motion, the temporal coincidence of the rotational motions with the filament eruption time in twelve events suggest that the observed rotational motion is not randomly occurring in the vertices of the supergranulations (Innes *et al.*, 2009).

When the filament starts to erupt, it expands axially towards higher heights. The immediate consequence of the deformation of the axial component of the magnetic field in the flux rope is the launch of a shear Alfven waves by shearing its footpoints (by the Lorentz force) that in turn carry the axial component of the flux into the expanded portion of the flux rope (Manchester *et al.*, 2004). The increase in the axial flux in the flux rope will increase the magnetic pressure. The tendency of the outward directed magnetic pressure will push the flux rope slowly to higher heights. Once the top of the flux rope reaches a critical height where the “torus instability” criteria are satisfied then the flux rope becomes unstable and eventually it will erupt (Kliem and Török, 2006).

Another possibility is that, if there is an emergence of a poloidal flux results in a rotation of the footpoints. The injection of the poloidal flux into the flux rope, will increase the magnitude of the outward Lorentz self force (hoop force). This will push the flux rope slowly to critical height where the external poloidal flux is deceasing faster than the decrease of the hoop force. This condition will again lead to the “torus instability” and in that condition the flux rope is no longer in equilibrium scenario and eventually it erupts. But, the generation and emergence of the poloidal field is very unlikely and there is no observational report to this [*see also;* Chen and Kunkel 2010].

Martin (2003b) and Panasenco *et al.* (2011) reported that there is a correlation between the direction of the rolling motion observed in the erupting filament and the chirality of the filament. The observed direction of rotation in both legs of the prominence is opposite to each other. In future, we plan to study the rotation in the footpoints of a large number of erupting filaments using spectroscopic technique both in the photosphere and chromosphere simultaneously along with their sign of chirality using vector magnetic field measurements. This may provide a vital clue to the origin of the rotational motion near the ends of the erupting filaments.

To study the rotational motions at chromospheric height, near footpoints of the active region filament during their activation, we proposed a Fabry perot interferometer based narrow band imager (NBI) at Indian Institute of Astrophysics, Bangalore. The NBI is able to image the solar atmosphere at chromospheric height and produce the dopplergrams using some post-facto techniques. In next chapter of the thesis, I have discussed about the development of NBI and preliminary observations carried out using this instrument.

Chapter 5

Development of a Fabry-Pérot based Narrow Band Imager for Solar Filament Observations

5.1 Introduction

It is well known that features in the solar atmosphere change very rapidly. During the active periods on the sun, there is a rapid change in the magnetic field and velocity field at various heights in the solar atmosphere. To understand the solar activity on the Sun, it is important to measure the magnetic and velocity fields on the solar atmosphere at different heights. To measure the solar magnetic and velocity fields, a high resolution spectrograph or tunable narrow-band imager is needed in an imaging system (Zirin, 1995). The spectrograph based instruments obtain spectra with very high spectral resolution but to obtain a two-dimensional image of the Sun, a spatial scanning is required across the field-of-view (FOV) (Judge *et al.*, 2010). Moreover the FOV is limited by the length and scan range of the spectrograph slit. Using imaging spectroscopy one can obtain two-dimensional images of the Sun, but it requires scanning across multiple wavelength positions to build up the spectra. It also suffers from low spectral resolution. The rasterization of the spectrograph to make the two-dimensional image can be avoided in the narrow band imaging system. In both cases, the ground based observations are affected by atmospheric turbulence. By using the high-order adaptive optics and/or post-facto techniques, one can minimize the atmospheric seeing effects to achieve high spatial resolution imaging for a limited FOV.

Narrow-band imaging can be carried out by using Fabry-Perot (FP) interferometer. Using a single FP a narrow band imaging system can be developed. But when two FPs are used in tandem gives a very good spectral resolution. Since the light throughput is very high for the FP based imaging system, one can obtain two-dimensional images by scanning across the spectral lines in shorter time periods depending upon the number of wavelength positions to be scanned along the line profile. One of the major advantages of this system is that it can be switched between wavelengths very fast. Hence one can obtain the images in different wavelengths by combining the FP with different set of pre-filters. Fabry-perot interferometers can be of two types; a) solid etalons b) air gap FP. In case of air gap FP, tuning is achieved by varying the separation between the two plates of the FP. But for solid etalons the tuning is done by varying the refractive index of the electro-optic material. To obtain the 2-D images with a fast cadence some of the instruments use either air gap FPs (*e.g.,* Bello González and Kneer 2008; Cavallini 2006; Kentischer *et al.* 1998) or solid etalons (*e.g.,* Kleint, Feller, and Gisler 2011; Martínez Pillet *et al.* 2011; Mathew *et al.* 1998; Raja Bayanna *et al.* 2014; Rust *et al.* 1996) in the imaging systems. Air gap based FPs requires a control system that maintain the parallelism between the two highly polished plates to an accuracy better than $\lambda/100$. It provides a larger wavelength shift than electro-optically tunable solid-state etalons for the same FOV because of their lower refractive index. It can also be operated at a faster rate as fast as $LiNbO_3$ etalons while tuning (Martínez Pillet *et al.*, 2011).

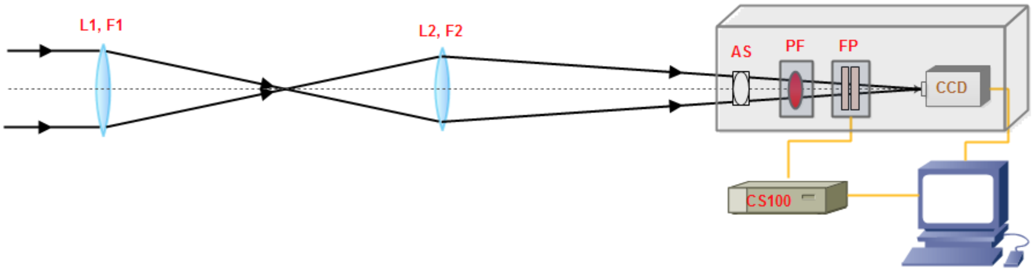

Figure 5.1: A schematic representing the optical and control layout of the narrow band imager. L1–15 cm objective lens with focal length F1=225 cm, L2–10 cm re-imaging lens with focal length F2=100 cm, AS– circular aperture stop, PF–pre-filter inside temperature controlled oven, FP–Fabry-Perot interferometer and CCD– camera.

At the Indian Institute of Astrophysics (IIA), a narrow-band imaging system (imager) has been developed using an air gap based Fabry-Perot interferometer in combination with a order sorting Hα filter. The FP has 50 mm clear aperture with transmission wavelength range 400 nm to 700 nm. The effective FWHM and free spectral range of the FP are 238 mÅ and 5 Å at $\lambda = 630$ nm, respectively. We have used a Hα filter (central wavelength at 6562.8 Å with FWHM 2.34 Å at 30^0C) as an order sorting pre-filter. In this chapter of the thesis, we discuss the characterization of the FP and order-sorting pre-filter in detail and evaluate their suitability for observations at the spectral line (Hα-6563 Å). In Section 5.2 we discuss about the schematic layout of the narrow band imager, various tuning options and the observations made with this instrument. In Section 5.3 we have shown some of the images of the filament taken with this instrument and generated dopplergrams from the observed images.

5.2 Description of the Instrument

Figure 5.1 shows the schematic layout of the instrument. Light from coelostat is imaged by the achromatic doublet lens (L1) of 15 cm aperture at its focal point (F1). We have used 10 cm aperture during observations to reduce the intensity. The focal length of the objective lens is 225 cm, this makes $F_{22.5}$

beam. The image size of the Sun at this focal plane is 21 mm. Then it is re-imaged by another achromatic doublet lens (L2) of diameter and focal length 10 cm and 100 cm respectively. The lens L2 is placed at a distance of 130 cm away from the focal point of the objective lens. Hence the final image is formed at 433.3 cm away from lens L2 . This makes F_{75} beam at the imaging plane on CCD. The image size of the Sun at this imaging plane is 70 mm. A circular aperture stop (AS) is placed infront of the pre-filter (PF) to cut down the stray light induced scattering inside the instrument box. The main component of the narrow band imger is Fabry-Perot interferometer (FP), which is mounted after the pre-filter in the optical path. The details about FP and PF are given in Section 5.2.1 and Section 5.2.4, respectively.

5.2.1 Fabry Perot Interferometer (FP)

A Fabry-Perot interferometer is a device which consists of two highly polished reflecting parallel glass plates. In combination with the order sorting filter, it selectively transmits a particular wavelength of light corresponding to the resonance of the etalon cavity. For the separation between two plates of FP is d, wavelength of incident light λ with incident angle θ and order m, the interference intensity attains the maximum value when the following formula is satisfied.

$$2\mu d cos\theta = m\lambda \tag{5.1}$$

The transmitted beam from the FP is a fringe pattern. A passband is produced with a very narrow FWHM due to multiple beam interference. The intensity distribution of the transmitted beam is given by the Airy's formula

$$I = \frac{I_{max}}{1 + F_R \sin^2(\frac{\delta}{2})} \tag{5.2}$$

Where, $I_{max} = A^2T^2/(1\text{-}R)^2$ is the maximum value of the intensity and $F_R = 4R/(1-R)^2$ is the finesse due to reflectivity of the FP plates. T

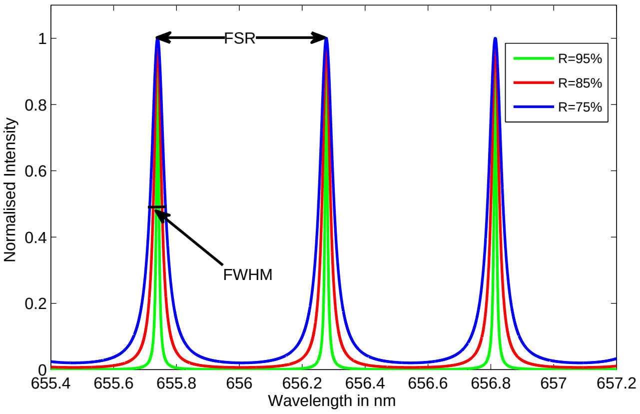

Figure 5.2: The transmission profile of the air gap based Fabry-Perot interferometer with different plate reflectivities. The intensity is normalized to unity.

and R are the transmitivity and reflectivity of the FP respectively. A is the amplitude of the incident light. δ is the phase difference between the successive transmitted rays and is given by,

$$\delta = \frac{2\pi}{\lambda}(2\mu d cos\theta) \tag{5.3}$$

where μ is the refractive index of the media between the plates and λ is wavelength of the incident ray, d is the distance between the plates and θ is the angle of the incident ray. The phase difference between the successive transmitted rays can be varied by changing the refractive index of the material between the plates or by changing separation between the plates of the FP or by changing the incidence angle of the rays. Hence the spectral line profile can be scanned by one of these methods. The transmitted beam consists of periodic fringes with a maximum intensity of I_{max} and the minimum intensity is $I_{min} = A^2T^2/(1+R)^2$. The transmission profile of FP working at 6563 Å wavelength is shown in Figure 5.2. The maximum values are reached for δ=2mπ.

5.2.1.1 Passband, finesse and spectral resolution of FP

The two key parameters for characterization of FP are: (i) the finesse (F) and (ii) the free spectral range (FSR). The finesse is related to the sharpness of the interference fringes. It is the ratio between the distance of two neighbouring peaks and their halfwidth. A measured finesse has a number of contributing factors: the mirror reflectivity, the mirror surface quality (flatness of the plates and parallelism of the plates) and the illumination conditions (beam alignment and diameter) of the mirrors. The FSR is the distance between two successive maxima and is given by

$$FSR = \frac{\lambda}{m} = \frac{\lambda^2}{2\mu d cos\theta} \tag{5.4}$$

Hence, the FSR is inversely proportional to the spacing between the plates. The FSR should be larger than the closely spaced solar spectral lines so that there will not be any overlapping of the other solar line while scanning in the desired wavelength band.

The passband of the FP can be estimated from the FSR and finesse. They are related as

$$\mathit{\Delta}\lambda = \frac{FSR}{F} \tag{5.5}$$

By decreasing the spacing between the plates of the FP the FWHM of the transmitted beam will increase. In a single FP system the spectral resolution depends on the finesse and is given by,

$$\frac{\lambda}{\mathit{\Delta}\lambda} \sim \frac{2dF}{\lambda} \tag{5.6}$$

The effective finesse (F_{coll}) in the collimated beam is given by

$$F_{coll} = \frac{\pi}{2} \frac{1}{\sqrt{\frac{1}{F_R} + (\pi \frac{\lambda_r}{\lambda_p} \frac{1}{q} \cos\theta)^2}} \tag{5.7}$$

The finesse is a function of surface flatness, parallelism, and reflectivity R of

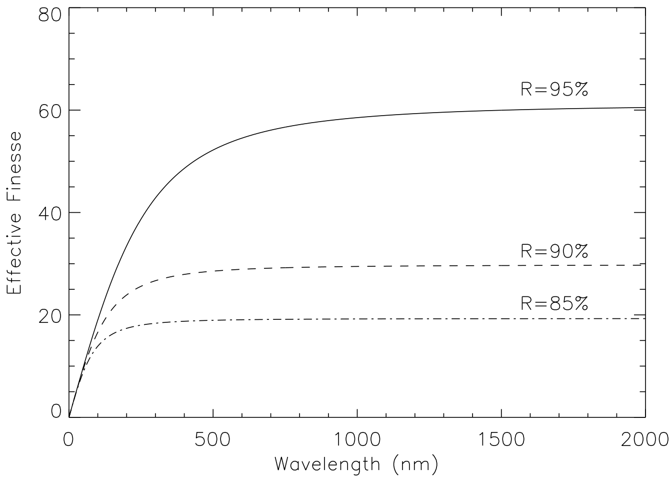

Figure 5.3: The variation of the effective finesse as a function of wavelength is shown here. The dash-dotted, dashed and solid curves are for the reflectance of 0.85, 0.90 and 0.95, respectively.

the plates. Here, F_R is the finesse due to reflectivity of the FP plates, λ_p is the peak transmission wavelength, 1/q full width fractions of a reference wavelength λ_r. The variation in finesse as a function of wavelength is shown in Figure 5.3. The plot is shown for three values of reflectivity 0.85, 0.90 and 0.95. The surface flatness is taken to be $\lambda/150$ or better at 5000 Å. From the plot it is clear that effective finesse decreases with decrease in reflectivity. But at the same time it does not depend on the wavelength in the visible and infrared regions.

The spectral resolution of the FP system in the collimated beam is given by,

$$Res = 2F_{coll}\frac{d_0 \cos\theta}{\lambda_p} \tag{5.8}$$

Figure 5.4 shows the plot of minimum spacing needed to obtain a resolution of 3×10^4 as a function of wavelength. The results are shown for three different reflectivities. It is clear from the plot that the spacing between the plates increases as the wavelength increases to maintain the same resolution of 3×10^4. For keeping the same resolution, the change of required spacing

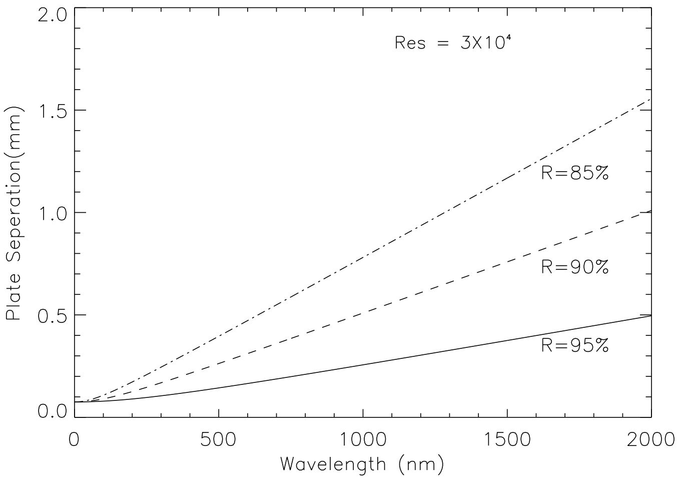

Figure 5.4: A plot of optimal spacing needed to obtain a resolution of 3×10^4 as a function of wavelength. The dash-dotted, dashed and solid curves are for the reflectance of 0.85, 0.90 and 0.95 respectively.

between the plates is comparatively smaller for the higher reflectivity of the plates. But at the same time one has to note that as the spacing increases, the FSR decreases which results in larger ghosts in the image.

Figure 5.5 shows the plot of resolution as a function of wavelength for a fixed spacing between the FP plates for the reflectivity 0.85. From the plot it is clear that the resolution decreases as the wavelength increases and the resolution is large for larger plate separation.

5.2.2 Specifications of the procured FP

We have used air gap based FP for NBI system. This FP was procured several years ago from *Queens gate, UK* (presently *IC Optical System Ltd., UK*). The servo-stabilized FP system comprises ET-Series II etalons and the CS100 control unit, which stabilizes the etalon spacing and parallelism. The CS100 is a three-channel controller, which uses capacitance micrometers and PZT actuators, incorporated into the etalon, to monitor and correct errors in mirror parallelism and spacing. Two channels control the parallelism and the third channel maintains spacing up to nanometer accuracy by referencing the

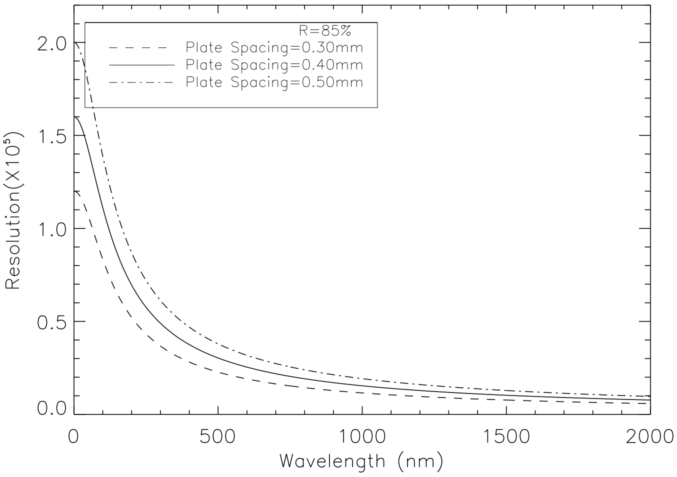

Figure 5.5: The variation of spectral resolution as a function of wavelength for a various plate spacing.

cavity length-sensing capacitance micrometer to a fixed reference capacitor. This is a closed-loop system. Hence, the non-linearity, hysteresis in the PZT drive, drifts in mirror parallelism and spacing are eliminated completely. The CS100 will control the etalon spacing and parallelism to better than 0.01% of a FSR. The CS100 can be operated manually from front panel controls, or under computer control using either the IEEE - 488, RS232C or analogue interfaces. We have developed GUI in LabVIEW using the IEEE - 488 as well as analogue interface using PCIe - DAQ to control the CS100 controller via PC. The separation between the plates is varied in discrete steps from 0 to 4095 via IEEE - 488 interface to the CS100 controller via PC. In addition to this, a two-pin socket is provided on the CS100 rear panel to enable analogue control of the etalon spacing. A ±10V differential input has been given using DAQ to produce ±1000 nm of plate movement for the cavity. The GUI developed in Labview. Figure 5.6 shows the GUI for the CS100 controller. We have used National Instruments PCIe-6361 DAQ to generate the square wave analogue signal with a frequency 1000 Hz. This signal is fed to CS100 controller to enable analogue control of the etalon spacing. The amplitude of the signal can be varied in step of 0.05 V. We changed the amplitude from

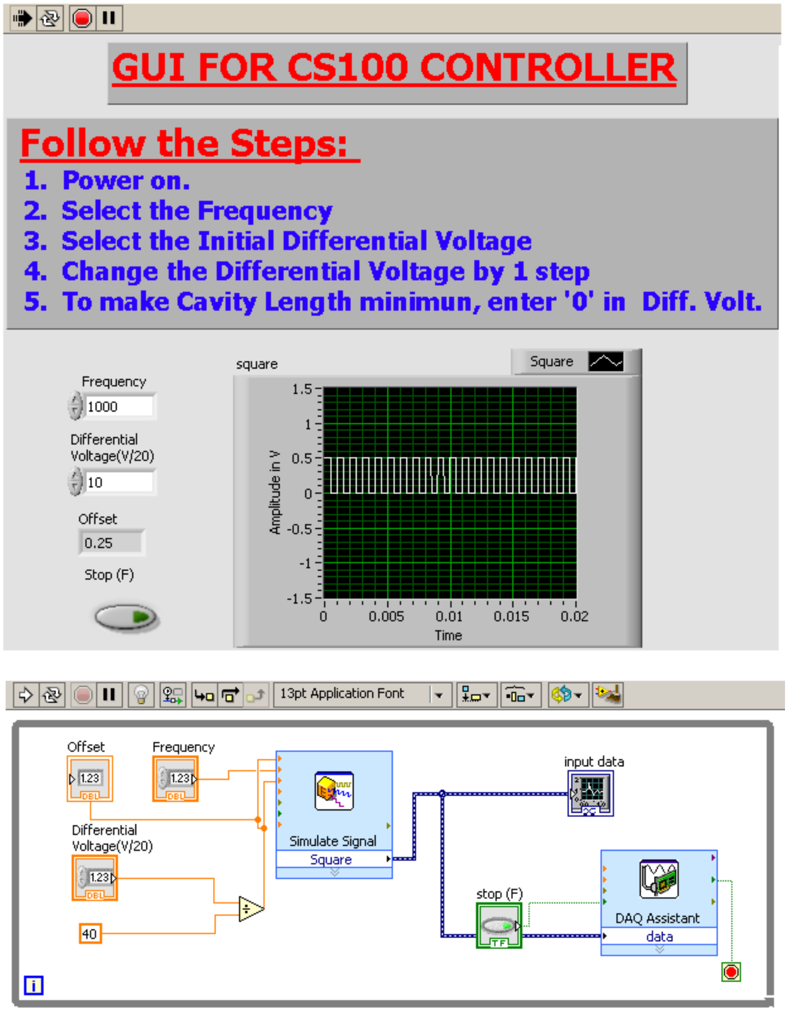

GUI FOR CS100 CONTROLLER

Follow the Steps:

1. Power on.
2. Select the Frequency
3. Select the Initial Differential Voltage
4. Change the Differential Voltage by 1 step
5. To make Cavity Length minimun, enter '0' in Diff. Volt.

Frequency: 1000

Differential Voltage(V/20): 10

Offset: 0.25

Figure 5.6: Top: Front panel of the GUI for CS100 controller unit using LabVIEW. The plate separation of the FP can be varied by applying differential voltage. Bottom: Block diagram of the GUI as shown in above using LabVIEW.

-1.5 V to 1.5 V in step of 0.1 V during observations.

Table 5.1: Details of the specifications of the procured FP for narrow band imager.

Specifications	Value
Fabry-Perot Model	ET-50-FS(SN 1006)
Clear Aperture	50 mm
Nominal Cavity Spacing	400 μm
Cavity Scan Range	± 2.5 μm
Reflectivity	$\sim$ 95% at 633 nm
Transmission Wavelength Range	400 nm to 700 nm
Controller Model	CS100 (SN 8088)

This FP has a clear aperture of 50 mm, high average reflectivity (∼95%) for the wavelength range from 400 nm to 700 nm. The calculated finesse due to reflectivity with 95% is ∼61 and FSR is ∼ 5.0 Å at λ= 633 nm. The specifications of FP system as provided by the vendor are listed in Table 5.1. The performance characteristic of the FP needs to be checked against the specifications given by the vendor before using it for NBI system. In the next section we describe the methods used to evaluate the performance characteristic of the FP and obtained results.

5.2.3 Characterization of FP

5.2.3.1 Experimental setup

Before using the procured Fabry-Perot interferometer in the NBI system, we have evaluated its specification in the laboratory experiments. We have characterized the Fabry-Perot using a collimated configuration, shown in Figure 5.7. A He-Ne laser of a central wavelength 633 nm was used as a source to perform the experiment. The laser beam was passed through a spatial filter. The spatial filtering setup is a combination of 15 μm pinhole and 40× microscopic objective. It is designed to be used with lasers to clean up the beam. In order to get a clean Gaussian beam, this spatial filter is used to remove the unwanted multiple-order energy peaks and pass only the central maximum of the diffraction pattern. Then the expanded beam from the spatial filter, was collimated by a lens (L1) with focal length f = 600 mm, resulting in a beam of diameter 50 mm to feed FP. The beam was re-imaged by a f = 225 mm lens (L2) on a CCD camera (2k×2k). In order to check the light beam after the lens L1 is collimated or not, we used shearing Interferometer as shown in Figure 5.8. The shearing interferometer consists of a wedged optical flat mounted at 45^0 angle and a diffuser plate on the top to view the interference fringe pattern with a reference wire in the middle. This interferometer is designed to provide qualitative analysis of a beam's collimation (Darlin *et al.*, 1995; Zhao *et al.*, 1995). The wedged optical flat is made of uncoated UV fused silica and the wedge angle for each plate size is optimized for the range of the acceptable beam sizes. Our shearing interferometer has wedge optical flat of 50 mm diameter. The interference fringes created by Fresnel reflections from the front and back surfaces of the optical flat can be seen in the diffuser plate. If the beam is collimated, the resulting fringe pattern will be parallel to the reference wire line (N1N2). Panel A in Figure 5.8 shows the observed fringe pattern parallel to the reference wire line when the beam is collimated.

The plate spacing was controlled via IEEE - 488 interface to the CS100 controller via a PC. The CCD camera was controlled by the same PC to capture images as the cavity spacing was varied in incremental steps. We have used 2k × 2k CCD, procured from *Princeton Instruments* to record the images. The CCD has pixel size = 13.5 μm with total imaging area 27.6 × 27.6 mm^2. The PIXIS CCD is a back-illuminated CCD and can be interfaced to the PC via USB 2.0. The CCD will collect a dark current, which is dependent on the exposure time and camera temperature. The readout noise is ∼40 counts which is less than photon noise in the image (∼220 counts).

5.2.3.2 Bandpass

Assuming that the bandwidth of laser beam is much narrower than the bandpass of FP and the FP bandpass profile does not change too much in a very narrow spectral range, the FWHM of the bandpass was measured in the following way. The spacing of the FP plates was changed by 5 steps to get different orders of fringes and at the same time CCD camera captures the images at each wavelength steps. The scan is performed in discrete steps from 0 to 4095. In this way, a 3D data cube is generated by the scan. Figure 5.9 shows the transmitted images of the laser beam through the Fabry-Perot as the cavity spacing was varied from one maximum to other maximum.

An intensity profile which is the average of intensity in the central part of each images (100×100 pixels^2) from the data cube, is shown in Figure 5.10

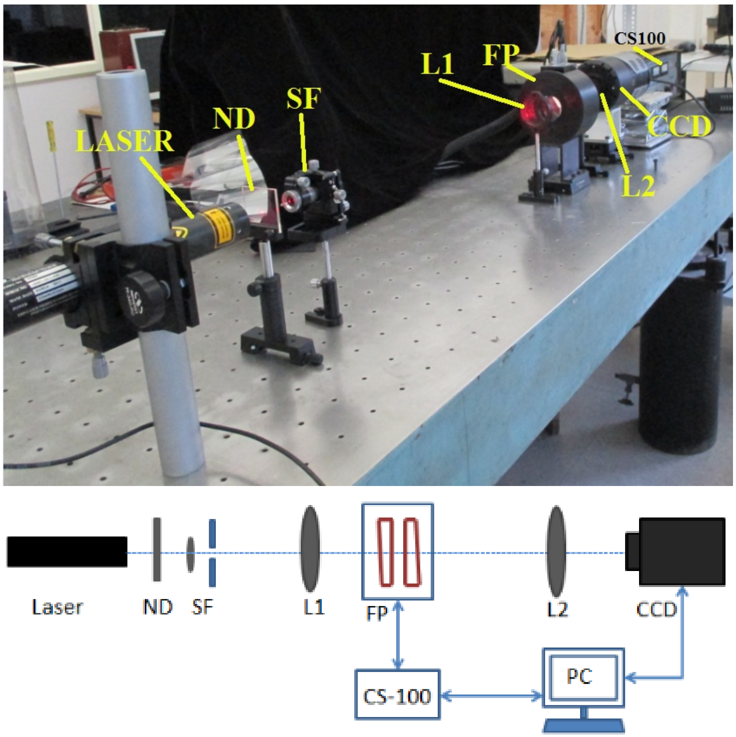

Figure 5.7: Top: Picture of experiment setup. Below: sketch of the optical set-up to characterize the FP. ND: neutral density filter, SF: spatial filtering set-up, L1: collimating Lens, L2: reimaging Lens and FP: Fabry- Perot interferometer.

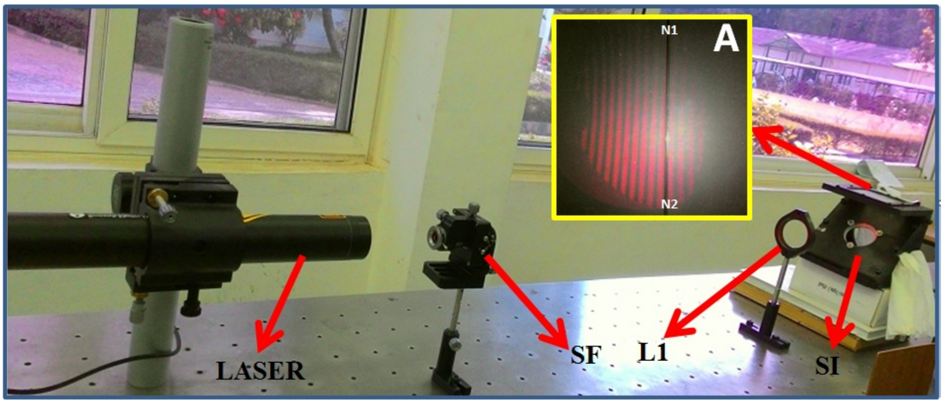

Figure 5.8: Top: Picture of experimental setup for examining collimated light. SF: spatial filtering set-up, L1: collimating lens, and SI: shearing interferometer. Panel A shows the obtained fringes observed in the top diffuser plate.

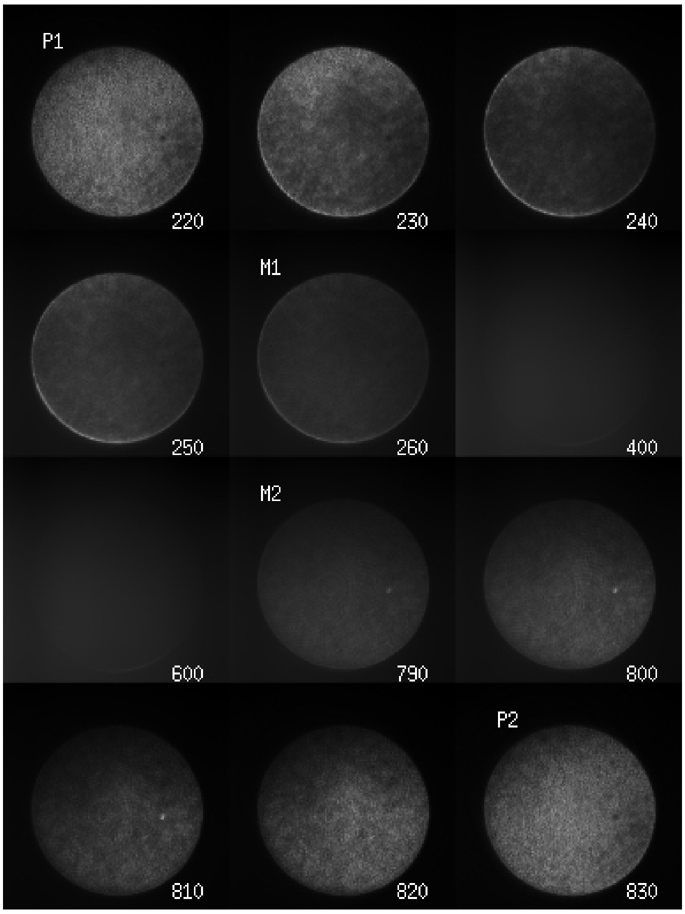

Figure 5.9: Captured images from the scanning of one transmission peak to other. The scanning steps corresponding to the images are shown in the label below. P1, M1 are the peak position and minimum position images respectively of the first transmission profile and P2, M2 are the peak position and minimum position images respectively of the second transmission profile.

(left). The effective FWHM of the bandpass is obtained by fitting a Gaussian profile of the measured intensity values. The effective FWHM is found to be 29 steps, which corresponds to ~23.77±0.46 pm. The conversion factor between wavelength units and discrete steps is given by 0.82 pm/step. In a similar way, a surface plot of the FP bandpass in 2D space was constructed for each resolution element from the same data cube. Figure 5.11(left) shows the surface plot of FWHM of the FP bandpass and its corresponding histogram is shown in Figure 5.11(right). The shape of the histogram implies that the bandpass is not homogeneous but possesses a pattern across the field-of-view

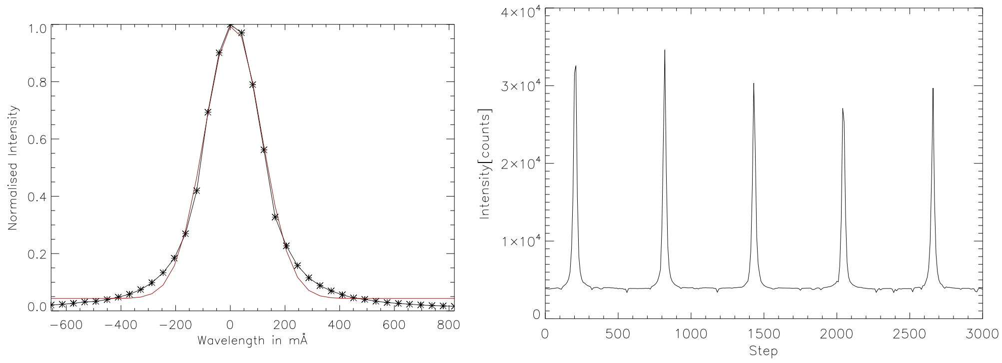

Figure 5.10: Left: The average intensity profile of one transmission peak. The red line shows Gaussian fitting to the measured intensity profile. Right: The average intensity profile of several transmission peaks. The wavelength regime is given in discrete steps (0-3000) of the CS100 controller.

(FOV). The bandpass varied from ∼14.75 pm (∼18 steps) to ∼31.97 pm (∼39 steps) at different position of the FP.

5.2.3.3 Free spectral range and finesse

If the scan range is extended further, more than one intensity peak can be obtained. Here, we carried out a scan from 0 to 4095 steps, which included five transmission peaks. Figure 5.10 (right) shows the several transmission peaks to illustrate the FSR of the FP. The measured FSR is 610 steps (∼499.93 pm). Since the nominal spacing between two parallel plates is 400 μm, then from the eq. 5.4, the calculated FSR is 500.9±4.1 pm at wavelength 633 nm. The total scanning range is 3.36 nm.

The average effective finesse is found to be 21.03. A 2D surface plot of the finesse and its corresponding histogram of the frequency distribution were constructed. These are shown in Figure 5.12. The distribution of finesse over the field of view is inhomogeneous and most of its values range from 13 to 35 (neglecting some spurious data at extreme edge). The effective finesse is the most important part for the performance evaluation of Fabry-Perot Interferometer. It is dependent on the finesse due to reflectivity (F_R), finesse due to plate defects (F_S, F_G and F_P) and the finesse due to the illumination of the

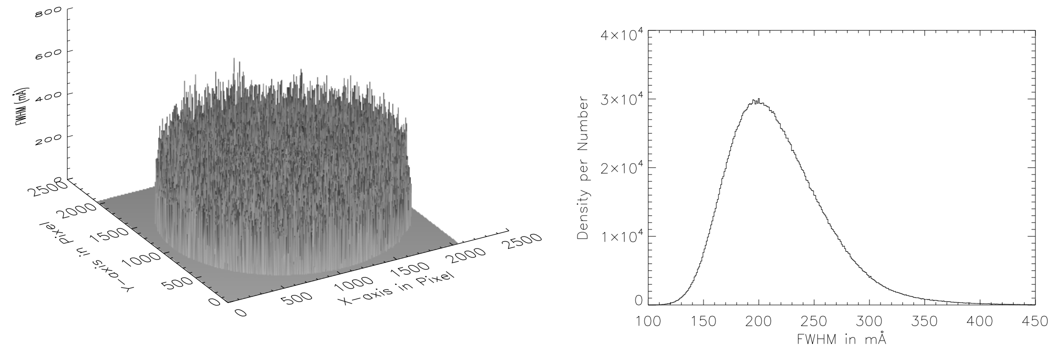

Figure 5.11: Left: The surface plot of the FP bandpass. Right: Histogram of the corresponding frequency distribution.

plates (F_I). In detail, the finesse due to plate defects is dependent on overall flatness and roughness of the FP plates and departure from the parallelism of the two plates. The effective finesse of a Fabry-Perot can be represented completely as (Gary, Balasubramaniam, and Sigwarth, 2003; Gullixson, 1998),

$$F = \left[\frac{1}{{F_R}^2} + \frac{1}{{F_S}^2} + \frac{1}{{F_G}^2} + \frac{1}{{F_P}^2} + \frac{1}{{F_I}^2} + ...\right]^{-1/2} \tag{5.9}$$

The eq. 5.9 reduces to the following after incorporating the terms into the individual finesse.

$$F = \left[\frac{(1-R)^2}{\pi^2 R} + \frac{4\delta t_s^2}{\lambda^2} + \frac{22\delta t_g^2}{\lambda^2} + \frac{3\delta t_p^2}{\lambda^2} + \frac{m^2\theta^4}{64} + ...\right]^{-1/2} \tag{5.10}$$

Where, δt_s is the peak-to-valley deviation from perfect flatness, δt_g is the plate rms deviation, δt_p is the plate deviation from parallel and θ is the angular size of the accepted beam.

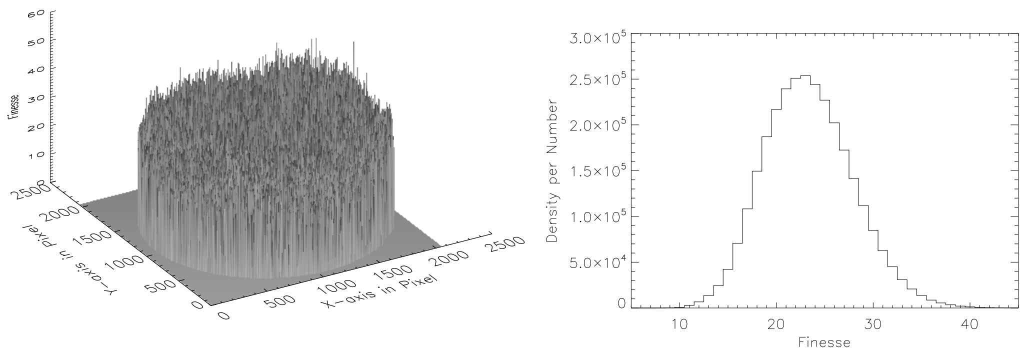

Figure 5.12: Left:The surface plot of the FP effective finesse. Right: Histogram of the corresponding frequency distribution.

5.2.3.4 Plate flatness

An appropriate understanding of the flatness of the Fabry-Perot plates is needed as it affects the bandpass and finesse of the system. With measurements of the surface flatness and surface roughness we can estimate the overall finesse of the FP plates. In this study, from the same data cube for each resolution element the peak position of transmission maxima is measured. A 3D map of the surface flatness and its corresponding histogram was constructed as shown in Figure 5.13(left). From the maximum and minimum of the histogram we have determined that the surface has a peak-to-valley deviation about 15 steps. This implies a surface flatness of about $\lambda/35$. The root mean square surface roughness calculated from the same data by neglecting some lower and upper pathological data is about 7 steps, which implies a surface roughness of $\lambda/74$.

Reflectivity of the FP plate given by the vendor is 95%. Hence, we can find out $F_R = 61.24$, $F_S = 17.28$ and $F_G = 15.76$ using eq. 5.9 and eq. 5.10. The comparison between vendor's specification and experimentally measured values are given in Table 5.2. In conclusion, the calculated effective finesse is not in agreement with the measured finesse. The following possible rea-

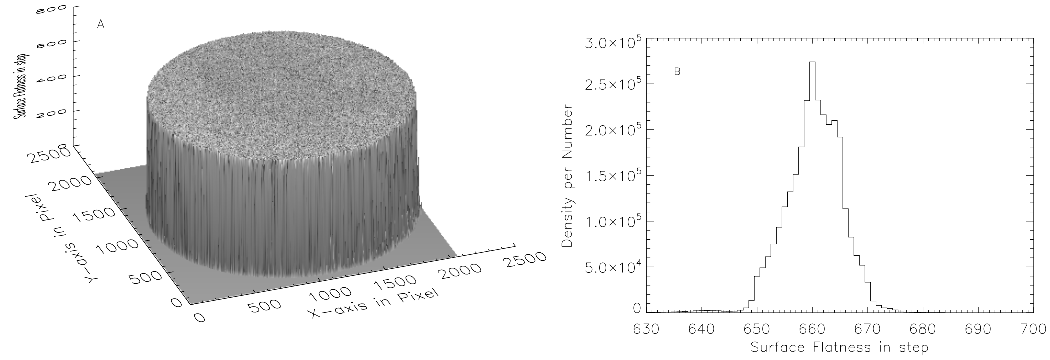

Figure 5.13: Left: The surface plot of the FP surface flatness. Right: Histogram of the corresponding frequency distribution.

Table 5.2: Comparison between vendor supplied value and experimentally measured value.

Parameters	Vendor's specification	Experimentally measured values
Reflectivity	±95%	±86%
FSR	~5Å(λ=656.3 nm)	~5Å(λ=633 nm)
FWHM	~81.7mÅ(λ=656.3 nm)	~237.7mÅ(λ=633 nm)
Finesse due to Reflectivity	~61.24	~21.38
Effective Finesse	~61.73	~21.03
Surface Quality	$\lambda/50$ - $\lambda/200$ at λ= 633 nm	Flatness: $\sim \lambda/35$, Roughness: $\sim \lambda/74$

son might be helpful to interpret the observed differences between calculated and measured values. a) The measured FWHM for this FP may have been broadened by the finite bandwidth of the laser beam, resulting in decreasing of the measured effective finesse. b) If the expanded source is not perfectly collimated to feed the FP, it will result in lowering the finesse. But before feeding the collimated beam to the FP, we have used shearing interferometer to check whether the collimation is proper or not? We achieved the proper collimation using this method. Hence, we can easily rule out this reason. c) From the measured finesse, the estimated reflectivity of the FP plates is about 86%, which is not consistent with the vendor specified values. Since our FP

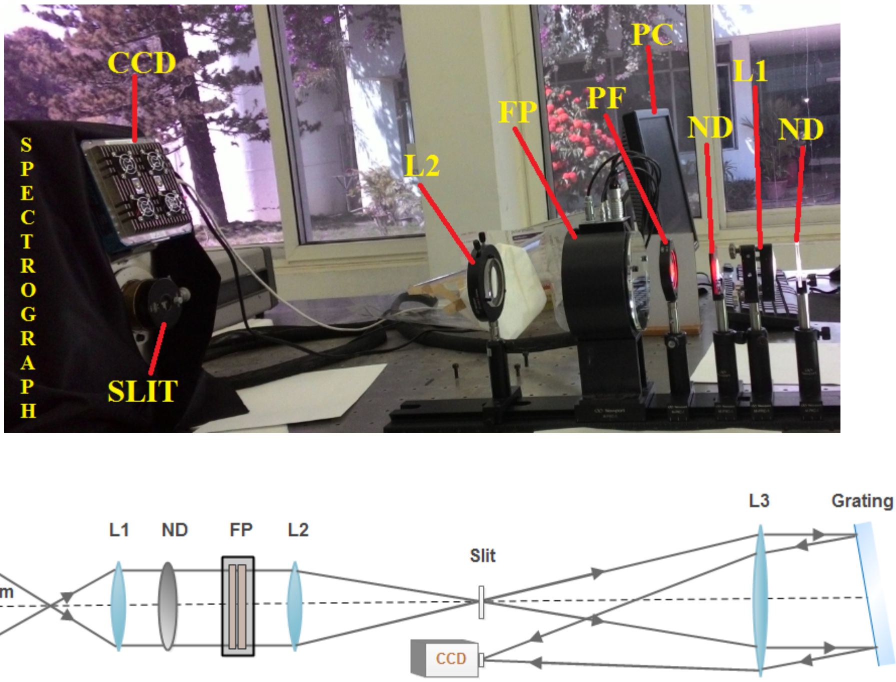

Figure 5.14: Top: A snap shot of the experimental setup placed before the spectrograph. Below: sketch of the optical set-up to characterize the FP. ND: neutral density filter, L1: collimating lens, L2: reimaging Lens and FP: Fabry-Perot interferometer.

was purchased several years ago, it is very likely that exposure to humidity and dust may have caused the gradual degradation in reflectivity over time.

5.2.3.5 FP channel spectra

It is to be noted that, a collimated set-up is preferred for characterizing the FP. The reason is that the collimated set-up is theoretically insensitive to any additional optical path length changes caused due to placing and removal of FPs depending on whether the etalons are being characterized individually or in tandem. For obtaining the channel spectra of the FP, Littrow spectrograph setup was used in conjunction with a telescope with a 15 cm clear aperture objective lens as the light feed. The schematic diagram of the spectrograph is shown in Figure 5.14. The F_{15} beam from the telescope was collimated and reimaged using lenses L1 and L2. L1 lens has diameter of 50 mm and focal length of 225 mm. The lens L2 has diameter of 60 mm and focal length of 600

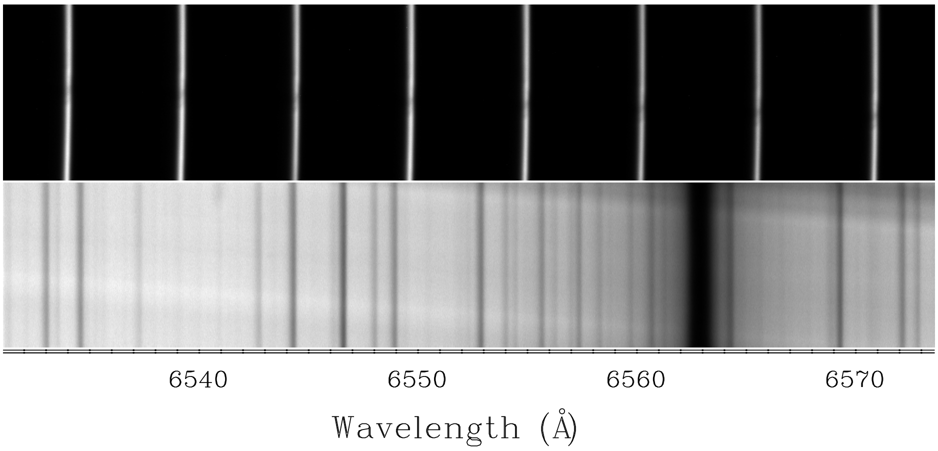

Figure 5.15: Top: Channel spectrum of FP. Bottom: Observed solar spectrum.

mm. Light passing through the slit (of width 80 μm) was collimated using a lens of focal length 1000 mm. The collimated light dispersed by a plane grating (1200 lines/mm) and reimaged using the same Littrow lens. On the CCD, the dispersion per pixel is 20.9 mÅ at 6563 Å. The spectral coverage of the spectrograph is 42.8 Å. We have used 2k × 2k CCD camera, procured from *apogee imaging system* to record the spectra. The CCD has pixel size = 7.4 μm with total imaging area 15.2 × 15.2 mm^2. The Alta F4000 CCD have a 4-megapixel interline transfer sensor with good quantum efficiency (41.5% at 400 nm) and the dynamic range 74.7 dB. The typical dark current and linear full well capacity are 0.0075 e$^-$/pixel/sec and 31,000e$^-$, respectively. The CCD can be interfaced to the PC via USB 2.0.

The FP was introduced in the collimated beam after L1. Figure 5.15 shows the channel spectra obtained with this optical setup. The bottom panel show the solar spectra which include the 6563 Å spectral line. The recorded channel spectra were analyzed to obtain the FSR and the FWHM for the FP. The central 100 pixels of the recorded spectrum were averaged in the slit direction to obtain the transmission profile of the FP. This is shown in Figure 5.16. The wavelength scale was calculated from the solar spectra, which were recorded before placing the FP in the beam path. All the channels

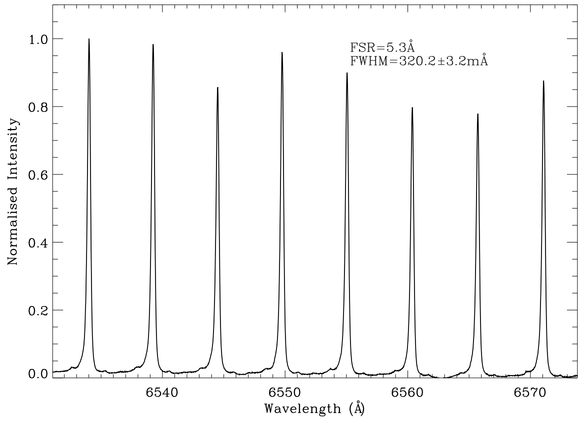

Figure 5.16: Transmission profile of the FP obtained by averaging the central 100 pixels of the recorded channel spectrum.

in the recorded channel spectrum were used to compute the mean FSR and FWHM. The measured FSR and FWHM from the transmission profile are 5.3 Å and 320.2±3.2 mÅ, respectively. Although the obtained FSR nearly matches the values obtained by experiment done using laser, the FWHM measured with the channel spectra is larger than for the previously measured values. The difference is mainly attributed to the low spectral resolution of the spectrograph due to the larger width of the slit. Theoretically calculated resolution of the spectrograph is 91 mÅ at 6563 Å. The FWHM of the spectrograph ($\delta\lambda_s$) is estimated as follows:

$$(\delta\lambda_r)^2 = (\delta\lambda_s)^2 + (\delta\lambda_c)^2 \tag{5.11}$$

Where, ($\delta\lambda_r$) is the FWHM of the recorded 6563 Å spectral line profile, ($\delta\lambda_c$) is the obtained FWHM from the BASS2000 atlas. The FWHM of the spectrograph is estimated to be about 182.6 mÅ. This higher value could be due to the larger slit width of 80 μm and also due to F_{10} beam which covers only $\frac{3}{4}$th of grating there by reducing the spectral resolution.

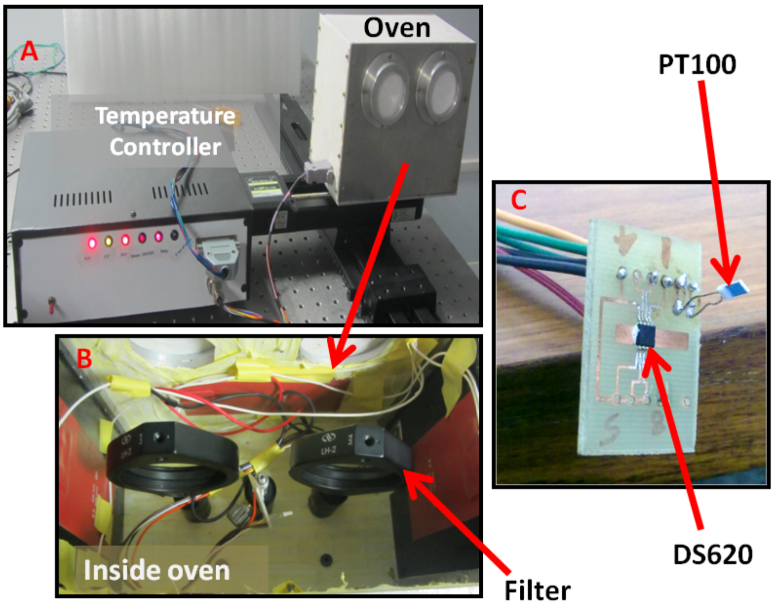

Figure 5.17: Panel A: Temperature controller and filter oven. Panel B: Inside view of the oven. The filter is kept inside this oven. Panel C: Temperature sensors DS620 and PT100, which are kept inside the oven.

5.2.4 Pre-filter

We used Hα filter centered at 6562.8 Å wavelength as a order sorting filter kept in front of FP. It is a interference filter procured from *Andover Corporation*. The central wavelength of the filter gets shifted towards lower wavelength with the increase of incident angle. Equation 5.12 implies that the central wavelength shift depending upon the angle of incidence and effective refractive index of the filter. The effective refractive index of the filter's dielectric material is 2.05. The specified temperature for the filter is 23^0C.

$$\lambda_\theta = \lambda_0 \sqrt{1 - \frac{\sin^2\theta}{n^2}} \tag{5.12}$$

Where λ_θ, λ_0 - central wavelength at an angle θ and zero, respectively. n is the effective refractive index of the dielectric material of the filter.

5.2.4.1 Temperature controller

We developed a temperature stabilized oven which can keep the filter within 0.1^0C of the set temperature in collaboration with Udaipur Solar Observatory. The oven temperature can be set between 30 and 50^0C. Figure 5.17 shows the developed temperature controller and the oven in the panel A and B, respectively. The filter is kept inside the oven during observations. Two ways of the temperature control are implemented in the oven. First one is a temperature stabilization circuit which keeps the temperature within 0.1^0C of the set temperature and second one is a safety circuit which switches-off the power to the heater in case the first stabilization circuit fails due to some reasons and the temperature crosses the preset temperature value. The circuit diagram for the overshooting cut-off and stabilization circuit are shown in panel B and C, respectively in Figure 5.18. The stabilization circuit uses a temperature sensor IC (DS620) from *Dallas Semiconductor*, which is a band-gap based temperature sensor. The wiring diagram for the DS620 is shown in Panel A (Figure 5.18). SDA and SCL pins in the IC are wired to the computer parallel port. The temperature is read out using a computer parallel port and the correction of the signal is generated through Pulse Width Modulation (PWM) and fed to the heater. The safety circuit uses a PT100 resistor connected to one arm of a Wheatstone resistor bridge to detect the threshold cross-over. Upon crossing the threshold a relay switch cut off the power to the heater until the temperature drops below the threshold (see Gupta *et al.* (2008) for details about the temperature controller). Panel C in Figure 5.17 shows the IC DS620 and PT100, which are kept inside the oven.

We have tested the performance of the temperature controller in the laboratory. Figure 5.19 shows the test results. We have set the temperature at 30^0C. Figure 5.19 (left) shows the oven temperature reached at the set temperature within 9 minutes and it maintained the temperature through out experiment. Figure 5.19 (right) shows the plot of safety cut-off temperature.

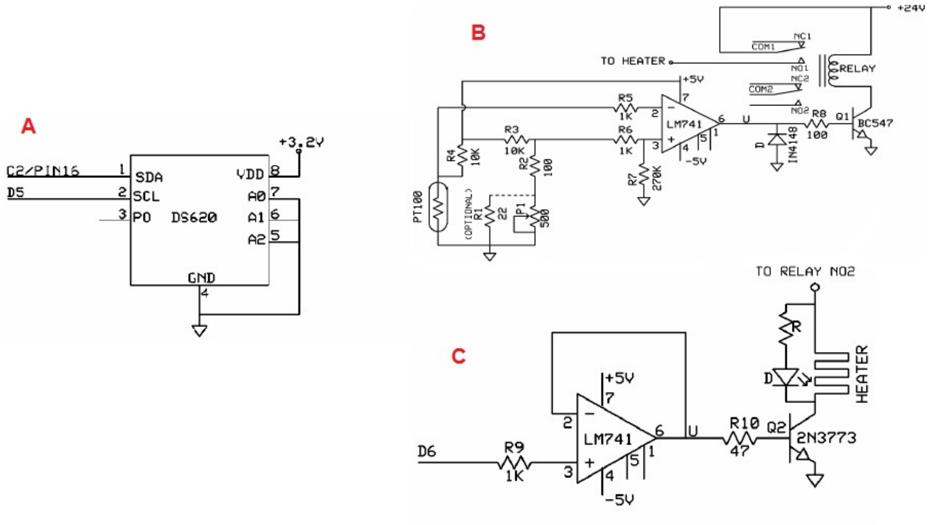

Figure 5.18: Panel A: Wiring diagram of DS620. Panel B: Overshooting cut-off circuit. Panel C: Schematic of the amplifier circuit (Courtesy of Gupta *et al.* 2008).

We have set the safety cut-off temperature at 40^0C. Upon crossing the cut-off temperature, the associated op-amp and relay circuit with PT100 switched off the power to the heater until the temperature is restored below the cut-off value.

5.2.4.2 Characterization of the pre-filter

We have also characterized the pre-filter using the spectrograph. We have used the optical setup before the spectrograph slit similar to the one used for the testing FP, as shown in Figure 5.15. The ND filter and FP were removed from the optical path and then the filter was placed in the collimated beam after the lens L1. The spectra have been obtained by placing the filter in different angle positions from 0 to 9^0 in step of 1.5^0. Figure 5.20 (top-left and right) show the obtained spectra at 0 and 4.5^0 filter positions, respectively. Hα absorption line is visible in the Figure 5.20 (top-left). We obtained the filter transmission profile at 3^0 angle position by averaging 200 pixel along y-direction of the spectrum. The normalized filter transmission profile is shown in Figure 5.20(bottom-left). The red line shows the Gaussian fitting to the measured profile. The FWHM of the filter at 3^0 angle position is

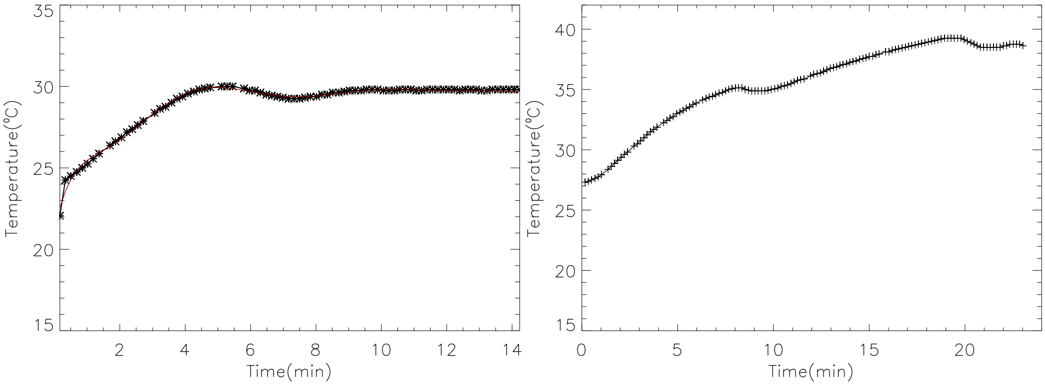

Figure 5.19: Left: Temperature vs time plot for the temperature controlled oven. Right: Temperature of the overshooting safety control unit is plotted as a function of time.

found to be 2.33±0.01 Å. We obtained the transmission profiles of the filter at different angle positions and fitted with Gaussian profile to obtain the peak transmission wavelength of the filter. Figure 5.20 (bottom-right) shows the variations of the measured peak transmission wavelength with different angle positions. The red curve shows the calculated peak transmission wavelength at different angle positions using the eq. 5.12. The central wavelength of the filter transmission peak gets blue shifted from 6563 to 6545 Å wavelength with the increase of incident angle from 0 to 9^0. The small deviation of the calculated and measured peak transmission wavelengths is due to the placing of the filter at different angles, which is within $\pm 0.5^0$ error.

5.2.5 Fabry-Perot interferometer in combination with the pre-filter

In the NBI setup, one FP kept in tandem with order sorting interference filter in narrow band imager (see Figure 5.1). If two such optical filters are kept in series then the resulting instrumental profile $I(\lambda)$ is obtained by (Cavallini, 2006; Ravindra and Banyal, 2010),

$$I(\lambda) = I_{PF}(\lambda) \cdot I_{FP}(\lambda) \tag{5.13}$$

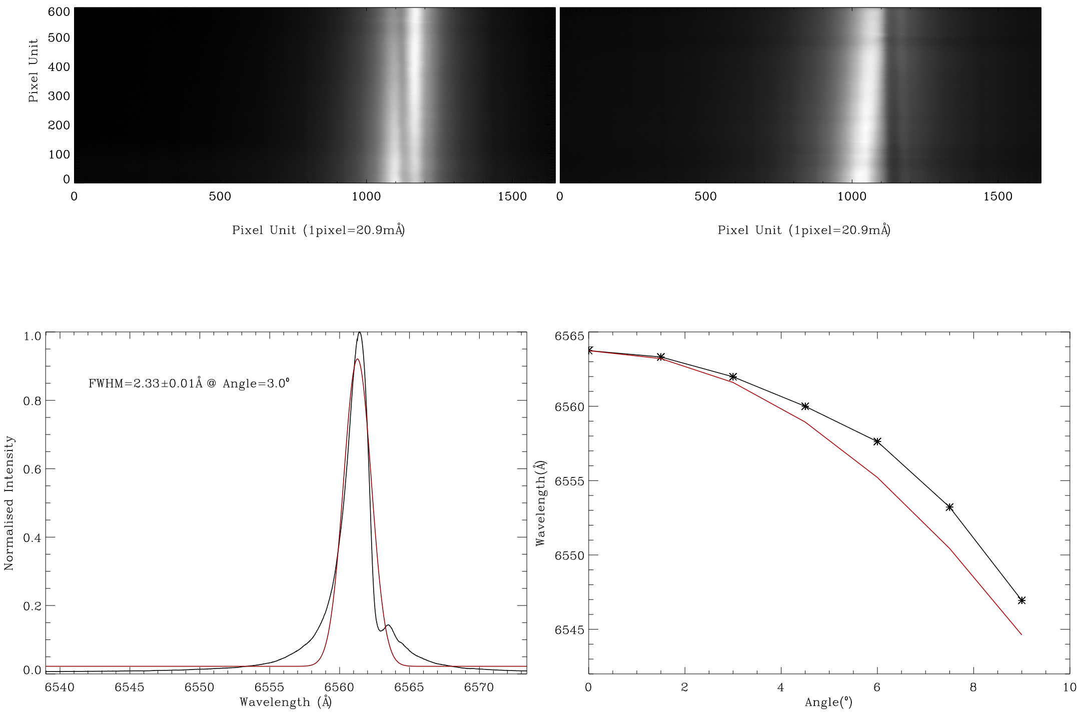

Figure 5.20: Top-Left: Observed Spectrum taken while filter is at 0^0 angle position. Hα absorption line is visible inside filter transmission. Top- Right: Observed spectrum taken while filter is kept at 3^0 angle position. Bottom-Left: Transmission profile of the filter at 3^0 angle position. It has been obtained by averaging along the y-direction of top-right image. The red line shows Gaussian fitting to the measured intensity profile. Bottom-Right: The black line shows the measured peak transmission of the filter at different angle position and red line shows the estimated values for the same using eq. 5.12.

where, $I_{PF}(\lambda)$ and $I_{FP}(\lambda)$ is the transmission of the order sorting filter and FP, respectively. In estimating the transmission profile of the NBI we have used the spacing of the FP as 0.4 mm with a plate reflectivity of 85% and the FWHM of the interference filter 2.3 Å. The FP and pre-fiter kept in tandem in a collimated beam. The red curve in Figure 5.21 shows theoretically estimated transmission profile of the FP in combination with a pre-filter. As the pre-filter is an interference filter, we assumed the profile of the pre-filter as Lorentzian (Cavallini, 2006), which can be expressed as

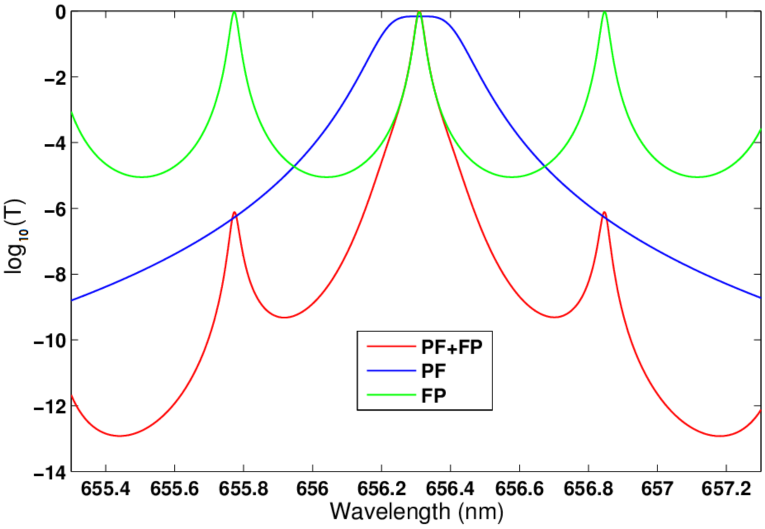

Figure 5.21: The red curve shows the transmission profile of the FP in combination with a pre-filter (pass band 2.3 Å). The green and blue curves shows the transmission profiles of the FP and pre-filter, respectively.

$$I_{IF}(\lambda) = \frac{\tau_{IF}}{1 + (\frac{2\Delta\lambda}{FWHM_{IF}})^{2n}} \tag{5.14}$$

where, n is the number of cavities, $\Delta\lambda$ is the wavelength separation from the transparency peak and τ_{IF} is the peak transparency of the filter. The green and blue curves shows the transmission profiles of the FP and pre-filter, respectively. From the combined transmission profile it is clear that the out of band rejection is large out side the pre-filter profile.

We have also done the experiment to see the out of band rejection and recorded the FP channel spectra by keeping the pre-filter and FP in a collimated beam configuration using the optical setup shown in Figure 5.14. The channel spectra is shown in the top panel of Figure 5.22. The bottom panel shows the the observed solar spectra using the pre-filter, while FP is removed from the optical path. The position of the channel spectra can be shifted by changing the plate separation of the FP and obtain the images at different wavelength positions.

When the FP is mounted in a collimated setup, a wavelength gradient will be developed across the FOV of the interest. In this set up the FP is

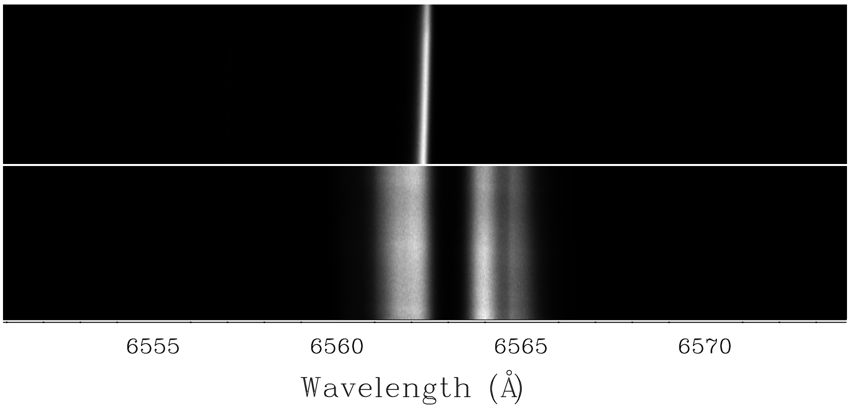

Figure 5.22: Top panel shows the channel spectra of the FP in combination with pre-filter using the optical setup as show in Figure 5.14. Bottom panel shows the observed solar spectra using only the pre-filter (Figure 5.14), while FP is removed from the optical path.

mounted close to the image of the telescope's entrance pupil. Every point on the image will subtend certain angle with respect to the optical axis of the FP and hence experiences different plate separations for each image point. This will develop a wavelength gradient across the FOV and the wavelength shifts radially towards the blue, from the center to the edge of the field. The shift in the wavelength due to the angle of incidence is given by well-known equation (Cavallini, 2006; Ravindra and Banyal, 2010),

$$\delta\lambda_\theta = -\frac{\lambda}{2}\frac{\theta^2}{\mu^2} \tag{5.15}$$

where θ is the angle of incidence. The maximum angle of incidence can be obtained as

$$\theta = FOV_{1/2}\frac{A_{telescope}}{A_{fp}} \tag{5.16}$$

where, $FOV_{1/2}$ is the half diagonal of FOV. $A_{telescope}$ and A_{fp} are the aperture of the telescope and FP, respectively. In our NBI set up (Figure 5.1), the FP is mounted in a slowly converging beam. The diameter of the objective

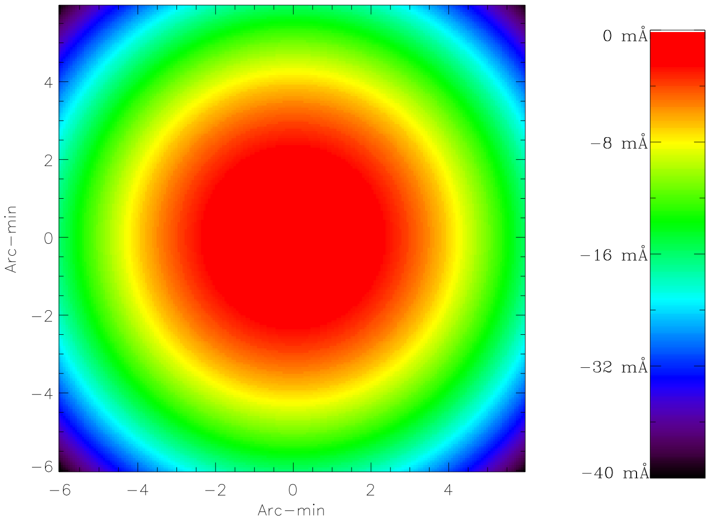

Figure 5.23: Surface plot of the wavelength gradient developed across the FOV in the FP.

lens (L1) was used 100 mm during observations and finally, F_{75} beam was created at the imaging plane on CCD. The image size of the Sun at this imaging plane is 70 mm. Assuming this as a collimating set up, we have calculated the wavelength gradient plot over the 12′ FOV for the central wavelength 6562.8 Å. The plot is shown in Figure 5.23. One can see the calculated maximum wavelength shift towards edge is around -40 mÅ, which is much less than the passband of the NBI system.

5.3 Preliminary Observations

After testing the FP, we have used it as a main component for developing narrow band imager (NBI). The schematic layout of the NBI is shown in Figure 5.1. The NBI system is setup in the laboratory of IIA, Bangalore campus. The pre-filter centered on 6562.8 Å was placed before the FP to select the desired wavelength channel for observations. A series of images were obtained by tuning the plate separation of FP across different wavelength positions on the Hα spectral line. Figure 5.24 shows the images taken on different days in the line center at 6563 Å. Top-left panel in the figure shows the image of active regions NOAA 11960 and NOAA 11959 and a quiet filament taken using the NBI. These two sunspots (NOAA 11960 and NOAA 11959) were visible on the southern hemisphere of the Sun from 19th January to 29th January, 2014 and they were associated with series of C-class flares. We have observed these sunspot regions on 22nd January, 2014 and is shown in Figure 5.24 (top-left). This image is compared with the image taken from *Global Oscillation Network Group* (GONG) observed in the $H\alpha$ wavelength taken close to the time of our observations (top-right). Clearly, both images show the sunspots and filament structure. The contrast of the filament is better in the FP based NBI image compared to the GONG. This is because of very narrow passband of the NBI filter compared to the GONG, which is about 0.4 Å (Harvey *et al.*, 2011). Middle-left and right images in Figure 5.24 show the image taken using the NBI and GONG for a quiet region filament, respectively on 26 February 2015. It was a very long filament and the size is about 750 Mm, which covers almost half the diameter of the Sun. This filament was visible on the solar disk from 22nd February to 2nd March 2015. We have observed the part of the filament on 26 February 2015 (shown in Figure 5.24 (middle-left)). Bottom-left and right panel in Figure 5.24 show the image of active region NOAA 12297 on 10 March 2015 using the NBI and GONG, respectively. In both the images, one can see dark sunspot surrounded by bright patches and a large quiet filament structure. This sunspot appeared on the solar disk at S17 E53 on 8th March 2015 and it was visible on the solar disk for next 10 days. This sunspot region was associated with series of C and M-class flare. We have observed this region for few days. In the NBI images we see more structures compared to the GONG image.

Images acquired at different wavelength positions on the line profile are shown in Figure 5.25. The images were obtained from 792 mÅ on the blue wing of the spectrum to 616 mÅ on the red wing away from the Hα line center, with a step size of 88 mÅ. After the dark current correction and flat

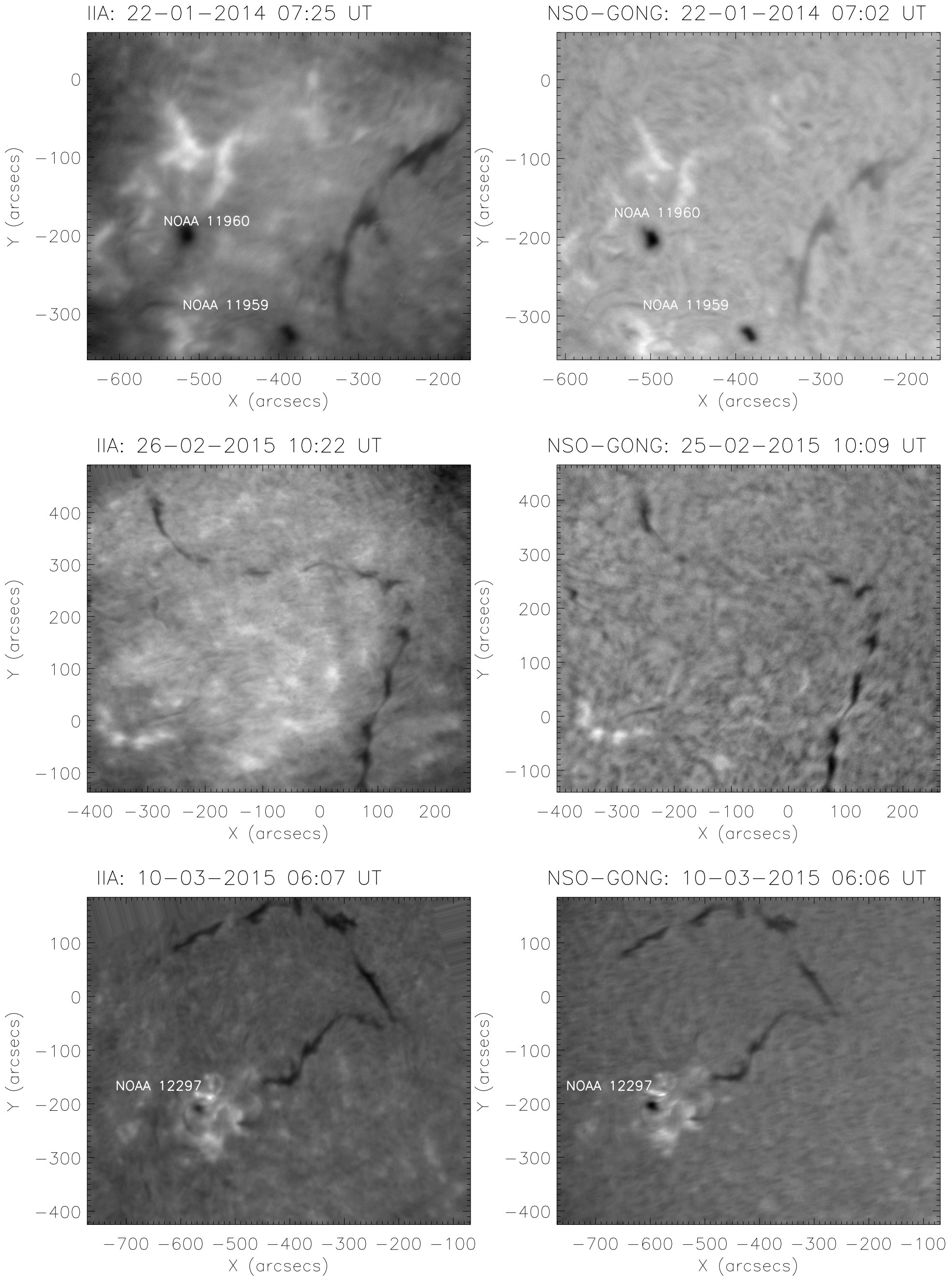

Figure 5.24: Left: top, middle and bottom panels show the observed filaments on different days using NBI at the Hα line core positions. Right: top, middle and bottom panels show the observed filaments on the same days close to the time of observations of left side panel obtained from NSO-GONG.

fielding, the images are shown here. In Figure 5.25 top-panel show the images obtained at different wavelength positions for the active region NOAA 11949. This sunspot was located at S17W46 on 17th January 2014. Two filament structures are visible in the line center and close to line center images, as shown by the two arrows. It should be kept in mind here that the quality of these images is affected by the poor seeing conditions at the Bangalore. The image is acquired with field of view $12.6'$ and has pixel resolution $0.37''$. We have also performed the spectral line scan for another active region NOAA 12297 on 10th March 2015. This active region was located at S16E26. The observed images at different wavelength positions are shown in Figure 5.25 (bottom-panel). We have constructed the Hα spectral line profile from the scanned images after dark current correction and flat fielding. The flat fields were taken at each wavelength positions on the line profile. We have calculated the mean intensity of 100×100 pixel^2 from the quiet part of the Sun to retrieve the line profile. Figure 5.26 shows the obtained mean intensity at different wavelength positions. We have fitted the higher order polynomial to construct the Hα absorption line profile. The red curve shows the polynomial fitting to the mean intensity. One can see the line profile could not be constructed completely. This could be due to small passband of the pre-filter.

5.3.1 Dopplergram

To study the line-of-sight velocity of solar features, Doppler shifts of the spectral lines are regularly used. The Doppler shift of the spectral line λ for a defined velocity v is calculated by using the relation

$$\frac{\Delta\lambda}{\lambda} = \frac{v}{c} \tag{5.17}$$

where c is the speed of light. In order to compute the Doppler velocity map, information of the line center and computed shift of wavelength from the line center is required. This can be done only if the simultaneous spectral line

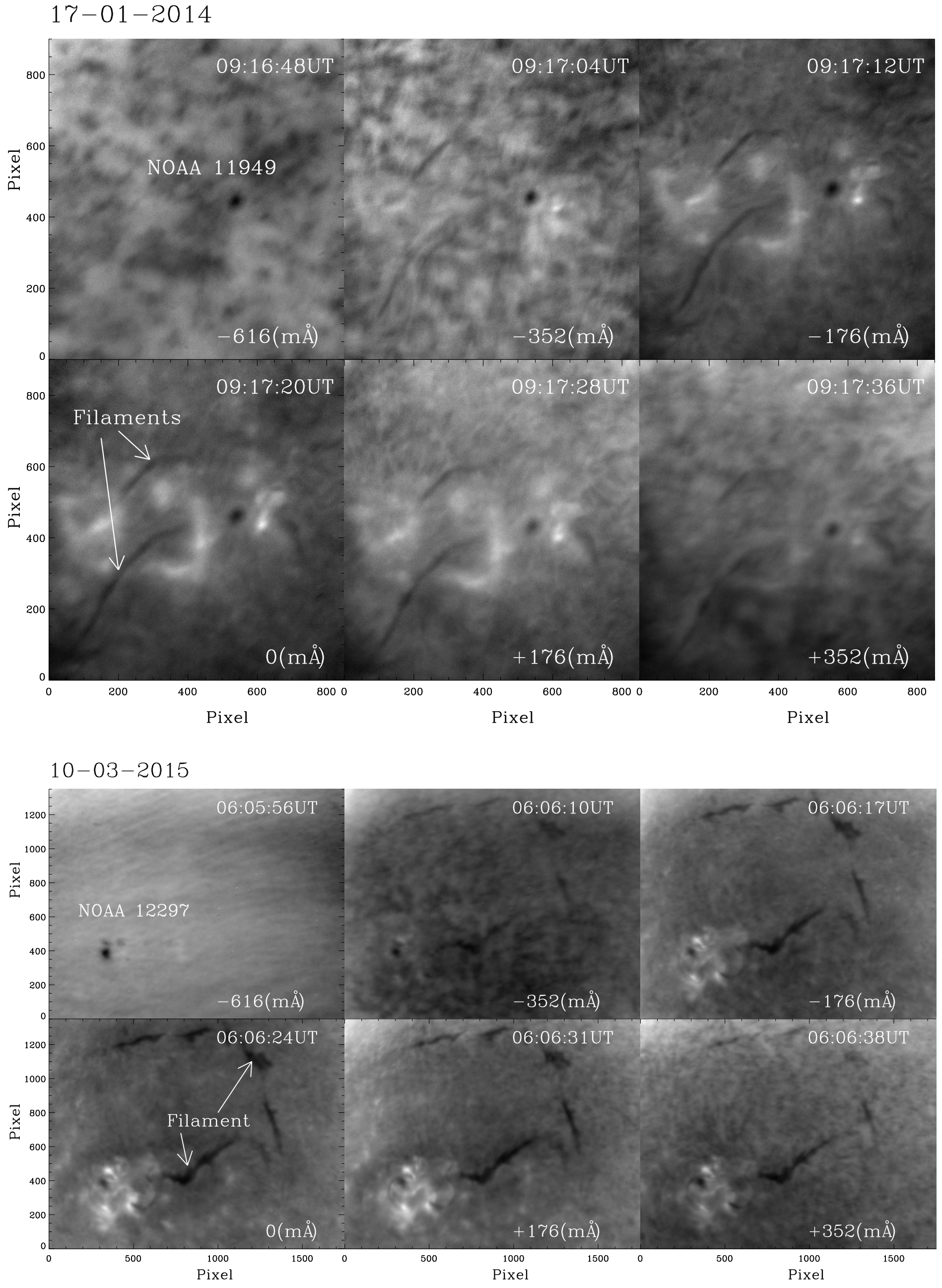

Figure 5.25: Images obtained at the different wavelength positions of the Hα 6563 Å line profile. The images have resolution $0.37''$/pixel. Top panel images are taken on 17th January 2014 for the active region NOAA 11949 and bottom panel images are taken on 10th March 2015 for the active region NOAA 12297.

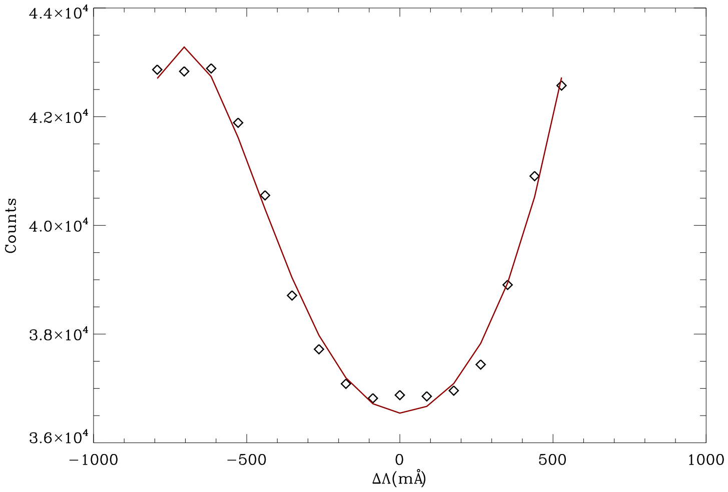

Figure 5.26: Constructed line profiles at 6563 Å from the observations. The line profile is scanned at 18 wavelength positions from -792 mÅ to +616 mÅ with a step of 88 mÅ.

data for the same region is available (one from the spectrograph and other from NBI).

Alternatively, using FP based tunable narrow band imager one can make the Doppler velocity maps by using the red- and blue-wing intensity images of a chosen spectral line. Intensity at a fixed wavelength point in the blue and red wing of any spectral line varies depending on the Doppler shift. Hence, from the intensity difference between the red- and blue-wing images, one can estimate the Doppler shift and hence the Doppler velocity at a fixed wavelength position. For small shift in line profile, one may assume the solar spectral line to be linear as well as symmetric, Doppler velocities are estimated by using the following relation:

$$v = K\frac{I_r - I_b}{I_r + I_b} \tag{5.18}$$

Where, I_r and I_b are the intensity images at red wing and blue wing of a spectral line. K is a calibration constant which depends on the chosen spectral line and the spectral resolution (Padinhatteeri, Sridharan, and Sankarasubramanian, 2010; Rimmele, 2004; Stix, 2004). The denominator in eq. 5.18

corrects the intensity variations. I_r and I_b can be expressed as

$$\begin{aligned} I_r &= I + \frac{dI}{d\lambda}\Delta\lambda \\ I_b &= I - \frac{dI}{d\lambda}\Delta\lambda \end{aligned} \tag{5.19}$$

Where, I is the photometric signal at the spectral line core position and dI represents the variations of signal with wavelength variation $d\lambda$ from the central wavelength λ. By combining the eq. 5.17 and eq. 5.19, we can get

$$\begin{aligned} \frac{I_r - I_b}{I_r + I_b} &= \frac{\frac{dI}{d\lambda}}{I}\frac{\lambda v}{c} \\ v &= \frac{Ic}{\lambda\frac{dI}{d\lambda}}\frac{I_r - I_b}{I_r + I_b} \end{aligned} \tag{5.20}$$

By comparing the eq. 5.18 and eq. 5.20, one can obtain the calibration constant K as

$$K = \frac{c}{\lambda} I \frac{d\lambda}{dI} \tag{5.21}$$

If we plot, the variations of $\frac{dI}{I}$ against $\frac{d\lambda}{\lambda}$, the slope of the graph will equal to $\frac{c}{K}$. To estimate the calibration constant K, we have taken Hα spectral profile from solar atlas *BASS 2000* (*http://bass2000.obspm.fr/*). We have used 240 mÅ FWHM of our narrow band imager. The spectral line is convolved with the instrumental profile. The convolved spectral line is then shifted by an amount of $d\lambda$ and the normalized intensity difference ($\frac{dI}{I}$) is calculated. We have repeated this exercise for a range of velocities. Figure 5.27 shows the variations of $\frac{dI}{I}$ as a function of $\frac{d\lambda}{\lambda}$. The linear part of the curve is fitted with a straight line (solid line) and c/slope provides the calibration constant value K. The calculated value of K is 56.5±0.1km/s.

To generate the dopplergrams, we have carried out observations using

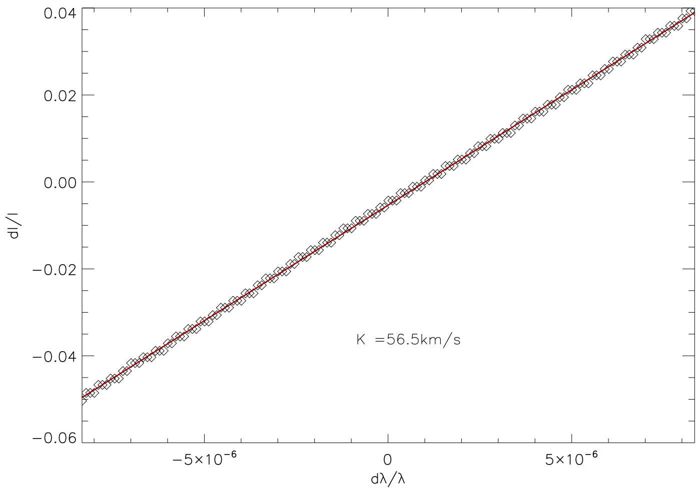

Figure 5.27: The normalized intensity difference versus $\frac{d\lambda}{\lambda}$ curve computed for the spectral line Hα 6562.8 Å. The solid line shows the straight line fit to the computed values.

our narrow band imager. We have obtained the blue and red wing images at ±176 mÅ wavelength positions, respectively away from the line center (6562.8 Å) of the Hα spectral line. The dopplergrams have been generated using eq. 5.18. Figure 5.28 (right panel) shows the obtained dopplergrams for a small field of view at chromospheric height for a quiet-Sun region. The left-side panels show the images taken at Hα line core wavelength position (6562.8 Å) for the same region. One can see a quiet filament structure is visible in the image. The white contour of the filament is overlaid on the dopplergram to locate its position. This filament was visible on the southern hemisphere of the Sun from 9th March to 16th March 2015. On 10th March, the location of the filament was at (-400$''$, -500$''$) and it was 180 Mm long. Along the spine of the filament we observed a blue shift. The maximum and minimum line-of-sight velocities are shown by the colour bar in images. By analyzing the doppler velocity maps, we found that redshifts appeared near the east end of the filament. We also generated the dopplergram for the active region NOAA 12297 and its surrounding region on 10th and 11th March, 2015. On 10th March, the active region was located at S19 E26. The angle subtended by the solar disk center and the active region is 32^0. The

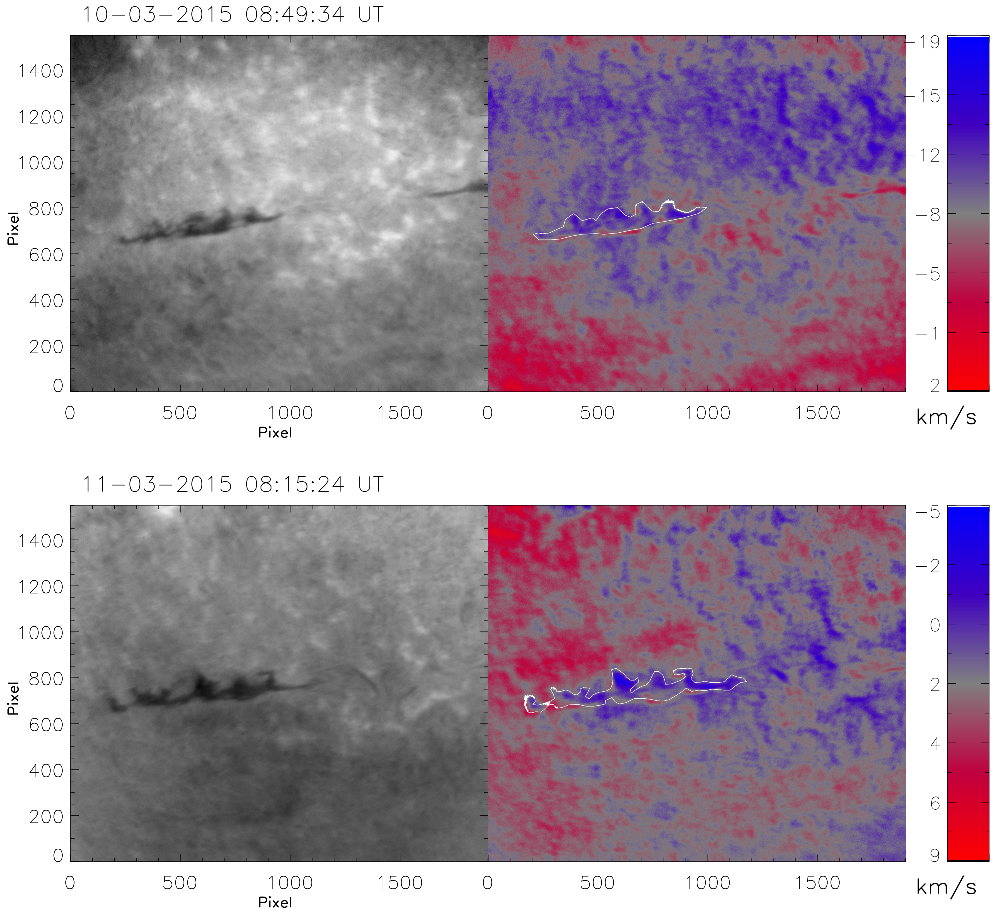

Figure 5.28: Left: top and bottom panel show the images taken at Hα line core position (6562.8 Å) for the quiet Sun filament region on 10th and 11th March 2015, respectively. Right: images show the corresponding generated dopplergrams at the chromospheric height. The filament contour is overlaid on the dopplergram.

maximum and minimum velocities along the line-of-sight (LOS) in the field of view of our observations are +5 km/s and −16 km/s, respectively, as shown in Figure 5.29. In the periphery of the filament of the same dopplergram, one can see blue and red-shift of LOS velocity. These maps appear similar to the one reported by Joshi *et al.* (2015). In this case, the true maximum and minimum velocities along the LOS in the spine of the filament are about +5.8 km/s ($= 5/\text{Cos}\ 32^0$) and −18.8 km/s ($= -\ 16/\text{Cos}\ 32^0$), respectively. We have observed the same filament for two more days and no significant change in the filament structure observed. Hence from our observations, we can infer

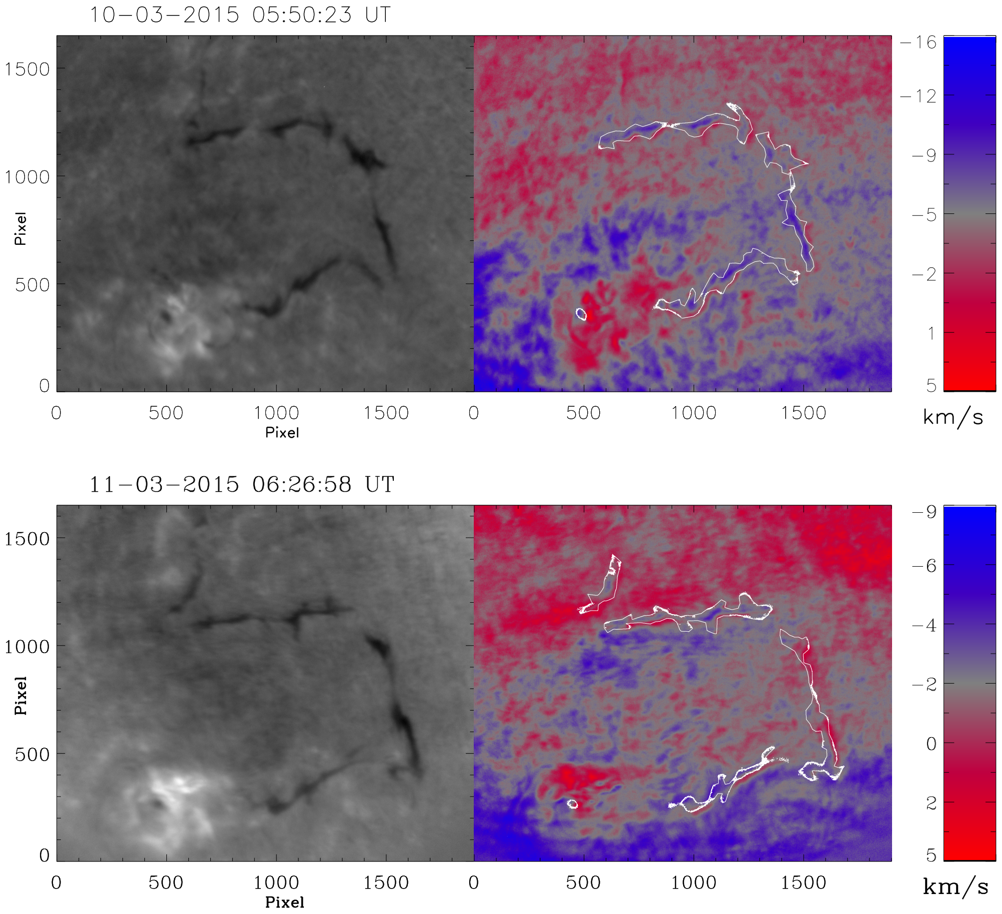

Figure 5.29: Left: top and bottom panel show the images taken at Hα line core position (6562.8 Å) for the active region NOAA 12297 on 10th and 11th March 2015, respectively. Right: images show the corresponding generated dopplergrams at the chromospheric height. The filaments and sunspot contours are overlaid on the dopplergram.

that the observed blueshift and reshift at the periphery of the filament as the downflows and upflows, respectively across the filament spine.

5.4 Discussions

We have developed single FP based narrow band imager at the Indian Institute of Astrophysics, Bangalore. We have tested each of the optical components at the laboratory for its parameter value and compared it with the vender specified parameters. Most of the observed parameters compare well with the vender's specifications with few deviations in some cases. This is mostly because of the reduced reflectivity of our FP over the time. We have tested the NBI system in the laboratory and finally we have made several days of solar observations. We have also scanned the Hα line profile and obtained the images at each positions. We compared our images with the GONG Hα images and found the features are matching well in both the images. In future, we will install this NBI system in the Kodaikanal Tunnel Telescope for regular observation of solar filaments.

A step further we have also made the dopplergrams by making the observations in the blue and red wing of the Hα spectral line. The Hα line center forms at the upper chromosphere and the wing forms from the photosphere to chromosphere. There are a few more ways to produce the dopplergrams (Joshi, 2011). Unlike the other methods in the present procedure we need the intensity only in two positions on the line profile-one in the red and another one in blue wing. using this method we can produce dopplergrams at high cadence. At present there is no chromospheric dopplergrams available on regular basis. Hence we cannot make a detailed comparison of the developed dopplergrams with the other data. However, we find some similarity in velocity patterns in and around the filament regions with the velocity maps produced by Joshi *et al.* (2015). In future, we would like to compare the dopplergrams made in the Hα from the Kodaikanal observatory using the Lyot filters.

The spectral resolution of a single FP based narrow band imager directly proportional to the separation between the two plates of the FP. To get better spectral resolution one needs to increase the plate separation. But at the same time the parasitic light from the out of band will increase due to the reduced FSR. Hence, it is difficult to optimize between FSR and desired spectral resolution. To overcome this problem, one can use either Fabry-Perot etalon in double-pass configuration (e.g., Álvarez-Herrero *et al.* 2006) or two FPs in tandem (e.g., Cavallini 2006). In future, we would like to develop a dual

FP based narrow band imager at the Indian Institute of Astrophysics, which will have spectral resolution 40 mÅ or better and FSR of the system will be sufficiently large to reduce parasitic light from the out of band from the desired spectral line. In the next chapter of this thesis, I have discussed about the preliminary design of a dual FP based narrow band imager, which will be used for the proposed National Large Solar Telescope (NLST; Hasan *et al.* 2010a).

Chapter 6

Summary, Conclusions and Future Works

In this thesis, I studied the solar filament eruption and given the explanation based on the observations and theory in detail. Few case studies are presented. Attempts have been made to understand and explain the eruption mechanism using multi-wavelength observations. The first chapter introduces the topic of my research, discusses the related studies of filament eruptions conducted in the past, and also describes some of the unsolved problems. Here, I will summarize the major results reported in four chapters. Later I will briefly describe a few directions in which I would like to continue my work in future.

6.1 Major Results

6.1.1 Two-phase filament eruption in association with flux cancellations and coronal loop dynamics

In this chapter, I have presented the results on the filament eruptions associated with the active region NOAA 11444 using space-based data. The filament has erupted in two different phases. During the first phase of filament activation, we observed a converging motion between opposite-polarity regions for few hours near the PIL. Cancellation of the magnetic flux was also observed at the same location followed by transient brightenings related to the idea of runaway tether-cutting mechanism, which could eventually destabilized the bottom filament in the first phase of eruption and pushed the top filament to little higher heights. Afterwards, the top filament showed a slow rise, followed by the bright flows and it eventually erupted during the flare. Later, the postflare loops over the filament in the western side were observed to be contracting. The coronal loops in eastern side were seen to be expanding towards higher heights. At the same location, we observed the magnetic flux cancellations. A brightened cusp shaped loop was observed near the east end of the filament due to the reconnection between the expanding loops and the overlying loops. At the same time we have also observed another set of loops collapsing in the west end of the filament. Our results suggest that the first phase of filament eruption occurred due to the decreasing of the tension under the loops, caused by the magnetic flux cancellation and reconnection occurring first under the bottom of the loop and then at higher level. The second phase of eruption is also due to the magnetic flux cancellations. The brightened cusp shaped coronal loops near the east end of the filament is the result of reconnection at coronal height, which could have removed a sufficient amount of overlying magnetic flux. Thus, it could have made an opening for filament to expand and finally leading towards eruption. We observed the contracting and falling back of the coronal loops near western side of the filament, which could be due to the decrease in magnetic pressure after the reconnection.

6.1.2 An active region filament eruption associated with rotational motion near footpoints

In the third chapter, I have investigated another active region filament eruption occurred in the southern hemisphere of the Sun on 08 July 2011 using *HMI* and *AIA*/SDO data. During observations, the magnetic flux was emerging in the active region and also in the plage regions. The flux emergence was stopped in West-most footpoint of the plage region about an hour before the filament eruption. The new magnetic flux emergence with opposite magnetic sign can destabilize the filament by decreasing the magnetic tension of the overlying field (Wang and Sheeley, 1999). The filament had left-handed twist and the net injected magnetic helicity was positive in Eastern footpoint. Both signs of magnetic helicity were observed in the Western footpoint of the filament where the eruption has initiated. The coexistence of opposite helicity flux could cause a reconnection while merging of different helicity flux system takes place, as numerically simulated by Kusano *et al.* (2003, 2004). The reconnection in the system can reduce the tension of the overlying field and thereby pushing the filament to higher heights in the corona, where the torus instability can set in and finally drive the filament eruption (Aulanier *et al.*, 2010; Démoulin and Aulanier, 2010; Zuccarello *et al.*, 2012).

As an interesting phenomena, we observed an anti-clockwise rotational motion in both the ends of the filament when the eruption had just set in. This rotational motion was lasted for 6 min during the eruption process. After the filament activation, there will be an axial expansion of the filament flux rope. If the footpoint of the flux rope is still anchored to the photosphere, the expansion of the filament flux rope usually leads to the torque imbalance between the photospheric footpoints and the coronal counter part of the expanded flux rope. Hence, as a immediate consequence of the torque imbalance there will be a generation of the shear flows at the photospheric footpoints (Jockers, 1978; Parker, 1974). We believe that the torque imbalance between the expanded portion of the flux tube and the photosphere could have caused the rotation in the footpoint region. However, there could be other reasons for the observed rotation in filament footpoints and are explained in the summary of next chapter. The rotational motion was no longer persisted after the footpoints were detached from the photosphere.

6.1.3 Photospheric vortical motions during active region filament eruption

In this chapter, I have analyzed several erupting active region filaments at different times during Solar Cycle 24 and searched for the rotational motions in and around the end points of these filaments. The photospheric dopplergram data from HMI/SDO have been used for each event for about six hours covering the whole event of filament eruption. We have observed the rotational/vortical motion in the photosphere near the ends of the filaments during their initial phase of eruption, at the onset of the fast rise phase. The photospheric vortical motions we observed are about supergranulation size and lasted for 4–29 minutes. In the vicinity of the conjugate ends of the filament the direction of rotation was opposite. The observed photospheric rotational motion near the ends of the filament could possibly be resulting from the photospheric or subphotospheric shearing flows. We observed that the fast rise of the filament was initiated during/after the vortical motion of the plasma had set in. The spatial correlation between the observed end points of the filament and the location of the rotational motion and the temporal coincidence of the rotational motions with the filament eruption time signifies that this is not due to something what is seen normally in the vertices of the supergranulations (Innes *et al.*, 2009). When the filament starts to erupt, it expands axially towards higher heights. The immediate consequence of the deformation of the axial component of the magnetic field in the flux rope is the launch of a shear Alfven waves by shearing its footpoints (by the Lorentz force) that in turn carry the axial component of the flux into the expanded portion of the flux rope (Manchester *et al.*, 2004). Our study suggest that the sudden onset of a large photospheric vortex motion could have played a role in destabilizing the filament by transporting axial flux into the activated filament thereby increasing the outward magnetic pressure in it. The tendency of the outward directed magnetic pressure will push the flux rope slowly to higher heights. Once the top of the flux rope reaches a critical height where the torus instability criteria are satisfied then the flux rope becomes unstable and eventually it could have caused the filament instability and eruption (Kliem and Török, 2006).

6.1.4 Development of a Fabry-Pérot based Narrow Band Imager

Panasenco *et al.* (2011, 2013) observed rotational motion of the prominence legs in the chromosphere during its eruption. When a filament erupts non-radially, the top of its axis bends first to one side and propagates the rolling motion into sideways, known as the *roll effect* which results in a large scale twists in both legs of erupting filaments. One can study such events with narrow band imager, capable of producing dopplergrams. The chromospheric dopplergrams of the erupting filament and simultaneous photospheric LCT velocities can help us to understand what is causing the rotational motion observed in the footpoint of the filament. Hence a narrow band imager is required which can produce the dopplergram of the chromosphere for this study. In this chapter of the thesis, I described about the development of narrow band imager, which we have developed using an air gap based Fabry-Perot interferometer at the Indian Institute of Astrophysics, Bangalore. A detailed technical description of the NBI system including lab test results of individual components and some initial observations carried out with this instrument are presented here. Narrow band imaging is achieved by using Fabry-Perot interferometer working in combination with an order sorting pre-filter. The NBI can be tuned to different wavelength position on the line profile by changing the plates separation of the FP. The developed NBI is used to observe the solar filament in Hα wavelength. The instrument is capable of imaging the sun at chromospheric height and it is also able to scan the Hα spectral line profile at different wavelength positions, thereby able to observe the sun from photosphere to chromosphere. We have made a few Doppler velocity maps at chromospheric height by taking the blue and red wing images at ±176 mÅ wavelength positions, respectively away from the line center of the spectral line (Padinhatteeri, Sridharan, and Sankarasubramanian, 2010; Rimmele, 2004; Stix, 2004). In the periphery of the filament of the same dopplergram, we observed blue and red-shift of LOS velocity, similar to the velocity maps shown by Joshi *et al.* (2015). We could not make a detailed comparison of the developed dopplergrams with the other data due to unavailability of chromospheric dopplergram on regular basis. In future, we would like to install this NBI in Kodaikanal observatory to produce the dopplergrams on regular basis and compare with the chormospheric dopplergrams made in the Hα using the Lyot filter available at the Kodaikanal Observatory.

6.2 Future Directions

In this thesis I made an attempt to show that eruption mechanisms are different for each filament eruptions. Broadly speaking, the filament destabilization is related to either the flux cancellation or emergence in the photosphere. In both of my observations, I found that mostly filament eruption is associated with the converging motion and subsequent flux cancellation/emergence near the footpoints of the filament or in PIL. However, a few question still remains unsolved about how the filaments are accelerated and eventually disappear, which prompt us to carry this work forward. Some of the possible future directions are explained here.

Our study suggests that in each filament event the onset of trigger and instability mechanism could be different. In one event (discussed in chapter 3), we concluded that the progress of events towards eruption, is broadly consistent with flux cancellation, that subsequently erupts due to onset of a runaway tether cutting magnetic reconnection. In other event (discussed in chapter 4), we found that the emerging flux, converging motion and injection of opposite magnetic helicity could be responsible for destabilizing of the filament leading towards its eruption. The increasing spatial resolution in the EUV wavelength and high temporal cadence observations provided a good data to study the different filament eruption events in details. In future, we plan to study more filament eruption events statistically to understand the trigger mechanisms behind a broad range of eruption events from a large pool of space based data observed by the AIA telescope and ground based Hα data provided by GONG and Kodaikanal Hα telescope.

To observe the photosphere and chromosphere of the Sun near simultaneously and to study the rotational motion near the end of solar filaments and also to find the speed of the erupted prominences/filaments, we have developed a NBI system using FP. It is needed to look for the rotational motion at the legs of the filaments and associated changes in the magnetic helicity after the onset of filament eruption statistically. There could be a correlation between the chirality of the filament and the direction of the rolling motion observed in the erupting filament (e.g., Martin 2003b; Panasenco *et al.* 2011). In future, we plan to study the rotational motion in the legs of a large number of active region erupting filaments using spectroscopic technique both in the photospheric and chromospheric height simultaneously along with their sign of chirality using vector magnetic field measurements. This may provide the important informations about the rotational motion which could be a cause or effect of filament eruption. Hence, in future we are planning for more observations from the NBI instrument for the erupting filaments/prominences to produce dopplergrams at chromospheric height.

The spectral resolution of the single FP based NBI system is small. Using two or more FPs in tandem one can increase the spectral resolution of the imaging system as has been done in IBIS (Cavallini, 2006; Reardon and Cavallini, 2008) and TESOS (Tritschler, Bellot Rubio, and Kentischer, 2004). At the Indian Institute of Astrophysics we have designed dual Fabry-Perot based narrow band imager, which will be a good exercise to develop a narrow band imager as a back-end instrument for National Large Solar Telescope (NLST: Hasan *et al.* 2010a) or any existing telescopes at Kodaikanal Observatory in future. Using this instrument we will be able to study the dynamics of the filaments both in the photosphere and chromosphere near simultaneously at very high spectral resolution. In the next section, I will discuss about the preliminary design and required specification about this instrument.

6.2.1 Dual Fabry-Perot based narrow band imager

When the FPs are used in tandem, the system has better performance than just a single FP. In this case the unwanted side interference orders will be suppressed and the spectral resolving power will also increase. But using this complicated system, the overall throughput of the system decreases. To scan Hα spectral line, we would like to have: (1) high spectral resolution ($\sim$40 mÅ), (2) large spectral range (5000Å–8600Å), (3) large field-of-view ($\sim$4 - 5 arc-min, at least to cover the sunspot as a whole), (4) high transmission throughput to have sufficient light, (5) fast tunning rate ($\geq$ 10 pm/ms), (6) good wavelength stability ($\leq$ 10 mÅ/hr), and (7) minimum stray light. Hence, we preferred a dual FP system rather than triple or more. In this proposed narrow band imager, there are two FPs kept in tandem with the narrow bandpass order sorting interference filter (IF) in a collimated beam. If $I_{IF}(\lambda)$ and $I_i(\lambda)$ are the transmission profiles of the IF and i-th FP, one can obtain the resulted instrumental profile $I(\lambda)$ as

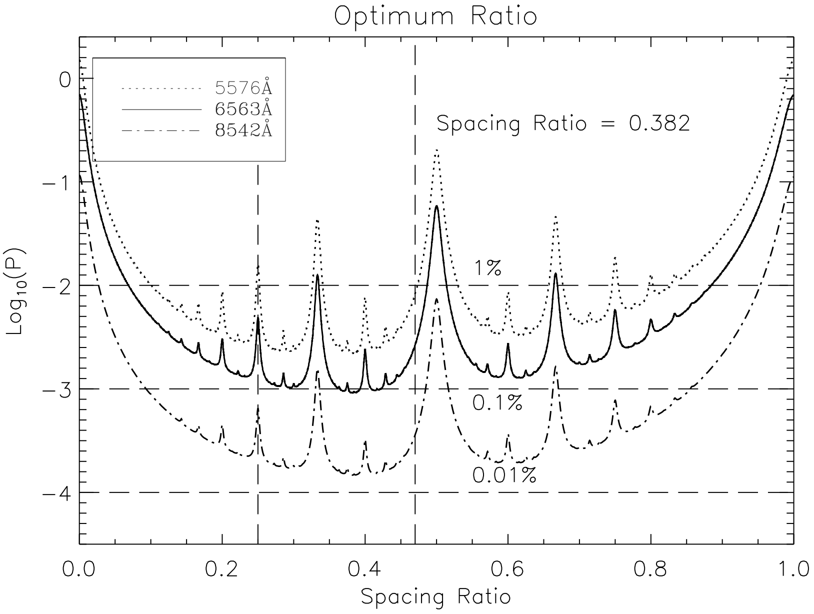

Figure 6.1: A plot of parasitic light vs spacing ratio of two FPs. Solid line, dotted line and dash-dotted line show the parasitic light plot for wavelength 6563 Å, 5576 Å and 8542 Å, respectively. The three horizontal lines indicate the 1%, 0.1% and 0.01% level of the parasitic light. The two vertical dashed lines define a range where the deepest minima can be obtained.

$$I(\lambda) = I_{IF}(\lambda) \prod_{i=1}^{n} I_i(\lambda) \tag{6.1}$$

One can adopt a Lorentzian transparency profile for the interference filter. The transmission profile $I_{IF}(\lambda)$ of the pre-filter can be estimated using the eq. 5.14. Transmission profile $I_i(\lambda)$ of the FPs is given in the eq. 5.2.

After defining the number of FPs and the optical mount of the imaging system, one needs to search for the optimum ratio between the separation of two plates of the interferometer. At a particular spacing ratio of FPs it is possible to reduce the parasitic light from the side bands drastically. The parasitic light is defined as the ratio between the flux outside and inside the instrumental profile. By using the methodology given in Cavallini (2006); Ravindra and Banyal (2010), we estimated the parasitic light (P) for this dual FP system. To generate the filter profile using eq. 6.1, we have chosen $FWHM_{IF} = 4$ Å (centered at Hα 6563 Å, Fe-I 5576 Å and Ca-II 8542 Å),

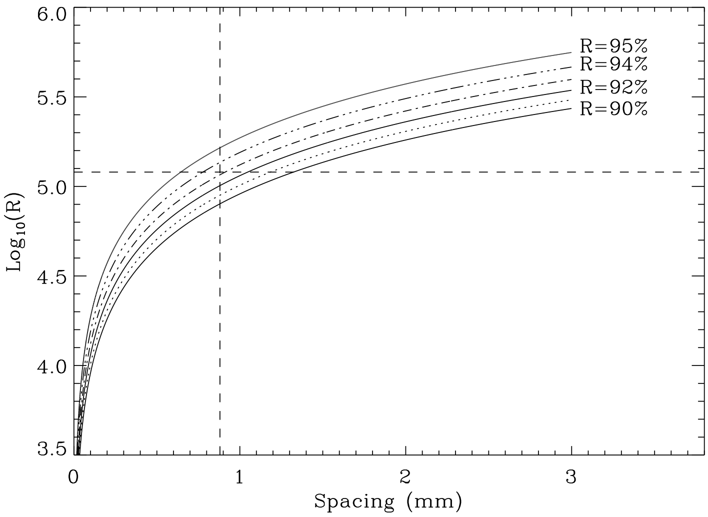

Figure 6.2: A plot of spectral resolving power (R) at 6563 Å vs spacing of the thickest FP for a plate reflectivity 90%, 91%. 92%, 93%, 94% and 95%.

cavity number (n) = 2 and peak transmission (τ_{IF}) = 0.3. There are few advantages for selecting wider passband of the order-sorting filter as follows: 1) one can cover the full desired line profile, which allows to scan the line profile from blue continuum to red continuum, 2) high accuracy temperature controlled oven is not required to keep the passband of the filter in the desired wavelength position, and 3) it reduces the cost of the filter. We obtained the over all transmission for the filter $I_{IF}(\lambda) \simeq 10^{-5}$ for $\Delta\lambda = \pm$ 2 nm and found similar value as mentioned in Cavallini (2006). We have selected the following parameters for the air gaped based FPs: absorption coefficient (A) = 0.01, coating reflectivity (R) = 0.95, the refractive index = 1 and the incidence angle = 0. In dual FP system of a imager, plate separation of each FP play an important role for the imager. The FP with a lower plate spacing, decides the FSR of the imager. The other FP with larger plate spacing, determines the spectral resolution of the system. First, we selected the spacing between two plates of the first FP (FP-I) d1 = $880\mu m$ to achieve the spectral resolution $\sim$ 40 mÅ at λ=6563 Å. Then, we varied the spacing (d2) of the second FP (FPI-II) insteps of 0.01, till the ratio (d2/d1) equal to 1. Figure 6.1 shows the plot of parasitic light versus spacing ratio for different wavelengths. Solid line, dotted line and dashed-dotted line show the parasitic light plot for $\lambda =$ 6563 Å, 5576 Å and 8542 Å, respectively. The plot shows a series of minima and maxima in the level of the parasitic light. It is clear from the plot that the parasitic light decreases with increasing wavelength. The smallest level of the parasitic light is obtained for the spacing ratio 0.382 for all the selected wavelengths.

Once the optimum ratio has been found, one has to look for the best spacing for the both FPs. Hence, the spectral resolving power (R_p) is need to estimate, which is dependent on different instrumental parameters. For a single FP, it can be expressed as (Cavallini, 2006)

$$R_p = \frac{2\mu d R^{1/2}}{\lambda(1-R)} \tag{6.2}$$

Figure. 6.2 shows a plot of spectral resolving power at 6563 Å versus spacing of the thickest FP for a different reflectivity. It shows the resolving power increases with the increase of the spacing. But with increasing spacing the parasitic light increases. Hence, the best spacing will be a compromise between a low parasitic light and a high resolving power. For our NBI, we have the spectral resolution $\sim$ 40 mÅ at λ=6563 Å. To achieve this, the plate spacing for the first FP should be 880 μm, and while maintaining the low parasitic light, the spacing ratio is 0.382. Hence, we require the 2nd FP with plate spacing 336 μm.

Figure 6.3 shows the transmission profile of narrow band imager (red curve) using the air gap based spacing of the dual FPs. We have used the spacing of the 1st and 2nd FP as 880 μm and 336 μm with a reflectivity of 93% (as one can obtain the optimum reflectivity from Figure 6.1). We have used a order sorting filter with a FWHM of 4 Å centered at 6563 Å. The transmission profile shown is for prefilter (pink color) and two FPs (solid blue and dotted green curves) while placing them in a collimated beam in tandem.

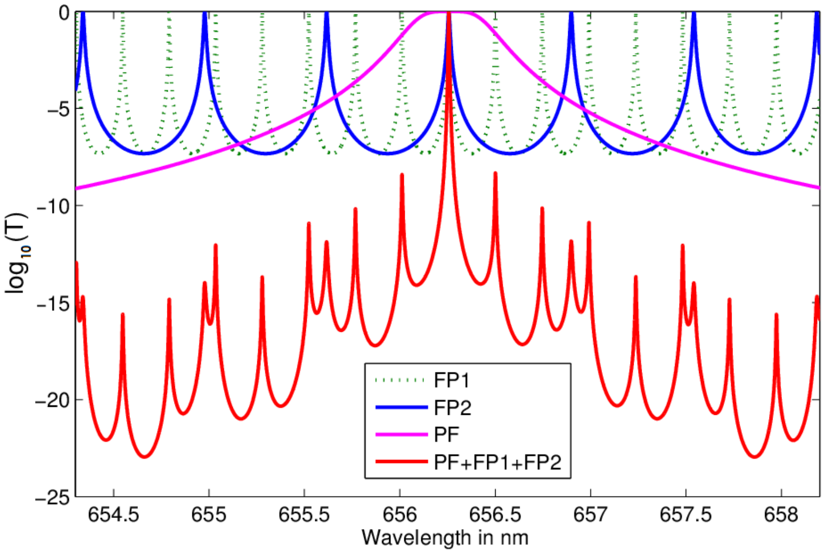

Figure 6.3: The transmission profile (red color) of the dual air-gap based FPs in combination with a transmission filter of FWHM 4 Å centered at 6563 Å. The reflectivity of FP plate 93% is taken in computing the transmission profile. PF–pre-filter, FP1 and FP2–air gaped Fabry-Perot interferometers

To design a NBI system, the next step is to decide the size of the FPs, which depends on the diameter of the telescope used and desired field-of-view (FOV). To make the preliminary design of NBI, we used the concept design of NLST (Hasan, 2010; Hasan *et al.*, 2010a,b), which has a FOV of 3.3 arc-min and the final image at the focal plane produces $F_{40.43}$ beam, which produces a image scale of $2.5''$/mm. We have selected a FOV of 1.2 arc-min for narrow band imaging and used Zemax software to make the preliminary optical design of it for multiple wavelengths 6563 Å, 6302 Å and 5576 Å. The optical layout is shown in Figure 6.4. The light beam from image plane of NLST (I1, as shown in Figure 6.4) is collimated using an achromatic doublet (L1) of focal length 1617.2 mm to generate a collimated beam of diameter 40 mm. We require minimum size of the FPs are of 40 mm. There are few advantages of using smaller size of FPs are :

1) A pre-filter of that small size (∼4 cm) is easy to procure and it costs less.

2) It is easy to maintain the plate parallelism in small sized FPs.

3) Small size of air-gap based FPs reduces the other optical component's size

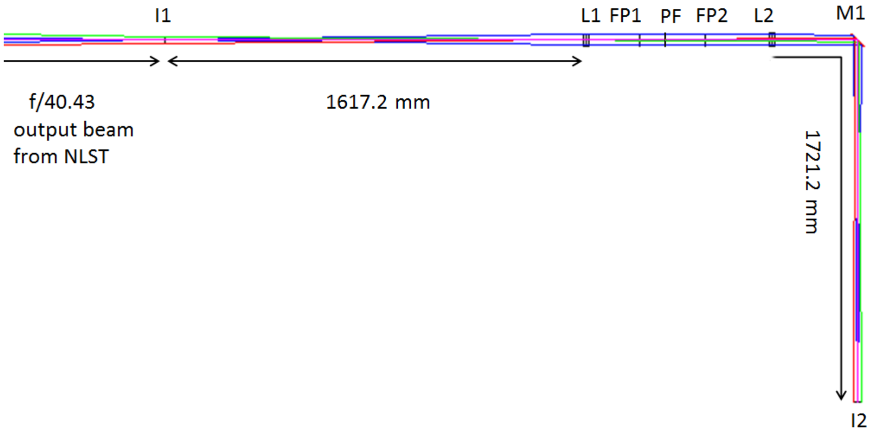

Figure 6.4: Zemax software design of optical configuration of the dual FP based narrow band imaging system for NLST. I1 –focal plane of NLST, L1–achromatic doublet with focal length F1=1617.2 mm to collimate the beam, L2–re-imaging achromatic doublet with focal length F2=1721.2 mm, I2 – focal plane of L2, M1– plane mirror, PF–pre-filter, FP1 and FP2–air gaped Fabry-Perot interferometers.

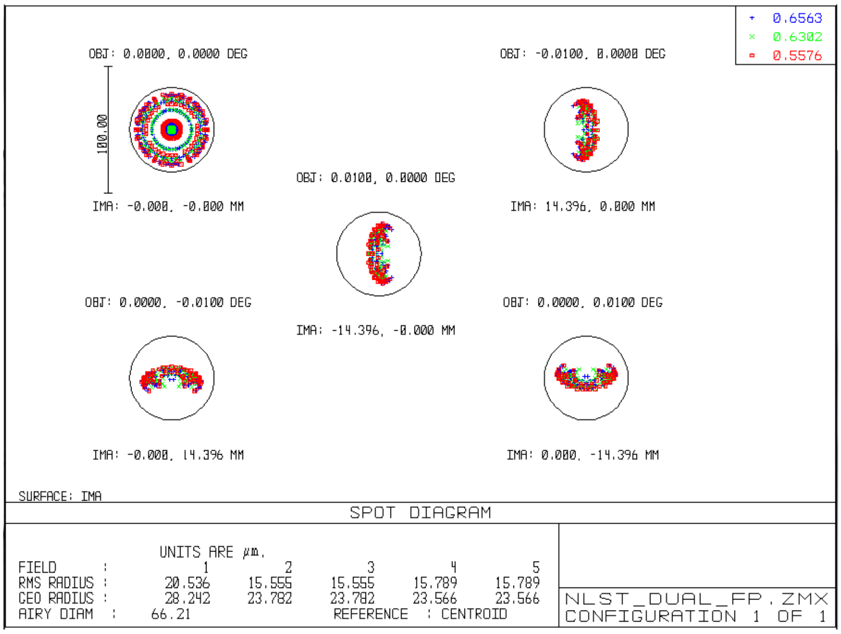

```
               UNITS ARE µm.
FIELD       :        1        2        3        4        5
RMS RADIUS  :   20.536   15.555   15.555   15.789   15.789
GEO RADIUS  :   28.242   23.782   23.782   23.566   23.566
AIRY DIAM   :  66.21             REFERENCE   : CENTROID
```

Figure 6.5: Diffraction limited spot diagram of the optical design for 1.2 arc-min field-of-view at I2 in Figure 6.4. The black circle indicates the Airy disk.

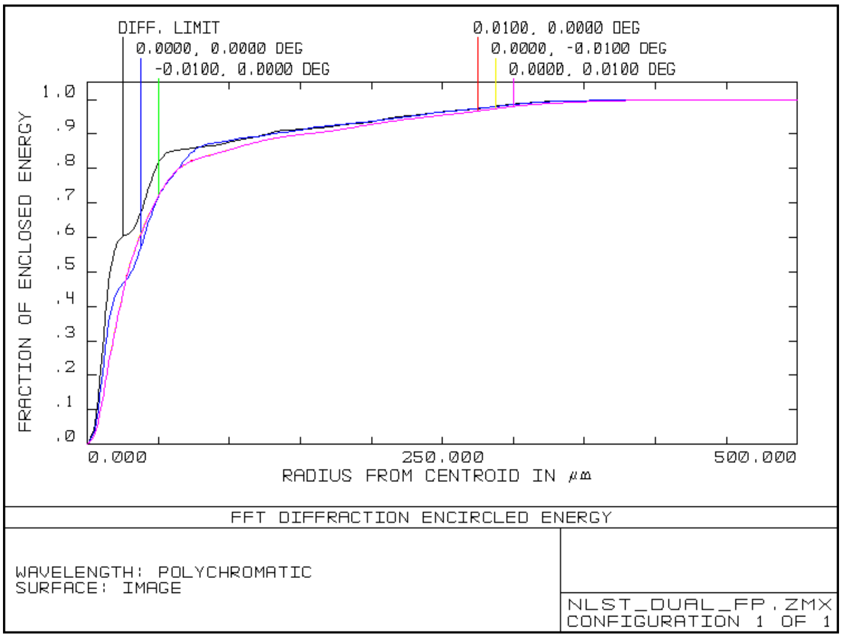

Figure 6.6: Encircled energy at I2 for 0, 1.2 arc-min field-of-view.

and space.

Two FPs (FP1 and FP2) are placed in collimated beam and finally, the beam is re-imaged by another achromatic doublet (L2), which has the focal length of 1721.2 mm. The whole setup has a length of about 4 m. To reduce the size of the instrument, we have folded the beam using a plane mirror (M1) keeping at -45^0 angle in x-y plane. The spot diagrams and encircled energy plots at image plane I2 for 1.2 arc-min FOV for NBI system are shown in Figure 6.5 and Figure 6.6, respectively for three different wavelengths. From the Figure 6.5 it is clear that aberrations are minimized and the configuration is optimized for the diffraction limited performance. The blue line in Figure 6.6 denote a 0th field angle whereas the pink line belongs to 1.2 arc-min FOV. Both the achromatic doublets (L1 and L2) are contact doublet and we have selected BK7 and SF7 material to design the lenses. After optimizing the radii of curvatures and focal lengths of both the achromatic lens (L1 and L2) for a desired FOV of 1.2 arc-min, we obtained the image size at the focal plane (I2) is 28.8 mm. Hence, we require a standard 2k×2k CCD with pixel size 15μm to image the 1.2 arc-min FOV with a pixel resolution $0.038''$.

To this end, we have presented a preliminary design of a dual air gap FP based narrow band imager to study various aspects of solar atmosphere at different wavelengths. The initial designed specification is achieved by the studies comprising stray light modeling, optimum plate spacings of the FPs and simulations described in the previous Section 6.2.1. These results show that the imager will be capable of achieving the desired spectral resolution. Still a more efficient design can be made. In future, we would like to continue the work on a detailed design study including the stability of the instrument, signal to noise ratio (SNR) at the detector, and optimization of the instruments, space etc.

Coelostat used for observations of the solar chromosphere using narrow band imager at Indian Institute of Astrophysics, Bangalore

Bibliography

Alexander, C.E., Walsh, R.W., Régnier, S., Cirtain, J., Winebarger, A.R., Golub, L., Kobayashi, K., Platt, S., Mitchell, N., Korreck, K., DePontieu, B., DeForest, C., Weber, M., Title, A., Kuzin, S.: 2013, "Anti-parallel EUV Flows Observed along Active Region Filament Threads with Hi-C". *Astrophys. J. Lett.* **775**, L32. doi:10.1088/2041-8205/775/1/L32.

Álvarez-Herrero, A., Belenguer, T., Pastor, C., Heredero, R.L., Ramos, G., Martínez Pillet, V., Bonet Navarro, J.A.: 2006, "Lithium niobate Fabry-Perot etalons in double-pass configuration for spectral filtering in the visible imager magnetograph IMaX for the SUNRISE mission". In: *Society of Photo-Optical Instrumentation Engineers (SPIE) Conference Series*, *Society of Photo-Optical Instrumentation Engineers (SPIE) Conference Series* **6265**, 2. doi:10.1117/12.671966.

Amari, T., Luciani, J.F., Aly, J.J., Mikic, Z., Linker, J.: 2003, "Coronal Mass Ejection: Initiation, Magnetic Helicity, and Flux Ropes. II. Turbulent Diffusion-driven Evolution". *Astrophys. J.* **595**, 1231 – 1250. doi:10.1086/377444.

Amari, T., Aly, J.-J., Mikic, Z., Linker, J.: 2010, "Coronal Mass Ejection Initiation: On the Nature of the Flux Cancellation Model". *Astrophys. J. Lett.* **717**, L26 – L30. doi:10.1088/2041-8205/717/1/L26.

Amari, T., Aly, J.-J., Luciani, J.-F., Mikic, Z., Linker, J.: 2011, "Coronal Mass Ejection Initiation by Converging Photospheric Flows: Toward a Realistic Model". *Astrophys. J. Lett.* **742**, L27. doi:10.1088/2041-8205/742/2/L27.

Antiochos, S.K.: 1998, "The Magnetic Topology of Solar Eruptions". *Astrophys. J. Lett.* **502**, L181. doi:10.1086/311507.

Antiochos, S.K., DeVore, C.R., Klimchuk, J.A.: 1999, "A Model for Solar Coronal Mass Ejections". *Astrophys. J.* **510**, 485 – 493. doi:10.1086/306563.

Aulanier, G., DeLuca, E.E., Antiochos, S.K., McMullen, R.A., Golub, L.: 2000, "The Topology and Evolution of the Bastille Day Flare". *Astrophys. J.* **540**, 1126 – 1142. doi:10.1086/309376.

Aulanier, G., Török, T., Démoulin, P., DeLuca, E.E.: 2010, "Formation of Torus-Unstable Flux Ropes and Electric Currents in Erupting Sigmoids". *Astrophys. J.* **708**, 314 – 333. doi:10.1088/0004-637X/708/1/314.

Babcock, H.W., Babcock, H.D.: 1955, "The Sun's Magnetic Field, 1952-1954.". *Astrophys. J.* **121**, 349. doi:10.1086/145994.

Bangert, P.D., Martin, S.F., Berger, M.A.: 2003, "Solar Coronal Magnetic Filaments: The Roll Effect in Erupting Prominences". In: *AAS/Solar Physics Division Meeting #34, Bulletin of the American Astronomical Society* **35**, 815.

Bateman, G.: 1978, "MHD Instabilities". *Cambridge, MA: MIT Press.*

Bello González, N., Kneer, F.: 2008, "Narrow-band full Stokes polarimetry of small structures on the Sun with speckle methods". *Astron. Astrophys.* **480**, 265 – 275. doi:10.1051/0004-6361:20078567.

Berger, M.A.: 1984, "Rigorous new limits on magnetic helicity dissipation in the solar corona". *Geophys. Astrophys. Fluid Dyn.* **30**, 79 – 104. doi:10.1080/03091928408210078.

Berger, M.A., Field, G.B.: 1984, "The topological properties of magnetic helicity". *J. Fluid Mech.* **147**, 133 – 148. doi:10.1017/S0022112084002019.

Bocchialini, K., Koutchmy, S., Solomon, J., Tavabi, E.: 2012, "Homologous flares inducing EUV filament oscillations with subsequent eruption". In: Faurobert, M., Fang, C., Corbard, T. (eds.) *EAS Publications Series*, *EAS Publications Series* **55**, 335 – 338. doi:10.1051/eas/1255046.

Boerner, P., Edwards, C., Lemen, J., Rausch, A., Schrijver, C., Shine, R., Shing, L., Stern, R., Tarbell, T., Title, A., Wolfson, C.J., Soufli, R., Spiller, E., Gullikson, E., McKenzie, D., Windt, D., Golub, L., Podgorski, W., Testa, P., Weber, M.: 2012, "Initial Calibration of the Atmospheric Imaging Assembly (AIA) on the Solar Dynamics Observatory (SDO)". *Solar Phys.* **275**, 41 – 66. doi:10.1007/s11207-011-9804-8.

Borrero, J.M., Tomczyk, S., Kubo, M., Socas-Navarro, H., Schou, J., Couvidat, S., Bogart, R.: 2011, "VFISV: Very Fast Inversion of the Stokes Vector for the Helioseismic and Magnetic Imager". *Solar Phys.* **273**, 267 – 293. doi:10.1007/s11207-010-9515-6.

Cavallini, F.: 2006, "IBIS: A New Post-Focus Instrument for Solar Imaging Spectroscopy". *Solar Phys.* **236**, 415 – 439. doi:10.1007/s11207-006-0103-8.

Chae, J.: 2000, "The Magnetic Helicity Sign of Filament Chirality". *Astrophys. J. Lett.* **540**, L115 – L118. doi:10.1086/312880.

Chae, J.: 2001, "Observational Determination of the Rate of Magnetic Helicity Transport through the Solar Surface via the Horizontal Motion of Field Line Footpoints". *Astrophys. J. Lett.* **560**, L95 – L98. doi:10.1086/324173.

Chae, J.: 2003, "The Formation of a Prominence in NOAA Active Region 8668. II. Trace Observations of Jets and Eruptions Associated with Canceling Magnetic Features". *Astrophys. J.* **584**, 1084 – 1094. doi:10.1086/345739.

Chae, J., Moon, Y.-J., Rust, D.M., Wang, H., Goode, P.R.: 2003, "Magnetic Helicity Pumping by Twisted Flux Tube Expansion". *Journal of Korean Astronomical Society* **36**, 33 – 41.

Chandra, R., Pariat, E., Schmieder, B., Mandrini, C.H., Uddin, W.: 2010, "How Can a Negative Magnetic Helicity Active Region Generate a Positive Helicity Magnetic Cloud?". *Solar Phys.* **261**, 127 – 148. doi:10.1007/s11207-009-9470-2.

Chen, H., Jiang, Y., Ma, S.: 2009, "An EUV Jet and Hα Filament Eruption Associated with Flux Cancelation in a Decaying Active Region". *Solar Phys.* **255**, 79 – 90. doi:10.1007/s11207-008-9298-1.

Chen, H., Zhang, J., Cheng, X., Ma, S., Yang, S., Li, T.: 2014, "Direct Observations of Tether-cutting Reconnection during a Major Solar Event from 2014 February 24 to 25". *Astrophys. J. Lett.* **797**, L15. doi:10.1088/2041-8205/797/2/L15.

Chen, J.: 1989, "Effects of toroidal forces in current loops embedded in a background plasma". *Astrophys. J.* **338**, 453 – 470. doi:10.1086/167211.

Chen, J., Kunkel, V.: 2010, "Temporal and Physical Connection Between Coronal Mass Ejections and Flares". *Astrophys. J.* **717**, 1105 – 1122. doi:10.1088/0004-637X/717/2/1105.

Chen, P.F.: 2011, "Coronal Mass Ejections: Models and Their Observational Basis". *Living Reviews in Solar Physics* **8**, 1. doi:10.12942/lrsp-2011-1.

Cheng, X., Ding, M.D., Guo, Y., Zhang, J., Vourlidas, A., Liu, Y.D., Olmedo, O., Sun, J.Q., Li, C.: 2014, "Tracking the Evolution of a Coherent Magnetic

Flux Rope Continuously from the Inner to the Outer Corona". *Astrophys. J.* **780**, 28. doi:10.1088/0004-637X/780/1/28.

Chifor, C., Tripathi, D., Mason, H.E., Dennis, B.R.: 2007, "X-ray precursors to flares and filament eruptions". *Astron. Astrophys.* **472**, 967 – 979. doi:10.1051/0004-6361:20077771.

Contarino, L., Romano, P., Zuccarello, F.: 2006, "Cancelling magnetic feature and filament activation". *Astronomische Nachrichten* **327**, 674. doi:10.1002/asna.200610619.

Contarino, L., Romano, P., Yurchyshyn, V.B., Zuccarello, F.: 2003, "Themis, BBSO, MDI and trace observations of a filament eruption". *Solar Phys.* **216**, 173 – 188. doi:10.1023/A:1026107727149.

Dalmasse, K., Pariat, E., Démoulin, P., Aulanier, G.: 2014, "Photospheric Injection of Magnetic Helicity: Connectivity-Based Flux Density Method". *Solar Phys.* **289**, 107 – 136. doi:10.1007/s11207-013-0326-4.

Darlin, J.S., Sriram, K.V., Kothiyal, M.P., Sirohi, R.S.: 1995, "Modified double-wedge-plate shearing interferometer for collimation testing". *Applied Optics* **34**, 2886 – 2887. doi:10.1364/AO.34.002886.

De Rosa, M.L., Toomre, J.: 2004, "Evolution of Solar Supergranulation". *Astrophys. J.* **616**, 1242 – 1260. doi:10.1086/424920.

Delaboudinière, J.-P., Artzner, G.E., Brunaud, J., Gabriel, A.H., Hochedez, J.F., Millier, F., Song, X.Y., Au, B., Dere, K.P., Howard, R.A., Kreplin, R., Michels, D.J., Moses, J.D., Defise, J.M., Jamar, C., Rochus, P., Chauvineau, J.P., Marioge, J.P., Catura, R.C., Lemen, J.R., Shing, L., Stern, R.A., Gurman, J.B., Neupert, W.M., Maucherat, A., Clette, F., Cugnon, P., van Dessel, E.L.: 1995, "EIT: Extreme-Ultraviolet Imaging Telescope for the SOHO Mission". *Solar Phys.* **162**, 291 – 312. doi:10.1007/BF00733432.

Démoulin, P., Aulanier, G.: 2010, "Criteria for Flux Rope Eruption: Non-equilibrium Versus Torus Instability". *Astrophys. J.* **718**, 1388 – 1399. doi:10.1088/0004-637X/718/2/1388.

Démoulin, P., Berger, M.A.: 2003, "Magnetic Energy and Helicity Fluxes at the Photospheric Level". *Solar Phys.* **215**, 203 – 215.

Denker, C., Johannesson, A., Marquette, W., Goode, P.R., Wang, H., Zirin, H.: 1999, "Synoptic Hα Full-Disk Observations of the Sun from BigBear Solar Observatory - I. Instrumentation, Image Processing, Data Products, and First Results". *Solar Phys.* **184**, 87 – 102. doi:10.1023/A:1005047906097.

Dhara, S.K., Ravindra, B., Banyal, R.K.: 2014a, "Filament eruption in association with rotational motion near the filament footpoints". *New Astron.* **26**, 86 – 97. doi:10.1016/j.newast.2013.07.001.

Dhara, S.K., Ravindra, B., Banyal, R.K.: 2014b, "Observations of Photospheric Vortical Motions During the Early Stage of Filament Eruption". *Solar Phys.* **289**, 4481 – 4500. doi:10.1007/s11207-014-0597-4.

Domingo, V., Fleck, B., Poland, A.I.: 1995, "SOHO: The Solar and Heliospheric Observatory". *Space Sci. Rev.* **72**, 81 – 84. doi:10.1007/BF00768758.

Donnelly, R.F., Grubb, R.N., Cowley, F.C.: 1977,, *NOAA TM ERL /SEL-48.*

Elsasser, W.M.: 1956, "Hydromagnetic Dynamo Theory". *Reviews of Modern Physics* **28**, 135 – 163. doi:10.1103/RevModPhys.28.135.

Engvold, O.: 1998, "Observations of Filament Structure and Dynamics (Review)". In: Webb, D.F., Schmieder, B., Rust, D.M. (eds.) *IAU Colloq. 167: New Perspectives on Solar Prominences*, *Astronomical Society of the Pacific Conference Series* **150**, 23.

Fainshtein, V.G., Ivanov, E.V.: 2010, “Relationship between CME Parameters and Large-Scale Structure of Solar Magnetic Fields”. *Sun and Geosphere* **5**, 28 – 33.

Fan, Y.: 2005, “Coronal Mass Ejections as Loss of Confinement of Kinked Magnetic Flux Ropes”. *Astrophys. J.* **630**, 543 – 551. doi:10.1086/431733.

Fan, Y., Gibson, S.E.: 2007, “Onset of Coronal Mass Ejections Due to Loss of Confinement of Coronal Flux Ropes”. *Astrophys. J.* **668**, 1232 – 1245. doi:10.1086/521335.

Feynman, J., Martin, S.F.: 1995, “The initiation of coronal mass ejections by newly emerging magnetic flux”. *J. Geophys. Res.* **100**, 3355 – 3367. doi:10.1029/94JA02591.

Filippov, B.P., Gopalswamy, N., Lozhechkin, A.V.: 2001, “Non-radial motion of eruptive filaments”. *Solar Phys.* **203**, 119 – 130.

Finn, J.H., Antonsen, T.M.J.: 1985, “Magnetic helicity: what is it, and what is it good for?”. *Comments. Plasma Phys. Contr. Fus.* **9**, 111 – 126.

Forbes, T.G.: 2000, “A review on the genesis of coronal mass ejections”. *J. Geophys. Res.* **105**, 23153 – 23166. doi:10.1029/2000JA000005.

Garcia, H.A.: 1994, “Temperature and emission measure from GOES soft X-ray measurements”. *Solar Phys.* **154**, 275 – 308. doi:10.1007/BF00681100.

Gary, G.A., Balasubramaniam, K.S., Sigwarth, M.: 2003, “Multiple Etalon Systems for the Advanced Technology Solar Telescope”. In: Keil, S.L., Avakyan, S.V. (eds.) *Innovative Telescopes and Instrumentation for Solar Astrophysics, Society of Photo-Optical Instrumentation Engineers (SPIE) Conference Series* **4853**, 252 – 272.

Gibson, S.E., Foster, D., Burkepile, J., de Toma, G., Stanger, A.: 2006, “The Calm before the Storm: The Link between Quiescent Cavities and Coronal Mass Ejections”. *Astrophys. J.* **641**, 590 – 605. doi:10.1086/500446.

Gilbert, H.R., Alexander, D., Liu, R.: 2007, “Filament Kinking and Its Implications for Eruption and Re-formation”. *Solar Phys.* **245**, 287 – 309. doi:10.1007/s11207-007-9045-z.

Gilbert, H.R., Holzer, T.E., Burkepile, J.T., Hundhausen, A.J.: 2000, “Active and Eruptive Prominences and Their Relationship to Coronal Mass Ejections”. *Astrophys. J.* **537**, 503 – 515. doi:10.1086/309030.

Gold, T., Hoyle, F.: 1960, “On the origin of solar flares”. *Mon. Not. Roy. Astron. Soc.* **120**, 89.

Gopalswamy, N., Lara, A., Yashiro, S., Nunes, S., Howard, R.A.: 2003a, “Coronal mass ejection activity during solar cycle 23”. In: Wilson, A. (ed.) *Solar Variability as an Input to the Earth’s Environment*, *ESA Special Publication* **535**, 403 – 414.

Gopalswamy, N., Shimojo, M., Lu, W., Yashiro, S., Shibasaki, K., Howard, R.A.: 2003b, “Prominence Eruptions and Coronal Mass Ejection: A Statistical Study Using Microwave Observations”. *Astrophys. J.* **586**, 562 – 578. doi:10.1086/367614.

Green, L.M., Kliem, B., Wallace, A.J.: 2011, “Photospheric flux cancellation and associated flux rope formation and eruption”. *Astron. Astrophys.* **526**, A2. doi:10.1051/0004-6361/201015146.

Green, L.M., Kliem, B., Török, T., van Driel-Gesztelyi, L., Attrill, G.D.R.: 2007, “Transient Coronal Sigmoids and Rotating Erupting Flux Ropes”. *Solar Phys.* **246**, 365 – 391. doi:10.1007/s11207-007-9061-z.

Grubb, R.N.: 1975,, *NOAA TM ERL SEL-42.*

Gullixson, C.: 1998, In: *Characteristics of Available Fabry-Perot Filters*, *Tech. Memo. National Solar Observatory.*

Guo, Y., Schmieder, B., Démoulin, P., Wiegelmann, T., Aulanier, G., Török, T., Bommier, V.: 2010, "Coexisting Flux Rope and Dipped Arcade Sections Along One Solar Filament". *Astrophys. J.* **714**, 343 – 354. doi:10.1088/0004-637X/714/1/343.

Gupta, S.K., Mathew, D., S.K.J.A., Srivastava, N.: 2008, "A costanst temperature oven for Lithium Niobate Fabry-Perot etalon". In: *Astronomical Society of India Conference Series*, *National Space Science Symposium, NSSS–2008.*

Hart, A.B.: 1956, "Motions in the Sun at the photospheric level. VI. Large-scale motions in the equatorial region". *Mon. Not. Roy. Astron. Soc.* **116**, 38.

Harvey, J.W., Hill, F., Hubbard, R.P., Kennedy, J.R., Leibacher, J.W., Pintar, J.A., Gilman, P.A., Noyes, R.W., Title, A.M., Toomre, J., Ulrich, R.K., Bhatnagar, A., Kennewell, J.A., Marquette, W., Patron, J., Saa, O., Yasukawa, E.: 1996, "The Global Oscillation Network Group (GONG) Project". *Science* **272**, 1284 – 1286. doi:10.1126/science.272.5266.1284.

Harvey, J.W., Bolding, J., Clark, R., Hauth, D., Hill, F., Kroll, R., Luis, G., Mills, N., Purdy, T., Henney, C., Holland, D., Winter, J.: 2011, "Full-disk Solar H-alpha Images From GONG". In: *AAS/Solar Physics Division Abstracts #42*, 1745.

Hasan, S.S.: 2010, "The Indian National Large Solar Telescope (NLST)". In: Kosovichev, A.G., Andrei, A.H., Rozelot, J.-P. (eds.) *IAU Symposium*, *IAU Symposium* **264**, 499 – 504. doi:10.1017/S1743921309993206.

Hasan, S.S., Soltau, D., Kärcher, H., Süß, M., Berkefeld, T.: 2010a, "NLST: India's National Large Solar Telescope". *Astronomische Nachrichten* **331**, 628. doi:10.1002/asna.201011389.

Hasan, S.S., Soltau, D., Kärcher, H., Süss, M., Berkefeld, T.: 2010b, "NLST: the Indian National Large Solar Telescope". In: *Society of Photo-Optical Instrumentation Engineers (SPIE) Conference Series*, *Society of Photo-Optical Instrumentation Engineers (SPIE) Conference Series* **7733**, 0. doi:10.1117/12.856108.

Hoeksema, J.T., Liu, Y., Hayashi, K., Sun, X., Schou, J., Couvidat, S., Norton, A., Bobra, M., Centeno, R., Leka, K.D., Barnes, G., Turmon, M.: 2014, "The Helioseismic and Magnetic Imager (HMI) Vector Magnetic Field Pipeline: Overview and Performance". *Solar Phys.* **289**, 3483 – 3530. doi:10.1007/s11207-014-0516-8.

Hood, A.W., Priest, E.R.: 1979, "Kink instability of solar coronal loops as the cause of solar flares". *Solar Phys.* **64**, 303 – 321. doi:10.1007/BF00151441.

Innes, D.E., Genetelli, A., Attie, R., Potts, H.E.: 2009, "Quiet Sun mini-coronal mass ejections activated by supergranular flows". *Astron. Astrophys.* **495**, 319 – 323. doi:10.1051/0004-6361:200811011.

Jing, J., Yurchyshyn, V.B., Yang, G., Xu, Y., Wang, H.: 2004, "On the Relation between Filament Eruptions, Flares, and Coronal Mass Ejections". *Astrophys. J.* **614**, 1054 – 1062. doi:10.1086/423781.

Jockers, K.: 1978, "Transport of twist in force-free magnetic flux tubes". *Astrophys. J.* **220**, 1133 – 1136. doi:10.1086/155998.

Joshi, A.D.: 2011, "Morphology and Dynamics of Solar Prominences". *PhD Thesis.*

Joshi, A.D., Forbes, T.G., Park, S.-H., Cho, K.-S.: 2015, "A Trio of Confined Flares in AR 11087". *Astrophys. J.* **798**, 97. doi:10.1088/0004-637X/798/2/97.

Judge, P.G., Tritschler, A., Uitenbroek, H., Reardon, K., Cauzzi, G., de Wijn, A.: 2010, "Fabry-Pérot Versus Slit Spectropolarimetry of Pores and

Active Network: Analysis of IBIS and Hinode Data". *Astrophys. J.* **710**, 1486 – 1497. doi:10.1088/0004-637X/710/2/1486.

Kahler, S.W., Moore, R.L., Kane, S.R., Zirin, H.: 1988, "Filament eruptions and the impulsive phase of solar flares". *Astrophys. J.* **328**, 824 – 829. doi:10.1086/166340.

Kentischer, T.J., Schmidt, W., Sigwarth, M., Uexkuell, M.V.: 1998, "TESOS, a double Fabry-Perot instrument for solar spectroscopy". *Astron. Astrophys.* **340**, 569 – 578.

Khan, J.I., Fletcher, L., Nitta, N.V.: 2006, "Observations of simultaneous coronal loop shrinkage and expansion during the decay phase of a solar flare". *Astron. Astrophys.* **453**, 335 – 339. doi:10.1051/0004-6361:20054604.

Kim, S., Moon, Y.-J., Kim, K.-H., Kim, Y.-H., Sakurai, T., Chae, J., Kim, K.-S.: 2007, "Two-Step Reconnections in a C3.3 Flare and Its Preflare Activity Observed by Hinode XRT". *Pub. Astron. Soc. Japan* **59**, 831.

Kleint, L., Feller, A., Gisler, D.: 2011, "Imaging spectropolarimetry with two $LiNbO_3$ Fabry Pérot interferometers and a spectrograph". *Astron. Astrophys.* **529**, A78. doi:10.1051/0004-6361/201015870.

Kliem, B., Török, T.: 2006, "Torus Instability". *Physical Review Letters* **96**(25), 255002. doi:10.1103/PhysRevLett.96.255002.

Kliem, B., Su, Y.N., van Ballegooijen, A.A., DeLuca, E.E.: 2013, "Magnetohydrodynamic Modeling of the Solar Eruption on 2010 April 8". *Astrophys. J.* **779**, 129. doi:10.1088/0004-637X/779/2/129.

Kusano, K., Yokoyama, T., Maeshiro, T., Sakurai, T.: 2003, "Annihilation of magnetic helicity: A new model for solar flare onset". *Adv. Space Res.* **32**, 1931 – 1936. doi:10.1016/S0273-1177(03)90628-4.

Kusano, K., Maeshiro, T., Yokoyama, T., Sakurai, T.: 2004, "The Trigger Mechanism of Solar Flares in a Coronal Arcade with Reversed Magnetic Shear". *Astrophys. J.* **610**, 537 – 549. doi:10.1086/421547.

Leese, J.A., Novak, C.S., Clark, B.B.: 1971,. *J. Appl. Meteorol.* **10**, 118.

Leighton, R.B., Noyes, R.W., Simon, G.W.: 1962, "Velocity Fields in the Solar Atmosphere. I. Preliminary Report.". *Astrophys. J.* **135**, 474. doi:10.1086/147285.

Lemen, J.R., Duncan, D.W., Edwards, C.G., Friedlaender, F.M., Jurcevich, B.K., Morrison, M.D., Springer, L.A., Stern, R.A., Wuelser, J.-P., Bruner, M.E., Catura, R.C.: 2004, "The solar x-ray imager for GOES". In: Fineschi, S., Gummin, M.A. (eds.) *Telescopes and Instrumentation for Solar Astrophysics*, *Society of Photo-Optical Instrumentation Engineers (SPIE) Conference Series* **5171**, 65 – 76. doi:10.1117/12.507566.

Lemen, J.R., Title, A.M., Akin, D.J., Boerner, P.F., Chou, C., Drake, J.F., Duncan, D.W., Edwards, C.G., Friedlaender, F.M., Heyman, G.F., Hurlburt, N.E., Katz, N.L., Kushner, G.D., Levay, M., Lindgren, R.W., Mathur, D.P., McFeaters, E.L., Mitchell, S., Rehse, R.A., Schrijver, C.J., Springer, L.A., Stern, R.A., Tarbell, T.D., Wuelser, J.-P., Wolfson, C.J., Yanari, C., Bookbinder, J.A., Cheimets, P.N., Caldwell, D., Deluca, E.E., Gates, R., Golub, L., Park, S., Podgorski, W.A., Bush, R.I., Scherrer, P.H., Gummin, M.A., Smith, P., Auker, G., Jerram, P., Pool, P., Soufli, R., Windt, D.L., Beardsley, S., Clapp, M., Lang, J., Waltham, N.: 2012, "The Atmospheric Imaging Assembly (AIA) on the Solar Dynamics Observatory (SDO)". *Solar Phys.* **275**, 17 – 40. doi:10.1007/s11207-011-9776-8.

Li, X., Morgan, H., Leonard, D., Jeska, L.: 2012, "A Solar Tornado Observed by AIA/SDO: Rotational Flow and Evolution of Magnetic Helicity in a Prominence and Cavity". *Astrophys. J. Lett.* **752**, L22. doi:10.1088/2041-8205/752/2/L22.

Liewer, P.C., de Jong, E.M., Hall, J.R., Howard, R.A., Thompson, W.T., Culhane, J.L., Bone, L., van Driel-Gesztelyi, L.: 2009, "Stereoscopic Analysis of the 19 May 2007 Erupting Filament". *Solar Phys.* **256**, 57 – 72. doi:10.1007/s11207-009-9363-4.

Liggett, M., Zirin, H.: 1984, "Rotation in prominences". *Solar Phys.* **91**, 259 – 267. doi:10.1007/BF00146298.

Liu, R., Wang, H.: 2009, "Coronal Implosion and Particle Acceleration in the Wake of a Filament Eruption". *Astrophys. J. Lett.* **703**, L23 – L28. doi:10.1088/0004-637X/703/1/L23.

Liu, R., Wang, H.: 2010, "Fast Contraction of Coronal Loops at the Flare Peak". *Astrophys. J. Lett.* **714**, L41 – L46. doi:10.1088/2041-8205/714/1/L41.

Liu, R., Alexander, D., Gilbert, H.R.: 2007, "Kink-induced Catastrophe in a Coronal Eruption". *Astrophys. J.* **661**, 1260 – 1271. doi:10.1086/513269.

Liu, W., Wang, T.-J., Dennis, B.R., Holman, G.D.: 2009, "Episodic X-Ray Emission Accompanying the Activation of an Eruptive Prominence: Evidence of Episodic Magnetic Reconnection". *Astrophys. J.* **698**, 632 – 640. doi:10.1088/0004-637X/698/1/632.

Lynch, B.J., Antiochos, S.K., MacNeice, P.J., Zurbuchen, T.H., Fisk, L.A.: 2004, "Observable Properties of the Breakout Model for Coronal Mass Ejections". *Astrophys. J.* **617**, 589 – 599. doi:10.1086/424564.

Mackay, D.H., Karpen, J.T., Ballester, J.L., Schmieder, B., Aulanier, G.: 2010, Physics of solar prominences: II – magnetic structure and dynamics. *Space Sci. Rev.* **151**, 333 – 399. doi:10.1007/s11214-010-9628-0.

Manchester, W. IV, Gombosi, T., DeZeeuw, D., Fan, Y.: 2004, "Eruption of a Buoyantly Emerging Magnetic Flux Rope". *Astrophys. J.* **610**, 588 – 596. doi:10.1086/421516.

Martin, S.F.: 1980, “Preflare conditions, changes and events”. *Solar Phys.* **68**, 217 – 236. doi:10.1007/BF00156861.

Martin, S.F.: 1998a, “Conditions for the Formation and Maintenance of Filaments (Invited Review)”. *Solar Phys.* **182**, 107 – 137. doi:10.1023/A:1005026814076.

Martin, S.F.: 1998b, “Filament Chirality: A Link Between Fine-Scale and Global Patterns (Review)”. In: Webb, D.F., Schmieder, B., Rust, D.M. (eds.) *IAU Colloq. 167: New Perspectives on Solar Prominences*, *Astronomical Society of the Pacific Conference Series* **150**, 419.

Martin, S.F.: 2003a, “Signs of helicity in solar prominences and related features”. *Advances in Space Research* **32**, 1883 – 1893. doi:10.1016/S0273-1177(03)90622-3.

Martin, S.F.: 2003b, “Signs of helicity in solar prominences and related features”. *Adv. Space Res.* **32**, 1883 – 1893. doi:10.1016/S0273-1177(03)90622-3.

Martin, S.F., Livi, S.H.B.: 1992, “The Role of Cancelling Magnetic Fields in the Buildup to Erupting Filaments and Flares”. In: Svestka, Z., Jackson, B.V., Machado, M.E. (eds.) *IAU Colloq. 133: Eruptive Solar Flares*, *Lecture Notes in Physics, Berlin Springer Verlag* **399**, 33.

Martin, S.F., Livi, S.H.B., Wang, J.: 1985, “The cancellation of magnetic flux. II - In a decaying active region”. *Australian Journal of Physics* **38**, 929 – 959.

Martínez Pillet, V., Del Toro Iniesta, J.C., Álvarez-Herrero, A., Domingo, V., Bonet, J.A., González Fernández, L., López Jiménez, A., Pastor, C., Gasent Blesa, J.L., Mellado, P., Piqueras, J., Aparicio, B., Balaguer, M., Ballesteros, E., Belenguer, T., Bellot Rubio, L.R., Berkefeld, T., Collados, M., Deutsch, W., Feller, A., Girela, F., Grauf, B., Heredero, R.L., Herranz, M., Jerónimo, J.M., Laguna, H., Meller, R., Menéndez, M., Morales, R., Orozco Suárez, D., Ramos, G., Reina, M., Ramos, J.L., Rodríguez, P., Sánchez, A., Uribe-Patarroyo, N., Barthol, P., Gandorfer, A., Knoelker, M., Schmidt, W., Solanki, S.K., Vargas Domínguez, S.: 2011, "The Imaging Magnetograph eXperiment (IMaX) for the Sunrise Balloon-Borne Solar Observatory". *Solar Phys.* **268**, 57 – 102. doi:10.1007/s11207-010-9644-y.

Mathew, S.K., Bhatnagar, A., Prasad, C.D., Ambastha, A.: 1998, "Fabry-Perot filter based solar video magnetograph". *Astron. Astrophys. Suppl.* **133**, 285 – 292. doi:10.1051/aas:1998312.

Moore, R.L., Labonte, B.J.: 1980, "The filament eruption in the 3B flare of July 29, 1973 - Onset and magnetic field configuration". In: Dryer, M., Tandberg-Hanssen, E. (eds.) *Solar and Interplanetary Dynamics*, *IAU Symposium* **91**, 207 – 210.

Moore, R.L., Roumeliotis, G.: 1992, "Triggering of Eruptive Flares - Destabilization of the Preflare Magnetic Field Configuration". In: Svestka, Z., Jackson, B.V., Machado, M.E. (eds.) *IAU Colloq. 133: Eruptive Solar Flares*, *Lecture Notes in Physics, Berlin Springer Verlag* **399**, 69.

Moore, R.L., Sterling, A.C.: 2006, "Initiation of Coronal Mass Ejections". *Washington DC American Geophysical Union Geophysical Monograph Series* **165**, 43.

Moore, R.L., Sterling, A.C., Hudson, H.S., Lemen, J.R.: 2001, "Onset of the Magnetic Explosion in Solar Flares and Coronal Mass Ejections". *Astrophys. J.* **552**, 833 – 848. doi:10.1086/320559.

Mordvinov, A.V., Willson, R.C.: 2003, "Effect of Large-Scale Magnetic Fields on Total Solar Irradiance". *Solar Phys.* **215**, 5 – 16. doi:10.1023/A:1024832809100.

Nagashima, K., Isobe, H., Yokoyama, T., Ishii, T.T., Okamoto, T.J., Shibata, K.: 2007, “Triggering Mechanism for the Filament Eruption on 2005 September 13 in NOAA Active Region 10808”. *Astrophys. J.* **668**, 533 – 545. doi:10.1086/521139.

Nelson, C.J., Shelyag, S., Mathioudakis, M., Doyle, J.G., Madjarska, M.S., Uitenbroek, H., Erdélyi, R.: 2013, “Ellerman Bombs Evidence for Magnetic Reconnection in the Lower Solar Atmosphere”. *Astrophys. J.* **779**, 125. doi:10.1088/0004-637X/779/2/125.

Neupert, W.M.: 2011, “Intercalibration of Solar Soft X-Ray Broad Band Measurements from SOLRAD 9 through GOES-12”. *Solar Phys.* **272**, 319 – 335. doi:10.1007/s11207-011-9825-3.

November, L.J., Simon, G.W.: 1988, “Precise proper-motion measurement of solar granulation”. *Astrophys. J.* **333**, 427 – 442. doi:10.1086/166758.

Padinhatteeri, S., Sridharan, R., Sankarasubramanian, K.: 2010, “Seeing-Induced Errors in Solar Doppler Velocity Measurements”. *Solar Phys.* **266**, 195 – 207. doi:10.1007/s11207-010-9597-1.

Panasenco, O., Martin, S.F.: 2008, “Topological Analyses of Symmetric Eruptive Prominences”. In: Howe, R., Komm, R.W., Balasubramaniam, K.S., Petrie, G.J.D. (eds.) *Subsurface and Atmospheric Influences on Solar Activity, Astronomical Society of the Pacific Conference Series* **383**, 243.

Panasenco, O., Martin, S., Joshi, A.D., Srivastava, N.: 2011, “Rolling motion in erupting prominences observed by STEREO”. *Journal of Atmospheric and Solar-Terrestrial Physics* **73**, 1129 – 1137. doi:10.1016/j.jastp.2010.09.010.

Panasenco, O., Martin, S.F., Velli, M., Vourlidas, A.: 2013, “Origins of Rolling, Twisting, and Non-radial Propagation of Eruptive Solar Events”. *Solar Phys.* **287**, 391 – 413. doi:10.1007/s11207-012-0194-3.

Panesar, N.K., Innes, D.E., Tiwari, S.K., Low, B.C.: 2013, "A solar tornado triggered by flares?". *Astron. Astrophys.* **549**, A105. doi:10.1051/0004-6361/201220503.

Pariat, E., Démoulin, P., Berger, M.A.: 2005, "Photospheric flux density of magnetic helicity". *Astron. Astrophys.* **439**, 1191 – 1203. doi:10.1051/0004-6361:20052663.

Parker, E.N.: 1974, "The Dynamical Properties of Twisted Ropes of Magnetic Field and the Vigor of New Active Regions on the Sun". *Astrophys. J.* **191**, 245 – 254. doi:10.1086/152961.

Pesnell, W.D., Thompson, B.J., Chamberlin, P.C.: 2012, "The Solar Dynamics Observatory (SDO)". *Solar Phys.* **275**, 3 – 15. doi:10.1007/s11207-011-9841-3.

Pizzo, V.J., Hill, S.M., Balch, C.C., Biesecker, D.A., Bornmann, P., Hildner, E., Grubb, R.N., Chipman, E.G., Davis, J.M., Wallace, K.S., Russell, K., Cauffman, S.A., Saha, T.T., Berthiume, G.D.: 2005, "The NOAA Goes-12 Solar X-Ray Imager (SXI) 2. Performance". *Solar Phys.* **226**, 283 – 315. doi:10.1007/s11207-005-7417-9.

Priest, E.R., Forbes, T.G.: 2002, "The magnetic nature of solar flares". *Astron. Astrophys. Rev.* **10**, 313 – 377. doi:10.1007/s001590100013.

Priest, E.R., Parnell, C.E., Martin, S.F.: 1994, "A converging flux model of an X-ray bright point and an associated canceling magnetic feature". *Astrophys. J.* **427**, 459 – 474. doi:10.1086/174157.

Pulkkinen, T.: 2007, "Space Weather: Terrestrial Perspective". *Living Reviews in Solar Physics* **4**, 1. doi:10.12942/lrsp-2007-1.

Raja Bayanna, A., Mathew, S.K., Venkatakrishnan, P., Srivastava, N.: 2014, "Narrow-Band Imaging System for the Multi-application Solar Telescope at

Udaipur Solar Observatory: Characterization of Lithium Niobate Etalons". *Solar Phys.* **289**, 4007 – 4019. doi:10.1007/s11207-014-0557-z.

Ravindra, B.: 2006, "Moving Magnetic Features in and out of Penumbral Filaments". *Solar Phys.* **237**, 297 – 319. doi:10.1007/s11207-006-0144-z.

Ravindra, B., Banyal, R.K.: 2010, "A Dual Fabry-Perot Based Imaging Spectrometer for the National Large Solar Telescope". In: *A Dual Fabry-Perot Based Imaging Spectrometer for the National Large Solar Telescope*, *IIA Technical Report Series.*

Ravindra, B., Longcope, D.W., Abbett, W.P.: 2008, "Inferring Photospheric Velocity Fields Using a Combination of Minimum Energy Fit, Local Correlation Tracking, and Doppler Velocity". *Astrophys. J.* **677**, 751 – 768. doi:10.1086/528363.

Reardon, K.P., Cavallini, F.: 2008, "Characterization of Fabry-Perot interferometers and multi-etalon transmission profiles. The IBIS instrumental profile". *Astron. Astrophys.* **481**, 897 – 912. doi:10.1051/0004-6361:20078473.

Rimmele, T.R.: 2004, "Plasma Flows Observed in Magnetic Flux Concentrations and Sunspot Fine Structure Using Adaptive Optics". *Astrophys. J.* **604**, 906 – 923. doi:10.1086/382069.

Romano, P., Contarino, L., Zuccarello, F.: 2003, "Magnetic helicity transport in corona and filament eruptions". *Solar Phys.* **218**, 137 – 150. doi:10.1023/B:SOLA.0000013035.62270.e4.

Romano, P., Contarino, L., Zuccarello, F.: 2005, "Observational evidence of the primary role played by photospheric motions in magnetic helicity transport before a filament eruption". *Astron. Astrophys.* **433**, 683 – 690. doi:10.1051/0004-6361:20041807.

Romano, P., Pariat, E., Sicari, M., Zuccarello, F.: 2011, "A solar eruption triggered by the interaction between two magnetic flux systems with opposite magnetic helicity". *Astron. Astrophys.* **525**, A13. doi:10.1051/0004-6361/201014437.

Rust, D.M.: 2003, "The helicial flux rope structure of solar filaments". *Advances in Space Research* **32**, 1895 – 1903. doi:10.1016/S0273-1177(03)90623-5.

Rust, D.M., Kumar, A.: 1996, "Evidence for Helically Kinked Magnetic Flux Ropes in Solar Eruptions". *Astrophys. J. Lett.* **464**, L199. doi:10.1086/310118.

Rust, D.M., LaBonte, B.J.: 2005, "Observational Evidence of the Kink Instability in Solar Filament Eruptions and Sigmoids". *Astrophys. J. Lett.* **622**, L69 – L72. doi:10.1086/429379.

Rust, D.M., Murphy, G., Strohbehn, K., Keller, C.U.: 1996, "Balloon-Borne Polarimetry". *Solar Phys.* **164**, 403 – 415. doi:10.1007/BF00146652.

Sakurai, K.: 1976a, "Motion of sunspot magnetic fields and its relation to solar flares". *Solar Phys.* **47**, 261 – 266. doi:10.1007/BF00152263.

Sakurai, T.: 1976b, "Magnetohydrodynamic interpretation of the motion of prominences". *Pub. Astron. Soc. Japan* **28**, 177 – 198.

Scherrer, P.H., Bogart, R.S., Bush, R.I., Hoeksema, J.T., Kosovichev, A.G., Schou, J., Rosenberg, W., Springer, L., Tarbell, T.D., Title, A., Wolfson, C.J., Zayer, I., MDI Engineering Team: 1995, "The Solar Oscillations Investigation - Michelson Doppler Imager". *Solar Phys.* **162**, 129 – 188. doi:10.1007/BF00733429.

Scherrer, P.H., Schou, J., Bush, R.I., Kosovichev, A.G., Bogart, R.S., Hoeksema, J.T., Liu, Y., Duvall, T.L., Zhao, J., Title, A.M., Schrijver, C.J., Tarbell, T.D., Tomczyk, S.: 2012, "The Helioseismic and Magnetic Imager (HMI) Investigation for the Solar Dynamics Observatory (SDO)". *Solar Phys.* **275**, 207 – 227. doi:10.1007/s11207-011-9834-2.

Schmieder, B., van Driel-Gesztelyi, L., Aulanier, G., Démoulin, P., Thompson, B., de Forest, C., Wiik, J.E., Saint Cyr, C., Vial, J.C.: 2002, "Relationships between CME's and prominences". *Adv. Space Res.* **29**, 1451 – 1460. doi:10.1016/S0273-1177(02)00211-9.

Schmieder, B., Mandrini, C., Chandra, R., Démoulin, P., Török, T., Pariat, E., Uddin, W.: 2011, "Solar activity due to magnetic complexity of active regions". In: Prasad Choudhary, D., Strassmeier, K.G. (eds.) *IAU Symposium*, *IAU Symposium* **273**, 164 – 168. doi:10.1017/S1743921311015183.

Schnerr, R.S., Spruit, H.C.: 2011, "The Total Solar Irradiance and Small Scale Magnetic Fields". In: Kuhn, J.R., Harrington, D.M., Lin, H., Berdyugina, S.V., Trujillo-Bueno, J., Keil, S.L., Rimmele, T. (eds.) *Solar Polarization 6*, *Astronomical Society of the Pacific Conference Series* **437**, 167.

Schou, J., Scherrer, P.H., Bush, R.I., Wachter, R., Couvidat, S., Rabello-Soares, M.C., Bogart, R.S., Hoeksema, J.T., Liu, Y., Duvall, T.L., Akin, D.J., Allard, B.A., Miles, J.W., Rairden, R., Shine, R.A., Tarbell, T.D., Title, A.M., Wolfson, C.J., Elmore, D.F., Norton, A.A., Tomczyk, S.: 2012a, "Design and Ground Calibration of the Helioseismic and Magnetic Imager (HMI) Instrument on the Solar Dynamics Observatory (SDO)". *Solar Phys.* **275**, 229 – 259. doi:10.1007/s11207-011-9842-2.

Schou, J., Borrero, J.M., Norton, A.A., Tomczyk, S., Elmore, D., Card, G.L.: 2012b, "Polarization Calibration of the Helioseismic and Magnetic Imager (HMI) onboard the Solar Dynamics Observatory (SDO)". *Solar Phys.* **275**, 327 – 355. doi:10.1007/s11207-010-9639-8.

Schuck, P.W.: 2005, "Local Correlation Tracking and the Magnetic Induction Equation". *Astrophys. J. Lett.* **632**, L53 – L56. doi:10.1086/497633.

Schuck, P.W.: 2006, "Tracking Magnetic Footpoints with the Magnetic Induction Equation". *Astrophys. J.* **646**, 1358 – 1391. doi:10.1086/505015.

Schuck, P.W.: 2008, “Tracking Vector Magnetograms with the Magnetic Induction Equation”. *Astrophys. J.* **683**, 1134 – 1152. doi:10.1086/589434.

Schwenn, R.: 2006, “Space Weather: The Solar Perspective”. *Living Reviews in Solar Physics* **3**, 2. doi:10.12942/lrsp-2006-2.

Simon, G.W., Leighton, R.B.: 1964, “Velocity Fields in the Solar Atmosphere. III. Large-Scale Motions, the Chromospheric Network, and Magnetic Fields.”. *Astrophys. J.* **140**, 1120. doi:10.1086/148010.

Simon, G.W., Title, A.M., Topka, K.P., Tarbell, T.D., Shine, R.A., Ferguson, S.H., Zirin, H., SOUP Team: 1988, “On the relation between photospheric flow fields and the magnetic field distribution on the solar surface”. *Astrophys. J.* **327**, 964 – 967. doi:10.1086/166253.

Smyrli, A., Zuccarello, F., Romano, P., Zuccarello, F.P., Guglielmino, S.L., Spadaro, D., Hood, A.W., Mackay, D.: 2010, “Trend of photospheric magnetic helicity flux in active regions generating halo coronal mass ejections”. *Astron. Astrophys.* **521**, A56. doi:10.1051/0004-6361/200913275.

Sterling, A.C., Harra, L.K., Moore, R.L.: 2007, “New Evidence for the Role of Emerging Flux in a Solar Filament’s Slow Rise Preceding Its CME-producing Fast Eruption”. *Astrophys. J.* **669**, 1359 – 1371. doi:10.1086/520829.

Sterling, A.C., Moore, R.L., Freeland, S.L.: 2011, “Insights into Filament Eruption Onset from Solar Dynamics Observatory Observations”. *Astrophys. J. Lett.* **731**, L3. doi:10.1088/2041-8205/731/1/L3.

Sterling, A.C., Chifor, C., Mason, H.E., Moore, R.L., Young, P.R.: 2010, “Evidence for magnetic flux cancelation leading to an ejective solar eruption observed by Hinode, TRACE, STEREO, and SoHO/MDI”. *Astron. Astrophys.* **521**, A49. doi:10.1051/0004-6361/201014006.

Stern, R.A., Shing, L., Catura, P.R., Morrison, M.D., Duncan, D.W., Lemen, J.R., Eaton, T., Pool, P.J., Steward, R., Walton, D.M., Smith, A.: 2004, "Characterization of the flight CCD detectors for the GOES N and O solar x-ray imagers". In: Fineschi, S., Gummin, M.A. (eds.) *Telescopes and Instrumentation for Solar Astrophysics*, *Society of Photo-Optical Instrumentation Engineers (SPIE) Conference Series* **5171**, 77–88. doi:10.1117/12.506346.

Stix, M.: 2004, *"The sun : an introduction"*.

Sturrock, P.A. (ed.): 1980, *"Solar flares: A monograph from SKYLAB Solar Workshop II"*.

Su, Y., van Ballegooijen, A.: 2013, "Rotating Motions and Modeling of the Erupting Solar Polar-crown Prominence on 2010 December 6". *Astrophys. J.* **764**, 91. doi:10.1088/0004-637X/764/1/91.

Su, Y., Wang, T., Veronig, A., Temmer, M., Gan, W.: 2012, "Solar Magnetized "Tornadoes:" Relation to Filaments". *Astrophys. J. Lett.* **756**, L41. doi:10.1088/2041-8205/756/2/L41.

Svestka, Z.: 1976, "Solar flares". *Geophysics and Astrophysics Monographs* **8**.

Thompson, W.T.: 2011, "Strong rotation of an erupting quiescent polar crown prominence". *Journal of Atmospheric and Solar-Terrestrial Physics* **73**, 1138–1147. doi:10.1016/j.jastp.2010.07.005.

Titov, V.S., Démoulin, P.: 1999, "Basic topology of twisted magnetic configurations in solar flares". *Astron. Astrophys.* **351**, 707–720.

Török, T., Kliem, B.: 2005, "Confined and Ejective Eruptions of Kink-unstable Flux Ropes". *Astrophys. J. Lett.* **630**, L97–L100. doi:10.1086/462412.

Török, T., Berger, M.A., Kliem, B.: 2010, "The writhe of helical structures in the solar corona". *Astron. Astrophys.* **516**, A49. doi:10.1051/0004-6361/200913578.

Török, T., Panasenco, O., Titov, V.S., Mikić, Z., Reeves, K.K., Velli, M., Linker, J.A., De Toma, G.: 2011, "A Model for Magnetically Coupled Sympathetic Eruptions". *Astrophys. J. Lett.* **739**, L63. doi:10.1088/2041-8205/739/2/L63.

Tritschler, A., Bellot Rubio, L.R., Kentischer, T.J.: 2004, "Towards 2D-Spectropolarimetry with TESOS and Adaptive Optics". In: *American Astronomical Society Meeting Abstracts #204*, *Bulletin of the American Astronomical Society* **36**, 794.

Ugarte-Urra, I., Warren, H.P., Winebarger, A.R.: 2007, "The Magnetic Topology of Coronal Mass Ejection Sources". *Astrophys. J.* **662**, 1293 – 1301. doi:10.1086/514814.

van Ballegooijen, A.A.: 2004, "Observations and Modeling of a Filament on the Sun". *Astrophys. J.* **612**, 519 – 529. doi:10.1086/422512.

van Ballegooijen, A.A., Martens, P.C.H.: 1989, "Formation and eruption of solar prominences". *Astrophys. J.* **343**, 971 – 984. doi:10.1086/167766.

van Driel-Gesztelyi, L., Culhane, J.L.: 2009, "Magnetic Flux Emergence, Activity, Eruptions and Magnetic Clouds: Following Magnetic Field from the Sun to the Heliosphere". *Space Sci. Rev.* **144**, 351 – 381. doi:10.1007/s11214-008-9461-x.

Vemareddy, P., Ambastha, A., Maurya, R.A., Chae, J.: 2012, "On the Injection of Helicity by the Shearing Motion of Fluxes in Relation to Flares and Coronal Mass Ejections". *Astrophys. J.* **761**, 86. doi:10.1088/0004-637X/761/2/86.

Wang, J., Shi, Z.: 1993, “The flare-associated magnetic changes in an active region. II - Flux emergence and cancellation”. *Solar Phys.* **143**, 119 – 139. doi:10.1007/BF00619100.

Wang, Y.-M., Sheeley, N.R. Jr.: 1999, “Filament Eruptions near Emerging Bipoles”. *Astrophys. J. Lett.* **510**, L157 – L160. doi:10.1086/311815.

Wang, Y.-M., Muglach, K., Kliem, B.: 2009, “Endpoint Brightenings in Erupting Filaments”. *Astrophys. J.* **699**, 133 – 142. doi:10.1088/0004-637X/699/1/133.

Wedemeyer, S., Scullion, E., Rouppe van der Voort, L., Bosnjak, A., Antolin, P.: 2013, “Are Giant Tornadoes the Legs of Solar Prominences?”. *Astrophys. J.* **774**, 123. doi:10.1088/0004-637X/774/2/123.

Welsch, B.T., Fisher, G.H., Abbett, W.P., Regnier, S.: 2004, “ILCT: Recovering Photospheric Velocities from Magnetograms by Combining the Induction Equation with Local Correlation Tracking”. *Astrophys. J.* **610**, 1148 – 1156. doi:10.1086/421767.

Welsch, B.T., Abbett, W.P., De Rosa, M.L., Fisher, G.H., Georgoulis, M.K., Kusano, K., Longcope, D.W., Ravindra, B., Schuck, P.W.: 2007, “Tests and Comparisons of Velocity-Inversion Techniques”. *Astrophys. J.* **670**, 1434 – 1452. doi:10.1086/522422.

Williams, D.R., Török, T., Démoulin, P., van Driel-Gesztelyi, L., Kliem, B.: 2005, “Eruption of a Kink-unstable Filament in NOAA Active Region 10696”. *Astrophys. J. Lett.* **628**, L163 – L166. doi:10.1086/432910.

Xu, Y., Jing, J., Wang, H.: 2010, “Measurements of Filament Height in Hα and EUV 304 Å”. *Solar Phys.* **264**, 81 – 91. doi:10.1007/s11207-010-9573-9.

Yan, X.L., Qu, Z.Q., Kong, D.F., Xu, C.L.: 2012, “Sunspot Rotation, Sigmoidal Filament, Flare, and Coronal Mass Ejection: The Event on 2000 February 10”. *Astrophys. J.* **754**, 16. doi:10.1088/0004-637X/754/1/16.

Yan, X.L., Pan, G.M., Liu, J.H., Qu, Z.Q., Xue, Z.K., Deng, L.H., Ma, L., Kong, D.F.: 2013, “The Contraction of Overlying Coronal Loop and the Rotating Motion of a Sigmoid Filament during Its Eruption”. *Astron. J.* **145**, 153. doi:10.1088/0004-6256/145/6/153.

Yan, X.L., Xue, Z.K., Liu, J.H., Ma, L., Kong, D.F., Qu, Z.Q., Li, Z.: 2014, “Kink Instability Evidenced by Analyzing the Leg Rotation of a Filament”. *Astrophys. J.* **782**, 67. doi:10.1088/0004-637X/782/2/67.

Young, C.A.: 2007, “Mkit: An IDL Multiscale Toolbox”. In: *American Astronomical Society Meeting Abstracts #210*, *Bulletin of the American Astronomical Society* **39**, 133.

Zhao, M., Li, G., Wang, Z., Jing, Y., Li, Y.: 1995, “Improved self-reliance shearing interferometric technique for collimation testing”. In: Kujawinska, M., Pryputniewicz, R.J., Takeda, M. (eds.) *Interferometry VII: Techniques and Analysis*, *Society of Photo-Optical Instrumentation Engineers (SPIE) Conference Series* **2544**, 236 – 244.

Zhou, G.P., Wang, J.X., Zhang, J., Chen, P.F., Ji, H.S., Dere, K.: 2006, “Two Successive Coronal Mass Ejections Driven by the Kink and Drainage Instabilities of an Eruptive Prominence”. *Astrophys. J.* **651**, 1238 – 1244. doi:10.1086/507977.

Zirin, H.: 1988, *“Astrophysics of the sun”*.

Zirin, H.: 1995, “AG Ananth, K Kudela, D Venkatesan On the Comparison of Filter Magnetographs and the Advanced Stokes Polarimeter”. *Solar Phys.* **159**, 203 – 206. doi:10.1007/BF00733043.

Zirker, J.B., Engvold, O., Martin, S.F.: 1998, “Counter-streaming gas flows in solar prominences as evidence for vertical magnetic fields”. *Nature* **396**, 440 – 441. doi:10.1038/24798.

Zuccarello, F.P., Meliani, Z., Poedts, S.: 2012, "Numerical Modeling of the Initiation of Coronal Mass Ejections in Active Region NOAA 9415". *Astrophys. J.* **758**, 117. doi:10.1088/0004-637X/758/2/117.

Zuccarello, F.P., Romano, P., Zuccarello, F., Poedts, S.: 2011, "Magnetic helicity balance during a filament eruption that occurred in active region NOAA 9682". *Astron. Astrophys.* **530**, A36. doi:10.1051/0004-6361/201116700.

Zuccarello, F.P., Romano, P., Zuccarello, F., Poedts, S.: 2012, "The role of photospheric shearing motions in a filament eruption related to the 2010 April 3 coronal mass ejection". *Astron. Astrophys.* **537**, A28. doi:10.1051/0004-6361/201117563.

Zuccarello, F.P., Seaton, D.B., Mierla, M., Poedts, S., Rachmeler, L.A., Romano, P., Zuccarello, F.: 2014, "Observational Evidence of Torus Instability as Trigger Mechanism for Coronal Mass Ejections: The 2011 August 4 Filament Eruption". *Astrophys. J.* **785**, 88. doi:10.1088/0004-637X/785/2/88.

Zuccarello, F., Battiato, V., Contarino, L., Romano, P., Spadaro, D.: 2007, "Plasma motions in a short-lived filament related to a magnetic flux cancellation". *Astron. Astrophys.* **468**, 299–305. doi:10.1051/0004-6361:20066556.